

# **3D Printing of Soft and Biological Materials: Applications to Human Cochlear Modelling and Beyond**

**Iek Man Lei**

Department of Engineering  
Jesus College, University of Cambridge  
September 2021

*This thesis is submitted for the degree of Doctor of Philosophy.*

*I would like to dedicate this thesis to my parents and my sisters for their endless love, support  
and encouragement.*

## **Declaration**

This thesis is the result of my own work and includes nothing which is the outcome of work done in collaboration except as declared in the Preface and specified in the text. Briefly, the calibration of the stage speed of the printer in Chapter 3 was carried out by my colleague, Yaqi Sheng (Department of Engineering, University of Cambridge); The code for the heating control in Chapter 3 was jointly developed by me and Cillian Leon (Department of Engineering, University of Cambridge); The methacrylate hydroxypropyl cellulose used in Chapter 4 was produced by my collaborator Chun Lam Clement Chan (Department of Chemistry, University of Cambridge). The electrochemical impedance spectroscopy measurement in Chapter 5 was performed by my collaborator, Chen Jiang (Department of Clinical Neurosciences, University of Cambridge); The codes of the neural network model and lumped parameter model in Chapter 5 were developed by my collaborator, Chon Lok Lei (Department of Computer Science, University of Oxford). I further state that no substantial part of my thesis has already been submitted, or, is being concurrently submitted for any such degree, diploma or other qualification at the University of Cambridge or any other University or similar institution except as declared in the Preface and specified in the text. This thesis contains  $\sim 54,000$  words excluding bibliography and has 84 figures. It does not exceed the prescribed word limit for the relevant Degree Committee

Iek Man Lei

December 2021

# **Abstract**

## **3D Printing of Soft and Biological Materials: Applications to Human Cochlear Modelling and Beyond**

*Iek Man Lei*

3D printing has emerged as a promising tool for on-demand and rapid fabrication of materials. The field of soft material printing typically utilises inks that exhibit viscoelastic properties with elastic moduli in the kPa – MPa range, such as hydrogels and elastomers. Although soft material printing has been frequently used for creating biomimetic mini tissues, its ability to imitate organ functions as a direct result of organ anatomy is yet to be fully realised, and continued innovation in printing method and flexible machinery are needed to drive the field forward.

My PhD thesis focuses on advancing the field of soft material printing. Specifically, there are three main scopes in my work. **Firstly**, I developed an affordable and fully customisable extrusion-based printing platform for soft materials. The platform is equipped with multiple printheads for heterogeneous construct printing, and heating systems and a UV module for tuning the material rheology during and after printing. A detailed assembly instruction and the software design are provided, hence new users can facilely replicate the platform and contribute to the continued development of the platform. In summary, it is anticipated that this entirely hackable platform can facilitate the widespread adoption of the technology, overcoming the cost and flexibility barriers presented in commercial systems. **Secondly**, to realise the potential of 3D printing for imitating physiological phenomena related

to anatomical structures, I created 3D printed cochleae that exhibit similar electro-anatomical features resembling human cochleae. These biomimetic cochlear models were integrated with machine learning to advance clinical predictions of ‘current spread’ for cochlear implant (CI) patients. The co-modelling framework demonstrated autonomous predictions of patient electric field imaging profile or cochlear geometry, unfolded the electro-anatomical factors causing CI stimulus spread, assisted on-demand printing for CI testing, and inferred patients’ *in vivo* cochlear tissue resistivity by CI telemetry. This framework might facilitate physical modelling and digital twin innovations for neuromodulation implants in healthcare. **Lastly**, I demonstrate the high flexibility and versatile functionalities of the custom-made 3D extrusion printing platform. Apart from 3D CAD models, the standard geometry input used in 3D printing, the platform accepts unconventional geometry inputs to suit different needs, including coordinates, equations and pictures. Advanced operations, such as liquid dispensing, printing with variable speed and non-planar printing, are permitted with the platform. With the aid of support baths, heating and UV tools, a wide variety of soft materials, including naturally derived hydrogels, pH-responsive hydrogels and elastomers, were successfully printed using the platform. Overall, the perspective provided in this work might guide new users to efficiently design printing processes for soft materials that do not possess suitable rheological and mechanical properties for creating 3D structures with conventional extrusion methods.

## Acknowledgements

I would like to express my sincere gratitude to my supervisor, Dr Shery Huang. Thank you for your continuing guidance and encouragement during my PhD journey and giving me the opportunities to join your team and conduct the research work on soft material fabrication. Your work ethic and dedication have always motivated me to strive to improve. I am truly grateful for the insightful vision and immense knowledge you have shared with me. These have introduced me to the fascinating area of research and have greatly helped shape me as a researcher.

Thank you to all my collaborators, Prof. Manohar Bance, Chen Jiang, Simone De Rijk, Yu Chuen Tam, Chon Lok Lei and Chun Lam Clement Chan, for your patience, support and preserving with me throughout the project. The insightful comments you have provided were valuable, and I have learnt so much from working with you. I would also like to thank Ian Ganney and the technicians in Cavendish workshop for helping me with the machining work; Anthony Dennis for your assistance with  $\mu$ -CT imaging.

I would like to acknowledge the W D Armstrong Trust and Macao Postgraduate Scholarship for funding my PhD study, and Jesus College for supporting my attendance at conferences.

Lastly, I would like to thank all the past and present group members of the Biointerface team for your support and entertainment. It has been a great pleasure working with all of you. I am profoundly grateful to have met you all. A big thanks to Yaqi Sheng, Duo Zhang and Andy Wang for being my lab buddies. Your encouragement has helped me a lot when I was struggling. I truly cherish the time we have spent together in the lab.

# Publications

## Published:

1. Li Z, **Lei IM**, et al. (2019) Solution Formulation and Rheology for Fabricating Extracellular Matrix-Derived Fibers Using Low-Voltage Electrospinning Patterning. *ACS Biomater Sci Eng.*
2. Li Z, Tuffin J, **Lei IM**, et al. (2018) Solution fibre spinning technique for the fabrication of tuneable decellularised matrix-laden fibres and fibrous micromembranes. *Acta Biomater.* 78:111-122.
3. **Lei IM**, Jiang C, et al. (2021) 3D printed biomimetic cochleae and machine learning co-modelling provides clinical informatics for cochlear implant patients. *Nat. Commun.* 6260, 12. (*Chapter 5 utilises the excerpts of this manuscript.*)

## Submitted:

1. Chan CLC, **Lei IM**, et al. (2021) 3D printing of liquid crystalline hydroxypropyl cellulose – towards tunable and sustainable volumetric photonic structures. (*Chapter 4 (4.3.3.2) utilises the content of this manuscript.*)
2. Fathi S, **Lei IM**, Huang YYS. (2021) Visualizing cell extrusion deposition through a microcapillary tip with picolitre resolution.

## In preparation:

1. **Lei IM**, Huang YYS, et al. Development of a three-dimensional bioprinting platform with customizable printing strategies. (*Chapters 3 and 4 utilise the content of this manuscript.*)
2. **Lei IM**, Huang YYS, et al. Recent advances in the design of support baths for embedded 3D printing soft materials. (Review article) (*Chapter 1 utilises the content of this manuscript.*)

# Table of Contents

<b>Declaration.....</b>	<b>II</b>
<b>Abstract.....</b>	<b>III</b>
<b>Acknowledgements .....</b>	<b>V</b>
<b>Publications .....</b>	<b>VI</b>
<b>Table of Contents .....</b>	<b>VII</b>
<b>List of Figures.....</b>	<b>XII</b>
<b>List of Tables .....</b>	<b>XVI</b>
<b>Nomenclature .....</b>	<b>XVII</b>
<b>Chapter 1 Literature Review .....</b>	<b>1</b>
1.1    Introduction.....	1
1.2    Hydrogels.....	2
1.2.1    Crosslinking mechanisms .....	3
1.2.2    Reinforcement mechanisms .....	9
1.2.3    Swelling capability of hydrogels .....	11
1.3    Silicone and epoxy resins.....	12
1.4    Overview of 3D printing strategies.....	13
1.4.1    Light-based approach.....	14
1.4.2    Ink-based approach .....	15
1.5    Embedded 3D extrusion printing .....	16
1.5.1    General requirements of support bath and ink.....	18

1.5.2	Instabilities caused by the mismatch properties between the ink and the bath..	19
1.5.3	General rheological characteristics of the ink and the support bath .....	22
1.5.4	Development in support baths for embedded 3D extrusion printing .....	23
1.6	Printing with sacrificial inks .....	34
	Carbohydrate glass.....	37
	Pluronic F127.....	38
	Gelatin.....	40
	Agarose .....	40
	Wax .....	40
	Other sacrificial inks .....	41
	<b>Chapter 2 Research Contribution and Thesis Layout.....</b>	<b>42</b>
2.1	Motivation and research aims .....	42
2.2	Research contributions.....	44
2.3	Thesis Layout.....	45
	<b>Chapter 3 Development of a Printing Platform for Soft Materials.....</b>	<b>46</b>
3.1	Introduction.....	46
3.2	Materials and Methods.....	48
3.2.1	Materials .....	48
3.2.2	Creation of 3D printed parts .....	48
3.2.3	Calibration of printhead extrusion .....	50
3.2.4	Printing experiments for validating the coordinate transformation equations used in the control programme.....	50
3.3	Printer assembly .....	50
3.3.1	Stage and robotic arm as motion module.....	52
3.3.2	Dispensing module.....	53
3.3.3	Heating modules .....	58
3.3.4	UV module and camera .....	59

3.4 Calibration of components .....	59
3.4.1 Printhead extrusion .....	59
3.4.2 Stage speed.....	60
3.5 Control programme.....	61
3.5.1 Control programme for printing operation .....	62
3.5.2. Heating .....	69
3.6 System specification .....	71
3.7 Limitations and future improvement .....	73
3.8 Conclusion .....	73
<b>Chapter 4 An Investigation on Methods for Soft Material Printing.....</b>	<b>75</b>
4.1 Introduction.....	75
4.2 Materials and Methods.....	76
4.2.1 Materials .....	76
4.2.2 Solution preparation.....	77
4.2.3 Support bath preparation and the methods for releasing the printed constructs from the baths .....	79
4.2.4 Soft material printing .....	81
4.2.5 Dispensing of cell suspension.....	85
4.2.6 Non-planar printing.....	86
4.2.7 Printing and removal of sacrificial template .....	86
4.2.8 Printing of PAA strips for pH-responsive morphing .....	87
4.3 Results and discussion .....	87
4.3.1 A versatile platform for flexible geometry inputs.....	87
4.3.2 Multi-functionalities in one platform – from conventional 3D extrusion printing to advanced techniques .....	89
4.3.3 Fabricating complex structures with a wide range of soft materials .....	91
4.3.4 A guide to the selection of printing approach .....	108

4.4 Conclusions.....	110
<b>Chapter 5 3D Printed Biomimetic Cochleae and Machine Learning Co-modelling Provides Clinical Informatics for Cochlear Implant Patients .....</b>	<b>111</b>
5.1 Introduction.....	111
Box 5.1 - Background of cochlear implants .....	114
5.2 Materials and Methods.....	115
5.2.1 3D printing material preparation.....	115
5.2.2 Embedded 3D printing of biomimetic cochleae .....	115
5.2.3 EFI measurements in 3D printed biomimetic cochleae .....	119
5.2.4 Resistivity measurements.....	120
5.2.5 Electrochemical impedance spectroscopy (EIS) measurements .....	121
5.2.6 Micro-computed tomography scans of the 3D printed biomimetic cochleae..	121
5.2.7 Patient EFI profiles and CT scans.....	122
5.2.8 Development of 3PNN.....	123
5.2.9 Clinical predictions of 3PNN.....	126
5.2.10 Production of 3D printed models that give patient-specific EFI profiles ....	126
5.2.11 Finite element modelling of the intracochlear voltage distribution in cochlea	
128	
5.2.12 Statistical method .....	130
5.3 Results and Discussion .....	131
5.3.1 Designable electro-mimetic bone matrices.....	131
5.3.2 3D printed biomimetic cochleae .....	135
5.3.3 Development of the neural network model .....	141
5.3.4 Applicability of 3PNN on different electrode types .....	145
5.3.5 Clinically validated 3PNN shows high statistical predictive performance.....	145
5.3.6 Effect of cochlear electroanatomy on CI voltage spread .....	151
5.3.7 On-demand creation of biomimetic cochleae inheriting patient EFIs .....	154

5.3.8	Informing patient-specific cochlear tissue resistivity .....	157
5.3.9	Potential uncertainty in 3PNN .....	158
5.3.10	Limitation of finite element modelling .....	161
5.4	Conclusion .....	163
<b>Chapter 6 Conclusions and Future Work .....</b>		<b>166</b>
6.1	Conclusions.....	166
6.1.1	Development of a printing platform for soft materials .....	166
6.1.2	An investigation on methods for soft material printing .....	167
6.1.3	3D printed biomimetic cochleae and machine learning co-modelling provides clinical informatics for cochlear implant patients.....	168
6.2	Future work .....	169
6.2.1	Further development of the custom-made 3D extrusion printing platform ....	169
6.2.2	Fabrication of complex pH-responsive soft actuators .....	170
6.2.3	Rheological and interfacial measurements of inks and support baths .....	170
6.2.4	Further improvement on the 3PNN co-modelling framework.....	171
<b>References .....</b>		<b>172</b>

# List of Figures

Figure 1.1  Approximate Young's modulus of selected hydrogels, rigid materials and biological tissues.....	2
Figure 1.2  Crosslinking of hydrogels.....	7
Figure 1.3  Schematic showing the polymeric networks of traditional hydrogels and three common types of reinforced hydrogels.....	10
Figure 1.4  Schematics showing the pH-responsive swelling and the electro-responsive swelling mechanism of hydrogels. ....	12
Figure 1.5  Overview of 3D printing strategies.. ..	13
Figure 1.6  Comparison between in-air and embedded 3D extrusion printing. ....	17
Figure 1.7  Overview of embedded printing technology. ....	17
Figure 1.8  Rheological properties of materials .....	19
Figure 1.9  a) Pictures depicting the printing paths of rectilinear and concentric patterns. b) Schematic showing that the use of a fluid filler to fill the crevasse induced by nozzle translation through the bath. ....	21
Figure 1.10  Selected examples of support baths used for embedded printing in literature. ..	28
Figure 1.11  Examples of conventional methods for producing vascular structures. ....	35
Figure 1.12  Overview of sacrificial printing methods for producing vascular channel structures. ....	35
Figure 1.13  Selected examples of sacrificial inks to produce vasculature in literature. ....	39
Figure 2.1  Overview of the results chapters. ....	45
Figure 3.1  Factors controlling the print fidelity of soft materials. ....	46
Figure 3.2  A custom-made 3D extrusion printing platform. ....	51
Figure 3.3  Assembly procedure of the stage to the uArm.....	53
Figure 3.4  a) A printhead built with smooth rods as motion guide. b) the magnetic design of the printhead.....	54
Figure 3.5  Assembly procedure of the printhead. ....	56
Figure 3.6  Circuit diagram for connecting a stepper motor with Arduino and a motor drive.	56
Figure 3.7  Overall circuit diagram of the dispensing module composed of four printheads..	57

Figure 3.8  Circuit diagram of a heating module. ....	58
Figure 3.9  Performance and calibration of the printheads. ....	60
Figure 3.10  Relationship between the actual speed and the unitless speed quantity of uArm. ....	61
Figure 3.11  Overview of the control for the a) printing and b) heating operations. ....	61
Figure 3.12  Logical structure of the control programme for printing operation.....	62
Figure 3.13  The assigned keys of the printheads and the stages. ....	63
Figure 3.14  Flowchart showing the manual calibration procedure.....	67
Figure 3.15  Coordinate transformation. ....	68
Figure 3.16  Flowchart of the heating control.....	70
Figure 4.1  Figure comparing the print paths of a simple ‘Y’ shaped pattern generated via slicing a 3D CAD model and via the coordinate method. ....	88
Figure 4.2  Constructs printed using the coordinate, equation, CAD model and picture geometry input options.....	89
Figure 4.3  Versatile functionalities of the 3D extrusion printing platform. ....	90
Figure 4.4  3D printed constructs made of natural hydrogels, bioceramics-hydrogels, synthetic hydrogels and silicone elastomers. ....	92
Figure 4.5  The CAD models and the 2D pattern of the constructs shown in Figure 4.4. ....	92
Figure 4.6  Optical transparency of the frequently used support baths in literature. ....	93
Figure 4.7  Printing of collagen.....	95
Figure 4.8  Printing of gellan gum in a Carbopol bath.....	96
Figure 4.9  Printing of sodium carboxymethyl cellulose and post-printing crosslinking with a chitosan solution.. ....	98
Figure 4.10  Printing of Methacrylate hydroxypropyl cellulose. ....	100
Figure 4.11  Printing of chitosan.....	102
Figure 4.12  The pH-swelling effect of poly(acrylic acid) during embedded printing in aqueous baths. ....	103
Figure 4.13  Printing of poly(acrylic acid) (PAA) in oil-based support baths. ....	104
Figure 4.14  Evolution of asymmetrical pH-responsive morphing of PAA strips printed at different infill angles. ....	105
Figure 4.15  a) The transient and unfolding stages of a pH-responsive morphing system. b) The reversible morphing behaviour .....	106
Figure 4.16  Printing of Ecoflex.....	107
Figure 4.17  Decision flowchart guiding the selection of a suitable printing approach.....	109

Figure 5.1  Schematic of the auditory system and the cochlea with a CI implanted. ....	112
Figure 5.2  Overview of the 3PNN co-modelling framework for providing clinical informatics. ....	113
Figure 5.3  a) Sound transduction process in healthy auditory systems. b) Sketch of a cochlear implant. c) The tonotopic organisation of human cochleae. ....	114
Figure 5.4  Microchannel network of the electro-mimetic bone matrix. ....	116
Figure 5.5  Correlation of the actual dimensions of the model descriptors measured from $\mu$ -CT and the process parameters of the custom-built 3D printer. 117	
Figure 5.6  Appearance of 3D printed cochlear models made of an electro-mimetic bone matrix, a hydrogel, and a hydrogel-filters matrix.....	117
Figure 5.7  a) Electrical conductivity of NaCl solutions at various concentrations at ambient temperature. b) Photo demonstrating the insertion of a CI electrode array in a biomimetic cochlea during EFI measurements. ....	120
Figure 5.8  Hyperparameter tuning of the neural network model.....	125
Figure 5.9  Domain properties of the COMSOL cochlear models .....	129
Figure 5.10  Resistivities of live human, animal and human cadaveric cortical bones or skulls reported in literatur. ....	131
Figure 5.11  Schematic of the embedded 3D extrusion printing strategy to produce the electro-mimetic bone matrices and the biomimetic cochleae. ....	132
Figure 5.12  Electrical properties of electro-mimetic bone matrices.....	133
Figure 5.13  A map of resistivity versus Young's modulus of human tissues, thermoplastics, the hydrogel-filters matrices, and the electro-mimetic bone matrices. ....	134
Figure 5.14  Resistivity (plateau value) of the hydrogel matrices and hydrogel-filters matrices. ....	135
Figure 5.15  Schematic of the routine CI assessment process. ....	136
Figure 5.16  a) Finite element model of cochlea i) with the Reissner's membrane and the Basilar membrane and ii) without the intracochlear membranous structures. ....	136
Figure 5.17  $\mu$ -CT reconstructed images of the spiral lumen of the biomimetic cochleae with different features of geometric descriptors. ....	137
Figure 5.18  3D printed biomimetic cochleae enable geometrically-guided CI positioning. 140	
Figure 5.19  Comparison of the mean patient EFI profile, and the EFI profiles obtained from 3D printed models made of hydrogel, solid PDMS and electro-mimetic bone matrix.....	141
Figure 5.20  Long-lasting properties of the biomimetic cochleae. ....	141
Figure 5.21  Schematic of the workflow of 3PNN. ....	142

Figure 5.22  1 <sup>st</sup> order lumped parameter model proposed by Vanpoucke et al. for modelling the electrical volume conduction within cochleae.....	144
Figure 5.23  Applicability of 3PNN on different electrode types.....	146
Figure 5.24  The clinical EFIs used in the validation of 3PNN to represent the EFI variation in patient population.....	147
Figure 5.25  Validation of forward-3PNN.....	148
Figure 5.26  Comparison of the mean patients' EFI profile and the profile of subject 4 <sup>CI522</sup> .....	149
Figure 5.27  Validation of inverse-3PNN.....	150
Figure 5.28  Example showing the trend of the predicted EFI profiles along the 5 model descriptors.....	151
Figure 5.29  Example of the power-law fitting analysis of EFIs.....	153
Figure 5.30  Goodness-of-fit test to evaluate the choice of the fitting forms.....	154
Figure 5.31  The trend of <i>Slopex</i> = 1mm of the stimulus spreads toward the cochlear apex and the cochlear base across each model descriptor.....	154
Figure 5.32  On-demand creation of biomimetic cochleae for replicating patient EFIs. ....	155
Figure 5.33  The electrode positions in a model showing an atypical ‘mid-dip’ EFI profile and a model with a typical EFI profile. ....	156
Figure 5.34  3PNN estimating patient-specific resistivity of the cochlear tissue.....	157
Figure 5.35  Sensitivity analyses assessing the effect of the potential sources of uncertainty on EFIs.....	160
Figure 5.36  The effect of boundary conditions on finite element modelling of cochlear stimulation.....	162
Figure 6.1  A preliminary prototype of a micropipette printhead.....	169

## List of Tables

Table 1.1  Features and the typical physical crosslinking methods of natural hydrogels.....	4
Table 1.2  Features and the typical physical crosslinking methods of synthetic hydrogels.....	5
Table 1.3  Support baths developed for embedded printing applications in literature. ....	24
Table 1.4  Common sacrificial inks used in literature. ....	36
Table 3.1  Part list and the breakdown costs of the printing platform .....	48
Table 3.2  Arduino pin configuration for the current limiting procedure and normal operation. .....	57
Table 3.3  Examples of the equation format used in the Python programme. ....	65
Table 3.4  Specifications of the system developed in this chapter and the four commercial 3D extrusion-based bioprinters commonly used in the bioprinting community. ....	71
Table 3.5  Table comparing the system developed in this chapter with existing reported open-source extrusion bioprinters.....	72
Table 4.2  Formulations of inks and support baths used in Chapter 4.....	81
Table 4.3  Equations used for fabricating the one-stroke features demonstrated in Chapter 4. .....	84
Table 4.4  A summary of the adopted methods used for printing different soft materials. ...	107
Table 5.1  Specifications of the 82 biomimetic cochleae used in 3PNN training.....	118
Table 5.2  Input values of the stimulating and the recording electrode positions of different electrode types used in 3PNN. ....	126
Table 5.3  The final MAPE thresholds used in the inverse predictions.....	127
Table 5.4  Definitions and the ranges of the model descriptors investigated in this study in comparison with the reported variation in human cochlea .....	138
Table 5.5  3PNN performance compared with the MAPE obtained from the population mean EPI.....	149
Table 5.6  Table summarised the potential uncertainties in 3PNN, and their estimated effect on off-stimulation EFIs. ....	161

# Nomenclature

## Abbreviations

3PNN	3D printing and neural network co-modelling
ABS	Acrylonitrile butadiene styrene
AD	Adamantane
APS	Ammonium persulfate
CAD	Computer-aided design
CAL	Computed axial lithography
CI	Cochlear implant
CI <sup>1J</sup>	Advanced Bionics HiRes 90K® implant with HiFocus™ 1J electrode array
CI <sup>SlimJ</sup>	Advanced Bionics HiRes™ Ultra implant with HiFocus™ SlimJ electrode array
CI522	Cochlear™ Nucleus® Profile Plus with slim straight electrode CI522
CI622	Cochlear™ Nucleus® Profile Plus with slim straight electrode CI622
CMC	Critical micelle concentration
CMT	Critical micelle temperature
DIW	Direct Ink Writing
DLP	Digital light processing
DN	Double network
ECM	Extracellular matrix
EDC	1-Ethyl-3-(3-dimethylaminopropyl)carbodiimide
EFI	Electric field imaging
FDM	Fused deposition modelling
FEM	Finite element modelling
FRESH	Freeform reversible embedded suspending hydrogel
GelMA	Gelatin methacryloyl
HA	Hyaluronic acid
HEPES	(4-(2-hydroxyethyl)-1-piperazineethanesulfonic acid)
I2959	Irgacure 2959
IPN	Interpenetrating polymer network
LAP	Lithium phenyl-2,4,6-trimethylbenzoylphosphinate / Laser-assisted printing
LCST	Lower critical solution temperature
MA	Methacrylated
NaAlg	Sodium alginate
PAA	Poly(acrylic acid)
PAAm	Polyacrylamide
PBS	Phosphate buffered saline
PCL	Polycaprolactone
PDLGA	poly(D-lactide-co-glycolide)
PDMS	Polydimethylsiloxane
PEGDA	Poly(ethylene glycol) diacrylate
PEO	Polyethylene oxide
PF127	Pluronic F127
pKa	Acid dissociation constant
PNIPAM	Poly(N-isopropylacrylamide)
PVA	poly(vinyl alcohol)
RGD	Tripeptide Arg-Gly-Asp
SLA	Stereolithography

---

TEMED	Tetramethylethylenediamine
TPP	Tripolyphosphate
UCST	Upper critical solution temperature
$\beta$ -CD	$\beta$ -cyclodextrin

## Symbols

$(a, b)$	x, y coordinates of the nozzle tip of the printhead from the base of the uArm
$BL_d$	Basal lumen diameter
$e$	Boolean extrusion parameter
$f_{void}$	Void fraction
$G'$	Storage or elastic modulus
$G''$	Loss or viscous modulus
$h_c$	Cochlear height
$I_{max}$	Current limit of the motor drive
$I_{rating}$	Current limit of the stepper motor
$I_{stim}$	Stimulation current impulse used in EFI measurements
$R$	Distance between the centre point of the stage and the position sensor of the uArm
$r_{Basal}$	Basal resistor in lumped parameter model
$R_{cs}$	Current sense resistance of the motor drive
$r_L$	Longitudinal resistor in lumped parameter model
$r_T$	Transversal resistor in lumped parameter model
$spnp$	Speed of the non-printing path
$spp$	Speed of the printing path
$Tr_a$	Cochlear taper ratio
$t_s$	Time interval between consecutive steps of the stepper motor
$V$	Intracochlear voltage
$V_{ref}$	Reference voltage of the motor drive
$\dot{V}_s$	Steady-state extrusion flow rate
$W_c$	Cochlear width
$x', y'$	Transformed coordinates relative to the base of the uArm for printing
$x_{print}, y_{print}$	Coordinates of the geometry relative to the stage centre
$x_{shift}, y_{shift}$	Shifting values of the x, y positions in calibration
$z$	Transimpedance or impedance
$ z $	Plateau impedance magnitude or Plateau transimpedance magnitude
$Z_0$	$z$ position of the stage
$z_{shift}$	Shifting value of the z position in stage calibration
$\beta$ ,	Rotation angle used in transformation
$\gamma$	Interfacial tension
$\varepsilon_f$	Optimal MAPE threshold used in 3PNN inverse prediction
$\pi$	Osmotic pressure
$\rho_{matrix}$	Resistivity of the electro-mimetic bone matrix
$\sigma_{bone}$	Bone conductivity
$\tau$	Shear stress
$\tau_y$	Yield stress
$\theta$	Angle between a horizontal line and the line connecting the base and the stage centre
$\rho$	Density
$\dot{\gamma}$	Shear rate
$n$	Flow index
$k$	Consistency index

# Chapter 1

## Literature Review

### 1.1 Introduction

The advent of 3D printing opens up unprecedented freedom to create complex architected matter from a wide variety of functional materials, revolutionising a range of research sectors, such as material science, biomedicine and robotics [1–4]. Unlike conventional manufacturing methods, such as solvent casting or soft lithography that require toxic solvent and time-consuming fabrication process [5], the key advantages of 3D printing are its flexibility in rapid prototyping to shorten design cycles [4] and its capability of creating structures with heterogenous architecture and composition across different length scales [2, 4, 6]. Since the invention of the first 3D printing method by Charles W. Hull during 1980s in the form of stereolithography [7, 8], this technology have been widely adopted in myriad applications, from 3D printed anatomical models for surgical planning to patient-specific implants [9], from fluidic devices to bio-functional tissue models [1, 4], and many more.

Notwithstanding the exciting advancements in 3D printing technology, notable challenges, such as limited selection of compatible materials and the need for increased feature resolution and speed, are yet to be overcome [8, 10]. Conventional materials used in 3D printing are in the form of thermoplastic filaments, photocurable resins, ceramics or metal powders [6, 11]. However, the Young's moduli ( $E$ ) of these materials are in the MPa – GPa range [12, 13] that are in general too rigid and stiff for mimicking the wide spectrum of the stiffness of native biological tissues, ranging from  $E \sim 1$  kPa (very soft tissues) to  $E \sim 10$  GPa (hard tissues) [14] (see **Figure 1.1**). To unleash the vast potential of 3D printing for tissue engineering and soft robot applications, new printing strategies have been developed, enabling fabrication of functional soft materials, from elastomers ( $E = \sim 0.05 - 2.4$  MPa [15]) to hydrogels ( $E = 2 - 300$  kPa [6]).

This chapter begins by reviewing a wide variety of soft and biological polymeric materials, with a focus on their features and crosslinking methods. An overview of the 3D printing strategies is then presented, focusing on the extrusion-based 3D printing technologies. Finally, the emerging trends in embedded 3D extrusion printing and sacrificial printing for architecting soft materials and vasculature-like networks are comprehensively discussed.

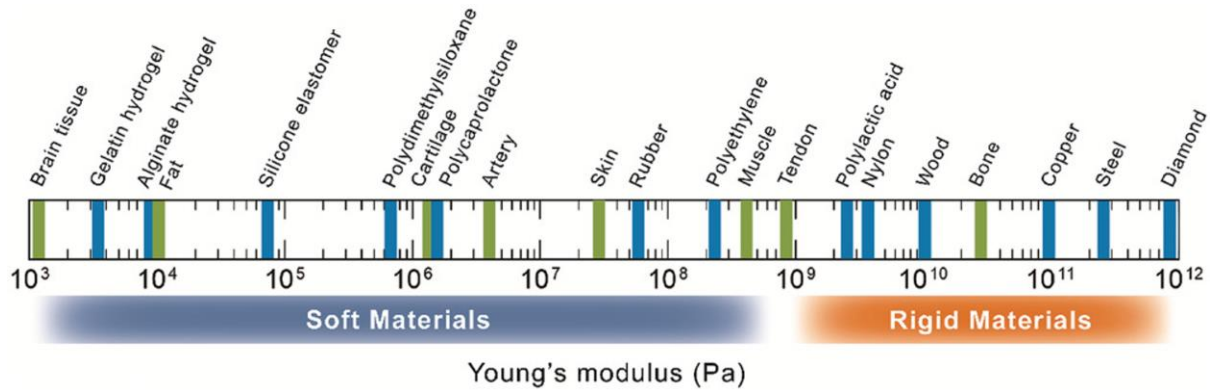


**Figure 1.1| Approximate Young's modulus of selected hydrogels, rigid materials and biological tissues.** Reproduced from [14].

## 1.2 Hydrogels

Hydrogels are formed by three-dimensional entangled networks of viscoelastic polymers networks that retain large amount of water in swollen state [16, 17]. Their good biocompatibility (i.e. good permeability for oxygen and nutrients) and/or stimuli-responsive functionality have endowed them with vast applications in soft electronics and tissue engineering [14, 18]. Based on their natural or synthetic origins, hydrogels can be classified into two groups. **Naturally-derived hydrogels** include proteins (e.g. collagen, fibrin, silk, Matrigel and extracellular matrix) and polysaccharides (e.g. alginate, chitosan, agarose and cellulose derivatives). They typically have advantages of cell-adhesive characteristics or biocompatibility, but are subject to batch-to-batch variability [19]. On the contrary, **synthetically-derived hydrogels** offer long-term stability, greater flexibility in tailoring properties and improved batch-to-batch consistency [16, 20], but they lack biological moieties for cell interaction and degradation, therefore require functionalisation with cell-adhesion motifs (such as RGD peptides) [19, 21]. Representative examples of synthetic hydrogels are polyethylene oxide (PEO), poly(acrylic acid) (PAA), polyvinyl alcohol (PVA) and Pluronics.

On the other side, hydrogel can be classified based on their ionic charges. For example, anionic hydrogels contain carboxyl groups ( $\text{-COO}^-$ ); cationic hydrogels contain amine groups ( $\text{-NH}_3^+$ ); amphoteric hydrogels contain both carboxyl and amine groups, and non-ionic hydrogels only contain hydroxyl ( $\text{-OH}$ ) or amide ( $\text{-CONH}_2$ ) groups. **Table 1.1 – 1.2** provide a detailed summary of the signature features and the usual physical crosslinking method of common hydrogel materials. The sections below discuss the crosslinking mechanisms of hydrogels, reinforcement methods and their stimuli-responsive behaviours.

### 1.2.1 Crosslinking mechanisms

The crosslinking of hydrogels controls their mechanical and swelling properties. This increases its viscosity for printing and preserves its shape after printing [22]. Various crosslinking mechanisms have been reported in literature, including **physical** (i.e. ionic, self-assembly induced by pH and temperature, cryogelation and host-guest interaction) and **covalent crosslinking** (i.e. UV, wet-chemical and enzymatic crosslinking) [17]. The advantages of physical crosslinking are its reversible interactions without the need for toxic solvents, however, physical hydrogels are in general mechanically weaker than covalent hydrogels [22, 23].

#### 1. Physical crosslinking

##### 1. Ionic/electrostatic interaction

Ionic crosslinking can be happened via two routes—(1) via ionic crosslinking with metal ions (**Figure 1.2a.i**) and (2) via electrostatic interaction (**Figure 1.2a.ii**). The former is usually used in crosslinking negatively charged polysaccharides, such as sodium alginate and gellan gum that crosslink with multivalent cations (e.g.  $\text{Ca}^{2+}$  and  $\text{Fe}^{3+}$ ) [17, 24]. The latter occurs when mixing oppositely charged polyelectrolytes to result polyelectrolyte complexes [17, 23]. Chitosan is a typical example that forms polyelectrolyte complexes with proteins and polyanions (e.g. tripolyphosphate (TPP) and alginate) [17, 25]. Of these two routes, electrostatic crosslinking with polyelectrolytes are more cell-friendly as metal ions might cause potential cytotoxic effects [23].

**Table 1.1| Features and the typical physical crosslinking methods of natural hydrogels.** GelMA: Gelatin methacryloyl.

	Materials	Cell adhesive	Functional groups	Origins	Features	Crosslinking methods	Ref.
Proteins	Collagen	✓	-NH <sub>3</sub> <sup>+</sup> -COO <sup>-</sup>	Mammal	<ul style="list-style-type: none"> <li>Type I: skin, vasculature, bone</li> <li>Type II: Cartilage</li> <li>Type IV: basement membrane</li> </ul>	<ul style="list-style-type: none"> <li>Thermal (37°C)</li> <li>pH 7</li> <li>Enzymatic</li> </ul>	[26]
	Fibrin	✓	-NH <sub>3</sub> <sup>+</sup> -COO <sup>-</sup>	Mammal	<ul style="list-style-type: none"> <li>Involved in blood clotting</li> <li>Fast degradation</li> <li>Very weak mechanical properties</li> </ul>		[27]
	Matrigel	✓	-NH <sub>3</sub> <sup>+</sup> -COO <sup>-</sup>	Mouse	• ECM secreted by mouse tumor cells		[27]
	Silk fibroin	✓	-NH <sub>3</sub> <sup>+</sup> -COO <sup>-</sup>	Silkworm	• Weakly adhere to cells		[28]
	Gelatin	✓	-NH <sub>3</sub> <sup>+</sup> ; -COO <sup>-</sup>	Mammal, fish	<ul style="list-style-type: none"> <li>Elastic</li> <li>Denatured form of collagen</li> <li>pH swelling</li> </ul>	• Thermal (< 25°C)	[29, 30]
	GelMA	✓	-NH <sub>3</sub> <sup>+</sup> -COO <sup>-</sup> -MA		• Low swelling compared to gelatin	• Thermal (< 25°C) • UV	[27]
Polysaccharides	Hyaluronic acid / Sodium hyaluronate	X	-COO <sup>-</sup> -OH	Mammal, bacteria	<ul style="list-style-type: none"> <li>Ink thickener</li> <li>Good shear thinning properties</li> </ul>	• Thaw-freeze	[31, 32]
	Agarose	X	-OH	Seaweeds	<ul style="list-style-type: none"> <li>Brittle</li> <li>Good stability</li> </ul>	• Thermal (< 20-70 °C)	[27]
	Sodium Alginate	X	-COO <sup>-</sup> -OH		<ul style="list-style-type: none"> <li>Popular hydrogel in bioprinting</li> <li>Good printability after ionic crosslinking</li> </ul>	• Ionic	[27]
	Carrageenan	X	-SO <sub>3</sub> <sup>-</sup> -OH		<ul style="list-style-type: none"> <li>Ink thickener</li> <li>3 types: <math>\iota</math>-, <math>\kappa</math>- and <math>\lambda</math>- types</li> <li>Only <math>\iota</math>- and <math>\kappa</math>- can be physically crosslinked</li> <li>Monovalent ions are effective on <math>\kappa</math>- type</li> </ul>	• Ionic • Thermal (< 40-70 °C)	[33]
	Gellan gum	X	-COO <sup>-</sup> -OH	Bacteria	• Brittle	• Ionic • Thermal (< 40-65 °C)	[34]
	Xanthan gum	X	-COO <sup>-</sup> -OH		<ul style="list-style-type: none"> <li>Thickener</li> <li>Effective crosslinking with trivalent ions</li> <li>pH-resistant properties</li> </ul>	• Ionic	[35]
	Carboxy-methyl-cellulose	X	-COO <sup>-</sup> -OH		• Ink thickener	-	[36]
	Methyl-cellulose	X	-OH	Plant	• LCST hydrogel	• Thermal (LCST > 60 °C)	[37]
	Hydroxy-propyl cellulose	X	-OH		<ul style="list-style-type: none"> <li>LCST hydrogel</li> <li>Enhanced ionic conductivity properties</li> </ul>	• Thermal (LCST > 30 °C)	[37, 38]
	Chitosan	✓	-NH <sub>3</sub> <sup>+</sup> -OH	Shrimp shells	<ul style="list-style-type: none"> <li>Only natural cationic polysaccharide</li> <li>Antibacterial</li> <li>pH-responsive swelling</li> </ul>	<ul style="list-style-type: none"> <li>Thaw-freeze</li> <li>pH</li> <li>Ionic</li> <li>Thermal</li> </ul>	[33, 39]

**Table 1.2| Features and the typical physical crosslinking methods of synthetic hydrogels.** PVA: Polyvinyl alcohol, PEO: Polyethylene oxide, PEG: Polyethylene glycol, PEGDA: Poly(ethylene glycol) diacrylate and PNIPAM: Poly(N-isopropylacrylamide).

Materials	Cell adhesive	Functional groups	Features	Crosslinking methods	Ref.
Glycerol	X	-OH	<ul style="list-style-type: none"> <li>• A humectant</li> <li>• A softener</li> </ul>	-	[29]
Polyacrylamide	X	-CONH <sub>2</sub>	<ul style="list-style-type: none"> <li>• Used in tough hydrogels</li> <li>• Elastic, stretchable, swellable</li> </ul>	• Chemical	[40]
Poly(acrylic acid)	X	-COO <sup>-</sup>	<ul style="list-style-type: none"> <li>• known to swell in alkali</li> <li>• Adhesive and stretchable</li> </ul>	• Chemical	[41]
PVA	X	-OH	<ul style="list-style-type: none"> <li>• Act as a coagent to promote intermolecular interaction</li> <li>• Good stretchability</li> </ul>	<ul style="list-style-type: none"> <li>• Thaw-freeze</li> <li>• Chemical (borax)</li> </ul>	[38, 42]
PEO / PEG	X	-OH	<ul style="list-style-type: none"> <li>• Ink thickener</li> <li>• Act as a coagent to promote intermolecular interaction</li> </ul>	-	[42]
PEGDA	X	-OH	<ul style="list-style-type: none"> <li>• Brittle</li> </ul>	• UV	-
Pluronic F127	X	-OH	<ul style="list-style-type: none"> <li>• Excellent printability</li> <li>• Sacrificial material</li> <li>• CMC ~ 21w/w%, CMT ~ 10°C</li> </ul>	• Thermal	[43]
PNIPAM	X	-CONH-	<ul style="list-style-type: none"> <li>• Thermo-sensitive hydrogels</li> <li>• LCST ~ 30°C</li> </ul>	• Thermal	[44]

Ionic crosslinking usually happens rapidly, as a consequence, the printed filaments can be poorly cohered [23]. Ionic gelation can be slowed down with the use of metal salts that dissociate slowly, such as CaCO<sub>3</sub> and CaSO<sub>4</sub>, or by incorporating retarding agents, such as Na<sub>2</sub>HPO<sub>4</sub> that competes with the reaction between alginate and Ca<sup>2+</sup> [45, 46]. A number of factors is known to affect the ionic crosslinking density, including concentrations of the oppositely charged molecules, pH controlling the ionisation degrees of polyelectrolytes, and solvents as further addition of salts can cause electrostatic screening effect [47, 48]. Ionic crosslinking is reversible by adding a chelating agent, such as sodium citrate or EDTA (ethylenediaminetetraacetic acid) that competitively bind with divalent and trivalent metal ions [49].

## 2. Macromolecular self-assembly

Self-assembled hydrogels are formed by spontaneous assembly of polymeric chains into compact configurations (e.g. coiled-coil and beta sheet) via physical interaction induced by

external stimuli [50] (**Figure 1.2b.i**). Various intermolecular interactions are involved in macromolecular self-assembly, such as hydrophobic interactions (**Figure 1.2b.ii**), hydrogen bonding and Van der Waals interactions [50]. Thermal and pH- induced self-assemblies are the common methods used in crosslinking proteins, such as collagen and extracellular matrix, which gel at physiological temperature and pH [50]. In particular, under physiological conditions, collagen molecules undergo fibrillogenesis to form a triple helical structure [51]. HEPES [52], 10x PBS and NaOH [53] solutions are commonly used to neutralise collagen and extracellular matrix (ECM).

Similarly, owing to the increased physical interactions induced by temperature, thermal-responsive hydrogels self-assemble and undergo phase transitions at their critical temperatures that are defined by lower critical solution temperature (LCST) or upper critical solution temperature (UCST) [50, 54] (**Figure 1.2b.iii**). The strength of the interaction can be tuned by the polymer concentration and molecular weight. UCST hydrogels, including gelatin and agarose, undergo gel formation upon cooling at a temperature below their UCST [55, 56]. On the contrary, gelling of LCST hydrogels occurs when increasing the temperature above their LCST [56]. This is attributed to the increased hydrophobicity (hydrophobic interaction) caused by the weakening of hydrogen bonding at higher temperature, and therefore increased insolubility [56]. Many cellulose derivatives, such as methylcellulose and hydroxypropyl methylcellulose, are examples of LCST hydrogels due to the presence of hydrophobic alkyl groups in their molecular structures [37]. Other notable LCST hydrogels are poly(*N*-isopropylacrylamide) (PNIPAM) that gels at > 32 °C in water [44] and PEO-PPO-PEO triblock copolymers (also known as Pluronics or Poloxamer) that self-assemble into micelles when the concentration and temperature are above their critical micelle concentration (CMC) and critical micelle temperature (CMT) [37].

The intermolecular interactions between self-assembled polymers can be promoted by various coagents. For example, NaCl, PVA and PEG have been used to promote gelation of collagen [42, 57], and a supplement of salt in a Pluronics solution facilitates the gelation by lowering its CMC due to the salting out effect [58].

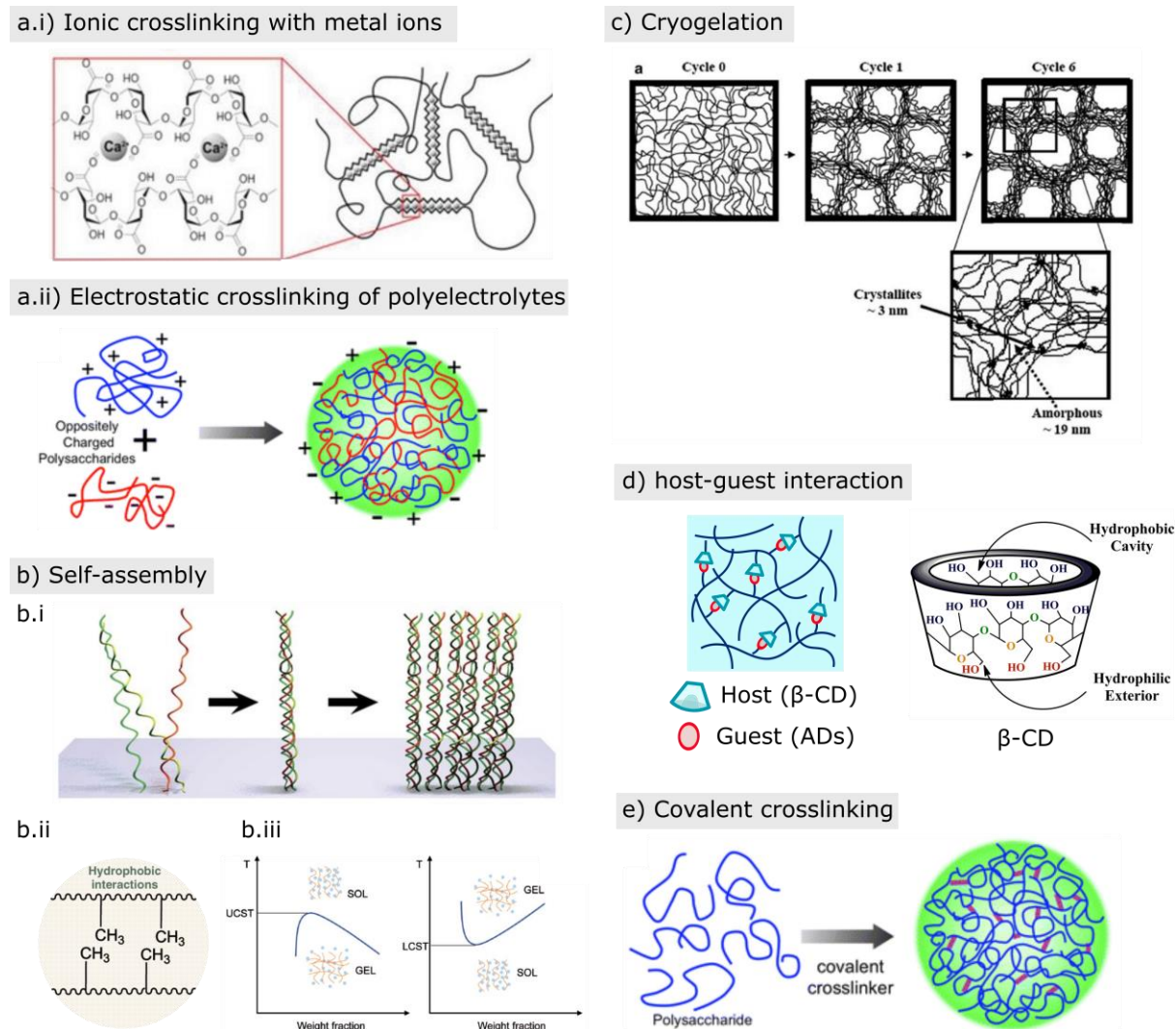


**Figure 1.2| Crosslinking of hydrogels.** **a(i)** Ionic crosslinking of alginate with metal ions  $\text{Ca}^{2+}$ , forming ‘egg-box’ junctions between alginate chains. **a(ii)** Electrostatic crosslinking between polyelectrolytes. **b(i)** Self-assembly of hydrogels induced by different physical interactions, such as **b(ii)** hydrophobic interaction. **b(iii)** Schematic showing the sol-gel transition of UCST and LCST hydrogels; **c**) Freeze-thaw cycles to form microcrystalline regions in hydrogels. **d**) Guest-host interaction between host molecules containing  $\beta$ -cyclodextrins ( $\beta$ -CDs) and ‘guest’ molecules containing adamantane moieties (ADs). **e**) Covalent crosslinking. Reproduced from [23, 54, 59–64].

### 3. Cryogelation via freeze-thaw cycles

Cryogels refer to macroporous gels developed by repeated freeze-thaw cycles [65]. During the freezing process, the polymeric chains are forced aligned into a microcrystalline structure due

to ice formation (**Figure 1.2c**) [65, 66]. As the number of freeze-thaw cycles increases, the strength and the stability of the crystallites increase due to the increased physical aggregation held together by hydrogen bonding [67, 68]. PVA, which contains abundant hydroxyl groups, is a well-known example of cryogels. In addition, most polysaccharides are capable of forming cryogels [65]. The key advantage of this method is that no toxicity issue is resulted as the method does not require any crosslinking agent [67], however, the preparation is usually long and require a number of days for repeating the thaw-freeze cycles.

#### 4. Host-guest interaction

Host-guest interaction involves ‘guest’ molecules adhere to a parent ‘host’ network via hydrophobic and van der Waals interactions to form physical supramolecular hydrogels [69]. Classic host-guest hydrogels used in biomedical applications involve a ‘host’ hydrogel containing amphiphilic  $\beta$ -cyclodextrins ( $\beta$ -CDs) and a ‘guest’ hydrogel containing hydrophobic adamantane moieties (ADs) [69] (**Figure 1.2d**).  $\beta$ -CD is a truncated cone-shaped molecule composed of a hydrophilic outer surface and a hydrophobic cavity. The cavity attracts the hydrophobic AD molecule. The hydrogels typically display self-healing properties due to the dynamic and reversible formations of host-guest interactions [63].

## 2. Covalent crosslinking

### 1. Photo-crosslinking

Photo-crosslinking requires a photoreactive polymer and a photoinitiator. A vast number of polymers can be functionalised with photoreactive moieties (i.e. methacrylate or acrylate groups) for photo-crosslinking. Common examples are gelatin methacryloyl (GelMA) [70], poly(ethylene glycol) diacrylate (PEGDA) and hyaluronic acid methacrylate [31]. Upon photo-radiation, the photoinitiators form reactive free radicals that initiate polymerisation, thus forming irreversible covalent bonding between polymer chains [23]. Common photoinitiators used in biomedical applications are LAP (Lithium phenyl-2,4,6-trimethylbenzoylphosphinate) and Irgacure 2959 [23]. LAP is in general less cytotoxic and more water soluble than Irgacure 2959 [17, 71], hence LAP is more commonly utilised in cell-laden materials. High level of light intensity, prolonged radiation time and the use of photoinitiators are known to cause detrimental effect on cell viability [17, 23]. It should also be noted that oxygen can inhibit free-

radical polymerisation [23]. This problem can be suppressed via crosslinking under an oxygen-free environment (i.e. N<sub>2</sub>) or using an oxygen scavenger, such as glucose oxidase [72].

## 2. *Wet-chemical crosslinking*

Several functional groups that are abundant in hydrogels can be used for covalent linkages, for instance, the amine (-NH<sub>3</sub>), carboxyl (-COOH) and hydroxyl (-OH) groups. The common methods are (1) Schiff's base crosslinking that involves reacting aldehyde/ketone-based crosslinking agents, such as glutaraldehyde and formaldehyde, with the hydroxyl or amine groups of hydrogels [23, 73, 74]; (2) carbodiimide crosslinking (known as EDC) that effectively reacts with the amine, carboxyl and hydroxyl groups of hydrogels [74], and (3) free radical polymerisation from monomers [74], such as polyacrylamide (PAAm) gels formed by reacting bis-acrylamide crosslinkers with acrylamide monomer using ammonium persulfate (APS) as initiators and TEMED as catalysts [75].

## 3. *Enzymatic crosslinking*

Enzymatic crosslinking is an attractive cytocompatible approach to synthesise protein-based hydrogels covalently [17, 23]. Transglutaminase, thrombin and horseradish peroxide are the common enzymes that catalyse protein crosslinking. Transglutaminase, also known as meat glue, is a slow-acting Ca<sup>2+</sup>-dependent enzyme that enables crosslinking of various proteins, such as gelatin, fibrinogen and collagen [76], as the enzyme promotes binding of ε-amino group of lysine with the carboxyl groups of glutamic acids [23]. By contrast, thrombin, the key enzyme of blood coagulation, activates the crosslinking of fibrinogen via cleaving fibrinogen to fibrin monomers that polymerise to insoluble fibrin [77]. Horseradish peroxide catalyses the crosslinking of silk fibroin in the presence of hydrogen peroxide [28].

### 1.2.2 Reinforcement mechanisms

Conventional hydrogels are composed of single networks, which are typically weak and brittle, causing them very difficult to manipulate and severely limiting their versatility in many applications [78, 79]. The brittleness of hydrogels can be attributed to two reasons – 1) the low density of polymer chains, and 2) the inhomogeneity of the randomly crosslinked polymeric network, leading to localised stress upon loading [78, 80]. Numerous approaches have been

reported to improve the toughness of hydrogels, including nanocomposite hydrogels and interpenetrating polymer network (**Figure 1.3**).

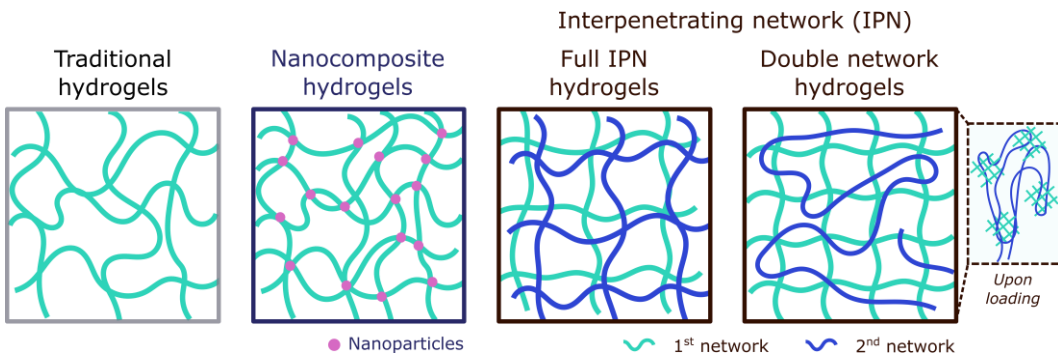


**Figure 1.3| Schematic showing the polymeric networks of traditional hydrogels and three common types of reinforced hydrogels.**

**Nanocomposite hydrogels** incorporate nanoparticles with high surface-to-volume ratios (i.e. carbon nanotubes, hydroxyapatite and silicates) to toughen hydrogels. In the reinforced networks, the nanoparticles serve as reversible interlinkages between polymer chains. The physical interaction between the polymers and the nanoparticle surface increases the entanglement of polymer chains, which efficiently dissipates stress across the network [80]. The reinforcement mechanism depends on the properties of nanoparticles, such as size, shape and surface chemistry [80].

Another reinforcement approach is achieved by an **interpenetrating polymer network** (IPN) composed of two or more polymeric networks with many physical interactions and entanglement between each other [81]. Various types of IPN have been developed, such as full-IPN hydrogels that are formed by two ideally juxtaposed polymeric networks [81]. **Double network (DN) hydrogels** are a special type of interpenetrating network hydrogels. They are composed of two asymmetric polymeric networks that typically involve a densely crosslinked, rigid and brittle polymer as the 1<sup>st</sup> network and a sparsely crosslinked soft and ductile polymer as the 2<sup>nd</sup> network [78]. Although still elusive, the toughening mechanism of DN hydrogels is believed to be associated with the introduction of sacrificial bonds, where the 1<sup>st</sup> network acts as sacrificial bonds that break into small cluster to effectively disperse the stress, and the 2<sup>nd</sup> ductile network is able to deform and extend extensively (**Figure 1.3**) [82, 83]. DN hydrogels are of particular interest among other toughening methods because they exhibit extremely high mechanical strength [82]. Representative examples are PAMPs-PAAm hydrogels (with fracture compressive stress and strain of 17.2 MPa and 92%) [84] and highly stretchable Ca<sup>2+</sup>-

alginate-PAAm hydrogels that can stretch more than 20 times of the original length by using a reversibly crosslinked alginate as the 1<sup>st</sup> network and a covalently crosslinked PAAm as the 2<sup>nd</sup> network [79].

### 1.2.3 Swelling capability of hydrogels

Hydrogels are notable for their swelling capability, enabling applications in drug release or soft actuation systems. Because of the osmolarity difference between the hydrogels and the surrounding medium, most hydrogels can swell. In addition, thermo-sensitive hydrogels swell or shrink because of the temperature-induced self-assembly behaviours, as discussed **above**. By contrast, the swelling behaviours of pH-responsive and electro-responsive hydrogels are controlled by their ionised functional groups (e.g. carboxyl and amine groups). The section below discusses the pH- and electro-responsive swelling behaviours of hydrogels.

#### *pH-responsive hydrogels*

pH-responsive hydrogels undergo swelling or shrinkage when there is a change in the environmental pH. The swelling capacity is controlled by the ionisation degree of the ionic functional groups in hydrogels. For example, when the pH of the environment is greater than the pKa of the carboxyl groups of anionic hydrogels ( $\text{pH} > \text{pKa}$ , **Figure 1.4a.i)**, more carboxyl groups on the polymer backbones become deprotonated. This increases the hydrophilicity of the hydrogel and the ionisation degree of the polymer, causing the hydrogel to imbibe more water and swell to reduce the electrostatic repulsion between the ionised groups until an equilibrium is reached [85, 86]. Conversely, cationic hydrogels swell when the pH of the environment is less than the pKa of amine groups ( $\text{pH} < \text{pKa}$ ) as this increases the amount of ionised amine groups on the polymer chains (**Figure 1.4a.ii**). The pH-responsive swelling behaviour could be affected by several factors, including molecular weight [87, 88], degree of crosslinking [89] and ionic strength [90]. The swelling behaviour is reversible by changing the pH environment back to the initial condition. Although pH-responsive swelling is isotropic, anisotropic response is achievable by incorporating an aligned fillers (i.e. cellulose) to guide the direction of swelling [72] or by exploiting a bilayer design composed of counter-acting hydrogels [91].

## *Electro-responsive hydrogels*

Utilising the ionic functional groups of hydrogels, electro-responsive hydrogels undergo directional bending when exposed to an electric field in an electrolyte solution. As depicted in **Figure 1.4b**, when an anionic gel (i.e. polyacrylic acid) is placed in a saline solution (Step 1), under an electric field, the positively charged  $\text{Na}^+$  ions can diffuse through the gel towards the negatively charged cathode, however, the diffusion of the negative  $\text{Cl}^-$  ions toward the positive anode is restricted by the anionic gel (Step 2) [92, 93]. This selective diffusion results in an increased concentration of anions on the gel surface facing the cathode. Therefore, water diffuses toward the cathode to reduce the osmotic pressure (Step 3). This in turn makes the side of the gel facing the anode swells more, leading to a directional bending towards the cathode. In reverse, a cationic hydrogel bent toward the anode due to the restricted diffusion of  $\text{Na}^+$  ions toward the negative cathode. Electro-responsive hydrogels have been utilised in many soft robotic actuation systems, such as gripping and locomotion [93, 94].

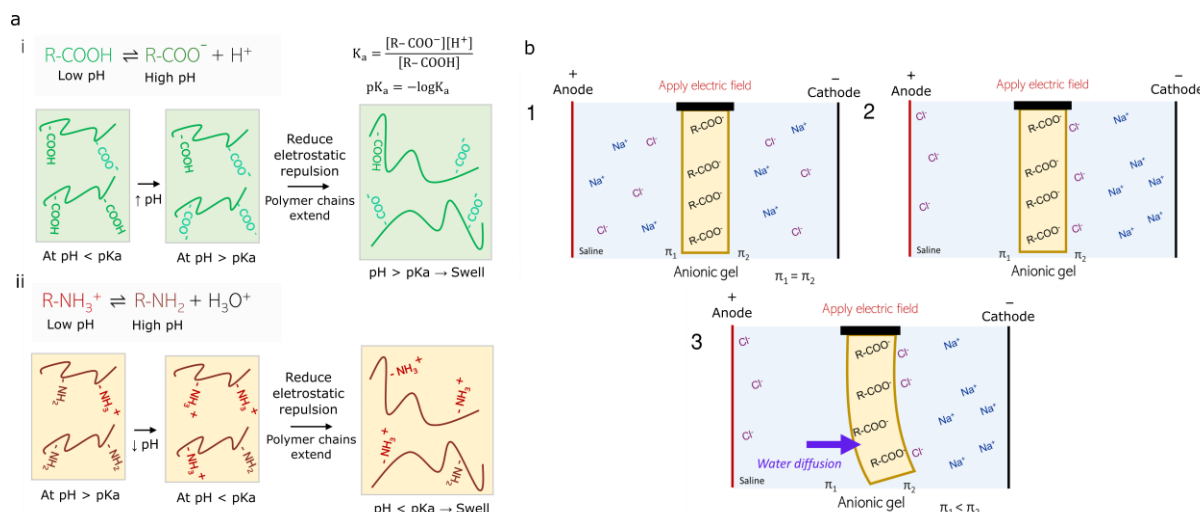


**Figure 1.4|** Schematics showing (a) the pH-responsive swelling mechanism of (i) anionic hydrogels and (ii) cationic hydrogels, and (b) the electro-responsive swelling mechanism of anionic hydrogels.  $\pi_1$  and  $\pi_2$  are the osmotic pressures at the sides facing the anode and the cathode, respectively.

### **1.3 Silicone and epoxy resins**

Silicone elastomers and epoxy are the key materials of soft robotics and microfluidic devices. A broad variety of resins have been successfully 3D printed, such as epoxy [95], SU-8 (a

photocrosslinkable epoxy) [96], polydimethylsiloxane (PDMS, the de facto standard in the microfluidics) [97], SE 1700 (a 20 wt% fumed silica-filled PDMS) [98] and ecoflex (a super soft and stretchable elastomer) [99]. The mechanical properties of silicone elastomers can be tuned by the curing temperature and the ratio of the pre-polymer base and the curing agent [100]. In addition, silicone thinners, thickeners (i.e. THI-VEX) and cure retarders (i.e. SLO-JO) can be mixed with silicone elastomers (i.e. Ecoflex) for modifying its viscosity and increasing the pot life [99].

## 1.4 Overview of 3D printing strategies

3D printing, also known as additive manufacturing, is a method of creating 3D objects using computer-aided designs (CAD). Conventionally, CAD designs are either created from scratch or constructed from imaging scans (e.g. MRI or CT scans) for capturing complex anatomical architectures. Various 3D printing technologies (**Figure 1.5**), including **light-based approach** (i.e. laser-assisted printing (LAP) and photolithograph) and **ink-based approach** (i.e. inkjet printing and extrusion printing), have been explored for soft material fabrication [3, 4, 6, 8, 101, 102]. The principles, the strengths and the limitations of the technologies are detailed below.

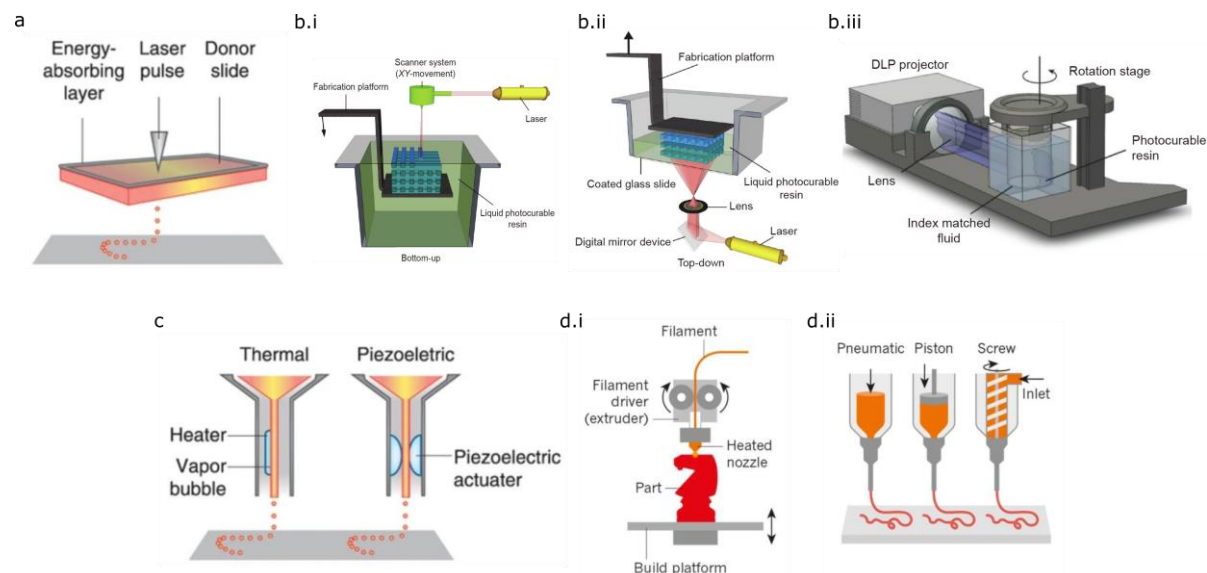


**Figure 1.5| Overview of 3D printing strategies.** a) **Laser-assisted printing.** b) **Photolithography** - (i) stereolithography, (ii) digital light processing and (iii) computed axial lithography. c) **Inkjet printing**. d) **Extrusion-based printing** – (i) fused deposition modelling and (ii) direct ink writing. Reproduced from [4, 8, 103].

### 1.4.1 Light-based approach

#### *Laser-assisted printing (LAP)*

Laser-assisted printing (LAP), also known as laser-induced forward transfer (LIFT) printing, involves focusing a pulsed laser beam onto a donor glass ribbon that is coated with a layer of laser-energy absorbing material on one side and a layer of printing material on the other side (**Figure 1.5a**) [8]. The laser-energy absorbing material is then vaporised, forming a vapor pocket at the glass-printing material interface that propels the printing material toward the substrate [104]. The nozzle-free and non-contact characteristics of this approach enable the deposition of inks with viscosity of 1 – 300 mPa/s, and innately avoid problems such as nozzle clogging and cell damage due to shear stress [8, 104]. By coupling with a rapid gelation kinetics, high printing resolution can be achieved [8]. However, the high associated cost of the system and its low throughput resulting from the generation of ultra-small droplets (ranging from fL to nL [105]) have greatly limited the wide adoption of this technology [8, 104].

#### *Photolithography*

Photolithography can be subdivided into stereolithography (SLA), digital light processing (DLP) printing and computed axial lithography (CAL) (**Figure 1.5b**). Fundamentally, they are based on the same working principle that uses a light source (UV or a visible light, depending on the photoinitiators) to selectively photopolymerise a resin or a polymer [4]. The primary difference between them is the exposure approach. SLA relies on a laser to locally photopolymerise a voxel of material [4]; DLP uses light that is masked by a digital micromirror device (e.g. a projector) to cure selected area of each layer at once [4]; And, CAL is a recently developed approach based on vat photo-polymerisation that projects a series of 2D light images onto a volume of material from multiple angles [106, 107]. Therefore, CAL vastly reduces the build time to several orders of magnitude faster than the layer-by-layer approaches (~30 – 120 s for centimetre-scale objects) [106].

As this technology offers a faster print speed [106, 108] and permits the creation of complex features with ease at superior resolution (10 – 100 µm range) compared to extrusion-based printing [2], photolithography becomes increasingly used in soft material fabrication [2]. However, numerous limitations of the technology have been reported. First, the technology is limited by the material choices of photocurable resin or acrylate-based hydrogels [109]. Only a few acrylate-based polymers are commercially available. And it is known that acrylate-based

hydrogels tend to shrink during photo-polymerisation [110], which may diminish the dimension accuracy. Second, using photolithography to fabricate complex multi-material objects is not straightforward as the system cannot easily switch between different materials during fabrication, as opposed to extrusion-based printing [2, 10]. However, it should be noted that recent studies have proposed the use of a microfluidic masking device [111] or a platform with multi-material puddles [112] to fabricate heterogeneous objects. Finally, the use of photoinitiators and UV light irradiation may potentially induce cell cytotoxicity, which might limit its versatility in tissue engineering applications [113].

#### 1.4.2 Ink-based approach

##### *Inkjet printing*

In inkjet printing, soft materials are deposited in a similar way as the method used in desktop inkjet printers, where liquid inside the nozzle is broken into droplets by thermal or acoustic force, followed by the ejection of droplets onto a substrate via a drop-by-drop mechanism rather than as continuous filaments (**Figure 1.5c**) [4, 6, 8, 104]. The droplet size depends on the ink properties (e.g. density, viscosity and surface tension), the nozzle diameter and the velocity of the ejected droplets [4]. For instance, satellite droplets may form if surface tension between the ink and the substrate is too high, and splashing may occur if ejection is at a high velocity, diminishing the print fidelity [4]. The key characteristics of inkjet printing are its high throughput, low cost and non-contact nature, therefore droplets on the substrate will not be deformed by the movement of the printhead [114]. However, the technology is in general not suited for dispensing high viscosity ( $> 30 \text{ mPa/s}$  [114]) or high cell density solution ( $> 10^6 \text{ cells/ml}$  [8]) because of its weak ejection force.

##### *Extrusion-based printing*

**Fused deposition modelling (FDM)** is the earliest form of extrusion-based printing, where a continuous thermoplastic filament is fed through an extruder heated to a temperature above its glass transition temperature during printing and the filament is solidified once it is deposited onto a substrate (**Figure 1.5d.i**) [4]. Compared with FDM, **Direct Ink Writing** (DIW, also referred to as robocasting), another extrusion-based method, allows fabrication of inks with broad range of viscosity (30 mPa/s to  $> 6 \times 10^7 \text{ mPa/s}$  [8], i.e. aqueous or paste-like ink) through a pneumatic or mechanical (piston or screw) dispensing systems (**Figure 1.5d.ii**) [3, 4, 6, 8].

Of the different printing technologies, extrusion-printing is the most popular method for printing hydrogels or other soft materials [2, 3, 8, 10] due to its flexibility, low cost, ease of use and compatibility with a wide variety of materials [4, 8, 115]. However, the technology is burdened by several drawbacks, including slow print speed and inferior print resolution, which strongly relies on the ink properties and process parameters (e.g. printing speed, extrusion flowrate, nozzle size and nozzle-to-substrate distance) [2, 4, 116, 117].

In my research work, I chose direct ink writing as the fabrication approach because of its facile use and popularity. Below sections discuss the recent advances in extrusion-based printing for architecting soft materials.

## 1.5 Embedded 3D extrusion printing

Despite direct ink writing (DIW) is compatible with a broad variety of soft materials (e.g. hydrogels and elastomer) [4], soft materials in general do not exhibit sufficient mechanical rigidity for supporting their own weight. Therefore, they tend to collapse or sag when printing them in air [3, 118, 119]. As demonstrated in **Figure 1.6a**, the sagging issue greatly diminishes the print fidelity, prohibiting the printing of thick and geometrically complex structures [119]. To overcome this issue, a new class of printing approach termed **embedded 3D extrusion printing** has emerged for freeform fabrication of soft materials [3]. Unlike conventional in-air printing, embedded printing involves printing inks inside a bath of ‘sacrificial’ material that serves as a support bath during printing and crosslinking (**Figure 1.6b**) [120]. Depending on the ink properties, the printed structures can be crosslinked via various mechanisms (see **Figure 1.7**, crosslinking method), including thermal- and photo-crosslinking, and methods involved crosslinking agents (such as pH, enzymatic, ionic and chemical crosslinkers). The crosslinking agents can be mixed with the support bath, such that the gelation process of the extruded ink can be immediately initiated after injection, for example, adding a  $\text{CaCl}_2$  solution to the bath can facilitate the crosslinking of the printed alginate ink [121]. After printing, the support bath (also called the matrix) can be either removed or kept in place as a permanent support (**Figure 1.6b**) [120].

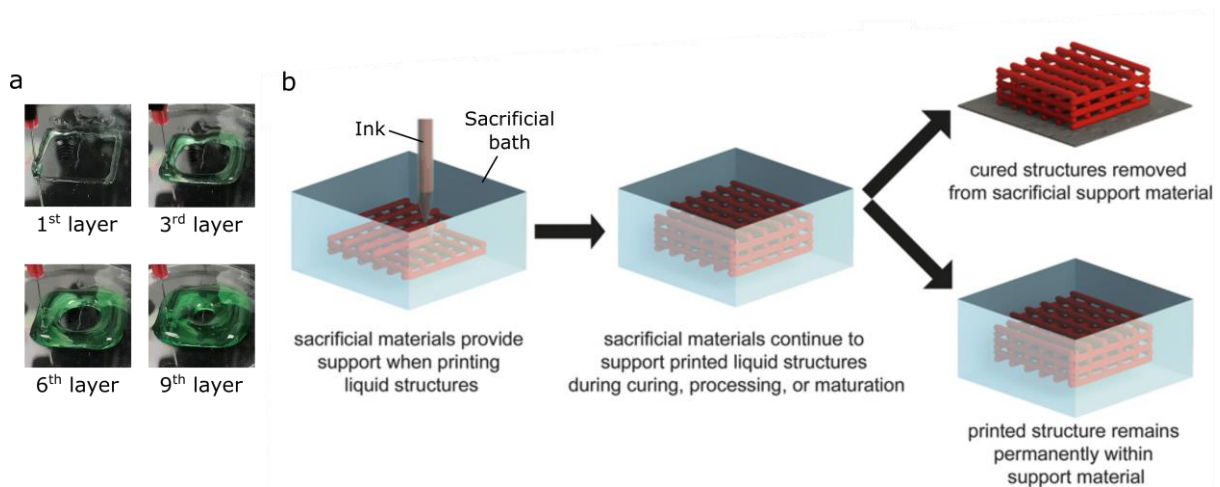


**Figure 1.6| Comparison between in-air and embedded 3D extrusion printing.** **a)** Pictures showing the sagging issue in conventional in-air 3D printing. **b)** Schematic showing the embedded 3D printing process. Adapted from [120].

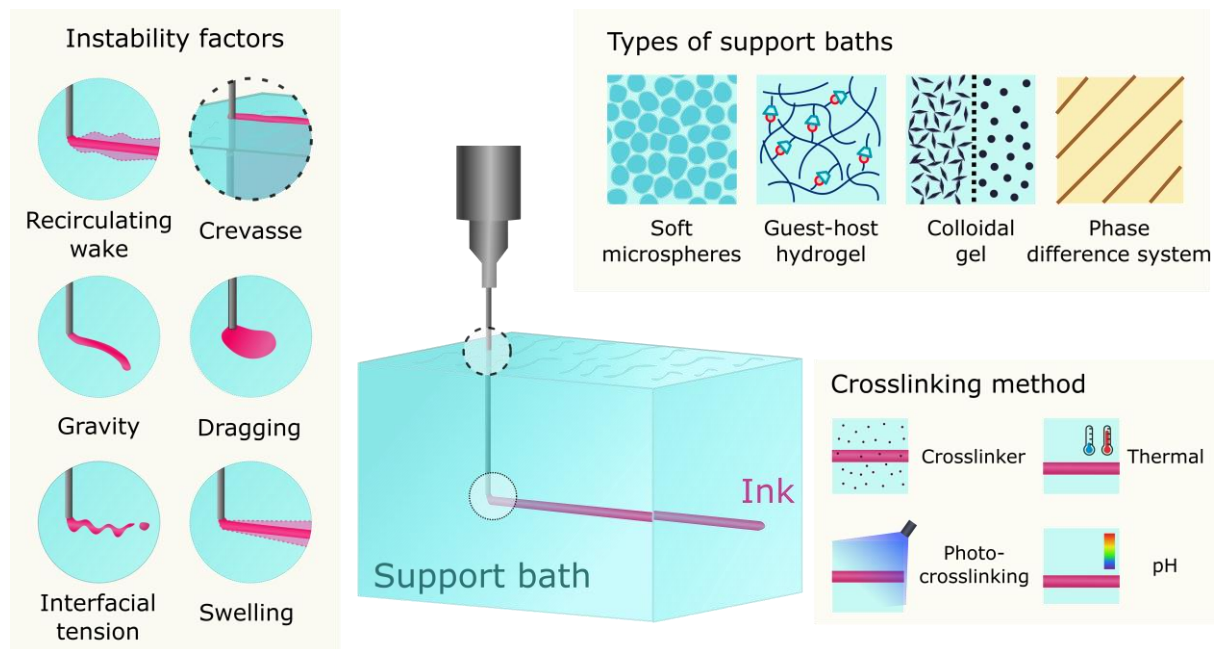


**Figure 1.7| Overview of embedded printing technology.** The figure depicts the instability factors occurred during the printing process, types of support bath materials developed in literature and the crosslinking methods of soft materials.

The method of embedded printing not only enables fabrications of limitless shapes for better biomimicry (e.g. overhanging and tree-like vascular structures [122, 123]), but also provides prolonged crosslinking of slow-gelling soft materials to solidify before they collapse due to gravity [124]. In contrast to traditional in-air printing where gelation is difficult to be initiated at ink-air interfaces, embedded printing allows a broad range gelation mechanism by leveraging the ink-bath interface [121]. Regarding cell printing, support baths with aqueous phases of culture media can provide nutrients to cells, therefore preventing cells from dehydrating during printing, which commonly happens in in-air printing [121, 125]. The use of support baths also bypasses the need for a perfectly level platform, which is a crucial prerequisite in in-air printing and involves tedious operation [121]. The following sections thematically review the requirements on the bath and the ink properties for a successful embedded printing process, the potential instabilities occurred during embedded printing and the development of support baths in literature (**Figure 1.7**).

### 1.5.1 General requirements of support bath and ink

The rheological properties of the support bath and the ink play a crucial role in embedded printing process. In general, the **ink** materials should exhibit shear-thinning behaviour as this allows the flow of materials under extrusion force [8, 126] (see **Figure 1.8a** for typical flow curves of different types of materials). Furthermore, the **support bath** should act like a Bingham plastic (Newtonian) or a Bingham pseudoplastic (shear-thinning) that exhibits a yield stress,  $\tau_{y,bath}$  [52, 121, 126]. At rest, the Bingham support bath should behave as a rigid elastic body. When the shear stress caused by the nozzle translation is larger than  $\tau_{y,bath}$ , the bath should turn into a viscous fluid, allowing the nozzle to move freely across the bath [52, 97, 123, 124, 126, 127]. After the nozzle departs and the applied shear stress drops, the support bath should revert to a solid-like behaviour, trapping the extruded ink in place till the printing is complete and the ink is crosslinked [122, 124].

Apart from the yield stress characteristics, a universal support bath should be easy to remove by means of a sol-gel transition property, transparent for visualisation and photo-crosslinking, and compatible with one or more gelation mechanisms, that is, insensitive to either pH, temperature, enzyme or ionic strength [96].

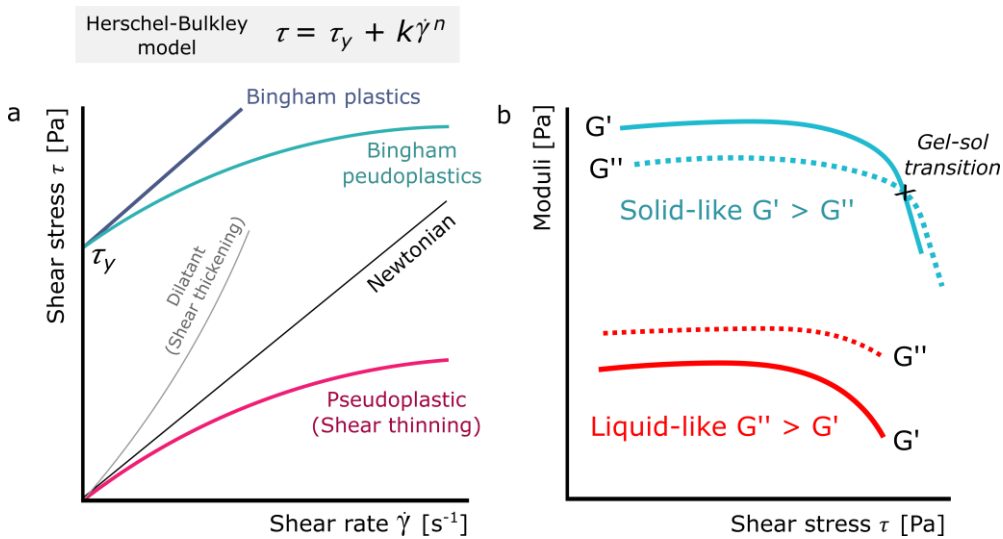


**Figure 1.8| Rheological properties of materials.** **a)** Flow curve of different types of materials. The rheology of Bingham plastic materials can be described by Herschel-Bulkley model, where  $\tau$  = shear stress,  $\tau_y$  = yield stress,  $\dot{\gamma}$  = shear rate,  $n$  = flow index with  $n < 1$  indicates shear-thinning, and  $k$  = consistency index. **b)** The characteristics of the storage modulus and the loss modulus of solid-like and liquid-like fluids. Determined by oscillatory shear measurements, storage modulus (also called elastic modulus,  $G'$ ) is a measure of the elastic behaviour of a viscoelastic material, whereas loss modulus (also called viscous modulus,  $G''$ ) represents the viscous part of the material.

### 1.5.2 Instabilities caused by the mismatch properties between the ink and the bath

In addition to the above prerequisites, embedded printing is generally a race against instabilities [122]. Several forces, such as gravity, viscous force and interfacial tension between the ink and the bath, will detrimentally change the shape of the printed object over time until the object is crosslinked [120, 122]. Recent studies have suggested that the storage modulus,  $G'_{bath}$ , and the yield stress,  $\tau_{y,bath}$ , of the bath should be approximately an order of magnitude less than those of the ink,  $G'_{ink}$  and  $\tau_{y,ink}$ , to mitigate instabilities [126, 128] (see definition of storage modulus in **Figure 1.8b**). Below summarises the common instabilities that affect the print fidelity, namely 1) recirculating wake, 2) gravity, 3) interfacial tension, 4) crevasses, 5) dragging, and 6) swelling, and their potential solutions (**Figure 1.7**).

### 1. Recirculating wake

Nozzle translation through a support bath could induce stress fields and create recirculating zones at the vicinity of the nozzle. This in turn yields and displaces the printed features [120, 126]. This problem usually happens when the yield stress of the bath,  $\tau_{y,bath}$ , is too low [126] and when the nozzle translation speed is too fast. Using small diameter nozzles and increasing the viscosities of the ink and the bath can avoid the instability [120].

### 2. Gravity

Gravity causes the printed features to sag when the storage modulus of the bath,  $G'bath$ , is not sufficiently enough to support the weight of the embedded ink [126]. Apart from using a support bath that has a sufficiently high  $G'bath$ , the problem can be alleviated by matching the densities of the ink and the bath to reduce the buoyancy difference [120, 126].

### 3. Interfacial tension

Interfacial instability (also known as Plateau-Rayleigh instability) usually occurs in two-phase (aqueous-oil) systems, where the stresses generated by interfacial tension are larger than the yield stress of the bath (Equation 1.1), causing the printed features to break up [97, 120, 123]. Breaking of the printed features can also happen when  $G'ink$  is much lower than  $G'bath$  [126].

$$\frac{\gamma}{l} > \tau_{y,bath} \quad (1.1)$$

where  $\gamma$  is the interfacial tension,  $l$  is the printed feature diameter and  $\tau_{y,bath}$  is the yield stress of the bath.

The instability induced by interfacial tension can be mitigated 1) by increasing the viscosities of the ink and the bath [129], 2) by the use of surfactants (e.g. Pluronic F127, Tween, SDS and nanoparticles) to lower the interfacial tension, or 3) by shortening the print time using a faster print speed. In addition, low aspect ratio printing paths (e.g. rectilinear pattern) are preferred against high aspect ratio printing path (e.g. concentric pattern) as this reduces the Laplace pressure between the ink filament and the bath during printing (Figure 1.9a).

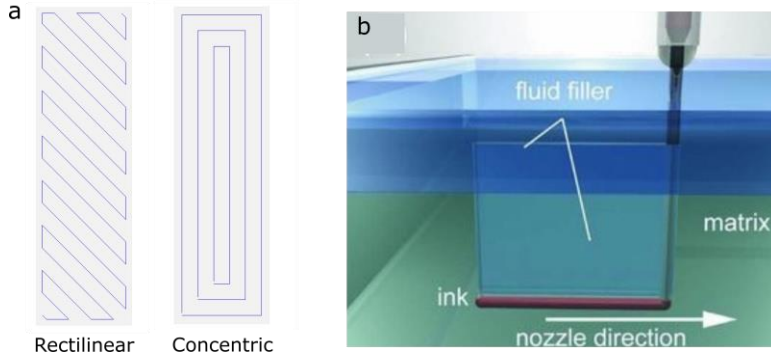


**Figure 1.9| a)** Pictures depicting the printing paths of rectilinear and concentric patterns. **b)** Schematic showing that the use of a fluid filler to fill the crevasses induced by nozzle translation through the bath. Reproduced from [43].

#### 4. Crevasses

Crevasses refer to the voids induced by the nozzle when translating through the bath. Transient crevasses emerge when the nozzle translation speed is high, while static crevasses arise when  $\tau_{y,bath}$  is larger than the hydrostatic pressure at the depth of the nozzle (Equation 1.2) [120, 130]. As a consequence, the extruded inks flow upward through the crevasses due to capillary action, greatly diminishing the print fidelity.

$$\tau_{y,bath} > \rho gh \quad (1.2)$$

where  $\rho$  is the density of the bath,  $g$  is the gravitational acceleration and  $h$  is the depth of the nozzle in the bath.

Several studies have suggested the use of thixotropic baths to avoid this problem [96, 99, 126]. Thixotropy refers to a time-dependent viscosity recovery behaviour, that is, the viscosity of the bath does not immediately recover after the applied force is removed, facilitating the flow of the bath [126]. Ideally, the thixotropic recovery time of the bath should not be too long as a long recovery time might increase the risk of the formation of recirculating wake [122]. Alternatively, the problem can be solved by adding a low viscosity fluid filler on top of the bath to readily fill the voids during printing (Figure 1.9b) [43, 131]. However, this method might not be suited for printing three-dimensional objects.

## 5. Dragging

Dragging of ink happens when  $G'_{ink}$  and the ink viscosity are too large, compared to the storage modulus,  $G'_{bath}$ , and the viscosity of the bath [126, 129]. Slowing down the crosslinking rate of the embedded ink may avoid the problem as a fast-crosslinking leads to a rapid increase in the ink viscosity and  $G'_{ink}$ .

## 6. Swelling/shrinkage behaviour

Swelling or shrinking of the printed features is associated with the osmolarity difference between the ink and the bath [129, 132] and the pH- or thermo-responsive swelling behaviour of hydrogels. Hydrogels are known to imbibe or expel water until an equilibrium is reached. The swelling problem can be overcome by utilising an oil-aqueous two-phase system to halt water transport between the bath and the ink (further discussed in **Chapter 4**) [97, 133–135]. In addition, printing can be carried out in less stimulating conditions to slow down the swelling/shrinking behaviours of pH- and thermo- sensitive inks.

### 1.5.3 General rheological characteristics of the ink and the support bath

This section summarises the above discussion on the rheological characteristics of the ink and the support bath.

- The ink should be shear thinning for extrudability.
- The support bath should be shear thinning and exhibits a yield stress (Bingham pseudoplastic) for smooth transition of nozzle inside the bath.
- A rule of thumb suggested in literature:  $G'_{bath} < 10 G'_{ink}$  and  $\tau_{y,bath} < 10 \tau_{y,ink}$
- Recirculating wake problem occurs when  $\tau_{y,bath}$  is too low.
- Sagging occurs when  $G'_{bath}$  is too low .
- Printed features bead up when  $G'_{ink}$  is much lower than  $G'_{bath}$  and when  $\frac{\gamma}{l} > \tau_{y,bath}$ , where  $\gamma$  is the interfacial tension,  $l$  is the printed feature diameter
- Static crevasses occur when  $\tau_{y,bath} > \rho g h$ , where  $\rho$  is the density of the bath,  $g$  is the gravitational acceleration and  $h$  is the depth of the nozzle in the bath.
- Dragging occurs when  $G'_{ink}$  and the ink viscosity are much larger than  $G'_{bath}$ , and the bath viscosity

### 1.5.4 Development in support baths for embedded 3D extrusion printing

Since the development of embedded printing, four classes of support baths have been used in literature. They are 1) soft microspheres (e.g. gelatin slurry and Carbopol), 2) guest-host hydrogel, 3) colloidal gels (e.g. Laponite® and fumed silica) and 4) gels in different phase to the ink (**Figure 1.7**). **Table 1.3** provides a detailed comparison of the existing support baths in literature, highlighting their removal methods, achievable resolution, tested inks, as well as their features and limitations.

#### 1. Soft microspheres

Soft microspheres are the major class of support baths used in literature. In this class, the microsphere size plays a crucial role in feature resolution as the feature dimension is theoretically limited by the microsphere size [122, 128]. A wide variety of soft microspheres with different microsphere sizes has been developed for this application (**Figure 1.10a**).

##### 1. Gelatin microspheres

Gelatin slurry [52, 136], also known as the FRESH (freeform reversible embedded suspended hydrogel) method, is one of the most well-known methods in embedded printing. The method was first developed by Hinton et al. in 2015 (FRESH v1.0, **Figure 1.10a.i**), where a solid block of gelatin was blended into microspheres with a mean diameter of  $\sim 55 \mu\text{m}$  [52] and the resulted print resolution was  $\sim 200 \mu\text{m}$ . The work was followed by advancement by Lee et al. in 2019 (FRESH v2.0, **Figure 1.10a.ii**), where print resolution was improved to  $\sim 20 \mu\text{m}$  using a complex coacervation approach to generate spherical gelatin microspheres with reduced polydispersity and smaller mean particle diameter of  $\sim 25 \mu\text{m}$  [136]. After printing and crosslinking, the gelatin slurry baths can be easily removed by melting it at  $\sim 37^\circ\text{C}$  [52, 136].

Low-cost, biocompatibility and thermo-reversibility are the key advantages of gelatin slurry [52]. While a wide variety of gelation mechanisms (i.e. pH, ionic and enzymatic crosslinking) and bioinks (i.e. alginate, fibrin, collagen I) are compatible with the gelatin slurry support baths, several shortcomings are noted. First, the preparation process of gelation slurry is relatively labour-intensive as gelatin slurry can only last for around a week. Second, the approach might not allow long-lasting support for inks that require long gelation above  $37^\circ\text{C}$  [137], such as low concentration collagen, extracellular matrix (ECM) and PDMS. Third, the method is not compatible with inks that have gel-sol transitions at temperature around  $37^\circ\text{C}$ , such as gelatin and low gelling temperature agarose [138].

**Table 1.3| Support baths developed for embedded printing applications in literature.** The references highlighted with \* indicate key studies. Concentration is expressed as weight in volume percent (w/v%) unless specified. † denotes cell-laden bioinks. CMs: Cardiomyocytes, ECs: Endothelial cells, hSKMs: Human skeletal myoblasts, hMSCs: Human mesenchymal stem cells, hESCs: Human embryonic stem cells, iPSCs: Induced pluripotent stem cells, hASCs: Human adipose-derived stem cells, NaAlg: Sodium alginate, SWCNT: single-wall carbon nanotubes, MA: Methacrylated, PF127: pluronics F127, PF127-DA: Diacrylated pluronics F127, HA: hyaluronic acid, and Pt: platinum.

	Support baths	Tested inks	Compatible crosslinking methods	Removal method	Features	Limitations	Feature resolution (μm)	Ref
Microspheres	Gelatin	Blended 4.5% gelatin (type A) microspheres	NaAlg, fibrinogen, collagen I, ECM <sup>†</sup>	Ionic, enzymatic, pH, thermal	Good viability with C2C12 [52, 136, 139], MC3T3 [52], hMSC [140], human corneal keratocytes [141], hESC-derived CMs [136], human ventricular cardiac fibroblasts [136], hSKMs [57]; inexpensive; compatible with various crosslinking methods	Labour-intensive preparation; Not allow prolonged crosslinking time at physiological temperature	200	[52] *
			SWCNT-NaAlg-nanofibrillated cellulose	Ionic			-	[142]
			Oxidised MA-alginate <sup>†</sup>	UV			-	[140]
			carrot cells-NaAlg	Ionic			-	[143]
			GelMA-PEDOT:PSS <sup>†</sup>	Ionic, photo-polymerisation			-	[139]
			Photocrosslinkable HA/calcium phosphate	UV			-	[144]
		Blended microspheres of 4.5% gelatin (type A) in sodium bicarbonate solution	Glycol chitosan, PEG chitosan, collagen-chitosan	pH, thermal			120	[145]
		Allevi gelatin microspheres	NaAlg/MA-collagen I <sup>†</sup>	Ionic, pH, thermal			-	[141]
		2% gelatin (type B) in 50 v/v% ethanol (coacervation)	NaAlg, collagen I, MA-HA, fibrinogen <sup>†</sup>	Ionic, enzymatic, pH, thermal			20	[136] *
			NaAlg	Ionic			250	[146]
		Blended microspheres of 8% gelatin in 10% PVA/PBS	ECM <sup>†</sup>	Thermal, physical interaction with PVA			300	[57]
		Blended 4.5% gelatin (type A) microspheres + 10% gelatin	Xanthan gum	Thermal (bath)	Not removed		-	[147]
		Blended 4% gelatin type A	NaAlg	Ionic	Freeze, then melt at 37°C		-	[148]
	Carbopol	0.2/0.7% Carbopol ETD 2020 (10mM NaOH)	Photocrosslinkable PVA, polyacrylamide, PEG, HA, NaAlg, PDMS, Collagen I, cell pellets <sup>†</sup>	UV, pH	Gentle agitation	Excellent transparency; thermal stability; Easy preparation;	Sensitive to pH and ionic strength	Single cell width [122] *

	Support baths	Tested inks	Compatible crosslinking methods	Removal method	Features	Limitations	Feature resolution ( $\mu\text{m}$ )	Ref
Microspheres	0.9% Carbopol ETD 2020 (pH 7.4)	Cell pellets <sup>†</sup>	-	Not removed	Good viability (>85%) with MCF10A, MDCK, MS1, HAEC endothelial cells, HuH-7 hepatocytes, CTLL-2 killer T-cells, MSCs, A375, MCF7, PC3, primary osteosarcoma [149], HUVECs [150], CMs [150], cardiac fibroblasts [150]	Cytotoxicity effect, potential crevasse formation	~100	[149]
	0.2% Carbopol ETD 2020 (10mM NaOH)	PEG, PEGDA, PEG-acrylate	UV	Harvest			24	[130]
	0.8% Carbopol ETD 2020 (pH 7)	NaAlg/gelatin	Thermal	Rinse with 0.9% NaCl			-	[151]
	0.1% Carbopol 980 (pH 7)	Bacteria solution, naproxen solution	Particle crystallisation	1M NaCl			300	[152]
	0.2% Carbopol ETD 2020 (10mM NaOH)-acrylamide-PPEGDA400	Emulsion of silicone oil-water with Tween20	UV	Peeling off			-	[153]
	1% Carbopol ETD 2020 (pH 7)	GelMA/NaAlg <sup>†</sup>	UV	Rinse with DPBS			100	[154]
	1.8% Carbopol ETD 2020 (pH 7)	MA-tropoelastin/GelMA <sup>†</sup>	UV	Rinse with media or DPBS			-	[150]
	0.4% Carbopol ETD 2020 (pH 7)	GelMA	UV	Rinse with PBS			~200	[155]
	Pluronic F127	23% PF127	NaAlg, PEGDA/NaAlg	UV, ionic	Liquefied at 4°C	Easy to remove; Good viability (<80%) with NIH-3T3 [156]	100	[157]
			NaAlg	ionic			50	[158]
		25% PF127-DA	PF127-DA	UV (bath)			200	[43]
		25% PF127/APS	Graphene oxide/PF127, MWCNT/PF127	Chemical			-	[159]
Alginate	10% PF127-3% Laponite EP	NaAlg <sup>†</sup>	Ionic	Rinse with 1% cold NaCl	Allow long-term culture (>4 wks); Good viability with hMSCs	Complex preparation method	-	[156]
	Blended photocrosslinkable NaAlg microspheres	Cell pellet <sup>†</sup>	-	Agitation or spontaneous degradation			300	[160]
	Homogenised 0.32% NaAlg microsphere in 1% xanthan gum	ECM <sup>†</sup>	Thermal	Degraded by alginate lyase			-	[137] *
Agarose	0.5% agarose fluid gel	Gellan gum/Hydroxyapatite	Thermal	Harvest	Non-ionic; Good stability against ionic strength;	Unsuitable for detailed structure [124]	-	[163]
		Gellan gum, collagen, I-carrageenan, NaAlg	Thermal, ionic	Gentle agitation			-	[119]

	Support baths		Tested inks	Compatible crosslinking methods	Removal method	Features	Limitations	Feature resolution (μm)	Ref
Guest-host			Gellan gum <sup>†</sup> , laponite/gellan gum <sup>†</sup>	Thermal, ionic	Rinse with HBSS	allow long-term culture; Good viability with C2C12 [161] and hASCs [162]		250	[161]
			Platelet lysate/cellulose nanocrystals <sup>†</sup> , NaAlg <sup>†</sup> , GelMA <sup>†</sup>	Thermal, ionic, UV	Rinse with PBS			100	[162]
		Blended 1% agarose microsphere	NaAlg, collagen, GelMA, GelMA -matrigel-fibronectin <sup>†</sup>	Thermal, ionic, UV	Gentle rinsing			-	[164]
	<b>Gellan gum</b>	Fragmented 0.5/1% gellan gum fluid gel	NaAlg, PEGDA, gellan gum-gelatin <sup>†</sup>	Ionic, UV, Thermal, enzymatic	Gentle agitation	Enable various gelation mechanisms; Good viability with NIH-3T3	Not suitable for low MW inks	-	[124]
		Organogel	SEP-SEPS copolymer in mineral oil	UV-curing silicone elastomer, RTV silicone elastomer	UV	Rinse with soapy water	Allow printing of resin inks	Not cytocompatible	30 [123] * [165]
	<b>Hyaluronic acid (HA)</b>	Guest-host HA	Ad-HA <sup>†</sup> , methacrylate HA	UV	Rinse with 2% β-cyclodextrin	Rapid self-healing, Good viability (>90%) with NIH-3T3 and hMSCs [31])	Require chemical modification	35 [31]*	[31]*
			Agarose, HA microgels	Thermal, UV				~350 [165]	[166]
Colloidal gels	<b>Laponite</b>	RGD modified guest-host HA with protease-degradable crosslinker	Guest-host HA	UV (bath)	Rinse with 2% β-cyclodextrin	Rapid self-healing, Good viability (>90%) with NIH-3T3 and hMSCs [31])	Require chemical modification	-	[166]
								-	[166]
								-	[166]
		4% Laponite EP	NaAlg, gelatin <sup>†</sup> , SU-8	Ionic, thermal, UV	Rinse with 0.9% NaCl	High yield-stress; Suitable for ionic, thermal and photo crosslinking; Good viability with NIH-3T3 [96, 156, 167], normal human dermal fibroblast [138]	Not compatible with high ionic strength crosslinking agents	-	[96]*
		2% Laponite EP	NaAlg/gelatin <sup>†</sup>	thermal				100	[167]
		5% Laponite EP	NaAlg/gelatin <sup>†</sup>	Ionic, thermal,				-	[138]
		3% Laponite XLG	NaAlg	Ionic	Harvest			290	[46]
		2.5% Laponite XLG-50v/v% PEG	Silk fibroin	Ion-dipole interaction, interpenetrating network with PEG	Rinse with PBS			100	[127]
		3% Laponite EP-10% PF127	NaAlg <sup>†</sup>	Ionic	Rinse with 1% cold NaCl			-	[156]
	<b>Fumed silica</b>	6% fumed silica in mineral oil	PDMS, SU-8	Thermal, UV, chemical	Rinse with water	High yield-stress; Suitable for ionic, thermal and photo crosslinking;	Not cyocompatible	30	[168]
		3% fumed silica in silicone oil	Electro 225-1, Ecoflex, PDMS	UV, chemical	Clean with acetone			-	[169]*
<b>Phase</b>	<b>Carbopol</b>	1.2% Carbopol 940 (10mM NaOH)	PDMS	Thermal, chemical	Rinse with 10x PBS	Good thermal stability; High transparency; Easy to prepare	Poor fusion between printed filaments; Interfacial	140	[97]*
		1.2% Carbopol 940 (10mM NaOH)	Photocrosslinkable bioelastomer	UV	Rinse with PBS			-	[170]

	Support baths		Tested inks	Compatible crosslinking methods	Removal method	Features	Limitations	Feature resolution (μm)	Ref
<b>Fluoro-carbon</b>	0.2% Carbopol 940 (pH 7)	PDMS, epoxy	Thermal, chemical	Harvest, Rinse with water			tension between the ink and the bath may damage the printed feature	-	[171]
	0.01% Carbopol 940 (pH 7)	PDMS	Thermal, chemical	Harvest, Rinse with water				-	[172]
	0.5% Carbopol 940 (pH 7)	Urethane, epoxy, silicones, UV curable resin	UV, chemical	Harvest				-	[173]
	Perfluorotributylamine (FC-43)	Agarose <sup>†</sup> , NaAlg <sup>†</sup>	Thermal, ionic	Harvest	Inert, transparent, high buoyant, readily available material;	Low resolution	570 [133]	570	[133]
	Perfluorotributylamine	Agarose <sup>†</sup>	Thermal	Harvest				575	[135]
	Polytetrafluoroethylene microparticles	Bacteria cellulose nanofibres	Ionic	Wash with DIW				500	[134]
	1:1 wt SE1700:PDMS	PF127	-	Not removed	Transparent, good thermal stability	Unknown cell toxicity effect	- [126]	-	[126]
	1:1 wt SE1700:PDMS	PF127, Pt-filled PF127-DA	Thermal, chemical (bath)	Not removed				50	[174] <sup>*</sup>
	1:12:12 fumed silica: PDMS:silicone oil	Silver nitrate-PVA	Thermal, chemical (bath)	Not removed				300	[152]
<b>PEO</b>	5% PEO (8M Da)	PAA-dextran <sup>†</sup> , PVA	Freeze-thaw	Not removed	Low bath-ink interfacial tension	Limited choices of aqueous 2-phase systems	200	[129]	
<b>Low viscosity Liquid media</b>	Water, Methanol, ethanol, isopropanol	PDMS, ecoflex, RTV silicone rubbers	Thermal, chemical	Harvest, by evaporation	Simple; Commercially available materials	Limit to 2D patterning	65	[175]	
<b>Ecoflex</b>	Ecoflex (SLO-JO and THI-VEX)	PF127	Thermal, chemical (bath)	Not removed	Stretchable elastomer	Not cytocompatible	-	[99]	
<b>Others</b>	<b>Ecoflex</b>	Ecoflex (SLO-JO and THI-VEX)	Carbon grease	Thermal, chemical (bath)	Not removed	Stretchable elastomer	Not cytocompatible	-	[131] <sup>*</sup>
	<b>HA</b>	Bisphosphonate-HA·Ca <sup>2+</sup>	Photocrosslinkable Bisphosphonate-HA·Ca <sup>2+†</sup>	UV	Acidified PBS (pH 5)	Good viability with ASC/TERT1 cells	Acidic removal medium, pH-sensitive	-	[118]
	<b>Xanthan gum</b>	1.5% xanthan gum/0.5% MA-XG <sup>†</sup>	NaAlg	Ionic, UV	Dilution	Low cost, easy to prepare; Good viability with L929	No liquefaction mechanism for removal	350	[176]

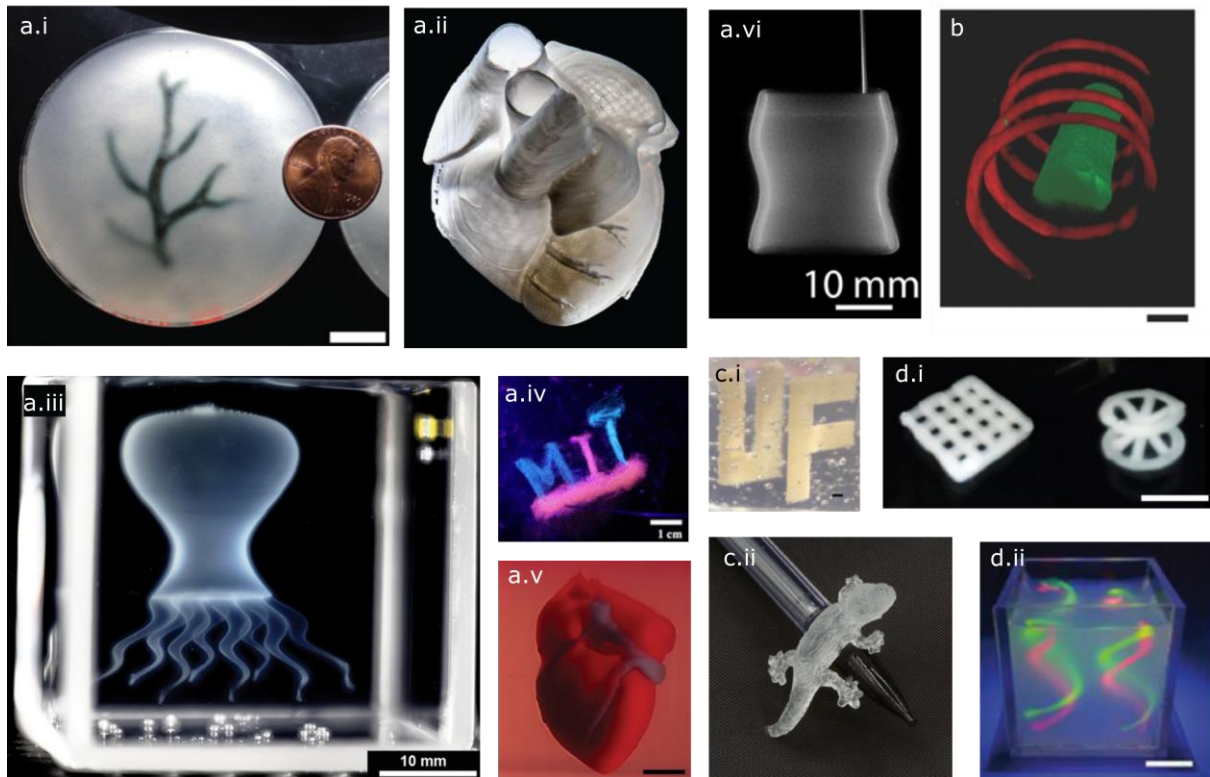


**Figure 1.10| Selected examples of support baths used for embedded printing in literature.** **A)** **Soft microsphere** support bath. A.i) An alginate arterial tree embedded in gelatin slurry (FRESH v.1.0) [52], a.ii) a collagen heart printed by FRESH v.2.0 [136], a.iii) a PVA octopus embedded in Carbopol [122], a.iv) an alginate construct embedded in Pluronic F127 support bath [158], a.v) a heart made of extracellular matrix embedded in a support bath composed of alginate microspheres and xanthan gum [137], and a.vi) silicone elastomers printed in oil-based organogels [123]. **B)** **Guest-host system** of hyaluronic acid hydrogels [31]. **C)** **Colloidal gel** support bath. C.i) A photopolymerisable SU-8 resin embedded in a Laponite® support bath [96], and c.ii) a PDMS gecko printed in fumed silica-silicone oil bath [169]. **D)** **Phase difference systems.** D.i) Printing of bacterial cellulose ink with the use of polytetrafluoroethylene (PTFE) microparticles as the solid matrix [134], and d.ii) an aqueous two-phase system composed of PAA-dextran as the ink and PEO as the bath [129]. Scale bars, (a.i) 2.5 mm, (a.v) 0.5 cm, (b) 200  $\mu$ m, (c.i) 200  $\mu$ m, (d.i) 500  $\mu$ m and (d.ii) 1 cm. Reproduced from [31, 52, 169, 96, 122, 123, 129, 134, 136, 137, 158].

## 2. *Carbopol*

Widely used as a thickening agent in cosmetic industry, Carbopol is a jammed microgels of crosslinked high molecular weight poly(acrylic acid) that swells maximally at pH  $\sim 7$  [122, 151, 152]. Like other support baths, Carbopol exhibits a yield stress, enabling jamming-unjamming transitions upon needle translation [122]. Among different types of Carbopol, Carbopol ETD 2020 is most used for embedded printing. A wide range of applications has been reported with Carbopol as support materials. For example, it has been shown that Carbopol allows high speed ( $\sim 1$  m/s) embedded printing of suspended features with high fidelity ( $24\text{ }\mu\text{m}$ ) [130], cell printing with good viability [149], embedded droplet printing for monitoring chemical reactions and biological assays [152] and many more (see **Table 1.3**).

The key merits of Carbopol are its high transparency for photo-polymerisation (**Figure 1.10a.iii**), thermal stability, easy preparation method, low cost and small microgel diameter of  $\sim 7\text{ }\mu\text{m}$  [121, 122]. In addition, the printed features can be readily released by adding an electrolyte (e.g. PBS and NaCl solutions), which de-swells and fluidises the microgel suspension [97, 151, 152]. However, as Carbopol microgel size is highly sensitive to pH and ionic strength [152], Carbopol is incompatible with inks that require ionic gelation mechanism [124], such as alginate.

## 3. *Pluronic F127 polymeric micelles*

Pluronic F127, also known as poloxamer 407, is a triblock copolymer arranged in a poly(ethylene oxide)-poly(propylene)-poly(ethylene oxide) configuration [43]. The material is well-known for its thermo-reversible sol-gel transition behaviour. As discussed **above**, at ambient temperature and above its critical micelle concentration (CMC  $\sim 21$  wt%), Pluronic F127 self-assembles into micelles and forms a physical gel [43]. Although the material is more notable for its use as sacrificial inks (discussed in **Section 1.6**), a few studies have reported its ability as support baths (**Figure 1.10a.iv**) [43, 157, 158]. The printed features can be easily released from the bath by cooling to  $4\text{ }^{\circ}\text{C}$  [157, 158].

Though a high print resolution ( $\sim 50\text{ }\mu\text{m}$  [158]) is achievable with Pluronic F127, its capacity as sacrificial baths is limited by several limitations. Firstly, the material lacks sufficient storage modulus for long printing process [156], and secondly, it exhibits a high yield stress that might lead to the formation of crevasses [43], though it should be noted that studies have addressed this problem by employing a fluid filler (Figure 1.9) [43] or incorporating

Laponite® nanoclay into Pluronic F127 bath that results in a thixotropic support bath with reduced yield stress and increased G' [156].

#### 4. *Other hydrogel-based microspheres*

In addition to the above hydrogels, several studies have established support baths made of jammed microspheres of alginate (**Figure 1.10a.v**) [137, 160], agarose [119, 163] and gellan gum [124], which were produced by either homogenisation [137], shear induction during sol-gel transition [119, 163] or fragmentation with a mesh [124], respectively. With respect to their removal methods, alginate microspheres can be easily fluidised by adding alginate lyase [137] or EDTA, whereas agarose and gellan gum microspheres do not exhibit a sol-gel transition in mild conditions, hence gentle agitation was used to release the printed objects [119, 124, 163] which could be problematic for releasing very soft gels.

#### 5. *Oil-based organogels*

Akin to the above aqueous systems, an oil-based organogel support bath (**Figure 1.10a.vi**) has been developed for embedded printing complex features of resins, including a RTV (room temperature vulcanizing) silicone elastomer and UV-curing silicone elastomers [123]. The organogels (gel composed of organic phase) were prepared from a mixture of 2.25 wt% SEP (styrene-ethylene/propylene) copolymers, 2.25 wt% SEBS (styrene-ethylene/butylene-styrene) copolymer and 95.5 wt% mineral oil, which self-assembles into organogel particles [123]. The bath is transparent with granular size of ~ 2 – 4 µm, and undergoes gel-sol transition at a temperature above ~ 60°C [123]. High fidelity with print resolution ~30 µm has been demonstrated [123]. As mineral oils and silicone oils are immiscible, a disadvantage of this approach is that the support material can be presented inside the voids of the printed structures of silicone elastomers, causing poor adhesion between layers [169].

## 2. *Guest-host hydrogels*

The use of guest-host supramolecular hydrogels as support baths was established by Highley et al. in 2015 [31], which is one of the earliest works in embedded printing (**Figure 1.10b**). In the work, hyaluronic acid (HA) was modified with either adamantane (Ad) or β-cyclodextrin (β-CD) (Ad-HA and CD-HA) [31]. Upon mixing Ad-HA and CD-HA, supramolecular

hydrogels form because of the guest-host bonds between Ad and  $\beta$ -CD moieties [31]. The resulted hydrogels act like a yield-stress material and have a shear-thinning property [31]. Printed structures can be easily released from the support bath by adding a  $\beta$ -CD solution to disrupt the guest-host bonds, as  $\beta$ -CD competes with CD-HA to bind with Ad-HA [31].

The widespread utilisation of this support bath is greatly limited by several shortcomings. First, the materials were prepared via chemical modification, which involves toxic solvents [118], and is labour-intensive for large-scale production [176]. Second, the need for Ad and  $\beta$ -CD moieties to form supramolecular hydrogels may limit the material choice [156]. Third, the highly hydrophobic AD moieties [118] may compromise the hydrophilicity of the bath.

### 3. *Colloidal gels*

Colloidal gels are physical gels formed by aggregation of sub-micron particles, leading to a 3D self-assembly network in a continuous medium phase [177]. Laponite<sup>®</sup> [46, 96, 127, 138, 156, 167] and fumed silica support baths [126, 152, 168, 169, 174] are the paradigms of this class of support baths (**Figure 1.10c**). Both of them are classic rheology modifiers used in personal care products and paints. The common advantages of this class of material are their simple preparation methods (just by dispersing the particles in a medium), highly thixotropic properties which prevent the formation of crevasses [96] and inexpensive [156]. The transparency of colloidal gels depends on its particle size and concentration.

#### 1. *Laponite<sup>®</sup>*

Well-known for its potential drug delivery applications, Laponite<sup>®</sup> is a disk-shaped synthetic nanoclay (~25 nm in diameter and ~1 nm in height) with low polydispersity, and has an empirical formula of  $\text{Na}^{+0.7}[(\text{Si}_8\text{Mg}_{5.5}\text{Li}_{0.3})\text{O}_{20}(\text{OH})_4]^{-0.7}$  [96, 178]. When dispersed in aqueous solutions, the  $\text{Na}^+$  ions and the  $\text{OH}^-$  ions at the edges of the crystals dissociate, and the particles readily self-assemble to a ‘house-of-cards’ arrangement, forming a transparent colloidal gel that behaves as a yield-stress material (**Figure 1.10c.i**) [96, 178]. Under a stress condition caused by a translating needle through the Laponite<sup>®</sup> support bath, the localised ‘house-of-cards’ arrangement is disrupted, but then rapidly recovers to trap the printed ink upon departure of the needle tip [96].

Laponite® bath can be easily fluidised to release the printed features by adding ionic solutions, such as NaCl [96, 156] or CaCl<sub>2</sub> [138], because this alters the ‘house-of-cards’ arrangement [96]. In addition, improved ease of removal can be obtained by combining Laponite® with Pluronic F127 to yield a thermo-responsive bath [156]. Several grades of Laponite® have been used in literature, including Laponite®-RDS (general grade) [156], Laponite®-XLG (good biocompatibility with cells due to its low level of heavy metals [178]) [46, 127] and Laponite®-EP (organically modified with reduced ionic strength sensitivity so that the gel is compatible with ionic gelation mechanisms) [96, 138, 167]. Features at ~ 100 µm resolution can be achieved with this support bath [127, 167]. The key advantages of Laponite® are its non-cytotoxicity and good compatibility with photo- and thermal gelation mechanisms [96, 138], however the material is not suited when crosslinkers with high strength are required.

## 2. *Fumed silica*

Fumed silica is spherical-like shaped particles with a diameter of ~20 nm [126]. Fumed silica or SE 1700 (a 20 wt% fumed silica-filled PDMS) are usually used in oil-based embedded printing systems [126, 152, 168, 169, 174]. When an oil-based medium is supplemented with fumed silica, a 3D network forms due to Van der Waals force [168], yielding a thixotropic gel that exhibits suitable storage modulus and yield stress for embedded printing [126]. Mineral oil and silicone-based oils (e.g. silicone oil and PDMS) were the common dispersion media used in literature for two general usages. First, suspensions of fumed silica in mineral oil or silicone oil can be used for embedded printing elastomers, such as PDMS and UV curable elastomers, where the printed objects were cured and collected after printing (**Figure 1.10c.ii**) [168, 169]. Using silicone oil as the dispersion medium here might be more superior than mineral oil as it solves the issue of poor fusion between layers of printed structures [169]. Second, fumed silica-PDMS baths can be used for embedded printing sacrificial inks or functional inks, where the bath was cured as a permanent structure after printing [174] or was not removed for long-term study [126, 152].

Features with resolution of ~30 µm were achievable with this system. In addition, its non-toxicity, good transparency and excellent thermal stability make it suitable for UV and thermal curing [168, 179]. Thus far, fumed silica has not been incorporated in aqueous

embedded printing systems, and its capacity for printing cell-laden bioinks is yet to be investigated.

#### 4. *Phase difference systems*

Phase difference systems (**Figure 1.10d**) exploit the immiscibility or the mismatch between the ink and the bath phases to prohibit diffusion of small molecules [97] and swelling of hydrogels. These systems are especially beneficial for printing pH-responsive hydrogels that can swell tremendously in aqueous baths (Further discussed in **Chapter 4**). Notable examples of this class are printing PDMS or elastomers in aqueous Carbopol baths [97, 170–173] and printing hydrogels in hydrophobic and oxygen-permeable fluorocarbon-based baths (**Figure 1.10d.i**) [133–135]. The former can be removed by adding an electrolyte solution [97], while the latter is chemically inert and does not exhibit a liquefying mechanism for removal.

Several drawbacks of this approach are noted, including the cytotoxicity effect caused by the hydrophobic baths during printing, the poor fusion between layers and the high interfacial tension between phases, compromising the print resolution [97]. As reported, the resolution of this type of systems is  $\sim 500 \mu\text{m}$  [133, 134]. Recently, a study has solved the problem of high interfacial tension by employing an aqueous two-phase system comprised of PEO as the bath and PAA-dextran as the ink to yield a higher resolution ( $\sim 200 \mu\text{m}$ ) (**Figure 1.10d.ii**) [129], however, it should be noted that aqueous two-phase systems only work with certain combinations of materials.

## 1.6 Printing with sacrificial inks

Nature is replete with vascular systems, from blood and lymphatic vessels in human to the hydraulic vascular systems in sea stars for locomotion. There has been considerable interest in emulating these systems via biofabrication strategies [180]. In particular, vascular networks are essential for preventing hypoxia occurred in engineered biologic tissues. Several methods have been developed for producing vascular structures, including patterning of PDMS microfluidic devices using soft lithography [181], droplet-by-droplet assembly of spheroids [182], and the use of coaxial nozzles to produce tubular constructs [183, 184] (**Figure 1.11**). However, the capability of these methods is severely limited by their poor flexibility in producing complex vascular networks [132]. As an important step forward, a promising strategy that involves printing sacrificial (or fugitive) inks to produce temporary and removable vasculature-like networks is emerged. The sacrificial inks can be printed either 1) in air then casted with a matrix material, 2) layer-by-layer in an alternating fashion with a permanent hydrogel ink, or 3) directly inside a support matrix (**Figure 1.12**). The surrounding matrix is then crosslinked, followed by the removal of the sacrificial ink to leave a hollow cavity inside the matrix [43]. Comparing to the layer-by-layer approach, casting and embedded printing methods allow direct creation of vasculature networks, therefore, reducing the fabrication time which are beneficial to systems that involve living cells. In addition, smooth, hierarchical and freeform structures with better biomimicry can be produced via embedded printing. **Table 1.4** summarises the common sacrificial materials used in 3D extrusion printing.

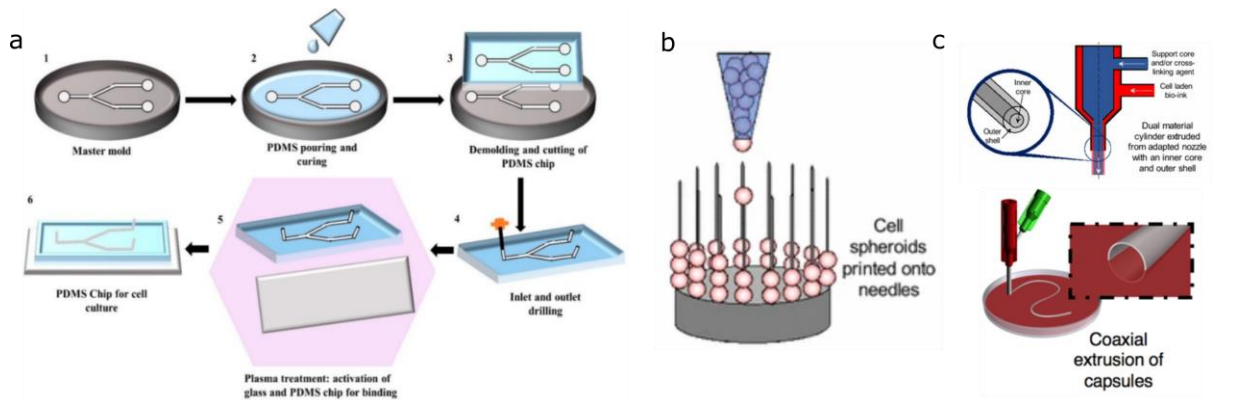


**Figure 1.11| Examples of conventional methods for producing vascular structures.**  
**a)** Soft lithography to produce PDMS microfluidic devices. **b)** Kenzan method to assemble cell spheroids into microneedles. **c)** Coaxial dispensing to produce core-shell strands. Reproduced from [184–186].

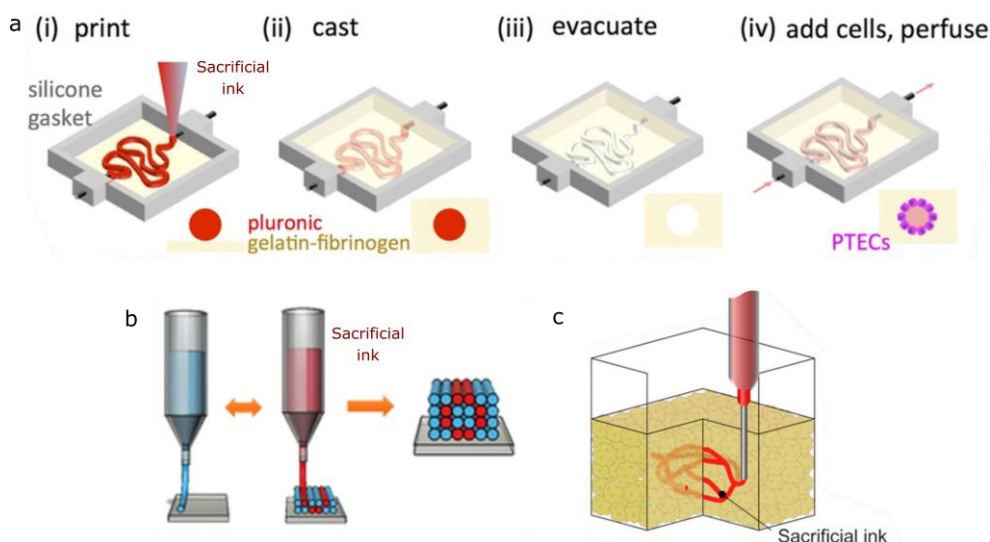


**Figure 1.12| Overview of sacrificial printing methods for producing vascular channel structures.** **a)** In-air printing, followed by casting with a matrix material. **b)** Layer-by-layer printing. **c)** Embedded printing of a sacrificial ink. Reproduced from [128, 187, 188].

**Table 1.4| Common sacrificial inks used in literature.** The references highlighted with \* indicate key studies. Concentration is expressed as weight in volume percent (w/v%); † denotes materials laden with cell. **CMs:** Cardiomyocytes, **ECs:** Endothelial cells, **hMSCs:** Human mesenchymal stem cells, **hESCs:** Human embryonic stem cells, **iPSCs:** Induced pluripotent stem cells, **Res.:** resolution, **HAMA:** hyaluronic acid methacrylate, **Ma:** methacrylated, **DCM:** dichloromethane, **SPELA:** star poly(ethylene glycol-co-lactide) acrylate, **DTT:** dithiothreitol, **CNF:** cellulose nanofibers, **PEGDMA:** poly(ethylene glycol) dimethacrylate and **PNIPAM:** Poly(N-isopropylacrylamide).

	Sacrificial inks	Matrix materials	Removal method	Fabrication approach	Pros	Cons	Res. (μm)	Ref.		
Carbohydrate glass-based	Sucrose-glucose-dextran	PEGDA <sup>†</sup> , fibrin <sup>†</sup> , Matrigel <sup>†</sup> , alginate <sup>†</sup> , agarose <sup>†</sup> (10T1/2 cells laden)	Dissolve in medium/water	Casting	Self-supporting material	Require high temperature for printing and post-printing coating due to its hydroscopic properties	150	[189]*		
		PDMS	Dissolve in isopropanol				300	[190]		
	PDMS						150	[191]		
	Sucrose-glucose	PDMS, Agarose					-	[192]		
	Sucrose-glucose-CaCl <sub>2</sub>	Alginate + CaCO <sub>3</sub>					-	[45]		
	Sucrose-corn syrup	Ecoflex					200	[193]		
	Glucose-fructose	PDMS					1	[194]		
	Isomalt	Epoxy, agarose					250	[195]		
	Maltitol	UV curable resin					-	[196]		
		PDMS					-	[197]		
Pluronic F127	38% PF127	Gelatin-fibrinogen	Liquefy at 4°C or dissolve in water	Casting	Excellent printability	Swelling of PF127 pattern due to large osmolarity difference; Potential cytotoxicity effect	150	[76, 188]*		
	25% PF127 + 1% PEO (8MDa)	Gelatin-fibrinogen					20	[98]		
	40% PF127	GelMA					100	[132, 198]*		
		Collagen-microvascular cells <sup>†</sup>					320	[199]		
		Collagen					250	[200]		
		HAMA					355	[201]		
	30% PF127	Epoxy		Layer-by-layer			330	[202]		
	40% PF127	Alginate MA-hMSCs <sup>†</sup> , HAMA					-	[203]		
	40% PF127	ECM-MDA-MB-231 <sup>†</sup>					500	[204]		
	24.5% PF127	GelMA- PF127 monocarboxylate					-	[187]		
	23% PF127	PF127 diacrylate		Embedded			200	[43]		
	25% PF127	Ecoflex					-	[99]		
	27% PF127	PDMS:SE1700					50	[174]		
Gelatin	10% Gelatin-HUVEC <sup>†</sup>	Collagen	Liquefy at 37°C	Layer-by-layer	Good cyto-compatibility	Lower resolution	500	[205]		
	7% Gelatin	Collagen-dermal fibroblasts <sup>†</sup>					200	[206]		
	15% Gelatin-iPSC derived ECs <sup>†</sup>	ECM-iPSC derived MCS <sup>†</sup>		Embedded			300	[137]		
	15% Gelatin	iPSC-derived Organoids/spheroids-Matrigel-collagen					400	[128]*		
	5% Gelatin	GelMA/HAMA-MCF-7 or C2C12 <sup>†</sup>					-	[201]		
Agarose	2 – 8% agarose	GelMA-MC3T3 <sup>†</sup> , SPELA, PEGDMA, PEGDA	Manual pulling or aspiration with vacuum	Casting	Good compatibility	Limited to simple architecture	150	[207]*		
	Agarose	Cell spheroids		Layer-by-layer			900	[208]		
	6% Agarose	8% GelMA-HepG2/C3A <sup>†</sup>		Embedded			100	[209]		
Wax	Pressian blue paste	Epoxy resin	Liquefy at ~70 – 80°C and remove under vacuum	Casting	Good resolution; Enable printing of thick network	Potential cytotoxicity effect; High processing temperature	10	[95]		
	Petroleum jelly- wax	Epoxy					10	[180, 210]		
	Wax/mineral oil	Epoxy					10	[202, 211]		
	Wax-PF127/mineral oil	Epoxy					100	[212]		
	Paraffin wax	PDMS					150	[213]		
	Petroleum jelly-paraffin wax	Cellulose					250	[214]		
Others	PEGDA-DTT-borax	Fibrin, chitosan	Dissolve in glucose medium	Casting	Sensitive to glucose	Complex preparation method	-	[215]		
	CNF-PNIPAM-PVA-boronate ester	GelMA	Dissolve in glucose at ~30°C				250	[44]		
	6% Alginate-3% Laponite XLG	Laponite EP-CaCl <sub>2</sub>	Liquefy in sodium citrate solution	Embedded	-	-	288	[46]		

3.5% Alginate	Ma-xanthan gum	Dissolve in EDTA	Embedded	-	-	-	[176]
0.5% Xanthan gum	Gelatin slurry-gelatin	Dissolve in water	Embedded	-	Difficult to remove	-	[147]
0.7% Carbopol ETD (pH 7.4)	PDMS	Dissolve in PBS	Casting	-	-	180	[216]
PVA	PDMS	Dissolve in water		-	-	300	[217]
ABS	PDMS	Dissolve in acetone	Simple fabrication method	Removal requires toxic solvents. Long removal process	200	[218]	
PCL	HAMA	Dissolve in acetone and DCM			-	-	[201]

## Carbohydrate glass

Carbohydrate glass (sugar glass) is an inexpensive and readily available material (**Figure 1.13a**). The use of carbohydrate glass as sacrificial materials was first demonstrated by Miller et al. in 2012, where a mixture of sucrose, glucose and dextran was printed in air at 110 °C after boiling off most water content, resulted in a stiff, optical transparent and self-supporting lattice [189]. In the material formulation Miller adopted, glucose was used to prevent unstable recrystallisation of sucrose, whereas dextran mechanically reinforced the glass with enhanced elasticity [189, 191]. Apart from these, various types of sugar or sugar alcohol with different melting temperature and mechanical properties have been used for printing. They are fructose [194], maltitol [197], corn syrup [193, 219] and isomalt [195, 196] (see **Table 1.4**). These elegant carbohydrate lattices were shown to be castable in numerous materials, including agarose [189, 192, 195], alginate [45, 189], PEGDA [189], fibrin [189], Matrigel [189], PDMS [190–192, 194], epoxy [195], Ecoflex [193] and UV curable resin [196]. After crosslinking the matrix, the carbohydrate glass network can be dissolved by placing it in a water-based medium [189, 190, 195].

A major drawback of carbohydrate glass is its extremely hygroscopic property, causing a rapid dissolution of lattices in water within seconds [195]. Therefore, an additional coating step of carbohydrate glass lattices, such as with a poly(D-lactide-co-glycolide) (PDLGA) [189] or polycaprolactone [195], is required prior to casting any water-based solution. The coating allows the dissolved carbohydrates flow through the channels instead of through the bulk of matrix [189], as such, avoiding potential osmotic damage and cytotoxicity caused by the high concentration of dissolved sugar [189]. Further, owing to its hygroscopicity, carbohydrate glass is not suitable for embedded printing application, though a study has shown that by incorporating a crosslinking agent (i.e. CaCl<sub>2</sub>) into the carbohydrate glass fugitive ink, the matrix (i.e. alginate) can be rapidly crosslinked without the need of coating [45]. In addition,

extrusion of carbohydrate glass requires high dispensing force and high heating temperature (> 100°C) [220].

### **Pluronic F127**

Owing to its easy removal, superior printability and shear-thinning property at room temperature, Pluronic F127 has been a well-known fugitive material (**Figure 1.13b**). This method is pioneered by Lewis et al., who utilised the unique thermo-sensitive sol-gel transition of Pluronic F127 to form thermo-reversible gels that can be promptly liquified below its critical micelle temperature (CMT, > ~10 °C) [43]. Pluronic F127 is compatible with various fabrication procedures, for example, a self-supporting Pluronic F127 sacrificial template can first be printed, followed by matrix casting and crosslinking [76, 98, 132, 188, 198, 199, 201]. It can be deposited with the permanent material layer-by-layer in an alternating fashion [187, 203, 204] or embedded printed inside a supportive matrix [43, 99, 126, 174]. Pluronic F127 not only can incorporate with water-based matrices (i.e. GelMA-based matrices), but also oil-based matrices (i.e. epoxy [202], Ecoflex [99] and PDMS/SE 1700 [126, 174]) due to its viscous and amphiphilic characteristics reducing the interfacial tension. In addition, crosslinking agents can be mixed with Pluronic F127 to facilitate the crosslinking of the matrix, such as mixing with thrombin for crosslinking fibrinogen-based matrix [188] or with CaCl<sub>2</sub> for crosslinking alginate matrix [200]. This approach has been used to produce thick and vascularised tissues, which has thickness > 1 cm and can be perfused over long time (> 6 weeks) [76].

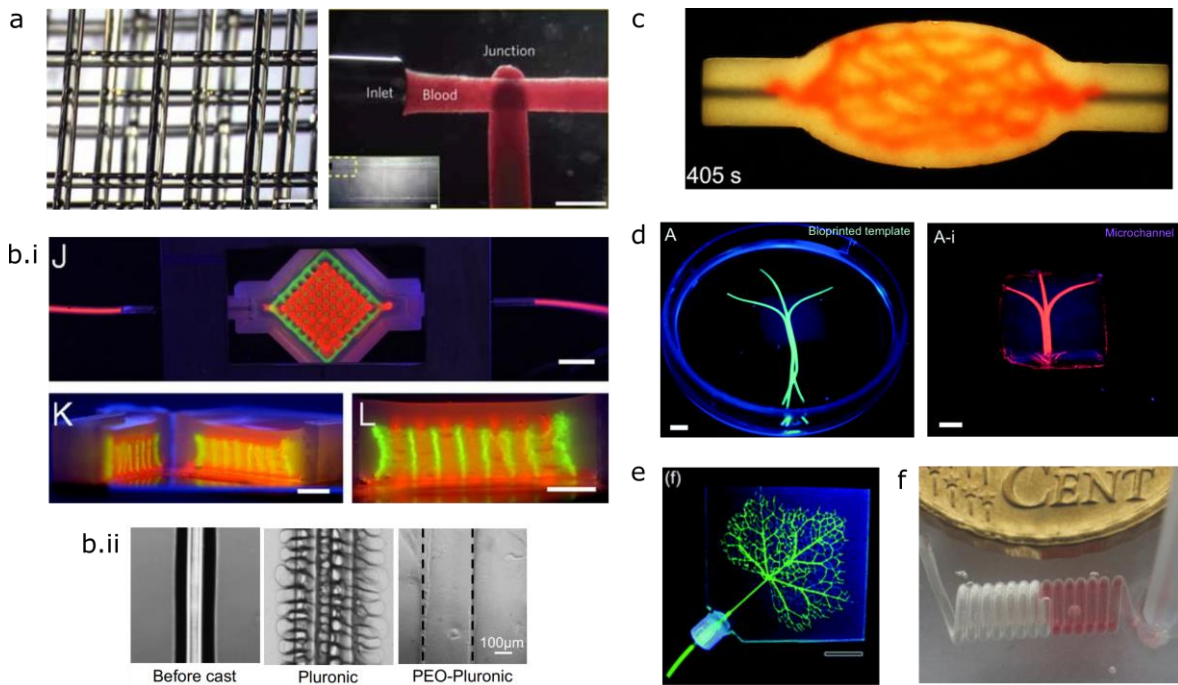


**Figure 1.13| Selected examples of sacrificial inks to produce vasculature in literature.** **a)** Lattice made of carbohydrate glass [189]. **b.i)** Perfusion network formed by Pluronic F127 (red) [76] and **b.ii)** modified Pluronic F127 ink with PEO to prevent ‘viscous fingering’ and yield smooth channels [98]. **c)** Embedded printing a gelatin sacrificial ink in an organoid-based tissue matrix [128]. **d.i)** An agarose template and **d.ii)** the resulted perfusable channel enclosed in GelMA hydrogels with agarose removed [207]. **e)** a 2D microchannel that mimics ivy leaf venation formed by a wax-based ink enclosed in an epoxy matrix [211]. **f)** A spiral PDMS microfluidic device fabricated using a ABS template as the sacrificial scaffold [218]. Scale bars, (a) 1 mm, (b.i) 5 mm, (d) 3 mm and (e) 15 mm. Reproduced from [76, 98, 128, 189, 207, 211, 218].

A few shortcomings of Pluronic F127 are noted. First, previous study has shown that Pluronic F127 at a concentration >10 w/w% can reduce cell viability [221]. This may limit its use with sensitive cell types. Second, the required high concentration (~30 – 40 w/w%) of Pluronic F127 can lead to osmolarity difference between the fugitive Pluronic F127 and the surrounding hydrophilic matrix, causing swelling and the pronounced ‘viscous fingering’ (see **Figure 1.13b.ii)** of the fugitive template [98, 132]. Nonetheless, It has been shown that the ‘viscous fingering’ problem can be suppressed using a modified fugitive ink composed of a lower concentration (25 w/w%) of Pluronic F127 and PEO [98] (**Figure 1.13b.ii)**.

## Gelatin

Although the above sacrificial inks display excellent shape fidelity, they might cause cytotoxic effects on cells [207]. On this account, several studies have proposed the use of cytocompatible natural hydrogels as fugitive inks, such as gelatin [128, 137, 201, 205, 206], and agarose [207, 208] (discussed in the **below section**). Gelatin can be removed easily by warming it to physiological temperature ( $\sim 37$  °C). Although self-supporting gelatin sacrificial template for casting cannot be constructed due to its weak mechanical properties, gelatin has been used to create sacrificial networks via layer-by-layer deposition approach [137, 205, 206] or via embedded printing (**Figure 1.13c**) [128, 201]. The cell-friendly characteristic of gelatin has showed promise in many applications. Vascularised, thick and densely cellular constructs composed of organoids (4 mm thick and  $\sim 2 \times 10^8$  cells/ml) have been produced using gelatin as a fugitive ink [128]. Gelatin sacrificial ink can also be mixed with endothelial cells to facilitate cells adhesion to the wall of the channels before the gelatin being washed away [137, 205].

## Agarose

Agarose is another notable example of cytocompatible fugitive inks (**Figure 1.13d**). Its non-ionic characteristics prevent itself from adhering to surrounding matrix, hence sacrificial agarose templates can be easily removed by aspiration with a light vacuum or manual pulling [207–209]. The approach has been used for creating tubular cavities embedded in a wide variety of photocrosslinkable hydrogels [207, 209] and cell-based tubular structures [208] (see **Table 1.4**). As yet, only very simple architecture of the fugitive templates has been demonstrated as its ability to create branched tubes with complex vascular tree-like architecture is restricted by its manual pulling or aspiration removal method.

## Wax

The use of microcrystalline wax and petroleum jelly as a fugitive material (**Figure 1.13e**) has been developed since 2003 by Lewis et al. [95]. Although the material is not suited for constructing microvascular networks in systems with cells, it is typically used in resin-based matrices, such as epoxy resins [95, 180, 202, 210–212] and PDMS [213]. Under ambient conditions, the materials display excellent printability, hence allowing fabrication of thick ( $\sim 2$

cm), high-resolution ( $\sim 10 \mu\text{m}$ ) and complex microvascular networks (i.e. chaotic mixers) [95]. The material can be liquified at a temperature above  $\sim 80^\circ\text{C}$ , [95].

### Other sacrificial inks

Other sacrificial inks, such as alginate [46], xanthan gum [147], Carbopol [216], glucose-sensitive hydrogels [44, 215], PVA [217], acrylonitrile butadiene styrene (ABS) [218] and polycaprolactone (PCL, **Figure 1.13f**) [201] have also been used as fugitive inks. Their features and removal methods are summarised in **Table 1.4**.

## Chapter 2

# Research Contribution and Thesis Layout

### 2.1 Motivation and research aims

3D printing has been guiding pivotal advances in many areas of science and technology. While conventional 3D printing technology for fabricating rigid materials is relatively mature, the field of soft material printing is still on its early stage. A number of challenges has significantly impeded the development of the technology, including the high cost and the lack of guideline for the standardisation of the printing process. In addition, up to now, the technology has been frequently used for fabricating biological mini-tissue scaffolds where shape resemblance is less essential, or creating complex anatomical models that do not exhibit similar electrical and biological properties to the native tissues. Hence, its shape-mimicking capability has not been fully leveraged for providing insights into human-relevant aspects.

In this respect, my research works set out to examine the below research aims and questions. Emphasis is made on soft materials in this thesis due to their mechanical resemblance to living soft tissues, which might advance vast opportunities for many biomedical applications, such as tissue engineering, soft robotics and flexible electronics. In addition, extrusion-based 3D printing technology is of interest here due to its popularity among the research community, ease-of-use and good compatibility with a wide range of soft materials.

#### 1) Establishing a versatile and hackable extrusion-based printing system for soft materials using a robotic arm

The overly high cost and lack of customisation options of commercial 3D printers for soft materials have greatly hindered the development of the soft material printing technology. On the other hand, although some custom-built extrusion-based systems have been reported in literature, their versatility is severely hindered by the lack of instruction on replicating the

systems. In addition, most reported open-source printers for soft materials rely on either a linear stage system or a modified commercial 3D printer. They are in general bulky in size, and the adaptation of a partially proprietary commercial 3D printer might limit their customisability. Therefore, reporting the development of a fully hackable extrusion-based system that can be compact in size and equipped with an essential set of auxiliary tools will promote facile reproducibility and adoption of custom-made systems.

**2) What are the capabilities and the advantages of a custom-made extrusion-based 3D printer? What are the rational factors in designing the printing approaches?**

Most reported open-source extrusion-based printers for soft materials were only tested with materials that have good printability (i.e. pre-crosslinked alginate) and lack an essential set of auxiliary tools (i.e. heaters and UV modules), which severely limits their ability to construct only a small subset of materials. Thus, the capability of these systems as affordable alternatives to commercial systems are uncertain. Therefore, this work intends to examine the capability and the flexibility of a custom-made printer that is equipped with essential tools for assisting the fabrication of soft materials.

In addition, apart from the function of the hardware, the success of soft material fabrication crucially depends on the ink formulation and the printing method as most soft materials do not intrinsically have an ideal rheology for extrusion printing. To date, a comprehensive guide on the design of the printing approaches to suit different materials is still lacking in literature. Hence, this work aims to provide a perspective on the selection of the printing approach, in an effort to help new users efficiently select an appropriate printing strategy from a vast array of options.

**3) How to model a clinical problem that is dependent on the electrical and anatomical characteristics of human organs by leveraging the uses of 3D printing and neural network?**

‘Current spread’ impedes the efficacy of cochlear implants (CIs) due to the intrinsic conductive nature of biological tissues. The ‘current spread’ problem is determined by the cochlear electro-anatomical features and the location of the implant inside the human cochlear lumen. Understanding the CI stimulus spread, and how it correlates to patient-dependent factors, is hampered by the poor accessibility of the inner ear and the lack of a predictive testing model

that can replicate the CI-evoked intracochlear voltage distribution in human. Therefore, there is a need to establish a new modelling approach that can provide clinical insight. In addition, it would be beneficial if the newly proposed model is economic, artificial, non-ethical and can be physical (non-virtual).

As 3D printing is capable of creating low-cost anatomical phantoms and machine learning is a powerful tool for unfolding relationships in high-dimensional and complex problems, harnessing these two techniques might open possibility for modelling the CI-evoked intracochlear voltage distribution. Therefore, this work attempts to combine 3D printing and neural network for developing a physical-manipulable and ethical model that can represent the electroanatomical-dependent voltage distribution in patients.

## 2.2 Research contributions

In the research work presented in this thesis, I developed an affordable and multi-printhead 3d extrusion printing platform and provide a detailed step-by-step instruction that will encourage new users to reproduce and implement the platform. The platform is equipped with an essential set of auxiliary tools and is controlled by hackable programmes that allow flexible and unconventional printing strategies, such as non-planar printing. The satisfactory performance and multi-functionality of this platform indicate its promising potential as an economical option for research groups with limited resources.

With the developed 3D extrusion printing platform, I explored methods for printing a wide diversity of soft materials, including naturally derived hydrogels (e.g. collagen), synthetic hydrogels (e.g. PVA, Pluronic F127), pH-responsive hydrogels (e.g. poly(acrylic acid)) and silicone elastomers (e.g. Ecoflex). I examined the printability of inks in different support baths previously reported in literature. The finding provided in my work might serve as a rational guide, helping users efficiently design a printing method for different needs.

I further extended this technology to model the ‘current spread’ phenomenon happened in cochlear implant (CI) patients. I developed a ‘3D printing-machine learning’ co-modelling for interpreting clinical electric field imaging (EFI) profiles of CI patients. The 3D printed cochleae with different electro-anatomical features can replicate clinical scenarios of off-stimulation EFI profiles, which contain information about the induced voltage spread characteristics of the cochleae. The co-modelling framework demonstrated autonomous and

robust predictions of patient EFI or cochlear geometry, unfolded the electro-anatomical factors causing CI stimulus spread, assisted on-demand printing for CI testing, and inferred patients' *in vivo* cochlear tissue resistivity by CI telemetry. This co-modelling strategy provides a new physical-manipulatable, ethical and economic approach, which may help reduce the need for animal experiments and facilitate digital twin innovations for neuromodulation implants in healthcare.

## 2.3 Thesis Layout

This thesis is composed of three result chapters (**Figure 2.1**). **Chapter 3** documents the development of a custom-made 3D extrusion printing platform for soft material fabrication. **Chapter 4** examines the performance of the custom-made 3D extrusion printing platform, and propose a rational guide on selecting an appropriate printing strategy for different soft materials. **Chapter 5** presents the fabrication of the 3D printed biomimetic cochleae to replicate the broad electroanatomical spectrum of human cochleae and the development of '3D printing-machine learning' co-modelling framework for providing clinical informatics of cochlear implant patients. The conclusions of this thesis and future work are discussed in **Chapter 6**.

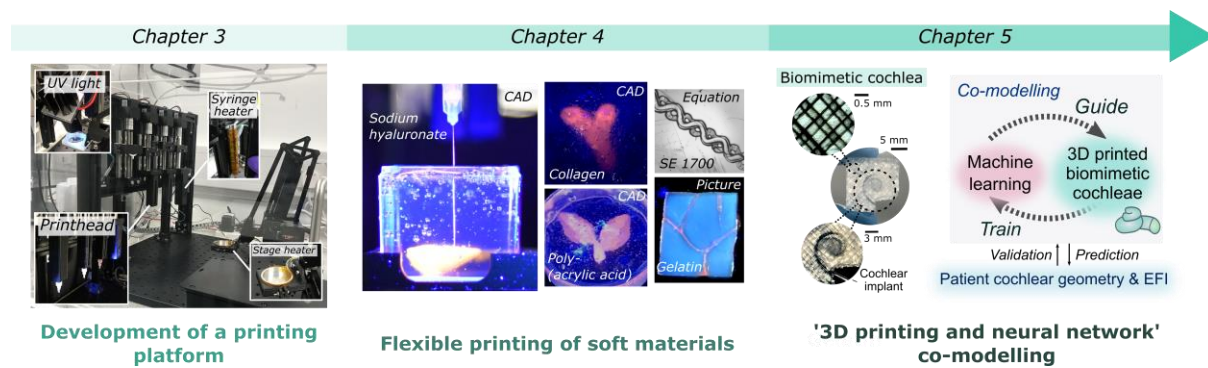


**Figure 2.1| Overview of the result chapters.**

## Chapter 3

# Development of a Printing Platform for Soft Materials

### 3.1 Introduction

Hydrogels and soft elastomers are the two most-used building blocks for soft devices. Their softness and biomimicry have enabled their uses across a vast range of applications. For example, hydrogels have been used for producing bio-functional vascularised mini-tissues for *in vitro* modelling, and silicone elastomers are promising materials for soft robots. In extrusion-based printing when using hydrogels or elastomers as inks, the resolutions are typically in the range of sub-millimetre ( $> 200 \mu\text{m}$ ) [201, 222]. While extrusion rate, nozzle shape and nozzle diameter have the greatest impact on the resolution [223], the print fidelity is affected by the ink rheological and interfacial properties, the printing process and the architecture of the construct [224] (**Figure 3.1**). Therefore, printing platforms that offer a machinery resolution in sub-millimetre range and allow flexible control on the construct architecture are crucial to the success of printing.

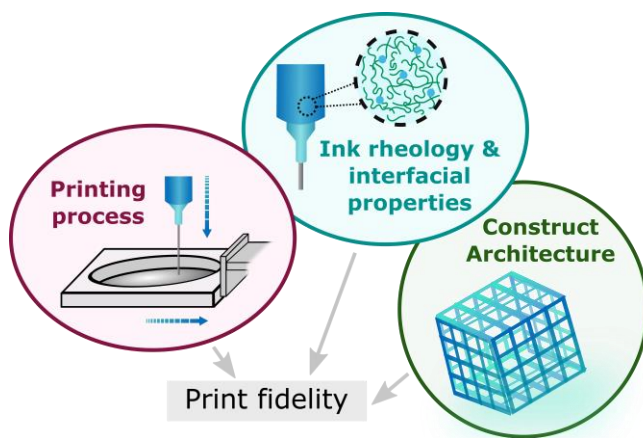


**Figure 3.1| Factors controlling the print fidelity of soft materials.**

Although a plethora amount of commercial 3D printers are available in the market for soft material printing, their high associated cost, ranging from a few thousands up to hundred

thousands of dollars [225–227], and their inability to customise attributed to their proprietary software greatly limit their widespread usage. Additionally, most commercial printers adopt CAD models as the only type of geometry input format, their capability of path-designed 3D printing (such as non-planar deposition and generating constructs with complex and diverse infill patterns) is greatly restricted. All of these constitute a barrier to innovation in research. As such, fully amendable and cost-effective systems would be advantageous to technology development and democratise the technology for new users.

While a few custom-made bioprinting systems have been reported [225, 226, 228, 229], these systems are often limited by their bulky dispensing systems (i.e. using a commercial syringe pump for dispensing), single material deposition [225, 226], lack of heating control [113, 225, 229, 230], and/or the inability to customise print path, in other words, only CAD model geometry input is allowed [225, 226, 230, 231]. Some of these systems were developed by converting conventional 3D printers, of which the firmware is still proprietary, making the operation difficult to customise [230]. More crucially, the lack of documented assembly and operation instructions provided with these systems might reduce the incentives for new researchers to replicate the systems.

To address the above issues, I developed a prototype of an affordable and customisable printing platform equipped with multiple printheads, heating systems and a UV module. The design of the platform is documented in detail, hence the system can be facilely reproduced by new users. To avoid bulky systems, the robotic arm chosen here is compact in size, programmable and possesses sufficiently precise machinery resolution ( $200\text{ }\mu\text{m}$  [232]) at a relatively low cost. The heating systems and the UV module allow modification of the ink rheology during and after printing, which is desirable for improving the print fidelity. To enable rapid customisation, the components of the platform were either 3D printed or can be easily acquired. In addition, the platform relies solely on customisable hardware and is controlled by a hackable Python programme. Not only can the platform allow 3D CAD model geometry input but also inputs of coordinates, equations and picture formats, hence enabling flexible path-designed printing. Overall, this printing platform is sought to provide an entirely customisable printing system (both software and hardware) for flexible operations. With the advances in customisable systems, I anticipate that the wide adaptability of the soft material printing technology can be pushed towards, facilitating the design of new printing strategies.

## 3.2 Materials and Methods

### 3.2.1 Materials

Agarose (A9539), calcium chloride (C5670), gelatin (G1890), Pluronic F127 (P2443) and sodium alginate (W201502) were obtained from Sigma. SE 1700 was obtained from Dow.

### 3.2.2 Creation of 3D printed parts

All 3D printed parts (see **Table 3.1** for the parts that were 3D printed) were designed on Autodesk Inventor and produced using Ultimaker S3. The parts used in the heating systems were printed with ABS (*1621, Ultimaker*) as ABS has a higher temperature resistance, and the rest were printed with PLA (*1609, Ultimaker*).

**Table 3.1| Part list and the breakdown costs of the printing platform.** The total cost refers to the associated cost of a platform equipped with 4 printheads, stage and syringe heating systems, a UV module and a camera. † denotes the custom-made components that were either 3D printed or made from aluminium as stated. \* denotes the components used in the electrical circuit.

Components	Part number	Manufacturer	Cost (£)
<b>uArm Swift Pro Desktop Robotic Arm - Professional Kit</b>	-	ufactory	<b>749.98</b>
<b>Frame</b>			
1. Aluminium rail (20 x 20 x 350 mm) x 4 units	VSL0T2020	Ooznest	10.08
2. Aluminium rail (20 x 40 x 350 mm) x 2 units	VSL0T2040	Ooznest	8.82
3. Breadboard	MB4545/M	Thorlabs	184.52
4. Clamp x 4 units	CL3/M	Thorlabs	14.76
5. Rod holder 1† x 2 units	-	-	-
6. Rod holder 2†	-	-	-
7. Rod holder 3†	-	-	-
8. Adapter plate 1†	-	-	-
9. Adapter plate 2†	-	-	-
10. Adapter plate 3†	-	-	-
11. Adapter plate 4†	-	-	-
			<b>Subtotal</b>
			<b>203.42</b>
<b>Printhead (Components per printhead)</b>			
12. Stepper motor, 3.8 V	5350344	RS	31
13. Shaft coupling	PSMR19-5-5-A	Ruland	18
14. Lead screw (107 mm)	DST-LS-6.35x2.54-R-500-ES	Igus	5.15
15. Lead screw nut	DST-JFRM-131315DS6.35X2.54	Igus	17.25
16. Linear rail (100 mm) x 2 units	WSQ-06	Igus	8.62
17. Linear guide pillow block x 2 units	WJ200QM-01-06	Igus	15.74
18. Ball bearing	624ZZ	NSK	3.65
19. Aluminium rail (20 x 40 x 150 mm)	VSL0T2040	Ooznest	1.89
20. Magnet (Height 3 mm diameter 4 mm) x 6 units	M1219-3	Comus	6.12
21. Magnet (Height 2 mm diameter 3 mm) x 6 units	M1219-2	Comus	2.7
22. Stepper motor drive*	A4988	Polulu	7.18

### 3.2 Materials and Methods

<b>Components</b>	<b>Part number</b>	<b>Manufacturer</b>	<b>Cost (£)</b>
23. Resistors (10 kΩ 0.6 W)*	MF006FF1002KIT	Royal Ohm	1.36
24. Capacitor 100 µF*	EEAGA1A101	Panasonic	0.06
25. Motor holder†	-	-	-
26. lead screw nut mount 1†	-	-	-
27. lead screw nut mount 2†	-	-	-
28. Syringe holder 1†	-	-	-
29. Syringe holder 2†	-	-	-
30. Heating syringe holder 1†	-	-	-
31. Heating syringe holder 2†	-	-	-
		<b>Subtotal</b>	<b>118.72</b>
<b>Printhead (Components for whole system)</b>			
32. Power adapter, 9V, 2A	VEL18US090-UK-JA	XP Power	10.24
33. Arduino mega*	A000067	Arduino	25
34. Breadboard*	TW-E40-1020	Twin Industries	4.13
35. USB A-male to USB B-male cable*	AK-300102-010-S	Digitus	0.42
		<b>Subtotal</b>	<b>39.79</b>
<b>Heating (Components per module)</b>			
36. Power adapter, 9V, 2A (syringe heater)	VEL18US090-UK-JA/	XP Power or	10.24/
37. Power adapter, 12V, 500mA (stage heater)	T6116ST	Stontronics	4.02
38. Type K thermocouple	Z2-K-1M	Labfacility	4.64
39. Thermocouple Amplifier (MAX31855K)*	269	Adafruit	12.76
40. MOSFET*	IRLRLU8743PBF	Infineon	1.04
41. Arduino Nano*	A000005	Arduino	14.23
42. Breadboard*	MCO1003	Multicomp	1.10
43. USB A-male to USB mini B-male cable*	ZUV0E3058769	StarTech	1.4
44. Al heating syringe barrel (made with aluminium)†	-	-	-
45. Al 35 mm petri dish holder (made with aluminium) †	-	-	-
		<b>Subtotal</b>	<b>~37</b>
<b>Heating (Components for whole system)</b>			
46. 31 AWG Nichrome wire	UMNICWIRE2	Ultimachine	5
47. High temperature tape	051-0002	Antistat	4.27
		<b>Subtotal</b>	<b>~50</b>
<b>Stage</b>			
48. 35 mm petri dish stage†	-	-	-
49. 35 mm petri dish stage_heating 1†	-	-	-
50. 35 mm petri dish stage_heating 2†	-	-	-
51. 55 mm petri dish stage†	-	-	-
52. 90 mm petri dish stage†	-	-	-
53. 30 mm square container stage†	-	-	-
54. 38 mm square container stage†	-	-	-
55. Glass slide holder†	-	-	-
<b>Others</b>			
56. UV365 LED UV Torch	NSUV365	Nightsearcher	162.5
57. HD Webcam	C922	Logitech	65.1
58. Drop-in Tee Nuts, M5 (~200 units)	VSLOT-H-DT-M5	OOZnest	40
59. MakerLink 90 Degree Hidden Tee Nut x 4 units	VSLOT-H-ML-90H-GS	Openbuilds	4.88
60. Universal L Brackets x 4 units	VSLOT-B-UL-S-C	OOZnest	4
61. Jumper cables	MIKROE-511	MikroElektronika	2.41
		<b>Subtotal</b>	<b>278.89</b>
		<b>TOTAL</b>	<b>~1870</b>

### 3.2.3 Calibration of printhead extrusion

The flow rate of the extruded materials of the printheads (printhead 2 and printhead 3) were measured using a flow sensor (Elveflow, OB1 MK3). All experiments were performed with a 3 ml syringe. The flow sensor was connected to the Elveflow controller. First, the channel of the flow sensor was slowly washed with 1 ml of acetone, followed by 1 ml of ethanol and 1 ml of DI water. It was then dried by applying an air pressure of 400 mbar. The inlet of the flow sensor was connected to the needle tip of a 3 ml syringe filled with water in a printhead via a tubing. The outflow water was collected in a container. During the calibration experiments, the stepper motor was run at a sixteenth microstep resolution and at different setting of the time interval between consecutive steps of the stepper motor,  $t_s$ . The resulted transient and steady-state flow rates were measured every 0.05 s for at least 1 min. After finishing the experiments, the flow channel was washed with water and ethanol, and was dried by applying an air pressure of 400 mbar. The average and the standard deviation of the steady-state flow rates,  $\dot{V}_s$ , were calculated from the measured flow rates during the steady state period.

### 3.2.4 Printing experiments for validating the coordinate transformation equations used in the control programme

The constructs shown in **Figure 3.15** were made of either agarose, alginate, Pluronic F127 or SE 1700. Prior to the printing experiments, 1 w/v% agarose, 3.5 w/v% alginate and 40 w/v% Pluronic F127 solutions were prepared by dissolving the materials in DI water according to their w/v concentrations. The SE 1700 ink was prepared by mixing the pre-polymer base with the catalyst in a 10:1 w/w ratio. The alginate ink was then pre-crosslinked by mixing a 40 mM CaCl<sub>2</sub> solution in a 5:3 v/v ratio. During the printing of agarose, the printhead was heated at 40 °C to prevent the agarose solution in the printhead from gelling. The SE 1700 and Pluronic F127 constructs were printed in-air, and the agarose and alginate constructs were printed in a gelatin slurry bath using a similar protocol described in [52, 233] (see **Chapter 4**).

## 3.3 Printer assembly

**Figure 3.2a** shows the overview of the extrusion-based 3D printing platform. Housed in an enclosure for ease of sterilisation and built on an aluminium breadboard for ease of mounting different modules, the printer consists of four piston-driven dispensing printheads and a stage

tightened to a movable robotic arm. The syringe and the stage can be coupled with heating modules for temperature control. In addition, a UV module and a camera can be integrated into the system for curing photo-polymerisable inks and monitoring the printing process (**Figure 3.2b**). The syringe holders and the stages were 3D printed using either PLA or ABS, thus they



**Figure 3.2| A custom-made 3D extrusion printing platform. a)** Setup overview. Printheads 1 – 3 can accommodate either 1 ml or 3 ml syringes, whereas printhead 4 is coupled with a heating system and can accommodate a 3 ml syringe. **b)** Incorporation of (i) a UV module and (ii) a camera into the platform. **c)** a detailed view showing the design of the 3D printed stage. **d)** 3D printed stages to fit various sizes of receiving substrates. **e)** Heaters. e.i) a portable 1 ml syringe heater, e.ii) a 3 ml aluminium syringe heater and e.iii) a 3.5 mm stage heater. **f)** Components of a printhead. The item number can be referred to Table 3.1.

can be easily modified to fit different sizes of syringes and petri dishes if needed. Below provides a detailed description of the design, assembly instructions and the electrical circuit diagram of the modules. **Table 3.1** summarises the required components and their costs.

### 3.3.1 Stage and robotic arm as motion module

The motion module of this platform is composed of a 3D printed stage coupled with a robotic arm. Here, I adopted a compact robotic arm (*uArm Swift Pro Desktop Robotic Arm*, called ‘uArm’ herein) that has adequate mechanical resolution (0.2 mm) and position repeatability (0.2 mm). The robotic arm is programmable with an available open-source python library (<https://github.com/uArm-Developer/uArm-Python-SDK>) [232, 234]. For ease of observation and centre point calibration, the 3D printed stages were designed with large open sides and a central hole (**Figure 3.2c**). Various stages with different sizes were custom-made to accommodate different receiving substrates or reservoirs, such as standard glass slides, petri dishes (90, 55 and 35 mm) and rectangular containers (40 and 30 mm) (**Figure 3.2d**). In addition, an aluminium holder was designed and made to fit with a 35 mm petri dish for heating (**Figure 3.2e**).

#### *Assembly procedure*

All 3D printed stages were designed to mount to the uArm with an adapter piece obtained from the laser engraving kit of the uArm. To connect the stage to the uArm, first, the adapter piece was disassembled from the laser engraving kit (**Figure 3.3a**, Step 1). The adapter piece was then attached to the 3D printed stage using M3 screws (Step 2), inserted and fastened to the uArm using the hand screw of the uArm (Step 3). The uArm was locked firmly on an aluminium breadboard (*MB4545/M, Thorlabs*) using clamps (*CL3/M, Thorlabs*) (Step 4).

For the heating stage, an aluminium holder was made based on my design for fitting a 3.5 mm petri dish. The machining work was carried out by the mechanical workshop of the Cavendish Laboratory, University of Cambridge. The aluminium holder was wrapped with a heating coil (see **Section 3.3.3** for more details). It was then clamped by two 3D printed parts to form the heating stage (**Figure 3.3b**). The installation of the heating stage to the uArm was the same as the procedure mentioned above.

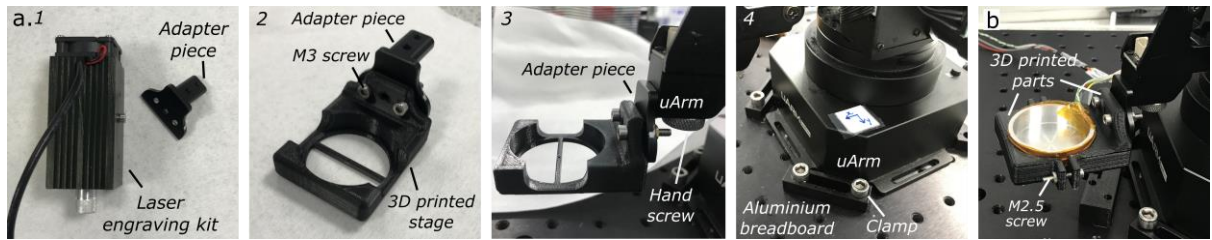


**Figure 3.3| a)** Assembly procedure of the stage to the uArm. **b)** A detailed view of the heating stage.

### 3.3.2 Dispensing module

The dispensing module is composed of 4 independent piston-driven printheads. Three of them can accommodate a 1ml or 3ml syringe (*1202751 and 1202743, BD*), and one of them contains a custom-made aluminium barrel wrapped with heating wires that can accommodate a 3 ml syringe for heating (**Figure 3.2a**). A portable heating unit was additionally made for heating a 1 ml syringe if needed (**Figure 3.2e**).

The printhead was made with simple mechanical components that can be acquired easily, such as a stepper motor, linear rails and a lead screw (**Figure 3.2f** and **Table 3.1**). In particular, I chose linear rails as the motion guides here because they are compact in size, and offer increased stability and smoother motion in contrast with smooth rods (**Figure 3.4a**). A microstepping stepper motor drive (*A4988, Pololu*) is chosen as it enables five microstep resolutions (full, 1/2, 1/4, 1/8 and 1/16 step) [235]. When using a 1/16 microstep resolution together with the selected stepper motor and threaded rod that have a step angle of 1.8° and a pitch spacing of 2.54 mm [236, 237], a superior theoretical resolution of ~ 0.06 µL per step can be yielded (see calculation below). In addition, aided by the magnetic design of the syringe holders (**Figure 3.4b**), syringes can be easily loaded to the syringe holders.

#### Theoretical resolution of the printhead

The theoretical volumetric resolution per step of the printhead when using a sixteenth microstepping resolution was calculated using below equations [230].

$$\text{Step per revolution} = 360/\text{step angle} = 360/1.8 = 200 \text{ steps per revolution}$$

$$\begin{aligned} \text{Steps per mm} &= \frac{1}{\text{pitch spacing}} \times \frac{1}{\text{micro-stepping resolution}} \times \text{steps per revolution} \\ &= \frac{1 \text{ revolution}}{2.54 \text{ mm}} \times \frac{1}{\frac{1}{16}} \times \frac{200 \text{ steps}}{1 \text{ Revolution}} = 1260 \text{ steps/mm} \end{aligned}$$

$$\text{Volume per step} = \text{Step size} \times \text{cross-sectional area of the syringe plunger}$$

$$= \frac{1 \text{ mm}}{1260 \text{ steps}} \times (\pi \times (4.78 \text{ mm})^2) = 0.057 \mu\text{L/step}$$

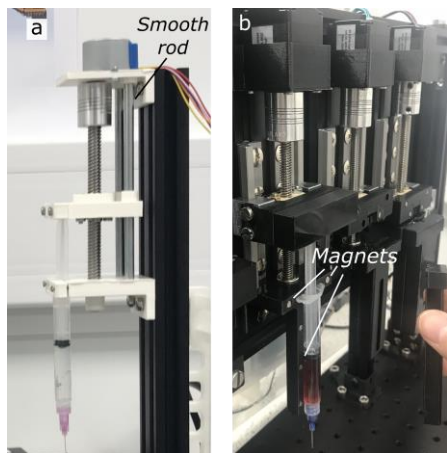


**Figure 3.4| a)** A printhead built with smooth rods as motion guide. **b)** the magnetic design of the printhead.

### Assembly procedure

#### 1. Printhead

**Figure 3.5a** shows the step-by-step assembly instruction of a printhead. **1.** Before assembling the printhead, the lead screw (*DST-LS-6.35x2.54-R-500-ES, Igus*) was milled to the designed dimension. **2.** Next, the stepper motor (*5350344, RS*) was attached to the 3D printed motor holder using M2.5 screws. **3.** The motor holder was then inserted to an aluminium rail (*VSL0T2040, Ooznest*) and locked in place with the drop in tee nuts (*VSL0T-H-DT-M5, Ooznest*) and M5 screws. **4.** A shaft coupling (*PSMR19-5-5-A, Ruland*) was connected to the motor shaft and tightened using the built-in set screw. **5.** Two 10 cm linear rails (*WSQ-06, Igus*) were tightened firmly on the aluminium rail using M5 screws at a position of ~28 mm from the top edge of the aluminium rail. **6.** A linear guide pillow block (*WJ200QM-01-06, Igus*) was inserted to each linear rail. **7.** The modified lead screw was combined with a lead screw nut (*DST-JFRM-131315DS6.35X2.54, Igus*), which was then tightened on a 3D printed lead screw nut mount. **8.** The lead screw was tightened to the shaft coupling, and the 3D printed lead screw nut mount was then linked to the linear guide pillow blocks on the linear rail using M4 screws. **9.** The end of the lead screw was connected to a ball bearing (*643ZZ, NSK*) that was fit to a 3D printed syringe holder. **10.** The 3D printed syringe holder was then tightened on the aluminium rail using M5 screws and the drop in Tee nuts. **11.** The printhead assembly was finished by placing magnets (*M1219-3 and M1219-2, Comus*) to the designed holes of the lead screw nut mounts and the syringe holders using super glue.

The heating printhead was assembled similarly using different 3D printed parts of syringe holders that were customised to fit an aluminium barrel.

## 2. Installation of printheads to frame

The frame of the dispensing module is made of six aluminium rails, and was assembled using hidden tee nuts (*VSL0T-H-ML-90H-GS, Openbuilds*) and L brackets (*VSL0T-B-UL-S-C, Ooznest*) as linkages according to **Figure 3.5b**. The frame was then fastened on the aluminium breadboard by means of the customised 3D printed adapters. In total, 4 printheads were built. They were firmly installed to the frame using the 3D printed adapter plates.

## *Electrical circuit*

**Figure 3.6** shows the circuit diagram of a printhead. The stepper motor of the printhead is controlled by an Arduino board. Before connecting the stepper motor to the Arduino board, a current limiting procedure was carried out with the motor drive to limit the loaded current. This procedure was to prevent the loaded current from exceeding the rated current of the stepper motor, hence avoiding overheating of the stepper motor. Following the instruction stated in [235], the procedure was carried as follows. First, the current limit of the motor drive,  $I_{max}$ , and the reference voltage of the motor drive,  $V_{ref}$ , were calculated using the below equations. The actual current limit of the stepper motor,  $I_{rating}$ , is usually 70% of the driver current limit,  $I_{max}$ .  $I_{rating}$  is 670 mA according to the stepper motor specification [236] and  $R_{cs}$  is the current sense resistance of the motor drive, which is 0.068 Ω [235].

$$I_{max} = \frac{I_{rating}}{0.7} = \frac{0.67}{0.7} = 0.96 \text{ A} \quad (3.1)$$

$$V_{ref} = 8 \times I_{max} \times R_{cs} = 8 \times 0.96 \times 0.068 = 390 \text{ mV} \quad (3.2)$$

Next, an Arduino script was written for running the motor drive in full step mode by setting the logic levels of the MS1, MS2 and MS3 pins to ‘LOW’. **Table 3.2** details the pin configuration defined in the Arduino script used in the current limiting procedure. After ensuring the motor was not connected to the motor drive, the script was uploaded to the Arduino board. A multimeter was then used to measure the voltage,  $V_{ref}$ , between the potentiometer and the GND pin connecting to the Arduino board (see **Figure 3.6**).  $V_{ref}$  was tuned to approximately 390 mV by rotating the potentiometer using a screwdriver.

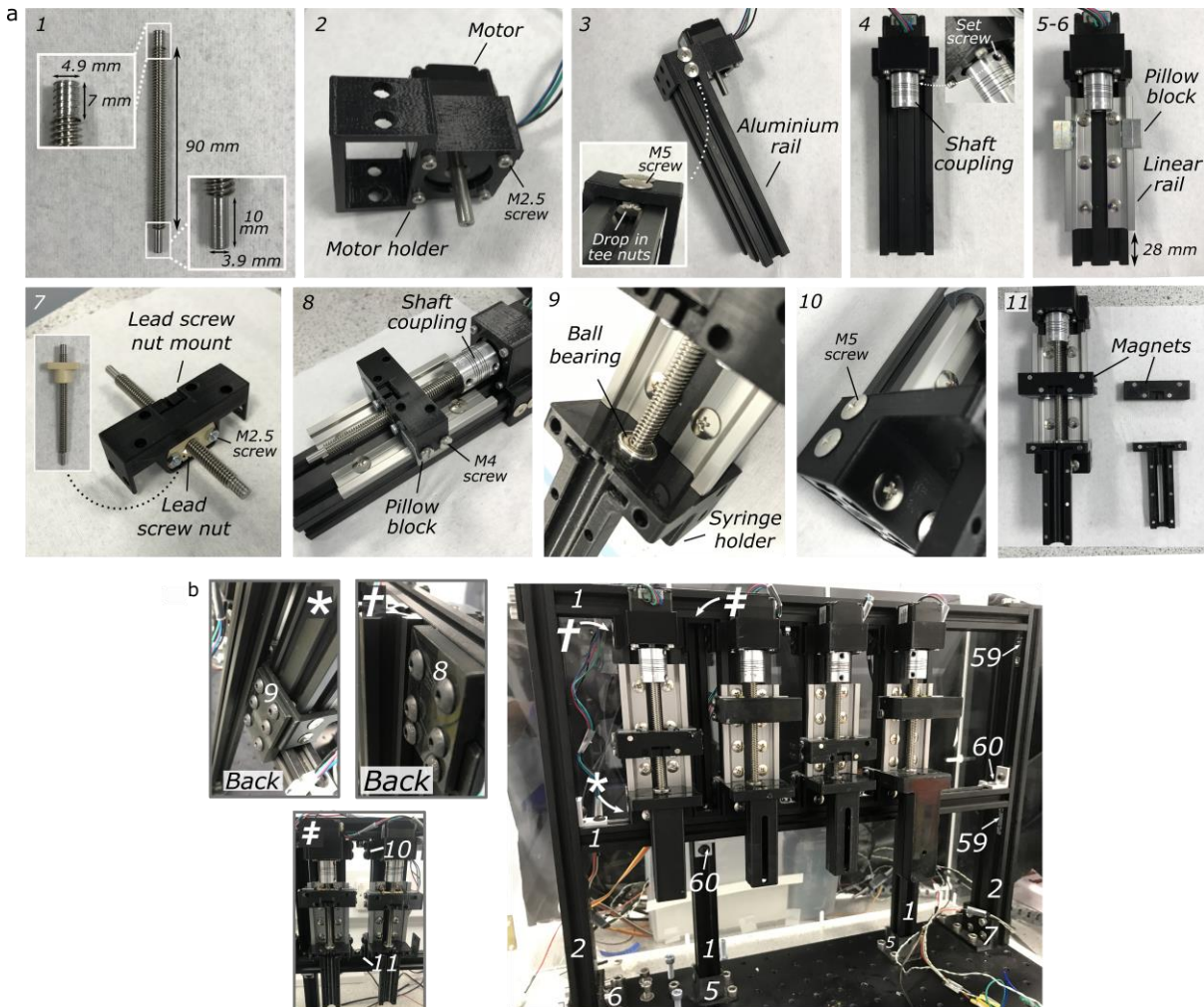


**Figure 3.5| a)** Assembly procedure of the printhead. **b)** Frame of the dispensing module. The item numbers in (b) can be referred to Table 3.1.

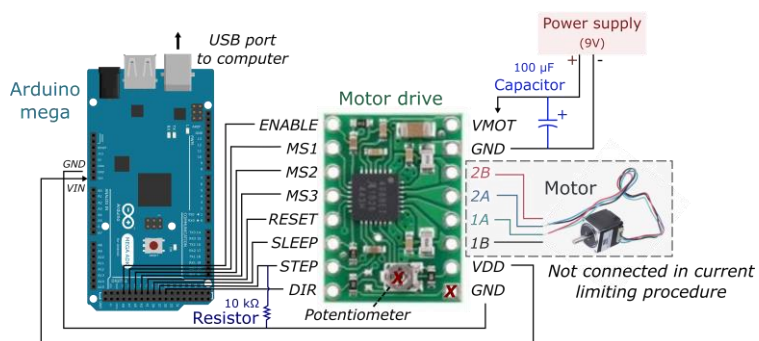


**Figure 3.6|** Circuit diagram for connecting a stepper motor with Arduino and a motor drive. In the current limiting procedure, the stepper motor was detached from the circuit.  $V_{ref}$ , was measured between the potentiometer and the GND pin to the Arduino board, as indicated by the red crosses.

After the current limiting procedure, the stepper motor was connected to the motor drive using the arrangement shown in **Figure 3.6**. The Arduino pin configuration for normal operation is listed in **Table 3.2**. Overall, a single Arduino mega board and a power supply were used to control and operate four printheads. **Figure 3.7** shows the overall circuit diagram. As an Arduino mega board has 54 digital pins and the control of each printhead requires 8 digital pins, more printheads can be incorporated into the system if needed.

**Table 3.2| Arduino pin configuration for the current limiting procedure and normal operation.** Descriptions of the pins of the A4988 motor drive can be found in [235]. In particular, the MS1, MS2 and MS3 are the microstep pins that enable selection from full, half quarter, eighth or sixteenth step resolutions. When they are set to a logic LOW, a full step microstep resolution is enabled, whereas a sixteenth microstep resolution is enabled when they are all set to a logic HIGH. DIR determines the direction of the rotation, with HIGH drives the motor clockwise and LOW drives the motor anticlockwise.

Digital pins	Input in current limiting procedure	Input in normal operation
ENABLE	LOW	
MS1	LOW	HIGH
MS2	LOW	HIGH
MS3	LOW	HIGH
RESET		HIGH
SLEEP		HIGH
STEP		Alternating from HIGH and LOW
DIR		HIGH

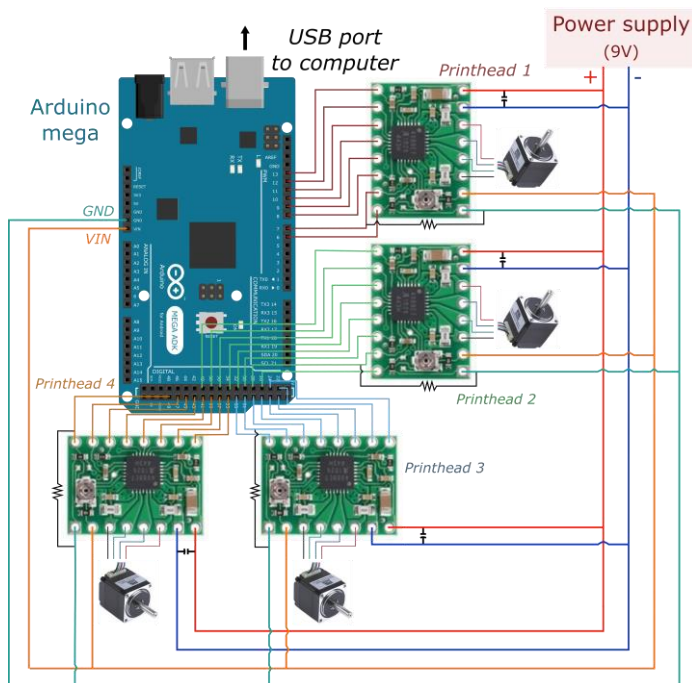


**Figure 3.7| Overall circuit diagram of the dispensing module composed of four printheads.**

### 3.3.3 Heating modules

As mentioned previously, an aluminium stage heater, a 3 ml syringe aluminium heater and a 1 ml portable syringe heater were made for controlling the pre- and post-printing rheology of the materials. Here, nichrome wires (*UMNICWIRE2, Ultimachine*) were employed as the heating element because of its high melting point and high resistivity, and a K-type thermocouple (Z2-K-1M, *Labfacility*) was used as the temperature sensor.

#### *Assembly procedure and electrical circuit*

All heaters consist of three layers. The first layer is composed of high temperature tape wrapped around the aluminium holders or a syringe. The second layer is made of nichrome wires wrapped around the first layer of high temperature tape. Another layer of high temperature tape was added to enclose the nichrome wires for protecting the wires. The thermocouple was placed on the heater using the high temperature tape for temperature sensing.

**Figure 3.8** shows the circuit diagram of the heating module. The syringe heater was connected to a power adapter with rating of 9 V and 2 A, whereas the stage heater was powered by a power adapter with a 12 V and 500 mA rating. An Arduino nano board and a MOSFET were employed to control each heating module because of their compactness in size. The IRLR/U8743PbF MOSFET was chosen here because it has a small gate threshold voltage that can be used with Arduino and a high drain-to-source voltage of 30 V that prevents the MOSFET from overheating when applying a drain-to-source voltage of 9 – 12 V [238].

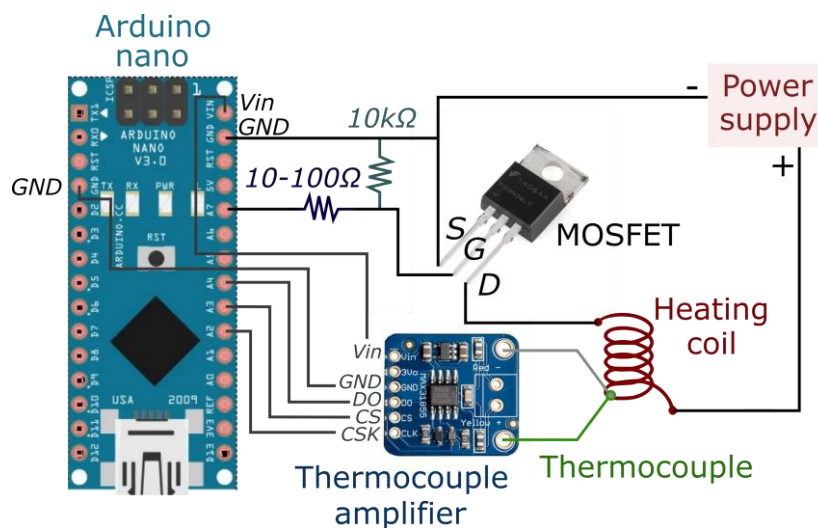


**Figure 3.8| Circuit diagram of a heating module.**

### 3.3.4 UV module and camera

A UV light source can be easily mounted onto the aluminium breadboard when needed. Here, a low power UV light torch (5 W, *NSUV365, Nightsearcher*) with wavelength of 365 nm was chosen as this wavelength is located in the range of the excitation of the common photoinitiators (i.e. Irgacure 2959 and LAP) used in crosslinking hydrogels. A camera unit (*C922, Logitech*) can also be added onto the breadboard for *in-situ* monitoring and recording the printing process.

## 3.4 Calibration of components

### 3.4.1 Printhead extrusion

In the printhead design here, the extrusion flow rate is controlled by the rotational speed of the stepper motor that is determined by the setting of the time interval between two consecutive steps of the stepper motor,  $t_s$ . A longer time interval leads to a slower rotational speed that in turn results in a slower flow rate, vice versa. To evaluate the performance of the printheads, I examined its transient flow behaviour and flow repeatability (see **Materials and Methods 3.2.3**). **Figure 3.9a** shows an exemplar flow profile upon starting and stopping the extrusion. From the zoomed-in profiles at the instant after the extrusion started (**Figure 3.9b.i**), it is found that a steady state was reached shortly after the extrusion initiated, around  $\sim 2.6 - 3.3$  s depending on the  $t_s$  used. When running the motor with a small  $t_s$  setting ( $t_s = 5,000 \mu\text{s}$ ), a large transient overshoot of flow was observed, though a  $t_s$  of 5,000  $\mu\text{s}$  results in a very fast flow rate and was not used in all my printing experiments. The delay time to stop the pump was around  $\sim 2$  s, regardless of the  $t_s$  setting (**Figure 3.9b.ii**). Next, I investigated the flow repeatability of the printhead (**Figure 3.9c**). The relationships between  $t_s$  and the steady-state flow rate,  $\dot{V}_s$ , were almost the same in five repeated measurements. In addition, the relative standard deviation of the steady-state flow rate was 4% - 10%, showing the good stability of the printhead. In summary, the printhead exhibited a good flow repeatability, and the flow reached a steady state or stopped almost instantaneously ( $\sim 2 - 3$  s) upon switching on or off the printhead.

**Figure 3.9d** presents the calibration graph depicting the relationship between the steady-state flow rate,  $\dot{V}_s$ , and the time interval between consecutive steps of the stepper motor,  $t_s$ . Despite the printheads were assembled manually, the performance of the printhead is reproducible as evidenced by the almost identical relationships of  $\dot{V}_s$  vs  $t_s$  of printhead 2 and

printhead 3. As the calibration was performed with a 3 ml syringe, a 1 ml calibration curve was estimated by scaling the equation based on the cross-section of the syringes, see below.

$$3 \text{ ml calibration curve: } \dot{V} = 15.3 + \frac{1.34 \times 10^6}{t_s} \quad (3.3)$$

$$1 \text{ ml calibration curve: } \dot{V} = \left( 15.3 + \frac{1.34 \times 10^6}{t_s} \right) \times \frac{d_{1ml}^2}{d_{3ml}^2} = 4.7 + \frac{0.41 \times 10^6}{t_s} \quad (3.4)$$

where  $d_{1ml}$  and  $d_{3ml}$  are the inner diameters of the 1 ml and 3 ml syringes, which are 4.78 mm and 8.66 mm, respectively.

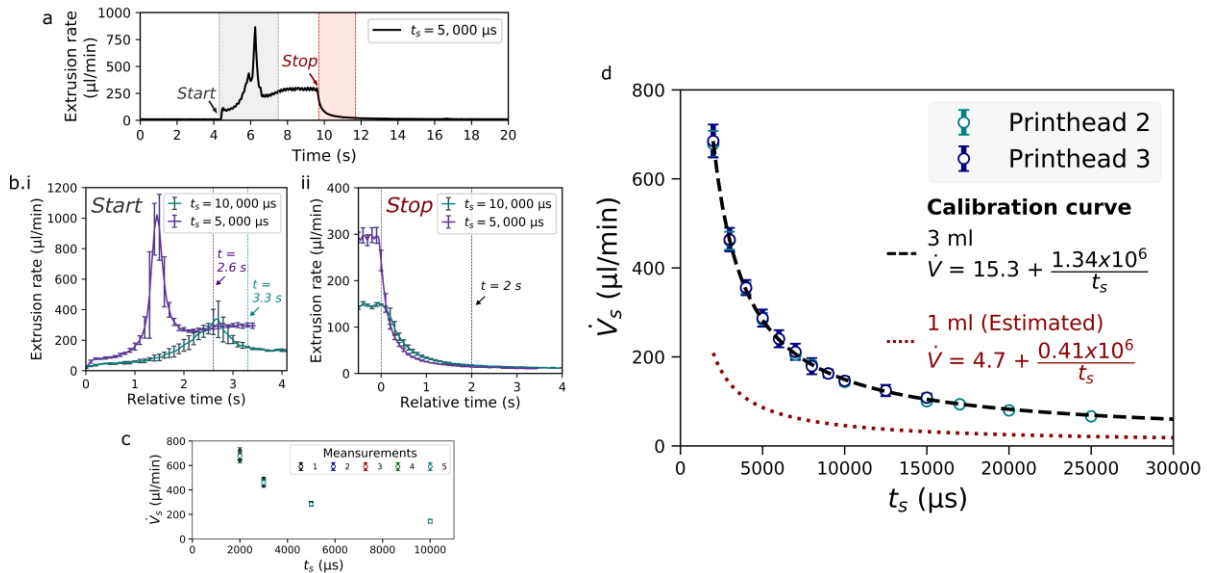


**Figure 3.9| Performance and calibration of the printheads.** a) An exemplar flow profile upon starting and stopping the extrusion. b) Zoomed-in flow profiles at the instant when extrusion (i) was started and (ii) was stopped. ( $n > 4$ ) c) Repeated measurements of the steady-state extrusion flow rate,  $\dot{V}_s$ , at different settings of the time interval between consecutive steps of the stepper motor,  $t_s$ . ( $n = 5$ ) d) Calibration graph showing the relationship between  $\dot{V}_s$  and  $t_s$ . All experiments were tested with a 3 ml syringe at a setting of sixteenth microstep resolution of the stepper motor.

### 3.4.2 Stage speed

As assigned by the manufacturer, the speed of uArm is described by an unitless quantity that only provides an indication of the speed. Therefore, a calibration experiment was performed by my colleague, Yaqi Sheng at the Department of Engineering, to show the relationship between the actual speed and the unitless speed quantity (Figure 3.10). In summary, the uArm employed here can travel from 100 mm/s to 0.3 mm/s (values obtained from the uArm specification [232] and the calibration experiment), and the relationship between the actual speed and the unitless speed quantity can be perfectly described by a linear equation (see equation in Figure 3.10).

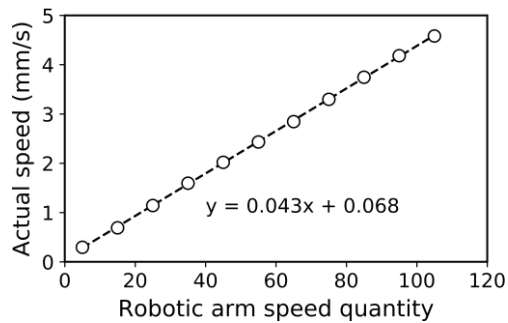


**Figure 3.10| Relationship between the actual speed and the unitless speed quantity of uArm.**

## 3.5 Control programme

Figure 3.11 shows the overview of the operational workflow of the setup. The printing operation is implemented by a Python programme that synchronously communicates with the Arduino boards of the uArm and the dispensing module (**Figure 3.11a**), whereas the heating modules are independently controlled by graphical user interfaces written on Processing that communicate with the Arduino boards of the heaters (**Figure 3.11b**). All programmes are written in a way that users only need to define the input parameters in the programmes (**Figure 3.11**, ‘Inputs’ section) and calibrate the stage if needed. The rest of the printing procedure will be executed automatically, hence users with no coding experience are able to operate the printer. Below details the design of the logical structure of the programmes.

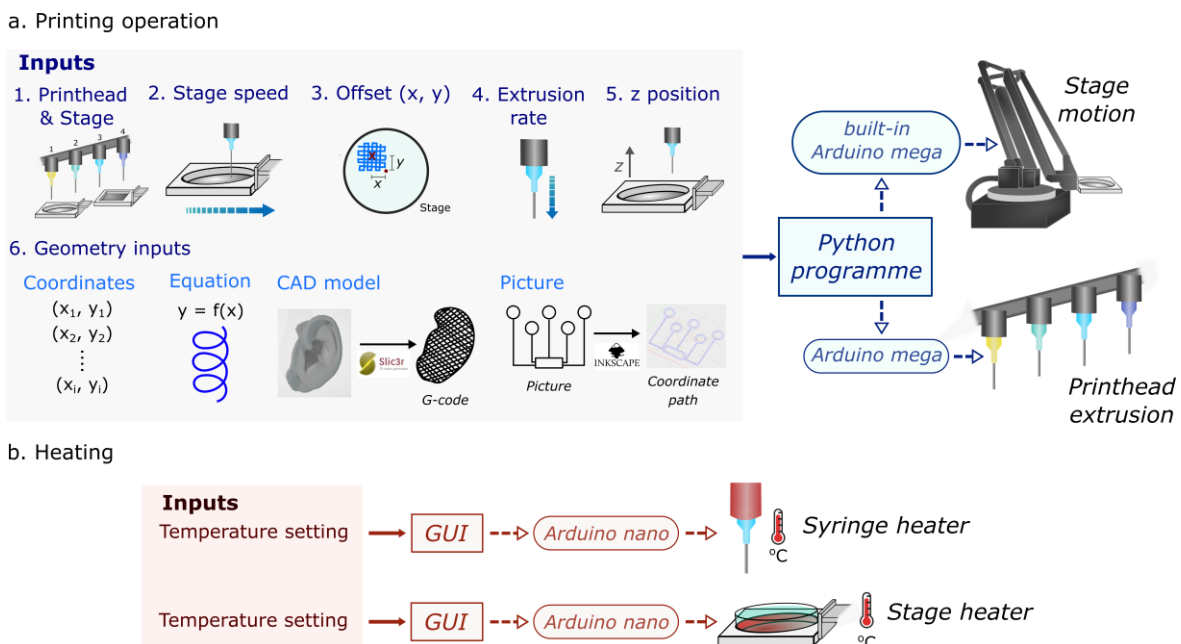


**Figure 3.11| Overview of the control for the a) printing and b) heating operations.**

### 3.5.1 Control programme for printing operation

To enable unconventional printing strategies and make the operation easy to implement, I wrote four python programme templates for interpreting different types of geometry inputs, namely coordinate, equation, CAD model, and picture inputs (**Figure 3.11a**, Geometry inputs). All templates follow the same logical structure, as depicted in **Figure 3.12**.

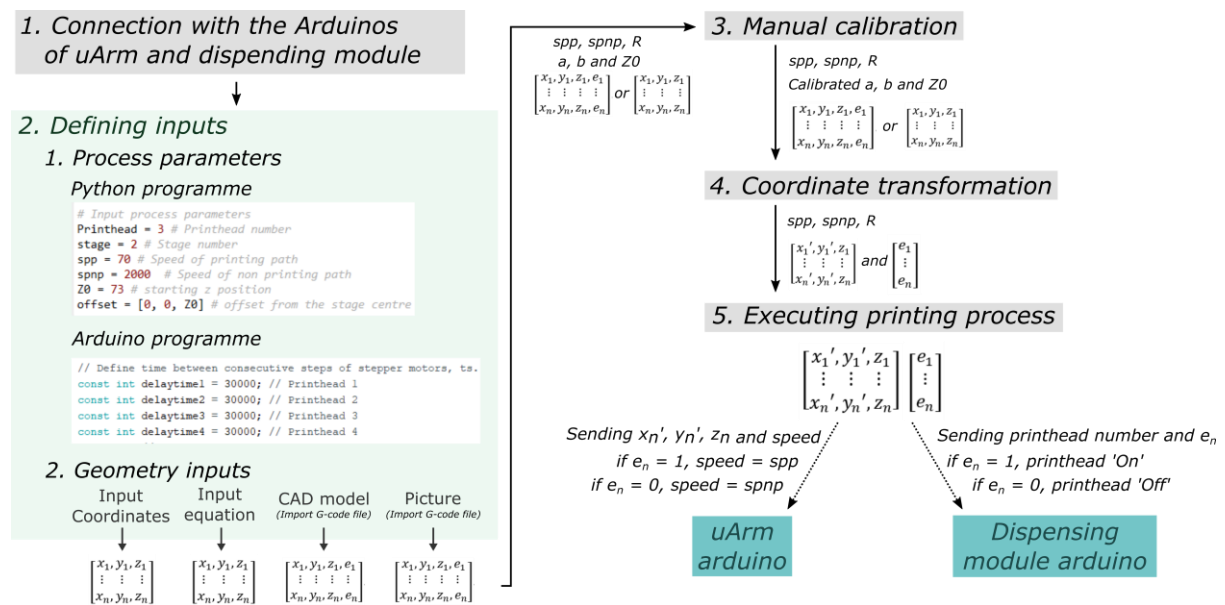


**Figure 3.12| Logical structure of the control programme for printing operation.**

#### 1. Setup connection

The pySerial python library was used to connect with the serial ports of the Arduino boards of the uArm and the dispensing module.

#### 2. Defining inputs

This section allows users to specify the process parameters and the geometry input (see **Figure 3.12**) based on the material being used and the desired final properties of the construct. Below provides a detailed description of the required inputs for the printing operation. In particular, the stage speed, extrusion rate and nozzle-to-stage distance crucially affect the print fidelity [117].

### 1. Printhead and stage

As previously mentioned in **Section 3.3.1**, I developed four syringe printheads that allow heterogenous material printing and steven stages for fitting different sizes of reservoirs. To inform the programme which printhead and stage are being used, each printhead and stage are assigned a key (see **Figure 3.13**), such that users only need to simply input the corresponding keys of the printhead and the stage being used to the programme. This information allows the programme to identify the approximate position ( $a, b$ ) of the printhead from the base  $(0,0)$  (**Figure 3.13a.iii**) and the distance between the centre point of the stage and the position sensor of the uArm,  $R$ , (**Figure 3.13b.ii**) that are used in the coordinate transformation step.

a.i			ii	iii
Printheads	Assigned keys	$a, b$ (mm)		
Printhead 1	1	286.5, 141.5		
Printhead 2	2	284, 70.5		
Printhead 3	3	284.5, -4		
Printhead 4	4	280, -74		

b.i			ii
Stages	Assigned keys	$R$ (mm)	
35 mm petri dish stage	1	33	
55 mm petri dish stage	2	44.5	
90 mm petri dish stage	3	60	
35 mm petri dish heating stage	4	36	
30 mm square dish stage	5	33	
38 mm square dish stage	6	38.2	
Glass slide holder	7	29.8	

**Figure 3.13| The assigned keys of the printheads and the stages.** (a.i) shows the corresponding assigned keys of the four printheads depicted in (a.ii) and their approximate values of the  $a, b$  coordinates, which are defined as the x, y coordinates from the base of the uArm to the nozzle tip of the printhead, as illustrated in (a.iii). (b.i) shows the assigned keys of the 3D printed stages.  $R$  is the distance between the centre point of the stage and the position sensor of the uArm, as shown in (b.ii). The values of  $a, b$  and  $R$  are stored in the Python programme, so that the programme is able to identify the corresponding values based on the user inputs.

### 2. Stage speed

Stage speed determines the speed of printing. The motion of the stage during the entire printing process is controlled by two speeds – speed of the printing path,  $spp$ , and speed of the non-printing path,  $spnp$ . Speed of the printing path,  $spp$ , controls the amount of materials being extruded. Less materials are being extruded with faster stage speed, vice

versa. A  $spp$  of 10 – 100 is in general preferred for printing hydrogel and elastomer materials, based on my experimental results in Chapter 4. Relationship between the actual speed and the uArm unitless speed quantity can be found in **Figure 3.10**. Additionally, the programme enables the specification of the speed of the non-printing path,  $spnp$ , hence the stage can travel at a different speed when transiting between the printing paths. By default, a  $spnp$  of 2000 is used for a fast transition. On a side note, by virtue of the customisable control programme, it is possible to set a variable stage speed along the print path (see **Section 4.3.2** for details).

### 3. *Offset*

The offset ( $x_{offset}, y_{offset}$ ) defines where the centre point of the print is located from the centre of the stage. The programme defaults to print objects at the centre of the stage unless an offset is specified.

### 4. *Extrusion rate*

Extrusion rate controls the volumetric flow rate of material deposited onto the stage. It is regulated by the time interval between consecutive steps of stepper motor,  $t_s$ . The conversion between the extrusion rate and  $t_s$  can be found in **Figure 3.9d**. Typically, a  $t_s$  of 20,000 – 30,000  $\mu$ s was used in my printing experiments.

### 5. *z position*

Controlling the nozzle-to-stage distance, the z position of the stage,  $Z0$ , is a crucial parameter affecting the print fidelity. With the nozzle too far from the stage, the material cannot adhere onto the stage. On the other side, if the stage is too close, the material cannot easily flow out from the nozzle, causing pressure build-up in the syringe and thus increased flow rate at subsequent print layers. A distance of approximately 0.5 mm from the stage to the nozzle tip is usually a good condition for the first layer to be printed successfully.

## 6. Geometry inputs

*Coordinate input* – Coordinates are the most ordinary form of geometry inputs. It is useful for printing simple lines or regular point patterns where a list of coordinates ( $x = [x_1, x_2, \dots, x_n]$ ,  $y = [y_1, y_2, \dots, y_n]$ ) can be directly loaded to the programme without the need for preparing the CAD models and the slice files.  $x_n$  and  $y_n$  denote the  $x$  and  $y$  coordinates of the  $n^{\text{th}}$  point.

*Equation input* – Printing path can be described by a set of cartesian or parametric equations together with a defined range of the independent variable (see **Table 3.3** for examples of the equation format). This input format is straightforward and enables a smooth print path in one stroke, however it is not suitable for complex patterns that are usually not describable by equations.

**Table 3.3| Examples of the equation format used in the Python programme.**

Cartesian equations	Parametric equations
$y = f(x), x_{\min} < x < x_{\max}$	$x = f(\theta), \theta_{\min} < \theta < \theta_{\max}$
$z = f(x), x_{\min} < x < x_{\max}$	$y = f(\theta), \theta_{\min} < \theta < \theta_{\max}$

*CAD model input* – CAD model is the standard geometry format used in 3D printing. Here, an open-source 3D slicing software (Slic3R) was used to generate G-code files from 3D CAD models. Various parameters that control the final properties of the printed object can be defined on Slic3R, including infill density and pattern, extrusion width and layer height. After the G-code file was generated, the file was imported to the Python programme.

*Picture input* – Picture input enables defining the print path via photos of hand-drawn patterns or pictures created by any drawing software. This format is convenient for users that have no CAD experience, and is particularly useful for path customisation when the desired print path of pattern cannot be described by equations. To convert pictures into a coordinate array, the free plugin ‘G-code Tools’ on Inkscape (<https://github.com/cnc-club/gcodetools>) that was intentionally designed for converting pictures into G-code for CNC machines is employed.

In all python programme templates of different types of geometry inputs, the programmes convert the user-defined geometry inputs into a coordinate array in form of

either  $\begin{bmatrix} x_1, y_1, z_1 \\ \vdots & \vdots & \vdots \\ x_n, y_n, z_n \end{bmatrix}$  or  $\begin{bmatrix} x_1, y_1, z_1, e_1 \\ \vdots & \vdots & \vdots & \vdots \\ x_n, y_n, z_n, e_n \end{bmatrix}$ . The first array format is used in coordinates and

equation inputs, where I assume all coordinates compose the printing path. The second array format is used in CAD model and picture inputs, where  $e$  is a Boolean extrusion parameter with  $e$  is set to 1 when the coordinates are part of the printing path and 0 for non-printing path. For G-codes generated from CAD models by Slic3R, the path recognition was done by identifying the ‘E’ commands in the G-code that indicate extrusion, whereas a G-code block without the ‘E’ command implies a non-printing path. For the CNC G-code file generated from the picture input using the Inkscape extension, the non-printing path is identified by scanning the ‘G00’ commands in the G-code, which indicate a rapid transition. Other ‘G’ commands are classified as printing paths. With path recognition, transition between the printing paths can be carried out with a faster stage speed and disabled extrusion. The offset coordinates, if defined, are also applied in this step by shifting the coordinate array accordingly.

### 3. *Manual calibration*

After executing the Python programme, the stage will move to an approximate position close to the nozzle tip based on the information of the stage and the printhead being used and the z position input defined in the above section. The programme will then halt indefinitely for the user calibration input (see **Figure 3.14**). Calibration is carried out in two steps. The first step calibrates the z position of the stage,  $Z0$ , which allow users to fine tune the z position by manually entering the shifting value of the z position,  $z_{shift}$ . The programme will proceed to the next calibration step after a good z position is determined by the users. The second step calibrates the x and y positions of the centre point of the stage, so that it aligns with the nozzle tip. Similar to the first step, the programme halts for the user input of the shifting values of the x, y positions,  $x_{shift}$  and  $y_{shift}$ . This procedure is for offsetting any variation caused by slightly bent nozzle tips. And according to the values of  $x_{shift}$  and  $y_{shift}$ , the programme infers the revised  $a, b$  coordinates of the printhead for accurately transforming coordinates in the next step.

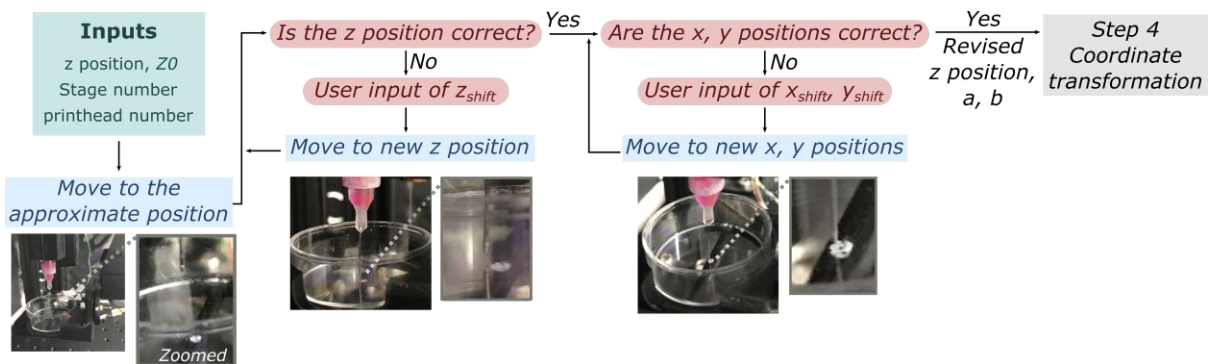


**Figure 3.14| Flowchart showing the manual calibration procedure.**

#### 4. Coordinate transformation

Two issues were noticed due to the circular y axis motion of the articulated uArm. First, as the position sensor, which relays the position for accurate movement, is located at the end point of the uArm but not at the centre of the stage (see **Figure 3.13b.ii**), the defined motion path of the position sensor does not identically translate to the motion path relative to the stage centre. The problem is exemplified in **Figure 3.15a**. When setting a print path of a circle at the position sensor, the motion path relative to the stage centre was distorted by the circular motion of the uArm, leading to an elliptical print path (**Figure 3.15a.i-ii**). Similarly, when setting a print path of a square at the position sensor, the print path along the y-axis was lengthened and resulted in an elongated rectangular shape (**Figure 3.15a.iii**). Therefore, to preserve the print shape, the desired coordinates of the printed object ( $x_{print}, y_{print}$ ) are converted to the equivalent coordinates of the position sensor ( $x', y'$ ) via a transformation. The transformation requires information of the distance between the stage centre and the position sensor,  $R$  (see **Figure 3.13b.i** for the values of  $R$  of different stages) and the calibrated position,  $(a, b)$ , of the nozzle tip from the base of the uArm, which is inferred from the x, y calibration in Step 3. The transformation function is depicted in **Figure 3.15b.i**. With the transformation applied, the shapes of the printed objects were preserved and were not distorted (**Figure 3.15b.ii-iii**).

The second issue was encountered when printing with multiple printheads. Demonstrated in **Figure 3.15c.i-ii**, when printing a multi-layered rectangular construct using different printheads (printing from printhead 1 to printhead 3), the layers were not aligned due to the circular motion of uArm, though all layers were printed around the stage centre (**Figure 3.15c.ii**). For this reason, a rotation transformation (Equations 3.5 and 3.6) is additionally applied to the  $x, y$  coordinates of the geometry coordinate array acquired in Step 2 prior to the above transformation. The rotation angle,  $\beta$ , is determined by the  $a$  and  $b$  position of the nozzle

tip from the uArm base (Equation 3.5), such that the coordinates of the print ( $x_{print}$ ,  $y_{print}$ ) are relative to the stage axes, but not the uArm axes. **Figure 3.15c.iii** illustrates a well-aligned construct printed using different printheads with the rotation transformation applied. Equations 3.5 – 3.9 denote the final transformation equations used. The output of this step is a transformed coordinate array of  $\begin{bmatrix} x_1', y_1', z_1 \\ \vdots & \vdots & \vdots \\ x_n', y_n', z_n \end{bmatrix}$ .

$$\text{coordinate array of } \begin{bmatrix} x_1', y_1', z_1 \\ \vdots & \vdots & \vdots \\ x_n', y_n', z_n \end{bmatrix}.$$

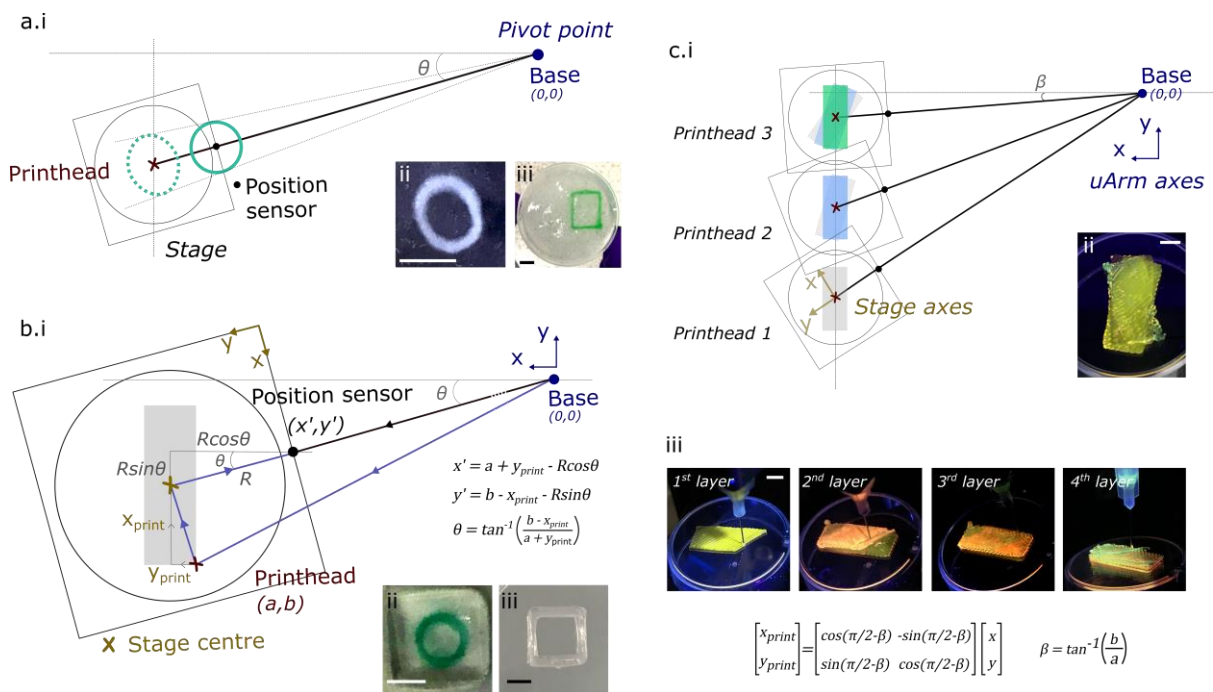


**Figure 3.15| Coordinate transformation.** (a) Print path distortion issue caused by the distance between the stage centre and the position sensor. (i) Schematic showing the resulted print path when setting a circular motion path about the position sensor. Images showing the distorted (ii) circle and (iii) square objects when setting a print path about the position sensor. (b.i) Transformation of the coordinate of the print object ( $x_{print}$ ,  $y_{print}$ ) to the coordinates of the position sensor ( $x'$ ,  $y'$ ). (ii) Images showing a circular object and a square accurately printed after the coordinate transformation was applied. (c.i) Schematic depicting the misalignment issue when creating a heterogeneous object using multiple printheads. Images of a multi-layered stack printed (ii) without applying the rotation transformation and (iii) with the rotation transformation applied. Scale bar = 5 mm. The materials used in the printing experiments here were (a.ii) agarose, (a.iii) alginate stained with a green dye, (b.i) Pluronic F127, (b.ii) SE1700, and (c.ii – c.iii) Pluronic F127 stained with either Fluorescein sodium (green), rhodamine B (orange) or rhodamine 6G (yellow). The concentrations of the inks can be found in **Materials and Methods 3.2.4**.

$$\beta = \tan^{-1}\left(\frac{b}{a}\right) \quad (3.5)$$

$$\begin{bmatrix} x_{\text{print}} \\ y_{\text{print}} \end{bmatrix} = \begin{bmatrix} \sin(\pi/2 - \beta) & -\sin(\pi/2 - \beta) \\ \sin(\pi/2 - \beta) & \cos(\pi/2 - \beta) \end{bmatrix} \begin{bmatrix} x \\ y \end{bmatrix} \quad (3.6)$$

$$\theta = \tan^{-1}\left(\frac{b-x_{\text{print}}}{a+y_{\text{print}}}\right) \quad (3.7)$$

$$x' = a + y_{\text{print}} - R\cos\theta \quad (3.8)$$

$$y' = b - x_{\text{print}} - R\sin\theta \quad (3.9)$$

where  $\beta$  is the angle between a horizontal line and the line connecting the base and the tip of the printhead,  $(x, y)$  are the  $x, y$  coordinates obtained from the geometry input,  $(x_{\text{print}}, y_{\text{print}})$  are the rotated coordinates of the geometry relative to the stage centre,  $\theta$  is the angle between a horizontal line and the line connecting the base and the stage centre point, and  $(x', y')$  are the transformed coordinates used in printing.

## 5. Executing printing process

During the printing execution process, the Python programme reads the transformed coordinate

array in the form of  $\begin{bmatrix} x_1', y_1', z_1 \\ \vdots & \vdots & \vdots \\ x_n', y_n', z_n \end{bmatrix}$  along with the extrusion information  $\begin{bmatrix} e_1 \\ \vdots \\ e_n \end{bmatrix}$  line-by-line. The

programme simultaneously sends information of the  $x_n', y_n', z_n$  coordinates to the uArm Arduino for stage translation and the corresponding extrusion signal to the Arduino of the dispensing system in a line-by-line manner. When the Arduino of the dispensing system receives an extrusion signal ‘On’ ( $e = 1$ ) of a specific printhead, the printhead will be turned on by configuring the pin settings in Arduino, vice versa. By default, a sixteenth microstep resolution of the stepper motor is used as this allows a higher number of discrete steps per revolution and a slower extrusion rate. The setting of the pin configuration under normal operation can be found in **Table 3.2**.

### 3.5.2. Heating

For ease of operation and independently communicating with multiple Arduino boards at the same time, I created a graphical user interface (GUI) using Processing ([processing.org](http://processing.org)) for controlling each heating element. The Arduino programme of the heating system was jointly developed by me and Cillian Leon, a student from the Department of Engineering.

**Figure 3.16** shows the flowchart of the feedback control employed in the heating system. The desired set-point temperature is specified by the user in the input field and is imported to the Arduino programme. At the first instant, the Arduino applies a full current power to the heating coil (by setting the heater analog pin on Arduino with a PWM (pulse width modulation) value of 256). The thermocouple then feeds back the temperature measurement of the heating coil to the Arduino, which was also logged on the GUI for temperature monitoring. Based on the deviation between the set point and the temperature measurement, the heating rate is adjusted by modifying the PWM of the applied current that is calculated using the below transfer function (Equation 3.10). This transfer function was found to prevent temperature overshoot for the specific rating of the power supply and the size of heating coil used in the system. When the deviation is within the acceptable deviation, which defaults to  $\pm 0.5$  °C here, no current (a PWM of 0) is applied to the heating coil. The feedback loop continues until the user turns off the heater by pressing ‘STOP’ on the GUI.

$$\text{PWM}_{\text{new}} = \text{PWM}_{\text{old}} + \frac{\text{PWM}_{\text{old}}}{6} \times (\text{T}_{\text{set}} - \text{T}_{\text{measurement}}) \quad (3.10)$$

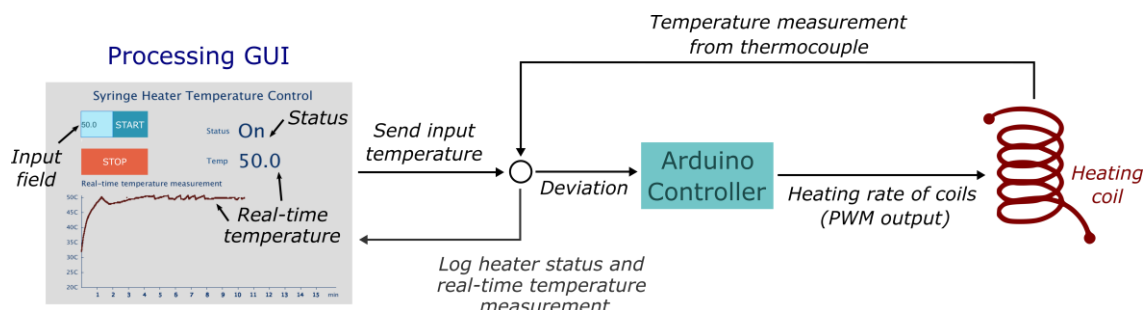


**Figure 3.16| Flowchart of the heating control.**

## 3.6 System specification

Below tables compare the specifications of the extrusion-based printing platform developed in this chapter with four commercial extrusion bioprinters commonly employed in the bioprinting community (**Table 3.4**) and the custom-made printers reported in literature (**Table 3.5**).

**Table 3.4| Specifications of the system developed in this chapter and the four commercial 3D extrusion-based bioprinters commonly used in the bioprinting community.** The commercial systems are Allevi 3 [239] (denoted as ‡ below), Cellink BioX [240, 241] (†) and Envision TEC 3D Bioplotter Starter Series [242] (\*) and GeSim BioScaffolder BS3.3 [243] (§).

	This setup	Commercial systems
Cost	£0.9k (single printhead system) - £1.9k (systems with 4 printheads, syringe and stage heaters, UV and camera)	\$10k – 100k [244]
No. of printhead slots	Unlimited	<ul style="list-style-type: none"> <li>• 3 (‡, †)</li> <li>• 2 (*, §)</li> </ul>
Geometry input (outer shape)	Coordinates, CAD, equations, picture	<ul style="list-style-type: none"> <li>• CAD (‡, †, *, §)</li> </ul>
Resolution	200 µm	<ul style="list-style-type: none"> <li>• 1 µm (‡, †, *)</li> <li>• 10 µm (§)</li> </ul>
Extruder temperature control	RT – 60 °C	<ul style="list-style-type: none"> <li>• 4 °C – 160 °C (‡)</li> <li>• 4 °C – 65 °C / 250 °C (†)</li> <li>• 30 °C – 250 °C (*)</li> <li>• 4 °C – 80 °C / RT – 190 °C or 250 °C (§)</li> </ul>
Printbed temperature control	RT – 60 °C (tested range)	<ul style="list-style-type: none"> <li>• RT – 60 °C (‡)</li> <li>• 4 – 65 °C (†)</li> <li>• Not available (*, §)</li> </ul>
UV power	365/405 nm	<ul style="list-style-type: none"> <li>• Yes (365/405 nm) (‡)</li> <li>• Yes (365/405/450/485/520nm) (†)</li> <li>• No (*)</li> <li>• UV LED (§)</li> </ul>
Extrusion method	Mechanical	<ul style="list-style-type: none"> <li>• Pneumatic or mechanical (†, §)</li> <li>• Pneumatic (‡, *)</li> </ul>
Compatible cartridge size	1 ml – 3 ml	<ul style="list-style-type: none"> <li>• 5 ml (‡)</li> <li>• 3 ml – 10 ml (†)</li> <li>• 3 ml – 30 ml (*)</li> <li>• 10 ml – 30 ml (§)</li> </ul>
Weight	• ~11 kg, 45x45x35 cm (excl. enclosure)	<ul style="list-style-type: none"> <li>• 21.8 kg, 47x40x36 cm (‡)</li> <li>• 18 kg, 48x44x37 cm (†)</li> <li>• 90 kg, 84x62x77 cm (*)</li> <li>• Information not available (§)</li> </ul>

**Table 3.5| Table comparing the system developed in this chapter with the reported open-source extrusion bioprinters**

Ref.	Hardware	Geometry inputs	Auxiliary tools	Tested materials	Geometry	Applications demonstrated
Lee, et al. (2017) [245]	Pneumatic extruders with linear stages	CAD	Syringe heater	PLGA, hyaluronic acid, $\alpha$ -TCP (tricalcium Phosphate)	Cell-laden lattice, Cylinder scaffolds	Cell-laden hybrid scaffold
Feinberg, et al. (2018) [136, 146, 227]	Piston-based extruder coupled with a commercial 3D printer	CAD	-	Alginate	3D constructs, full size model of the human heart	Patient-specific anatomical models
Bessler, et al. (2019) [225]		CAD	-	Alginate	Cylinder and rectangle scaffolds	Cell proliferation
Kahl, et al. (2019) [246]		CAD	-	Alginate, alginate-gelatin	Lattice, cylinder and pyramid scaffolds	Cell proliferation
Spiesz, et al. (2019) [247]		Coordinates	-	Alginate	2D patterns	Spatially-controlled model for E.coli bacteria culture
Ioannidis, et al. (2020) [226]		CAD	-	Alginate -gelatin	Line patterns	Cell proliferation and differentiation
Ozbolat, et al. (2014) [229]	Piston-based extruders with linear stages	CAD	-	Alginate	Cell-laden grid scaffold	Cell proliferation
Fitzsimmons, et al.(2018) [231]		CAD	Syringe heater	Gelatin, GelMA, gelatin-hyaluronan, gelatin-alginate, Pluronic F127	Cell-laden line pattern, 3D constructs (cube, cylinder and star), Constructs with channels	HUVEC culture in channels
Yenilmez, et al. (2019) [228]		• CAD • Picture	UV module	Alginate	Cell-laden grid scaffold	Cell proliferation
Shen, et al. (2021) [230]		CAD	-	Alginate	Alginate hydrogel with concentration gradient, A femur model	Cell proliferation
<b>This work</b>	Piston-based extruders with robotic arm	• Coordinates • Equations • CAD • Pictures	• Stage heater • Syringe heater • UV light • Camera	<ul style="list-style-type: none"> <li>• Natural hydrogels (i.e. collagen, gelatin, alginate, agarose, gellan gum, sodium hyaluronate, sodium carboxyl-methyl cellulose, methyl cellulose)</li> <li>• pH responsive hydrogels (polyacrylic acid, chitosan)</li> <li>• Bioceramics hydrogels (i.e. hydroxyapatite, silica, talc)</li> <li>• Synthetic hydrogels (i.e. Pluronic F127, PEO, PVA)</li> <li>• Silicone elastomers (i.e. SE1700, ecoflex)</li> </ul>	<ul style="list-style-type: none"> <li>• Multi-material 3D constructs,</li> <li>• 2D embedded vascular-like channels,</li> </ul>	<ul style="list-style-type: none"> <li>• Anatomical models</li> <li>• Core-shell structured tumoroids</li> <li>• Perfusion devices</li> <li>• Custom-made cell culture chambers</li> <li>• Liquid dispensing</li> <li>• Printing with variable speed</li> <li>• Non-planar printing</li> </ul>

### 3.7 Limitations and future improvement

Several limitations of the platform were noted. One limitation lies in the design of a moving stage system, hence any mechanical vibration during the stage translation could potentially compromise the fidelity of low viscosity objects that are printed in-air. To reduce the potential impact, a very slow speed of stage can be used when printing delicate structures of low viscosity materials. The reason a moving printhead system was not employed here is that the maximum payload of the uArm is 500 g, which is not sufficient for carrying a printhead, and uArm was chosen here as it is programmable and has good mechanical accuracy at low cost. Compared to commercial 3D extrusion printing platforms for soft materials, this platform lacks an automatic calibration system, which can be attained by incorporating an inductive sensor or a proximity sensor into the platform in future development. In addition, cooling systems, for example coolers made with Peltier elements and heat sinks, would be beneficial for printing protein-based inks, such as collagen and fibrin. An ink retraction mechanism would be advantageous for preventing ink from unintentional oozing during transition between non-printing paths, further enhancing the print fidelity. As the dispensing module of the platform is piston-driven, a retraction mechanism can be easily achieved by setting the stepper motor to rotate reversely for a set period of time. This is opposed to pneumatic control that is widely utilised in commercial bioprinters but cannot be utilised easily for retraction [248]. Lastly, several studies have noted that switching between multiple printheads greatly slows down the fabrication process [157, 158, 249]. A multi-channel microfluidic printhead can be employed for faster fabrication and accurate positioning.

### 3.8 Conclusion

In this chapter, an entirely hackable and affordable printing platform was made from scratch using an open-source robotic arm and simple mechanical components. As the syringe holders and stages were 3D printed, the prototype of the platform can be easily modified to suit different needs. Here, the printing platform is equipped with multiple printheads that are compatible with 1 ml and 3 ml syringes, and a wide variety of 3D printed stages to fit different sizes of collecting reservoirs. Printheads and the stage can also be heated for tuning the rheology of materials, and a UV module is coupled with the platform for *in situ* photopolymerisation. Controlled by Python, the printing operation is fully amendable for unprecedented printing strategies. Four Python templates were written for accepting different

geometry inputs, including coordinates, equations, CAD models and pictures, hence the operation should be easy to implement, even for users without programming experience. Unlike commercial bioprinting systems that are costly and closed source, the total cost of this fully customisable and multi-printhead system is around  $\sim$  £1900, while a single printhead system costs  $\sim$  £ 900 (see **Table 3.1**). The assembly method and the design of the programme are provided, hence other users can replicate the system and contribute to its future development. In the subsequent chapters, this printing platform was utilised for different applications, and its versatile capability is demonstrated.

## Chapter 4

# An Investigation on Methods for Soft Material Printing

### 4.1 Introduction

Soft materials, such as hydrogels and elastomers, capable of resembling the mechanical properties of biological soft tissues are promising material candidates in applications for promoting human-machine interactions, including flexible electronics [131, 250–254] and soft robotics [99, 174, 255–257]. In particular, hydrogels have been extensively used in myriad biomedical applications owing to their unique properties. For example, the high water content of hydrogels promotes moisture for tissue healing, making them ideal candidates for wound dressing [250, 254, 258, 259]. The ionic permeability of hydrogels allows their utilisation as sustained and flexible power sources for uses in implantable devices [260, 261]. The potential biocompatibility of hydrogels makes them attractive materials in tissue engineering and drug delivery applications [262]. And, stimuli-responsive hydrogels can actuate in accordance with environmental changes by harnessing their chemical energy without the need for external mechanical means, unlike actuators made of silicone elastomers [94].

The innovation in soft material technology has been remarkably springing up since the advent of 3D printing technologies in the last decades [4]. The technologies offer a high degree of design freedom and enable rapid prototyping of complex structures that cannot be attained with traditional methods, facilitating the fabrication of soft materials with tuneable mechanical and other functional properties [4]. Among the 3D printing technologies, extrusion-based printing (also known as direct-ink writing) and photolithography are commonly used for soft materials [2, 4]. While photolithography, such as digital light processing (DLP), significantly improves the resolution and the speed of fabrication, extrusion-based printing offers several key benefits over light-based methods [2, 106]. These include the ease of multimaterial

fabrication [4], greater biocompatibility as the process does not necessarily involve cytotoxic photoinitiators [113] and greater flexibility in material choices [109] (see Section for further discussion). More importantly, direct-ink writing does not require covalent crosslinking that typically causes increased brittleness in hydrogels [263] and therefore reduces its mechanical resemblance to biological soft tissues.

Notwithstanding, the present extrusion-based printing technology is hindered by several limitations, including their high cost, poor reproducibility and the lack of detailed investigation to standardise the printing process of soft materials [4, 264]. These limitations significantly discourage new users to adopt the technology. Therefore, in an attempt to address the above limitations encountered in the research community, this chapter aims to 1) investigate the capability of the low-cost custom-built extrusion-based printing platform developed in **Chapter 3** and 2) provide a rational guideline for extrusion-based printing of soft materials via exploring different printing strategies. Unlike other open-source 3D extrusion-based printers developed in literature, the setup developed in this study offers flexible geometry input options and unconventional printing strategies, such as non-planar printing and printing with variable speed. In addition, the setup is equipped with a complete set of auxiliary tools (i.e. heaters and UV module) that assists the fabrication of less printable materials. A wide diversity of soft materials, from natural hydrogels (e.g. collagen and agarose), pH responsive hydrogels (e.g. polyacrylic acid and chitosan) to elastomers (e.g. Ecoflex), were successfully printed using the setup with the adopted printing methods discussed. The findings reported in this chapter realise the capability of a low-cost printing system and suggest a rational guide to new users for efficiently designing a printing method from a wide array of options to suit different needs, advancing the widespread adoption of 3D extrusion-based printing technology for soft materials.

## 4.2 Materials and Methods

### 4.2.1 Materials

PEDGA (455008), poly(acrylic acid) (450 kDa, 181285), polyvinyl alcohol (31 -50 kDa, 363138), glycerol phosphate disodium salt hydrate (G6501), fumed silica (S5130) and mineral oil (330760) were purchased from Merck Life; Pluronic F127 (P2443), talc (243604), agarose (A9539), carboxymethylcellulose sodium salt (21902), xanthan gum (G1253), gellan gum (P8169), gelatin (G1890), chitosan from shrimp shells (C3646), collagen Type I (C9879),

sodium alginate (W201502), hydroxyapatite (21223), methyl cellulose (M6385), polyethylene oxide (8 MDa, 372839), polyethylene oxide (400 kDa, 372773), calcium chloride (C5670), Irgacure 2959 (I2959, 410869), sodium fluorescein (46960), fetal bovine serum (F0804), penicillin-streptomycin (P43333) and 10x PBS (D1408) from Sigma; Sodium chloride (10616082), glycerol (10579570), precipitated silica (10784571), chitosan (600-800 kDa, 10636695), citric acid (10345410), HEPES (11394379), sodium hyaluronate (251770250), Invitrogen™ Calcein AM (C3099), Invitrogen™ Tris Buffer (15504020), hydrochloric acid (H/1100/PB17), silicone oil (13435819), stearic acid (10002390), acetic acid glacial (10304980), 99.8% ethanol (12498740) and universal pH indicator (10090470) from Fisher Scientific; Sodium hydroxide pellets (S5881) from Scientific Laboratory Supplies; Ecoflex 00-30, THI-VEX and Slo-Jo (Smooth-On) from Bentley Advanced Materials; SE 1700 and PDMS from Dow; 1x PBS (10010056), Dulbecco's Modified Eagle medium (DMEM) (low glucose, pyruvate, 31885023) from Life technologies; Rhodamine 6G (J62315.14) and Rhodamine B (A13572.18) from Alfa Aesar; Carbopol ETD 2020 from Lubrizol. Pepsin was a gift from my colleague Zhaoying Li, a former PhD student from the Department of Engineering.

1 ml luer-lok (309628), 3 ml luer-lok (309658) and 1 ml luer-slip (303172) syringes were obtained from BD. Needle tips (AD Series General Purpose Dispensing Tips and Smooth Flow Tapered tips) at different gauge numbers and lengths were obtained from Adhesive dispensing Ltd.

#### 4.2.2 Solution preparation

**Pluronic F127:** Three formulations of Pluronic F127 inks were used in this chapter. They were 40 w/v% Pluronic F127 dissolved in DI water, 30 w/v% in DI water and 30 w/v% dissolved in 1 w/v% NaCl. The use of NaCl solution as the dissolving medium increases the viscosity of the Pluronic F127 ink due to the salting out effect, hence the ink has a good printability even without heating the ink. Pluronic F127 was dissolved in the dissolving medium (either DI water or NaCl solution) according to the required concentration. The solution was then kept in a 4 °C fridge for at least two days until fully dissolved.

**Alginate:** Three formulations of sodium alginate were used. They were 10 w/v% sodium alginate mixed with 200 mM CaCl<sub>2</sub> at a volumetric ratio of 10:3, and 3.5 w/v% sodium alginate with 40 mM CaCl<sub>2</sub> at volumetric ratios of 5:3 or 5:2. To avoid inhomogeneous gel formation, the CaCl<sub>2</sub> solution was added slowly to the solution of sodium alginate under vigorous stirring.

**Gellan gum and Agarose:** 2 w/v% gellan gum and 1 w/v% agarose solutions were prepared by adding the desired concentration of the material into DI water, followed by heating the solutions in a microwave until fully dissolved.

**Methacrylate hydroxypropyl cellulose:** 64 wt% and 68 wt% solutions produced by my collaborator, Chun Lam Clement Chan (Department of Chemistry), were directly used for printing. The inks were stored in a 4 °C fridge when not in use and can last for ~ 1 week.

**Gelatin:** Gelatin was dissolved in DI water at a concentration of 10 w/v%. The solution was warmed at 50 °C in an oven until fully dissolved.

**Collagen:** The collagen fibres (C9879) used here are not soluble in acetic acid, therefore a protocol [53] used to solubilise extracellular matrix was adopted here. The method dissolves 10 mg/ml collagen fibres in a 1 mg/ml pepsin-HCl solution (1 mg/ml pepsin dissolved in 0.01 N HCl). 4, 2, 1.5 and 1 mg/ml collagen solutions were prepared by diluting the 10 mg/ml stock solution with a NaOH-PBS buffer. The NaOH-PBS buffer was prepared by mixing 10x PBS, 1x PBS and 0.1 N NaOH in a volumetric ratio of 1:1:8. The prepared solution was then stored in a 4 °C fridge.

**Bioceramics-alginate hydrogels:** Three bioceramics-alginate inks were prepared. They were made of 15 w/v% of either hydroxyapatite, precipitated silica or talc dispersed in a 5 w/v% alginate solution. The solutions were pre-crosslinked with a 200 mM CaCl<sub>2</sub> solution at a 10:1 volumetric ratio prior to printing.

**Sodium hyaluronate:** A 3 w/v% sodium hyaluronate was dissolved in DI water. The sodium hyaluronate-PEDGA ink was prepared by mixing 3 w/v% sodium hyaluronate, PEDGA (700 Da), 10 w/v% Irgacure 2959/ethanol in at a volumetric ratio of 10:2:1. Irgacure 2959 (I2959) was a photoinitiator. The 10 w/v% **Irgacure 2959/ethanol stock solution** was prepared by dissolving 10 w/v% I2959 in pure ethanol.

**Sodium carboxymethyl cellulose, methyl cellulose and polyethylene oxide (PEO):** 15 w/v% methyl cellulose, 10 w/v% sodium carboxymethyl cellulose and 2 w/v% PEO (8 MDa) were prepared by mixing the materials in DI water for at least a day using a magnetic stirrer.

**Chitosan:** Two chitosan stock solutions were prepared for printing. They were chitosan from shrimp shells at 3 w/v% in 0.1 M acetic acid and a 600-800 kDa chitosan at 13 w/v% in 1 M acetic acid. The 3 w/v% chitosan ink derived from shrimp shells was further modified by mixing it with 5 w/v% 400 kDa PEO or with glycerol phosphate disodium salt (0.633g for

every 4 ml [39]). A photocrosslinkable chitosan ink was prepared by mixing the chitosan stock solution, with PEGDA (700 Da) and 10 w/v% I2959/ethanol at a volumetric ratio of 10:1:1. A 0.5 w/v% solution of chitosan from shrimp shells was prepared for crosslinking the sodium carboxymethyl cellulose construct.

**Poly(acrylic acid):** 20 w/v% and 25 w/v% of poly(acrylic acid) solutions were prepared by dissolving the material in 0.1 M NaOH solution under stirring for a week.

**Polyvinyl alcohol:** A 20 w/v% of polyvinyl alcohol was prepared using the following method. The granules were first added in cold DI water to avoid formation of lumps. The dispersion was then heated to ~ 80 °C and was stirred until the powder was fully dissolved (~1 – 2 hrs). The ink was drawn into a syringe, and the syringe was cooled in a 4 °C fridge for 1 hr before printing.

**Ecoflex 00-30:** The Ecoflex ink was prepared following the formulation described in [174]. First, 1.2 w/w% Slo-Jo and 1.2 w/w% THI-VEX were added to Part B Ecoflex. THI-VEX is a rheological modifier, and Slo-Jo is a silicone cure retarder that enables prolonged pot time for printing. Part A Ecoflex and the modified Part B were mixed in a 1:1 weight ratio. A drop of acrylic paint was added to the mixture for colouring.

**SE 1700:** The ink was produced by mixing the base precursor and the curing agent at a weight ratio of 10:1.

#### 4.2.3 Support bath preparation and the methods for releasing the printed constructs from the baths

##### **Xanthan gum support bath**

1.3 w/v% xanthan gum was dissolved in either DI water, 10 w/v% gelatin or 0.1 M citric acid under stirring using a magnetic stirrer for at least 2 hours until complete dissolution. For the xanthan gum-gelatin support bath, a 2.6 w/v% xanthan gum and a 20 w/v% gelatin solution were prepared. The solutions were then mixed at a 1:1 volumetric ratio under heat to obtain a homogeneous 1.3 w/v% xanthan gum and 10 w/v% gelatin solution. The xanthan gum support baths were not removed in all experiments here.

***Gelatin slurry***

Gelatin slurry was prepared using a similar protocol described in [52, 233]. 4.5 w/v% gelatin was dissolved in either 11 mM CaCl<sub>2</sub> or 10 mM HEPES solutions at ~ 50 °C. The dissolved solution was then stored overnight in a 4 °C fridge and was kept in a -20 °C freezer for 1 hour prior to the blending step. This step was to prevent the gelatin jelly from melting during the following blending and centrifugation steps. Before blending, the gelatin jelly was mixed with the same medium used for dissolving gelatin (either 11 mM CaCl<sub>2</sub> or 10 mM HEPES) in a volumetric ratio of 2:3. The mixture was blended for 90 s at ‘speed 1’ using a blender (VonShef 4-in-1 blender). The blended slurry was then transferred into 50 ml conical tubes, and centrifuged at 3600 g and 5 °C for 4 mins. The supernatant was removed and replaced with the dissolving medium. The mixture was then resuspended using a spatula and centrifuged again. The centrifugation step was repeated until no white foam was observed at the top of supernatant. The produced gelatin slurry was stored in a 4 °C fridge when not in use and can last for ~ 5 days. After printing and crosslinking, the printed constructs were released by warming the support bath at 37 °C.

***Carbopol***

Three Carbopol ETD 2020 solutions (0.1, 0.2 and 1 w/v%) were prepared by stirring Carbopol in DI water for ~ 5 hours until completely dissolved. To thicken the solutions, 10 µL of 10 M NaOH was added for every 7 ml Carbopol solutions. They were mixed using a thin needle to avoid the generation of bubbles. The printed constructs were released by adding a 1 w/v% NaCl solution to the bath.

***Fumed silica-oil support baths***

Fumed silica was dispersed in either mineral oil or silicone oil at 6 w/w% or 4.8 w/w%, respectively. The dispersion was stirred for ~ 30 min and was then degassed with a vacuum for at least ~30 min until most bubbles were removed. After crosslinking, the printed constructs were collected and washed with soapy water. Soapy acidic water (1 M citric acid) was used for rinsing the poly(acrylic acid) constructs.

### **SE 1700 oil baths**

SE 1700 and silicone oil were mixed in a weight ratio of 1:3 and 1:4 using a magnetic stirrer, followed by centrifugation at mild speed (300 G) for removing bubbles. The method used to collect the printed construct was the same as the method used in fumed silica-oil support baths.

#### **4.2.4 Soft material printing**

The concentrations of the ink and the support bath used for fabricating the constructs shown in Figures 4.2 – 4.4 and Figures 4.7 – 4.14 are listed in **Table 5.2**. Some of the inks were stained with a fluorescent dye, either sodium fluorescein (green), rhodamine B (purple orange) and rhodamine 6G (yellow). Prior to printing, the ink was centrifuged at 1000 g for 3 mins to remove bubbles. The ink was drawn into a 1 ml or 3 ml syringe, and the syringe was loaded to the syringe holder of the setup. A collecting reservoir, which was filled with support baths if needed, was loaded to the stage. Syringe heating, stage heating and UV light were applied when required. Inks that required photo-polymerisation were UV-crosslinked for 5 – 20 mins after printing, prior to the removal of the support baths. Below describes the methods for printing using different geometry inputs.

**Table 4.1| Formulations of inks and support baths used in Chapter 4.** Concentration is expressed as w/v% unless specified.

Inks	Support baths	Heating / UV	Figures
SE 1700 (base:curing agent 10:1 wt ratio)	-	-	4.2a.i
40% pluronic F127	-	-	4.2a.ii
30% pluronic F127	10% gelatin + 1.3% xanthan gum	Stage heating at 40°C	4.2a.iii
30% pluronic F127	10% gelatin + 1.3% xanthan gum	Stage heating at 40°C	4.2a.iv
40% pluronic F127	-	-	4.2b.i
30% pluronic F127/1% NaCl solution	-	Stage heating at 40°C	4.2b.ii
SE 1700 (base:curing agent = 10:1 wt ratio)	-	-	4.2b.iii
30% pluronic F127/1% NaCl solution	10% gelatin + 1.3% xanthan gum	Stage heating at 40°C	4.2b.iv
30% pluronic F127	-	-	4.2b.v
40% pluronic F127	-	-	4.2c.i
3.5% alginate:40 mM CaCl <sub>2</sub> (5:3 v/v ratio)	1.3% xanthan gum	-	4.2c.ii
3.5% alginate:40 mM CaCl <sub>2</sub> (5:2 v/v ratio)	Gelatin slurry in 11mM CaCl <sub>2</sub>	-	4.2c.iii
2% gellan gum (grid)	-	Stage heating at 37°C	4.2c.iv
30% pluronic F127	-	Stage heating at 40°C	4.2c.v

## 4.2 Materials and Methods

Inks	Support baths	Heating / UV	Figures
Methacrylate hydroxypropyl cellulose	-	<i>In situ</i> UV	4.2d.i
Methacrylate hydroxypropyl cellulose	-	<i>In situ</i> UV	4.2d.ii
10% gelatin	1.3% xanthan gum: PEGDA 700: I2959 (10:1:1 vol. ratio)	Syringe heating at 50 °C	4.2d.iii
30% pluronic F127/1% NaCl solution	-	-	4.2d.iv
40% pluronic F127	-	-	4.3a
3% sodium hyaluronate	1% Carbopol:10M NaOH (10 µL per 7 ml Carbopol)	-	4.3b
40% pluronic F127	-	-	4.3c.i
10% alginate:200 mM CaCl <sub>2</sub> (10:3 v/v ratio)	1.3% xanthan gum	-	4.3c.ii, c.iii
2 x 10 <sup>6</sup> cell suspension	-	-	4.3d.ii, d.iii
40% pluronic F127	0.2% Carbopol:10M NaOH (10 µL per 7 ml Carbopol)	-	4.3e
40% pluronic F127	-	-	4.3f
10 mg/ml collagen	4.5 % gelatin slurry – 10 mM HEPES	-	4.4a.i
10% alginate:200 mM CaCl <sub>2</sub> (10:3 v/v ratio)	4.5 % gelatin slurry – 11 mM CaCl <sub>2</sub>	-	4.4a.ii
1% agarose	0.2% Carbopol:10M NaOH (10 µL per 7 ml Carbopol)	-	4.4a.iii
2% gellan gum	-	Syringe heating at 50 °C	4.4d.iv, 4.8
10% gelatin	1.3% xanthan gum: PEGDA 700: I2959 (10:1:1 vol. ratio)	-	4.4a.v
3% sodium hyaluronate:PEDGA:I2959 (10:2:1 vol. ratio)	1% Carbopol:10M NaOH (10 µL per 7 ml Carbopol)	-	4.4a.vi
10% Sodium carboxymethyl cellulose	-	-	4.4a.vii, 4.9
15% Methyl cellulose	-	Stage heating at 50 °C	4.4a.viii
64% Methacrylate hydroxypropyl cellulose	-	<i>In situ</i> UV	4.4a.ix
13% Chitosan (600-800 kDa)	SE1700:silicone oil (3:1 wt ratio)	-	4.4a.x
5% Alginate-15% hydroxyapatite:200 mM CaCl <sub>2</sub> (10:1 v/v ratio)	-	-	4.4b.i
Alginate-15% precipitated silica:200 mM CaCl <sub>2</sub> (10:1 v/v ratio)	4.5 % gelatin slurry – 11 mM CaCl <sub>2</sub>	-	4.4b.ii
Alginate - 15% talc:200 mM CaCl <sub>2</sub> (10:1 v/v ratio)	-	-	4.4b.iii
40% Pluronic F127	-	-	4.4c.i, c.ii
25% Poly(acrylic acid) in 0.1M NaOH	SE1700:silicone oil (3:1 wt ratio)	-	4.4c.iii
2% Polyethylene oxide (8 MDa)	1.3% xanthan gum	-	4.4c.iv
20% Polyvinyl alcohol (31-50 kDa)	1.3% xanthan gum	-	4.4c.v
SE 1700 (base:curing agent 10:1 wt ratio)	-	-	4.4d.i
Ecoflex	6 w/w% Fumed silica in mineral oil	-	4.4d.ii, 4.14
10 mg/ml collagen	-	-	4.7a
1 w/v% agarose, 2 mg/ml collagen, 1.5 mg/ml collagen	4.5% gelatin slurry – 10 mM HEPES	-	4.7b
10 mg/ml collagen	0.1% Carbopol:10M NaOH (10 µL per 7 ml Carbopol)	-	4.7c
10 mg/ml collagen	0.2% Carbopol:10M NaOH (10 µL per 7 ml Carbopol)	-	4.7d
64% Methacrylate hydroxypropyl cellulose	-	<i>In situ</i> UV	4.10b
	-		4.10c
	-		4.10d
68% Methacrylate hydroxypropyl cellulose	-	Post-printing heating and crosslinking	4.10e
	-	Stage heating	4.10f
3% chitosan	1.3% xanthan gum	-	4.11b
3% chitosan-5% 400 kDa PEO:PEGDA:I2959 (10:1:1 vol. ratio)	1.2% Carbopol(10 µL per 7 ml Carbopol)	-	4.11c

Inks	Support baths	Heating / UV	Figures
3% chitosan:PEGDA:I2959 (10:1:1 vol. ratio)	4.5% gelatin slurry – 10 mM HEPES	-	4.11d.1
3% chitosan (modified with glycerol phosphate disodium):PEGDA:I2959 (10:1:1 vol. ratio)		-	4.11d.ii
13% high molecular weight chitosan PEGDA:I2959 (10:1:1 vol. ratio)	SE 1700: silicone oil (1:4 or 1:3 wt. ratio)	-	4.11e
20% Poly(acrylic acid): PEGDA:I2959 (10:1:1 vol. ratio)	1.3% xanthan gum 1.3% xanthan gum in 0.1M citric acid	- -	4.12a 4.12b
25% Poly(acrylic acid): PEGDA:I2959 (10:1:1 vol. ratio)	SE 1700: silicone oil (1:3 wt ratio)	-	4.13a
	6% Fumed silica in mineral oil	-	4.13b
	6% Fumed silica in mineral oil supplemented with stearic acid at different conc.	-	4.13c
	8% Fumed silica – 1% Stearic acid in mineral oil	-	4.14

### ***Printing with coordinate input***

The desired coordinates of the print path, stage speed and extrusion flowrate were defined in the control programme. 2D patterns (**Figure 5.2a.ii**) and 3D objects (**Figure 5.2a.i**) can be produced via this method. The 3D objects were created by repeatedly stacking the 2D layer described by the input coordinates at the defined layer height until the desired object height was reached.

### ***Printing with equation input***

Four forms of equations were used for fabricating the features presented in this chapter. They were equations of butterfly curve, Archimedean spiral, circle and sine wave (**Table 5.3**). The desired equations were inputted to the Python control programme, and were discretised by at least 100 evenly spaced points along the curve, depending on the length of the curve. 3D features were produced by either printing stacked layers of the 2D curve according to the defined object and layer heights (**Figure 5.2b.ii**) or setting the coordinates of the curve evenly distributed along a defined height (**Figure 5.3e**). The printing process was executed with the defined stage speed and extrusion flowrate.

**Table 4.2| Equations used for fabricating the one-stroke features demonstrated in Chapter 4.**

	Patterns	Equations
Butterfly curve		$x = \sin(\theta) \{ e^{\cos(\theta)} - 2\cos(4\theta) - \sin^5(\frac{\theta}{12}) \}$ $y = \cos(\theta) \{ e^{\cos(\theta)} - 2\cos(4\theta) - \sin^5(\frac{\theta}{12}) \}$ $0 \leq \theta \leq 12\pi$ <p>where <math>\theta</math> is the polar angle.</p>
Archimedean spiral		$R = a + b\theta$ $x = R\cos(\theta)$ $y = R\sin(\theta)$ <p>where <math>a</math> controls the distance between the origin and the first loop from the origin, <math>b</math> controls the distance between loops and <math>\theta</math> is the polar angle.</p>
Circle		$x = R\cos(\theta)$ $y = R\sin(\theta)$ $0 \leq \theta \leq 2\pi$ <p>where <math>R</math> is the radius and <math>\theta</math> is the polar angle.</p>
Sine wave		$y = Asin(Bx)$ $0 \leq x \leq 10$ <p>where <math>A</math> is the amplitude, <math>\frac{2\pi}{B}</math> is the period and <math>x</math> is the total pattern length.</p>

### Printing with CAD model input

3D CAD models were either designed using Autodesk Inventor or downloaded from GradCAD (<https://grabcad.com/library/software/stl>), Thingiverse ([www.thingiverse.com](http://www.thingiverse.com)) or the BodyParts3D database (<https://lifesciencecdb.jp/bp3d/>). Prior to the printing process, the CAD model was converted to a G-code file using Slic3r (<https://slic3r.org/>) based on the defined slicing parameters (i.e. fill pattern, fill density, extrusion width and layer height), of which the values depend on the ink properties. The G-code file was then imported to the Python control programme. The printing process was executed with the defined parameters of the stage speed and the extrusion flowrate.

### Printing with picture input

Printing with picture input was enabled by the ‘Geodetools’ extension [265] on Inkscape (<https://inkscape.org/>), which was an extension designed for CNC machines. The extension was installed on Inkscape. To convert a picture into printing paths, the workplace size on Inkscape was first adjusted according to the size of the stage by clicking ‘File → Document properties → Custom sizes’. The acceptable form of pictures can be photos of hand-drawn

sketches, pictures created by any drawing software or drawings created on Inkscape. For photos of hand-drawn sketches or pictures created by other drawing software, the pictures were imported to Inkscape and were converted to a vector path using the following procedures: 1) Convert the image to a binary image ('Filters → Color → Greyscale') and 2) Trace the centreline of the image ('Extensions → Images → Centerline Trace 0.8a [266] → Select 'Replace image with vector graphics' and 'Trace bright lines'). For drawings created on Inkscape, the drawing was converted to paths by clicking 'Path → Object to path'. After converting the picture to path, the path was then placed at the centre of the workplace and was converted to a G-code file by applying the following step: 1) Navigate to 'Extensions → Gcodetools → Orientation points' and select '2-points mode'; 2) click 'Extensions → Gcodetools → Tool library' and select 'Cone'; and 3) Select the path, navigate to 'Extensions → Gcodetools → Path to Gcode' and save the file by clicking 'Apply' under the 'Path to Gcode' tab with the file name defined in the 'Preferences' tab. The G-code file can be viewed on NC viewer (<https://ncviewer.com/>). The generated file was then imported to a Python programme, which was designed for reading the G-code files generated by this extension (see **Chapter 3** for details). The printing was executed with the defined extrusion flowrate and stage speed.

#### 4.2.5 Dispensing of cell suspension

*This experiment was carried out with the help of my colleague, Yang Cao.*

3T3 mouse embryo fibroblast cell line was cultured in a 25 cm<sup>2</sup> flask and was passaged following standard protocol. Cell culture media used here were 10 v/v% fetal bovine serum and 1 v/v% penicillin-streptomycin in DMEM. A cell suspension with 2 x 10<sup>6</sup> cells/ml was used in the dispensing experiments, with the cells stained with Calcein AM (at 2 µM working concentration for live cell staining). To prevent cell sedimentation, immediately after resuspension, the cell ink was drawn into a 1 ml luer-lok syringe and was loaded into the syringe holder of the printer. A tapered needle was used here to mitigate cell death caused by the shear stress at the nozzle. The control programme for dispensing operation was adapted from the programme used for coordinate geometry input. In the operations of constant volume dispensing, the stage was programmed to pause at an array of 5 x 4 evenly spaced coordinates one-by-one for 5 s and the extrusion was applied during the pause period. In the operation of variable volume dispensing, the stage was paused for 1 – 5 s with the time increased linearly in the order of the dispensing coordinates.

#### 4.2.6 Non-planar printing

The 3D scanning of the target object was carried out by Abby Thompson, an undergraduate student from the Department of Engineering.

A 2D line pattern for printing was designed on Inkscape and was converted to a G-code file using the same procedure described in ‘Printing with picture input’ (Section 4.2.4). The 3D shape of the target object (a Ecoflex nose model) was captured using a 3D scanner (EinScan H, SHINING 3D<sup>®</sup>) and was saved as a STL file. To analyse the surface of the target object, the STL model was converted into a G-code file using Slic3R with the following slicing settings (fill pattern = ‘Hilbert curve’, extrusion width = 0.2 mm, fill density = 100% and layer height = 0.2 mm). A dense infill setting and a Hilbert curve infill pattern were used here for precisely describing the target object. The G-codes of the target object (the nose model) and the printing pattern (a line pattern) were then imported to a custom Python programme. In the programme, each layer of the target object was discretised into tiny grids, and the highest z-position of each stack of grids (grids at similar x, y positions with a tolerance threshold = 0.2 mm) was computed. The z-position of the printing pattern was then shifted in accordance with the analysed z-position of the target object at the similar x, y positions (tolerance threshold = 0.2 mm). By default, the programme assumes that the pattern is printed around the centre of the target object. The offset function can be used for shifting the printing pattern away from the centre if needed. The programme outputs a text file of the analysed coordinate array, which was then imported to the Python control programme used for Picture input to execute the printing.

#### 4.2.7 Printing and removal of sacrificial template

Gelatin (Figure 4.4a.v) and Pluronic F127 (Figure 4.2a.iii-a.iv) inks were used as sacrificial inks for producing micro-channel networks in this chapter. The sacrificial inks were embedded printed in a supportive matrix, followed by crosslinking the matrix via thermal or UV mechanisms, depending on the properties of the matrix. To liquefy the sacrificial inks after matrix crosslinking, gelatin sacrificial inks were removed by warming the matrix above 37 °C, while the Pluronic F127 sacrificial inks were removed by cooling the matrix in a 4 °C fridge for 10 mins. A dye was then perfused to the channel network for removing the residual sacrificial material and visualising the channels.

#### 4.2.8 Printing of PAA strips for pH-responsive morphing

A 25 w/v% of PAA-PEGDA-I2959 solution (10:1:1, see Materials and Methods **4.2.2**) stained with sodium fluorescein was used for printing pH-responsive PAA strips. Prior to printing, CAD files of the strips were designed on Autodesk Inventor and sliced on slic3R using the following settings: fill angle of either 0°, 45° or 90°, a rectilinear fill pattern, infill density = 90%, extrusion width = 0.4 mm and layer height = 0.5 mm. The dimensions of the strips were 20x8x1 mm (**Figure 4.14a-c** and **Figure 4.15**), 10x10x1 mm (**Figure 4.14d**) and 20x20x1mm (**Figure 4.14e**). They were printed in a mineral oil bath supplemented with 8 w/v% fumed silica and 1 w/v% stearic acid. After printing, the features were UV-crosslinked for 10 min and collected from the bath, followed by rinsing with a soapy acidic water (1 M citric acid). The printed strips were then immersed in 1 M Tris solutions for pH-responsive morphing behaviour. The morphing was reversed by placing the strips in a 1 M citric acid solution.

### 4.3 Results and discussion

#### 4.3.1 A versatile platform for flexible geometry inputs

Most commercially available bioprinters employ proprietary software and are only able to read the G-code files generated from their proprietary slicing software with the 3D CAD models imported by the users. Although G-code is the standard language used in 3D printing and is advantageous for describing three-dimensional bulk objects with uniform print paths, several limitations are noted. First, the generation of G-code using 3D slicing software comes at the expense of restricted customisation of the print path. It is arduous to generate diverse print path with the currently available slicing software. In addition, using CAD models to describe simple patterns, such as 2D patterns or sacrificial templates for producing vascular-like networks, is redundant and may result in an inappropriate print path. As exemplified in **Figure 4.1**, to describe the intended shape of a 2D pattern with G-code, a CAD model first needs to be created and is then sliced using a slicing software. However, due to the limited choices of fill pattern available from the slicing software, a zig-zag or a repeated print path could be resulted, diminishing the smoothness and the fidelity of the print. On the contrary, this simple Y-shaped pattern can be easily described by four coordinates to give a smooth and non-repeated print path. Furthermore, the orientation of the print path has significant impacts on various properties of the printed objects, such as its final mechanical properties, cell adhesion behaviour and

swelling response (discussed in **Section 4.3.3.2**) [267]. All of these show the need for a greater flexibility in the geometry input options to enable path-designed printing.

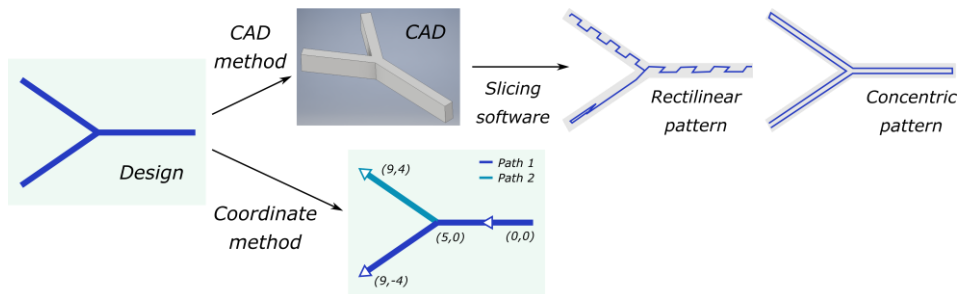


**Figure 4.1|** Figure comparing the print paths of a simple ‘Y’ shaped pattern generated via slicing a 3D CAD model and via the coordinate method proposed here.

On this account, I developed four programme templates for accepting different geometry inputs to suit different needs. They are coordinates, equations, CAD model and picture (see **Chapter 3** for the details of the programme design). **Figure 4.2** demonstrates a wide variety of patterns fabricated using different geometry inputs – from simple linear patterns produced by coordinates to seamless one-stroke curvy patterns described by equations; and from three-dimensional intricate objects described by 3D CAD models to customised motifs defined by pictures. Remarkably, one-dimensional channels (**Figure 4.2a.iii**) and simple tubular constructs (**Figure 4.2b.ii**) can be readily produced via coordinates and equations. By leveraging the picture input method, user-designed patterns, for example circuit- and vascular-like patterns (**Figure 4.2d.iii-iv**), can be readily fabricated. In particular, the feature shown in **Figure 4.2d.iv** was described by a hand-drawn sketch, hence this function might be helpful for users who are not familiar with computer-aided designs. Although the system does not offer a graphical user interface for operation, the pre-written programme templates are user-friendly and were specifically designed for users with no-programme experience. It is worth mentioning that the operation flexibility does not limit to the four geometry inputs provided here. As the software is entirely hackable and was written in Python, one of the most popular and easiest programming language, users can freely amend the codes to tailor the operation process.

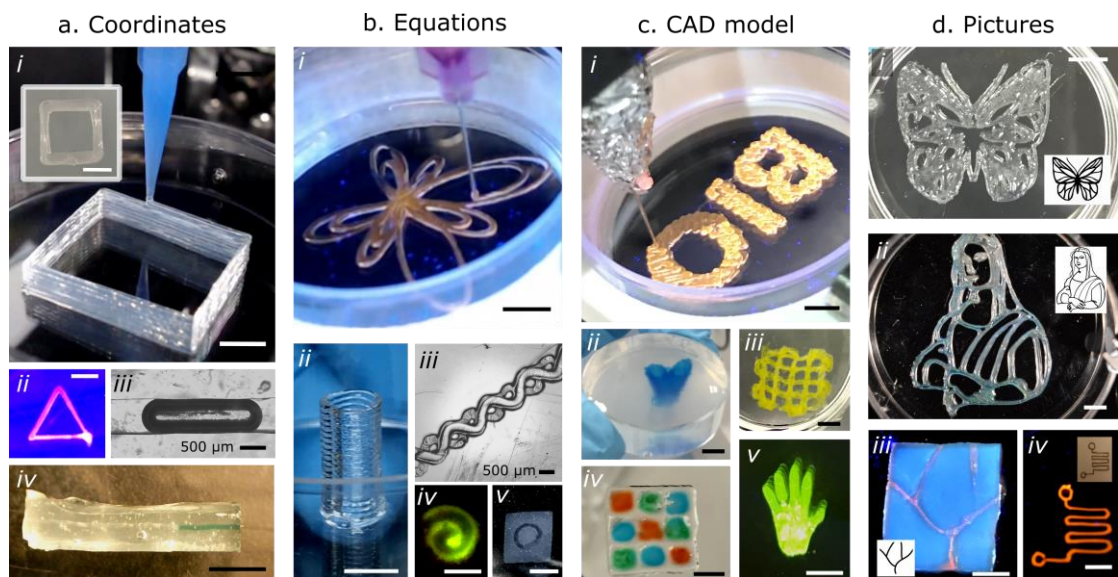


**Figure 4.2| Constructs printed using the a) coordinate, b) equation, c) CAD model and d) picture geometry input options.** The materials used were as follows: (a.i and b.iii) SE 1700, (a.ii, a.iii, a.iv, b.i, b.ii, b.iv, b.v, c.i, c.v and d.iv) pluronic F127, (c.ii and c.iii) alginate-CaCl<sub>2</sub>, (c.iv) gellan gum, (d.i and d.ii) methacrylate hydroxypropyl cellulose and (d.iii) gelatin. Detailed information of the ink formulation used here can be found in **Table 4.2**. (a.iii, a.iv, b.iv and d.iii) show perfusable channels stained with a green dye or a fluorescent dye. They were produced by printing (a.iii, a.iv and b.iv) pluronic F127 or (d.iii) gelatin in a matrix made of (a.iii, a.iv and b.iv) xanthan gum-gelatin or (d.iii) xanthan gum-PEDGA. (b.v) shows an agarose mould produced by casting an agarose solution on a pluronic F127 sacrificial pattern. The grid shown in (c.iv) were printed using a gellan gum ink, followed by manually dispensing collagen solutions at different concentrations (1, 2 and 4 mg/ml stained with red, green and blue dyes) onto the grid. Scale bar = 5 mm.

### 4.3.2 Multi-functionalities in one platform – from conventional 3D extrusion printing to advanced techniques.

Apart from **in-air** and **embedded** printings of single material that most bioprinters offer (**Figure 4.3a-b**), the system is capable of fabricating **multi-material** constructs using the multiple printheads equipped in the system. As a demonstration, **Figure 4.3c** shows a four-layer construct composed of Pluronic F127 inks coloured with different dyes (**Figure 4.3c.i**) and a model of respiratory system with lungs and trachea made of alginate inks (**Figure 4.3c.ii-iii**) successfully printed in-air or inside a support bath. The calibration step of the printheads to the stage centre (discussed in **Section 3.5.1**) is essential in multi-material printing as misalignment could be resulted when the system is not properly calibrated.

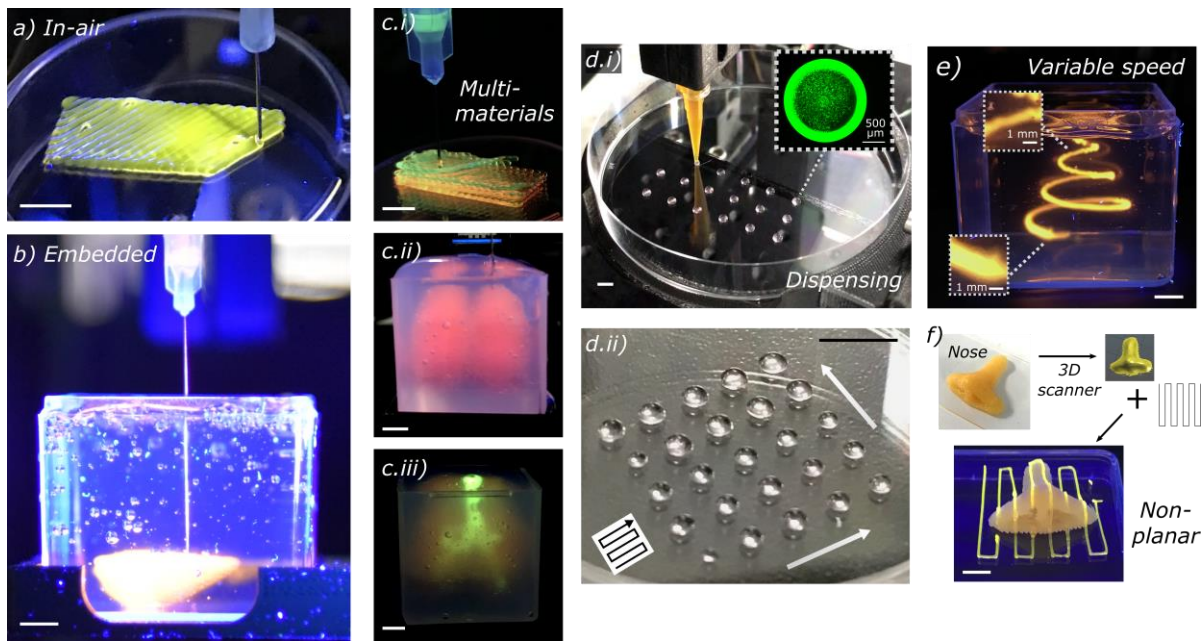


**Figure 4.3| Versatile functionalities of the 3D extrusion printing platform.** **a)** In-air printing of Pluronic F127. **b)** Embedded printing of sodium hyaluronate in a Carbopol bath. **c)** Figure demonstrating the capability of multi-material printing with the platform. Multiple printheads were used here to deposit different inks. (c.i) was printed with three Pluronic F127 inks stained with different colours and (c.ii-c.iii) was a construct made of two alginate inks printed in a xanthan gum bath. **d)** Automated dispensing of cell suspension on a petri dish at (d.i) constant droplet volumes and (d.ii) variable droplet volumes. The black arrow in (d.ii) indicates the direction of the dispensing path, and the white arrows depict the controllable droplet size variation from small to large volume. **e)** A spiral curve made of Pluronic F127 printed with variable speed. **f)** Non-planar printing of a Pluronic F127 line pattern on a 3D nose model. Scale bars = 5 mm.

By virtue of the customisable control programme, unconventional operations, such as automated dispensing, printing with variable speed and non-planar printing, were readily enabled. **Liquid handling** always plays an indispensable role in life science experiments, however manual pipetting is low throughput, unable to dispense viscous solutions and may cause fatigue-related mistakes due to repetitive operations. For this reason, I demonstrated the liquid handling capability of the system. The programme was modified such that the stage stopped at a set of defined coordinates one-by-one for a specific duration of time, while the printhead was dispensing the cell suspension. **Figure 4.3d.i** shows that droplets of 3T3 cell suspension with the same size were dispensed on a petri dish. The dispensed volume of the droplets is controllable by the extrusion flowrate and the dispensing duration. By simply setting different duration of dispensing time along the path from short to long duration, droplets with various sizes were obtained (**Figure 4.3d.ii**). This capability might be useful for automating the hanging drop method to produce cell spheroids and dispensing active ingredients in a

printed object. Likewise, extruded ink filaments with continuously narrowing diameter can be achieved by **varying the travelling speed** of the stage along the print path, as illustrated in **Figure 4.3e**. This strategy could be utilised for the generation of smooth and vascular networks with heterogenous dimensions.

Lastly, I demonstrate the capability of **non-planar printing** using the platform. As opposed to conventional commercial 3d printers that rely on plane-by-plane slicing, non-planar printing allows inks to be printed along a freeform surface by moving the motion system of the printer in all 3 axes at the same time to avoid collisions between the printhead and the target surface. **Figure 4.3f** shows the workflow of non-planar printing used in my experiment. With the use of a 3D scanner, the 3D shape of the target object can be accurately captured. In this example, a 3D printed nose model made of ecoflex was used as the target object. The surface of the target object was then analysed and the z-coordinates of the printing pattern (a line pattern in this example) were transformed according to the target surface using a custom python code (see **Materials and Methods 4.2.6** for details). As shown in **Figure 4.3f**, a line pattern was successfully printed onto the target nose model. With the ability to deposit inks directly onto small objects, novel applications of 3D extrusion printing technology could become possible, such as freeform circuits [268] and depositing drugs or functional materials on small organisms (e.g. plants, fish and reptiles). However, it should be noted that the payload capacity (500 g) of the robotic arm may limit the size and the mass of objects that can be placed onto the stage.

### 4.3.3 Fabricating complex structures with a wide range of soft materials

Most biomaterials do not have an ideal rheological property for printing, hence choosing a suitable printing method and having auxiliary tools, such as heating and UV tools, to modulate the material rheology are imperative for the success of constructing soft materials. Here, I explore the printing capability of the system with a wide variety of biomaterials. As shown in **Figure 4.4**, the printer is capable of printing different types of biomaterials, from collagen, natural polysaccharides, bioceramics-based hydrogels, synthetic polymers to silicone elastomers. The designated CAD models or 2D patterns of the printed structures are shown in **Figure 4.5**. A few of the materials possess good printability, while others were printed with the aid of support baths, heating or UV light.



**Figure 4.4| 3D printed constructs made of a) natural hydrogels, b) bioceramics-hydrogels, c) synthetic hydrogels and d) silicone elastomers.** (a.v) is a perfusible channel network (stained with the orange Rhodamine B dye) produced by embedded printing a gelatin ink in a supportive matrix. Scale bars = 5 mm.

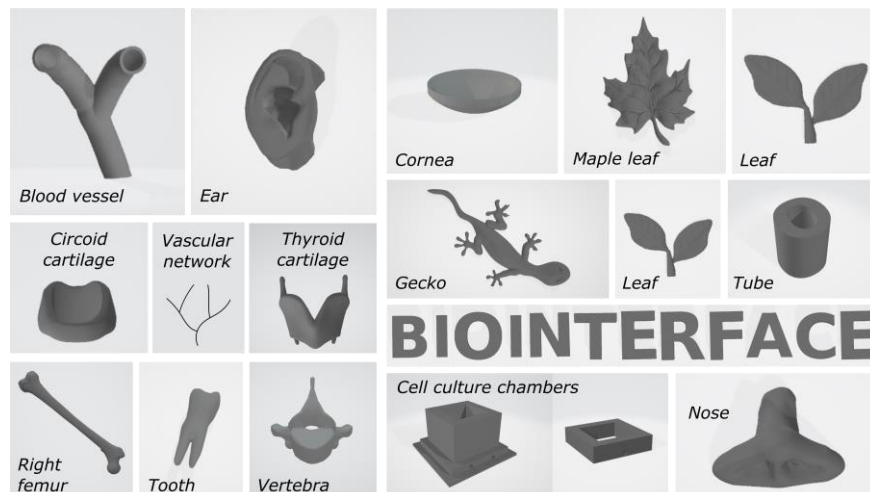


**Figure 4.5| The CAD models and the 2D pattern of the constructs shown in Figure 4.4.**

In the following sections, the transparency of the commonly used support baths in literature was first examined, as highly transparent baths are desirable for *in-situ* monitoring and photo-polymerisation. I then discuss the rationale for the method I utilised for printing each material. The selected printing methods of the inks are summarised in **Table 4.4**. Detailed methods of the solution preparation and the concentrations of the inks and the baths are provided in Materials and Methods (4.2.2 – 4.2.3) and **Table 4.2**. A decision flowchart (**Figure 4.17**) is presented at the end, providing my perspective on selecting an appropriate printing approach.

#### 4.3.3.1 Transparency of support baths for photo-crosslinking

**Figure 4.6** shows the transparency of the commonly used water- and oil-based support baths reported in literature. Apart from the fumed silica-silicone oil support bath, they were prepared using similar concentrations and protocols reported in literature (see Materials and Methods 4.2.3) [52, 126, 130, 168]. Carbopol is a modified high molecular weight poly(acrylic acid), of which the transparency depends on the pH of the solution. Exceptional transparency occurs at around neutral pH. As shown in **Figure 4.6**, Carbopol displays a superior transparency than gelatin slurry, therefore it is perfect for uses in printing processes that involve photo-polymerisation. Among the oil-based baths used in literature, both fumed silica-mineral oil and fumed silica-silicone oil baths offer adequate transparency, while SE 1700-PDMS bath is translucent and may impede the photo-polymerisation efficacy of the inks. Interestingly, a lower concentration of fumed silica is required with silicone oil to obtain a similar and adequate viscosity for printing, compared to fumed silica-mineral oil baths.

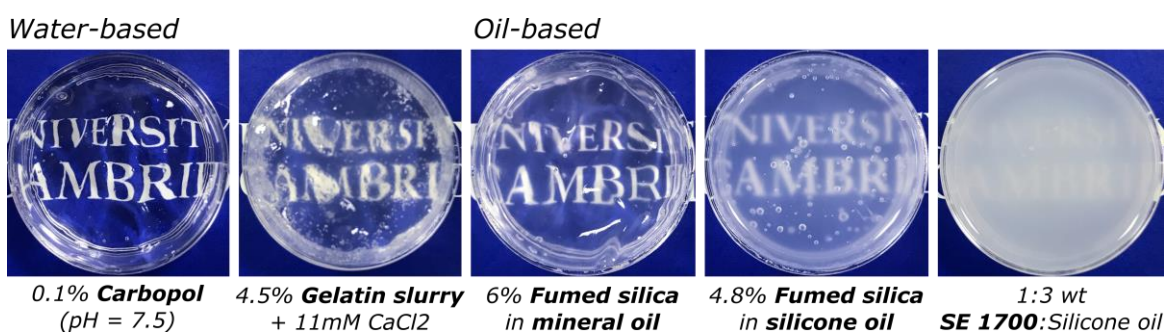


**Figure 4.6| Optical transparency of the frequently used support baths in literature.**

#### 4.3.3.2 Printing soft materials

##### 1. Collagen

**Figure 4.7a** shows the procedure I adopted for printing collagen. Collagen bioinks are typically composed of collagen fibres solubilised in an acid. Neutral pH and physiological temperature (pH 7 and 37 °C) are essential for crosslinking acidified collagen inks. A support bath of gelatin slurry supplemented with a 10 mM HEPES buffer solution [52] was used here to support the overhanging printed structure and to facilitate the neutralisation of the acidified collagen once the ink was deposited into the bath. It is noted that the printed ink cannot be properly crosslinked if the support bath is removed immediately after printing. Therefore, to avoid the dissolution of the printed object, the object was kept inside the bath for an hour after printing to ensure complete neutralisation, followed by incubation at 37 °C for an hour to thermal crosslink the printed ink while removing the support bath.

Although previous works have shown that the gelatin slurry support bath method (also known as the FRESH method) is well-compatible with high concentration collagen inks, from 9 to 35 w/v% [52, 136], its capability with low concentration collagen is yet to be demonstrated. A 1 – 2 mg/ml of collagen solution is a more relevant concentration used in cell culture experiments [269]. Therefore, I examined the compatibility of the FRESH method with low concentration collagen inks. As shown in **Figure 4.7b**, a simple heterogeneous construct composed of 2 and 1.5 mg/ml collagen inks was successfully produced, and the shape was preserved after removing the gelatin slurry support bath. This confirms the performance of the FRESH method for printing low concentration collagen inks, though complex features with high resolution might not be attainable at this concentration. Collagen inks with concentration less than 1.5 mg/ml were not printable in my experiments , possibly because the diffusion of the ink through the bath happened faster than the crosslinking of the ink.

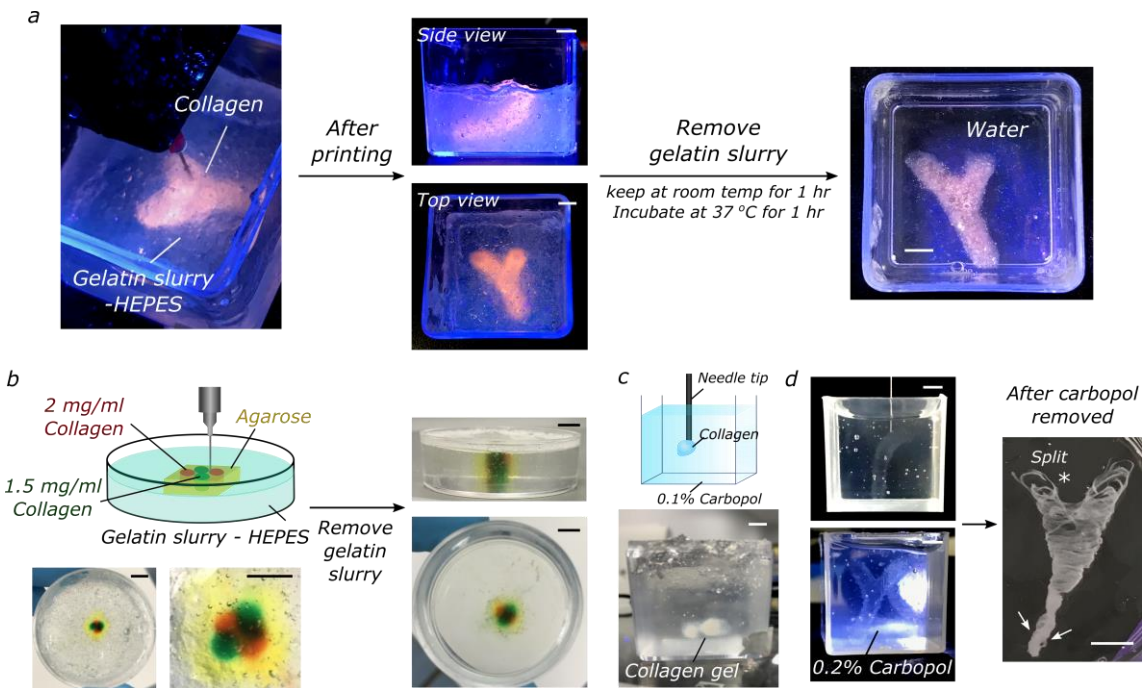


**Figure 4.7| Printing of collagen.** **a)** The method employed for fabricating collagen constructs. **b)** A construct made of low concentration collagen and agarose fabricated using gelatin slurry support baths. **c)** Cohesive and dragging problems experienced when a 0.1 w/v% Carbopol support bath (pH 7) was used. **d)** Shape evolution (indicated by the white arrow) and splitting (indicated by \*) problems of a collagen construct when a 0.2 w/v% Carbopol was used for embedded printing. Scale bar = 5 mm.

The print fidelity of collagen in Carbopol support bath, another frequently used support bath in literature, was also evaluated. Using a 0.1 w/v% of Carbopol gel (pH 7), the feature cannot be successfully printed. The ink stuck to the needle tip and was dragged within the bath, forming a lump of gel (**Figure 4.7c**). This observation potentially suggests that the storage modulus of Carbopol gel at 0.1 w/v% is insufficient and the crosslinking accompanied by neutralisation and electrostatic interaction between collagen and Carbopol happened too fast, rapidly increasing the storage modulus of the ink. Further experiments on rheological measurements can be carried out to verify this. Although collagen can be printed at 0.2 w/v% Carbopol (pH 7), the shape of the printed feature evolved over time and split into filaments possibly due to the mismatch in their interfacial tension and rapid crosslinking (**Figure 4.7d**). Other concentrations of Carbopol were not tested here because Carbopol gels at neutral pH and higher concentrations ( $\sim 1$  w/v%) are difficult to handle due to the large amount of bubbles trapped in the highly viscous gels, and the bubbles cannot be easily removed via centrifugation. The above findings suggest that Carbopol was not an ideal material for fabricating collagen.

## 2. Agarose, gellan gum and gelatin

Agarose, gellan gum and gelatin are thermo-reversible hydrogels that form solid gels at low temperature. When the inks are printed at room temperature, the printed filaments are usually rough and wavy because solid gels are being squished through a needle tip and cannot cohere to each other. Therefore, temperature control is crucial for creating smooth filaments that can cohere to form a bulk construct. Here, I demonstrate the freeform embedded printing of agarose (**Figure 4.4a.iii**) and gellan gum (**Figure 4.4a.iv**), and the printing of a sacrificial template using gelatin (**Figure 4.4a.v**).

Assisted by the custom-designed syringe heater, the agarose and gellan gum inks in the syringe were warmed at 50 °C and were printed inside a Carbopol support bath. **Figure 4.8** shows the printing of gellan gum in a Carbopol bath. Carbopol was chosen here because it is easy to prepare, and the gelation process of agarose and gellan gum does not necessarily require ionic or pH agents. To ensure thermal crosslinking is complete before releasing the constructs, the constructs were kept at room temperature for ~20 min after printing. The Carbopol support bath was liquified by adding a NaCl solution to the bath. As gellan gum can be crosslinked via ionic means, I further strengthened the gellan gum construct by crosslinking it with a CaCl<sub>2</sub> solution after the bath was removed. CaCl<sub>2</sub> was not used as the releasing agent in the first place because mixing CaCl<sub>2</sub> solution with Carbopol was found to form a white precipitate, possibly due to the excessive salting out effect under high ionic strength.



**Figure 4.8| Printing of gellan gum in a Carbopol bath.** Scale bars = 5 mm

Thermo-reversible gelatin and agarose hydrogels have been frequently used as sacrificial materials in literature as they are biocompatible and can be easily removed under mild condition [128, 207]. To demonstrate the sacrificial capability of gelatin, I designed a vascular-like template in a picture format and embedded printed it with a gelatin ink inside a PEGDA-xanthan gum matrix. Protein-based hydrogels, such as collagen and fibrinogen, can be incorporated into the matrix to enhance its biofunctionality for the creation of vascular

network. The gelatin ink was heated at a high temperature (50 °C) during printing because a higher temperature can avoid the ink from gelling too fast that will unfavourably cause the extruded ink sticking to the needle tip.

### 3. *Alginate and bioceramics-alginate composites*

Alginate solutions by itself has poor printability. The solution is usually pre-crosslinked with CaCl<sub>2</sub> to enhance its viscosity, such that the ink could exhibit superior printability. Two types of formulations were tested here, a 10 w/v% alginate ink and a bioceramics-alginate ink composed of 5 w/v% alginate and 15 w/v% bioceramics (either hydroxyapatite, talc or silica). Both were pre-crosslinked with CaCl<sub>2</sub> (see **Materials and Methods 4.2.2**). The former has adequate viscosity for in-air printing. The incorporation of bioceramics into alginate inks reinforced the alginate hydrogels, and therefore lower concentrations of alginate and CaCl<sub>2</sub> were required to obtain a printable ink. As crosslinking of alginate relies on ionic solutions, I utilised a gelatin slurry bath containing CaCl<sub>2</sub> to construct the freeform structures (**Figure 4.4a.ii & b**). When printing was completed, the constructed was further crosslinked with CaCl<sub>2</sub> solution and was released by warming the bath to 37 °C.

### 4. *Sodium hyaluronate-PEGDA*

Sodium hyaluronate (Na-HA) is a sodium salt of hyaluronate acid. Its shear thinning and high viscosity at low concentration make it an excellent candidate for thickening bioinks for printing applications. When dissolving Na-HA in water, an amorphous gel is resulted. Formation of solid gels of Na-HA requires chemical crosslinking or chemical modification of the materials. On the contrary, PEGDA is a photocrosslinkable low viscosity solution that forms brittle gels upon UV photo-polymerisation. By combining PEDGA with Na-HA, the resulting ink encompassed both crosslinkable and printable properties.

I chose a Carbopol support bath for printing the sodium hyaluronate-PEDGA inks (**Figure 4.4a.vi**) because its extraordinary transparency supports photo-polymerisation. While the crosslinking should be long enough to ensure proper crosslinking of the ink, it should also not be too long to avoid the crosslinking of the Carbopol around the printed features caused by the diffusion of low molecular weight PEGDA molecules and photoinitiators.

## 5. Cellulose derivatives

*Sodium carboxymethyl cellulose* (Na-CMC) is a polysaccharide that has been used as a thickener in bioprinting applications [36]. A 10 w/v% of Na-CMC ink allows a few layers of the material to be printed without the need of support baths, as shown by the ‘leaf’ construct in **Figure 4.9**. Akin to Na-HA, Na-CMC does not form solid gels by itself. To crosslink the construct, I chose a low concentration chitosan solution that weakly crosslinksed with Na-CMC via electrostatic interaction between the  $\text{NH}_3^+$  groups of chitosan and  $\text{COO}^-$  groups of Na-CMC.

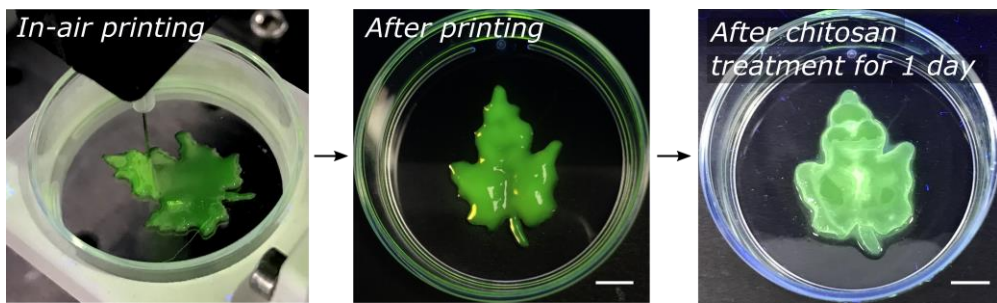


**Figure 4.9| Printing of sodium carboxymethyl cellulose and post-printing crosslinking with a chitosan solution.** Scale bars = 5 mm.

*Methylcellulose* (MC) is a thermo-reversible LCST hydrogel, of which the viscosity increases with elevated temperature. To make use of its thermo-thickening property, I printed the MC ink with a heated stage using the custom-made stage heater, such that the viscosity of the ink increased once the ink was deposited onto the stage, preserving the desired shape during printing.

## *Methacrylate hydroxypropyl cellulose*

*This part of work was carried out in collaboration with Chun Lam Clement Chan. The materials were produced by my collaborator. I established the printing method.*

In this study, a photocrosslinkable cholesteric hydroxypropyl cellulose (HPC-MA) solution developed by my collaborator was used as a sustainable 3D extrusion printing material with tuneable iridescent colour. The colour primarily depends on its concentration, water content and crosslinking temperature as these factors affect the cholesteric ordering of the material.

### 1. *In situ UV crosslinking*

The first issue we encountered was to enable the creation of 3D bulk objects of the material. Like most soft materials that tend to sag and spread out, thick structures of HPC- MA are not achievable via conventional in-air printing. In addition, the use of aqueous support baths is not feasible here because the diffusion of water from the aqueous bath to the printed ink will detrimentally affect the cholesteric ordering of the material and thus the colour. Therefore, to solve this problem, we utilised an *in situ* UV crosslinking strategy where a UV light source was placed near the stage during printing so that photo-polymerisation of HPC- MA could be immediately initiated once the ink was extruded, as illustrated in **Figure 4.10a**. Comparing the features created via *in situ* UV crosslinking and via post-printing crosslinking, a more well-defined feature was resulted via *in situ* crosslinking (**Figure 4.10b** vs **d**), but also a reduced coloration (**Figure 4.10c** vs **d**). We hypothesised that the reduced coloration was originated from the lack of relaxation time for recovering the HPC microstructure from an aligned orientation to a random orientation. The aligned orientation was caused by the shearing at the nozzle tip. In addition, the presence of internal interfaces and the increased surface roughness of the construct caused by *in situ* crosslinking also increase the scattering and thus obscure the reflected structural colour. In summary, the *in situ* UV crosslinking strategy enables fabrication of thick 3D constructs of HPC but at the expense of degraded colour (**Figure 4.10c**). Future research could investigate the use of oil-based support baths to solve the reduced coloration problem, as oil-based baths enable creation of 3D overhanging structures and avoids the water diffusion issue that happens in water-based baths.

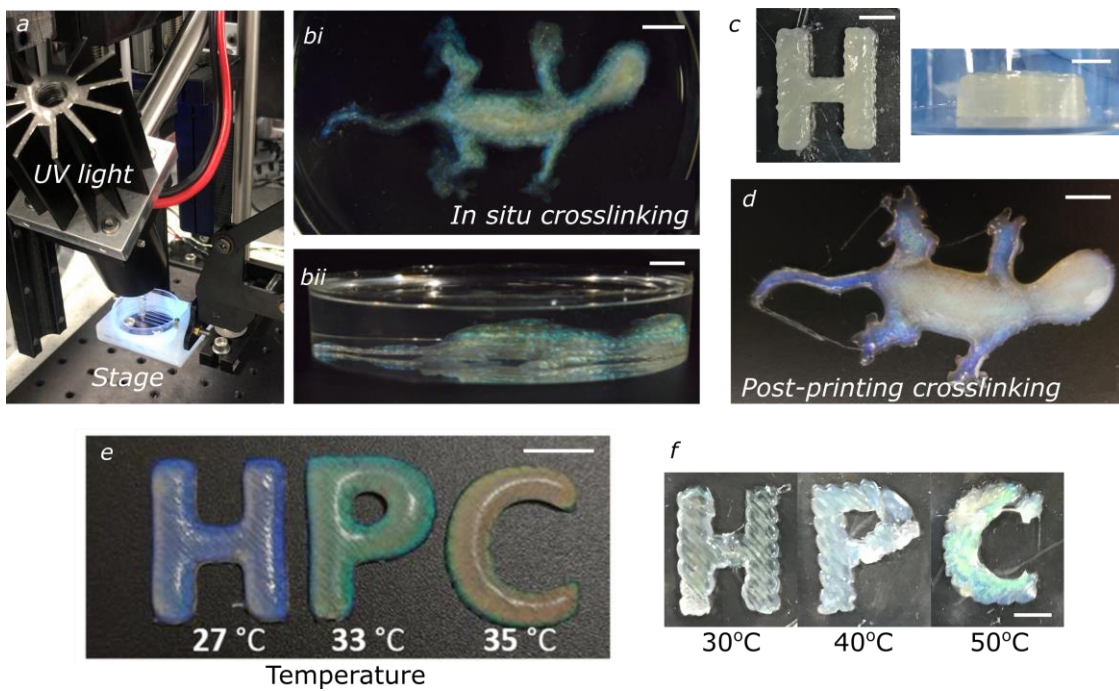


**Figure 4.10| Printing of Methacrylate hydroxypropyl cellulose.** **a)** Configuration of the setup with UV light for *in situ* crosslinking. **b)** A gecko produced from 64 wt% HPC-MA via *in situ* crosslinking. The object was encapsulated in PDMS to remove interfacial scattering. **c)** A tall construct of letter ‘H’ created via *in situ* crosslinking. **d)** A gecko created via post-printing crosslinking. The objects in (c-d) were not encapsulated in PDMS. **f)** ‘H’, ‘P’, ‘C’ produced from a single 68 wt% HPC-MA solution, but crosslinked at temperatures of 27, 33 and 35 °C, respectively. **f)** Reduced fidelity when letters were printed with *in situ* heating. Scale bars = 5 mm.

## 2. Creation of constructs with tuneable iridescent colour

The cholesteric HPC solution is thermochromic with its colour red-shifted with increasing temperature. This property enables different structural colour of constructs using a single stock solution at different temperatures. As shown in **Figure 4.10e**, 3D printed constructs of letters ‘H’, ‘P’, and ‘C’ were produced from a single 68 wt% HPC solution. They were UV-crosslinked at different temperatures after printing. The reason why post-printing crosslinking was adopted here is that it enables a more intense coloration. In addition, we did not employ *in situ* heating because it was found that this will cause evaporation of water from the ink, which tremendously increases the ink viscosity, making the ink less cohesive and unprintable, as shown in **Figure 4.10f**. To avoid the reduced moisture content during heating and crosslinking, the constructs were warmed in a humid incubator for 10 min, followed by UV crosslinking in the incubator.

## 6. Chitosan

Chitosan is a naturally cationic polysaccharide that is soluble in acid medium. The material can be crosslinked via ionic (i.e. with tripolyphosphate (TPP)), thermo- ( $\sim 37$  °C) and pH-crosslinking (phase separation at pH  $\sim 6.5$  [39]). Additionally, photo-crosslinking can be achieved by chemically modification of chitosan or adding a photocrosslinkable agent to the formulation, such as PEGDA. **Figure 4.11a** summarises the tested methods that are feasible for creating chitosan constructs. Below discusses the findings observed when testing an appropriate support bath for printing chitosan.

First, when an anionic support bath was used, such as xanthan gum and Carbopol, the extruded chitosan ink tends to unite, adhere on the needle tip, and drag in the support bath (**Figure 4.11b**). This behaviour is possibly caused by the rapid crosslinking arising from the electrostatic interaction between the anionic support bath and the cationic chitosan. The crosslinking rapidly increased the storage modulus of the ink, hence causing dragging. To enable printing of chitosan in Carbopol, I found that chitosan ink mixed with PEO can mitigate the dragging problem and is compatible with both gelatin slurry and Carbopol ( $> 1$  w/v%) support baths (**Figure 4.11c**).

The above observation suggests that the anionic Carbopol is not an ideal material for printing chitosan. Therefore, gelatin slurry support bath was tested. Remarkably, the support bath allows printing of chitosan inks and inks modified with either PEO or glycerol phosphate disodium salt (GP) (**Figure 4.11d**). GP is a weak base that can increase the pH of chitosan solution from acidic to neutral (pH 6.7) without phase separation, hence this formulation can be mixed with cells for fabricating cell-laden constructs [39].

As chitosan is a pH-responsive hydrogels that is known to swell under acidic and neural pH condition, the aqueous environment of gelatin slurry and Carbopol supportive baths, might potentially cause swelling of the chitosan ink during printing, diminishing the feature resolution. Hence, an oil-based bath would be advantageous for avoiding the swelling issue. Interestingly, an unmodified 600 – 800 kDa chitosan ink (13 w/v%) was printable in an oil-based bath (**Figure 4.11e.i**), possibly attributed to the adequate viscosity of this formulation and the prohibited neutralisation and electrostatic crosslinking of chitosan in an oil-based bath. The oil-based bath tested here was composed of SE 1700 mixed with silicone oil in a weight ratio of 1:3. While a lower SE 1700 content increases the transparency of the bath, the bath at a 1:4 weight ratio of SE 1700 and silicone oil was unsuitable for the application here because the

viscosity of the bath is insufficient to hinder the shape deformation of the printed object driven by interfacial tension (**Figure 4.11e.ii**).

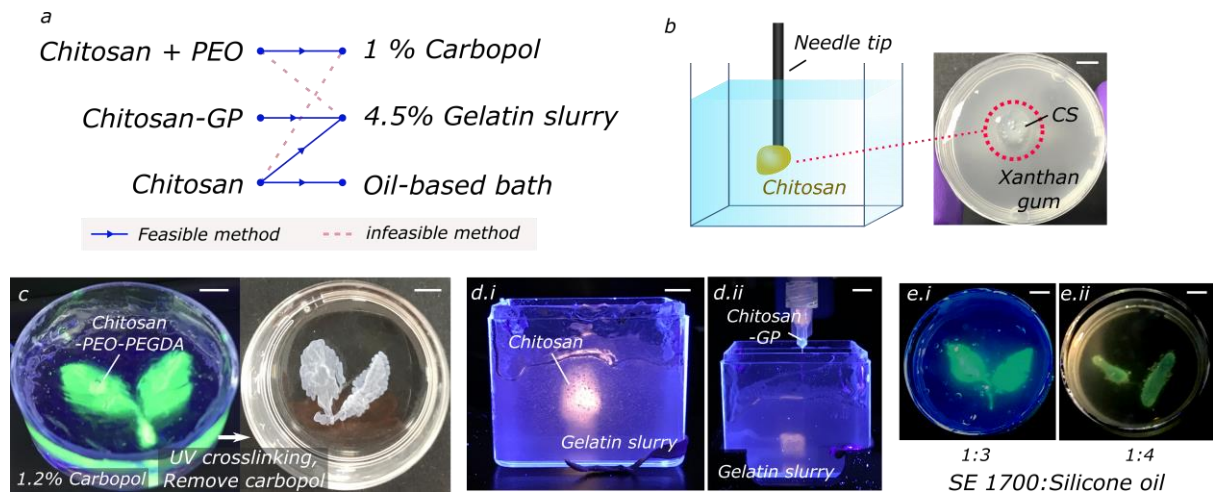


**Figure 4.11| Printing of chitosan.** **a)** The tested feasible and infeasible methods for embedded printing chitosan. PEO = polyethylene oxide and GP = glycerol phosphate disodium salt. **b)** The cohesive problem when printing chitosan in an anionic bath. **c)** Printing of a photocrosslinkable chitosan-PEO ink in a Carbopol bath. **d)** Printing of i) chitosan and ii) chitosan-GP inks in a bath of gelatin slurry. **e)** Printing of a 13 w/v% 600 – 800 kDa chitosan ink in a SE 1700:silicone oil bath mixed at i) 1:3 and ii) 1:4 wt ratios. Scale bars = 5 mm.

## 7. Pluronic F127

Pluronic F127 is a well-established sacrificial material that exhibits outstanding printability, allowing layer-by-layer printing. As shown in **Figure 4.4c.i**, a tall construct (~ 10 mm) was printed without the use of any support bath and heating tool.

## 8. Polyacrylic acid (PAA)

Polyacrylic acid is renowned for its extensive swelling capacity at pH > ~4.5 (the pKa of the carboxyl groups of PAA) as the polymer chains are endowed with abundant carboxyl groups [41, 87]. The PAA ink tested here was mixed with PEDGA for obtaining a photo-crosslinkable ink. When designing support baths for PAA, pH is a key consideration because the swelling behaviour of the printed structure in the bath during printing and crosslinking drastically hampers its fidelity (**Figure 4.12a**). As depicted in **Figure 4.12**, when the ink was printed in a bath at pH ~5.8, a poorly defined structure was resulted, while remarkably improved fidelity was observed in a highly acidic bath. Nonetheless, the use of aqueous bath cannot completely

avoid the swelling behaviour of PAA. In addition, conventional support baths such as Carbopol and gelatin slurry are incompatible with harsh pH conditions as the viscosity of the baths are greatly weakened at these conditions. Although acidic xanthan gum allows embedded printing of PAA, the bath is difficult to be removed due to the lack of sol-gel transition property of xanthan gum and the diffusion of PEGDA from the printed ink through the bath might cause undesired crosslinking of xanthan gum around the printed construct.

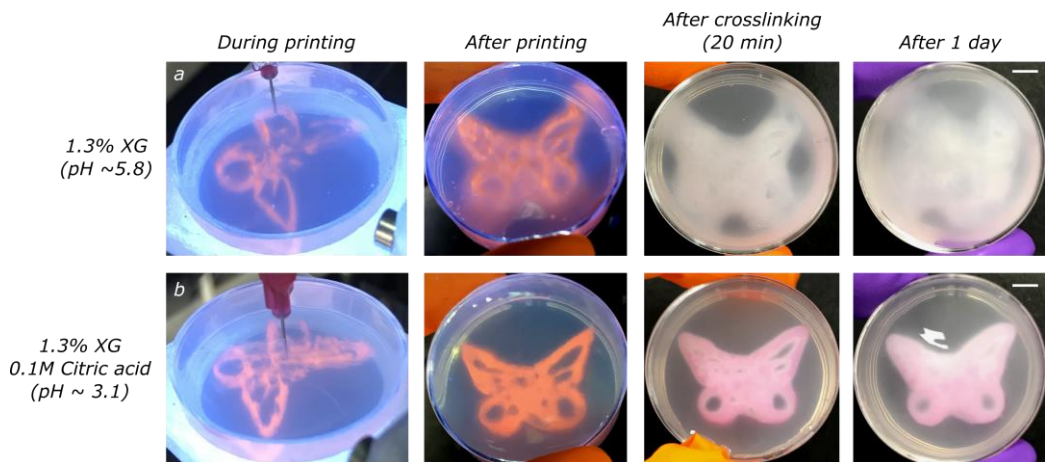


**Figure 4.12| The pH-swelling effect of poly(acrylic acid) during embedded printing in aqueous baths.** Printing of poly(acrylic acid) in a xanthan gum bath at **a)** pH 5.8 and **b)** pH 3.1. Scale bars = 5 mm.

To fully avoid the swelling problem, I examined the potential of oil-based support baths for fabricating PAA constructs because water is absent in oil-based media. As shown in **Figure 4.13a-b**, the ink was printable in both SE 1700-silicone oil bath and fumed silica-mineral oil bath. As expected, no undesired swelling effect was occurred. However, it was found that the printed shape can evolve over time due to the mismatch in interfacial tension of the bath and the ink, especially for features with high aspect ratio (**Figure 4.13c.i**). Therefore, I utilised a surfactant to reduce the interfacial tension (**Figure 4.13c**). Stearic acid, a long chain saturated fatty acid, was tested here because it is soluble in mineral oil. A 0 – 2 w/v% stearic acid was added to the fumed silica-mineral oil support baths, of which the viscosity at ambient temperature was slightly increased with the concentration of stearic acid added. Comparing the shapes of the constructs immediately after printing and after 50 min (**Figure 4.13c**), an addition of 1% stearic acid effectively preserved the shape of a PAA rectangular construct, hence this formulation (fumed silica-mineral oil bath with 1% stearic acid) is proposed for printing PAA. A higher concentration of stearic acid was not chosen here because this compromises the transparency of the bath (**Figure 4.13d**), which will hamper the photo-polymerisation efficacy

of the bath. After UV crosslinking, the construct can be easily harvested from the oil bath and was rinsed with soapy acidic water to remove any residual oil (**Figure 4.13e**).

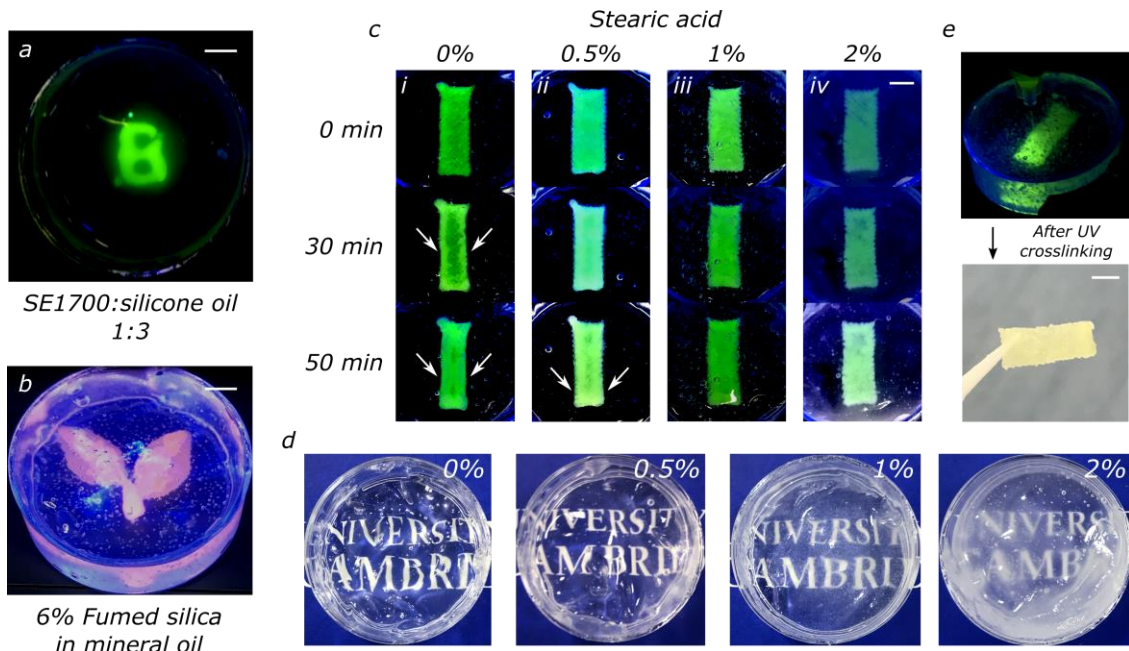


**Figure 4.13| Printing of poly(acrylic acid) (PAA) in oil-based support baths.** **a-b**) 3D printed PAA constructs with the use of **a)** SE 1700-silicone oil and **b)** fumed silica-mineral oil support baths. **c)** The effect of stearic acid on delaying the shape deformation of constructs in fumed silica-mineral oil support baths. The arrow indicates a visible change in the shape. **d)** Optical transparency of the fumed silica-mineral oil support baths supplemented with 0 – 2 w/v% stearic acid. **e)** A PAA construct collected after crosslinking and bath removal. Scale bars = 5 mm.

With the above established printable system, I further examined the use of PAA in creating anisotropic pH-responsive morphing systems. Although pH-responsive swelling of an unconstrained hydrogel is intrinsically isotropic [270], anisotropic swelling can be achieved by incorporating a structural stiffness inhomogeneity into the construct, which can be easily controlled by the print path. **Figure 4.14** shows the anisotropic pH-responsive swelling of PAA strips that were printed using different settings of fill angle. The infill filaments of the strips induce voids along the fill pattern, hence leading to anisotropic stiffness. Although the strips were only composed of two layers of materials, they were printed via embedded printing to avoid the non-flat edge feature that could be resulted in in-air printing and affect the swelling response. Using this strategy, different morphing shapes were produced, including roll, helix, twist and saddle. I hypothesise this morphing effect depends on both the fill angle and the bulk shape of the strip. Comparing **Figure 4.14c** and **Figure 4.14d**, different morphing shapes,

saddle and twist, were produced using the same degree of fill angle but different strip sizes. Interestingly, morphing to a roll structure with  $0^\circ$  infill seems to take place faster than morphing with  $90^\circ$  and  $45^\circ$  infills.

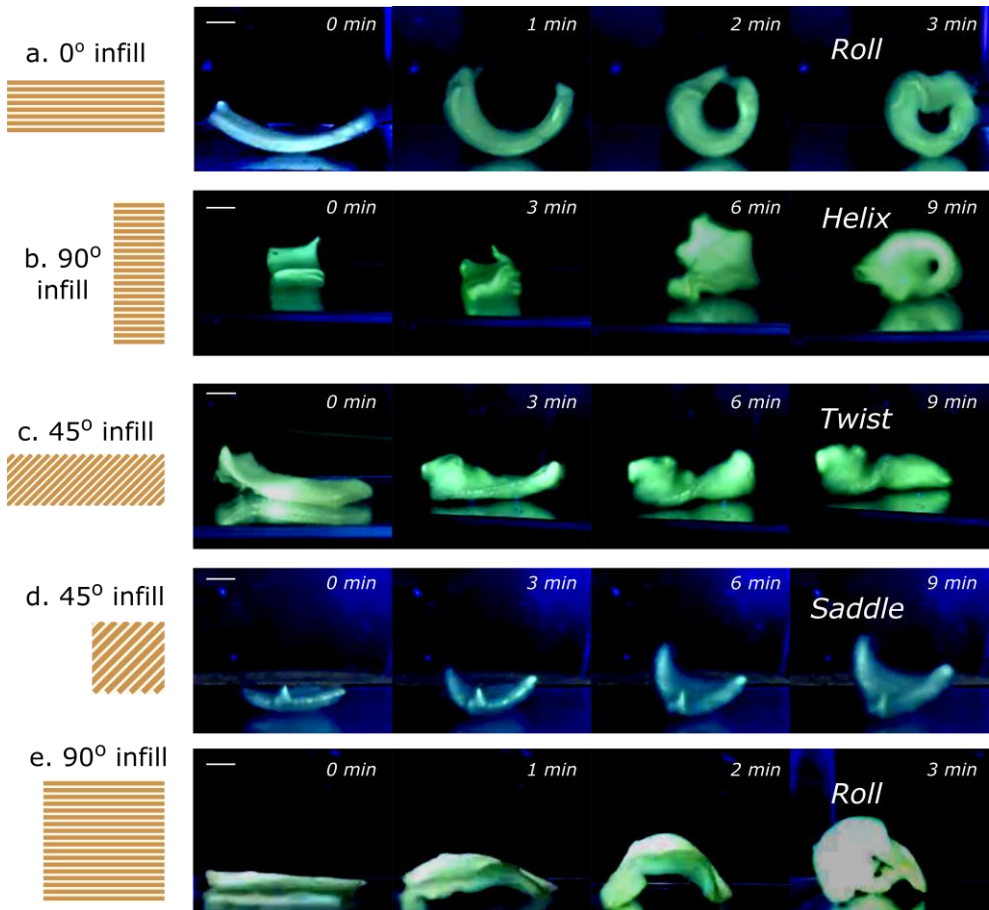


**Figure 4.14| Evolution of asymmetrical pH-responsive morphing of PAA strips printed at different infill angles.**

Another interesting behaviour of these pH-responsive morphing systems is that the morphing response underwent two stages over time – a transient stage and an unfolding stage. As shown in **Figure 4.15a**, beyond a critical time point, the excessive amount of water absorbed by the PAA hydrogel started to cause unfolding of the developed shape, eventually leading to an isotropic swollen gel. The results shown in **Figure 4.15a** also highlight the excellent water uptake capacity of PAA hydrogels. On another note, the pH-responsive morphing behaviour is reversible. As illustrated in **Figure 4.15b**, the developed shape can revert to its original shape by placing the morphed hydrogels in an acid.

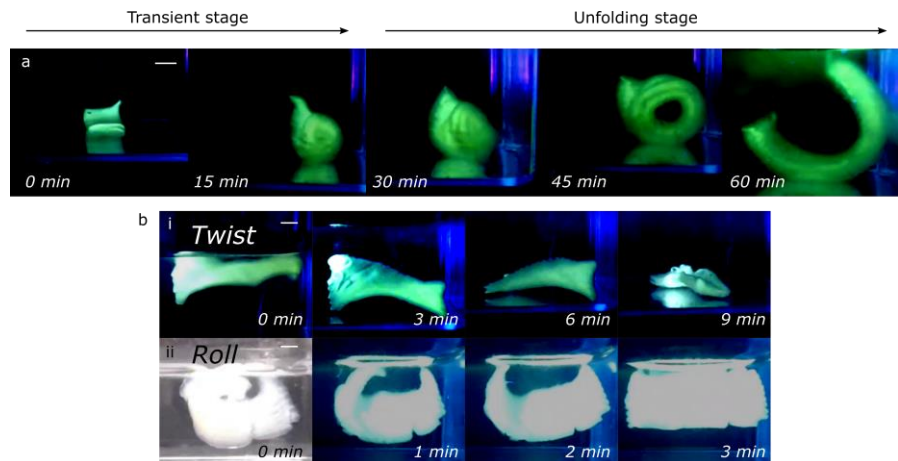


**Figure 4.15| a)** The transient and unfolding stages of a pH-responsive morphing system made of PAA. **b)** The reversible morphing behaviour achieved by placing the morphed hydrogel in a 1 M citric acid solution. The gels showed in (b) are i) the 45° strip showed in Figure 4.14c and ii) the 0° strip showed in Figure 4.14a. Scale bars = 3 mm.

#### 9. PEO

**Figure 4.4c.iv** shows letters made of PEO fabricated with the use of a xanthan gum support bath. PEO is a relatively stable polymer as carboxyl and amine groups are absent on its polymer backbone. Viscous PEO inks can be easily obtained using a high concentration and a high molecular weight of PEO. These properties enable less stringent requirements on the support bath properties for fabricating PEO constructs.

#### 10. PVA

When dissolving PVA granules in water, heating at high temperature is required. Solutions at this condition has poor printability because of the insufficient viscosity caused by the rupture of hydrogen bonds. Therefore, hot PVA solutions should be allowed to cool at room temperature for 1 day or at 4 °C for 1 hour prior to printing. This promotes the formation of hydrogen bonding such that the solution viscosity and thereby its printability can be enhanced (**Figure 4.4c.v**).

#### 11. SE 1700

SE 1700 is a silicone elastomer paste that contains fumed silica as a thixotropic and thickening agent in PDMS. The material has been used in fabrication of customised cell culture chambers [76, 98, 188] and soft actuation systems [174]. As shown in **Figure 4.4d.i**, owing to its good

printability, customised chambers were printed without the assist of any support bath or heating means.

### 12. Ecoflex

To fabricate constructs made of Ecoflex, a soft and stretchable elastomer, I utilised an oil-based support bath formulated from fumed silica and mineral oil (**Figure 4.16**). Aqueous baths were not chosen here in consideration of the interfacial tension between the bath and Ecoflex that might cause filament fusion issues. In addition, to avoid the expansion of fine bubbles inside the support bath that will affect the fidelity of the print, thermal curing method was not used here. The structure was cured at room temperature for 1 day.

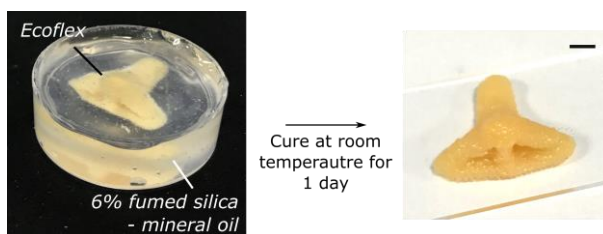


**Figure 4.16| Printing of Ecoflex.**

### 13. Summary

Below table (**Table 4.4**) summarises the methods I used for printing different materials. Detailed concentration of the solutions used can be referred to **Table 4.2**.

**Table 4.3| A summary of the adopted methods used for printing different soft materials.**

Materials	Support baths	Remark
Collagen	Gelatin slurry	-
Agarose, gellan gum, gelatin	Carbopol	Printhead heating.
Alginate, Alginate-bioceramics	Gelatin slurry	Further crosslink by CaCl <sub>2</sub> after printing.
Sodium hyaluronate-PEGDA	Carbopol	Avoid prolonged UV crosslinking time.
Sodium carboxymethylcellulose	-	Only a few layers can be printed in-air.
Methyl cellulose	-	Stage heating; Only a few layers can be printed in-air.
Methacrylate hydroxypropyl cellulose	-	<i>In situ</i> UV crosslinking.
Chitosan	Oil-based bath	-
Pluronic F127	-	Good printability.
Polyacrylic acid	Oil-based bath	-
PEO	Xanthan gum	-
PVA	Xanthan gum	Cool the ink before printing.
SE 1700	-	Good printability.
Ecoflex	Fumed silica-mineral oil	Cure at room temperature.

#### 4.3.4 A guide to the selection of printing approach

**Figure 4.17** presents a decision flowchart guiding the procedure for selecting a suitable printing approach. First, the ink formulation should encompass two parts - viscous components for printability and sol-gel species that can crosslink into shaped gels for preserving the intended shapes upon deposition (Step 1). The required ink viscosity depends on the printing process. In-air printing demands for a more stringent requirements on the ink viscosity, while embedded printing is well-suited for fabricating less printable inks and overhanging features (Step 2). The viscosity of the inks can be enhanced by the use of thickeners, such as sodium hyaluronate and xanthan gum that are viscous at low concentration and have excellent shear thinning properties. When highly viscous solutions (i.e. SE 1700) are used in in-air printing, tapered tips are recommended for ease of flow, hence preventing the tips from clogging (Step 3.1). On the selection of support baths for embedded printing (Step 3.2), I suggest utilising

- Oil-based baths for resin-based inks and pH-sensitive hydrogels,
- Gelatin slurry baths for hydrogels that require ionic or pH crosslinking, and
- Carbopol baths for thermal- or photo-crosslinkable hydrogels.

This is because oil-based baths mitigate the interfacial tension issue when printing resin-based inks and they can avoid swelling of pH-sensitive hydrogels. Surfactants can be added to the oil-based baths to alleviate the shape evolution of the printed object caused by the interfacial tension between the hydrogel ink and the oil bath. On the other hand, Carbopol gels offer excellent transparency and thermal stability, making it well-compatible with thermal- and photo-crosslinking mechanisms. Comparing with Carbopol, gelatin slurry is less sensitive to ionic and pH changes, hence it is recommended for hydrogels that require ionic and pH crosslinking. Lastly, depending on the thermal gelation and photo-polymerisation properties of the inks, the printing process can be assisted by *in situ* heating or/and UV tools for enhancing the print fidelity (Step 4).

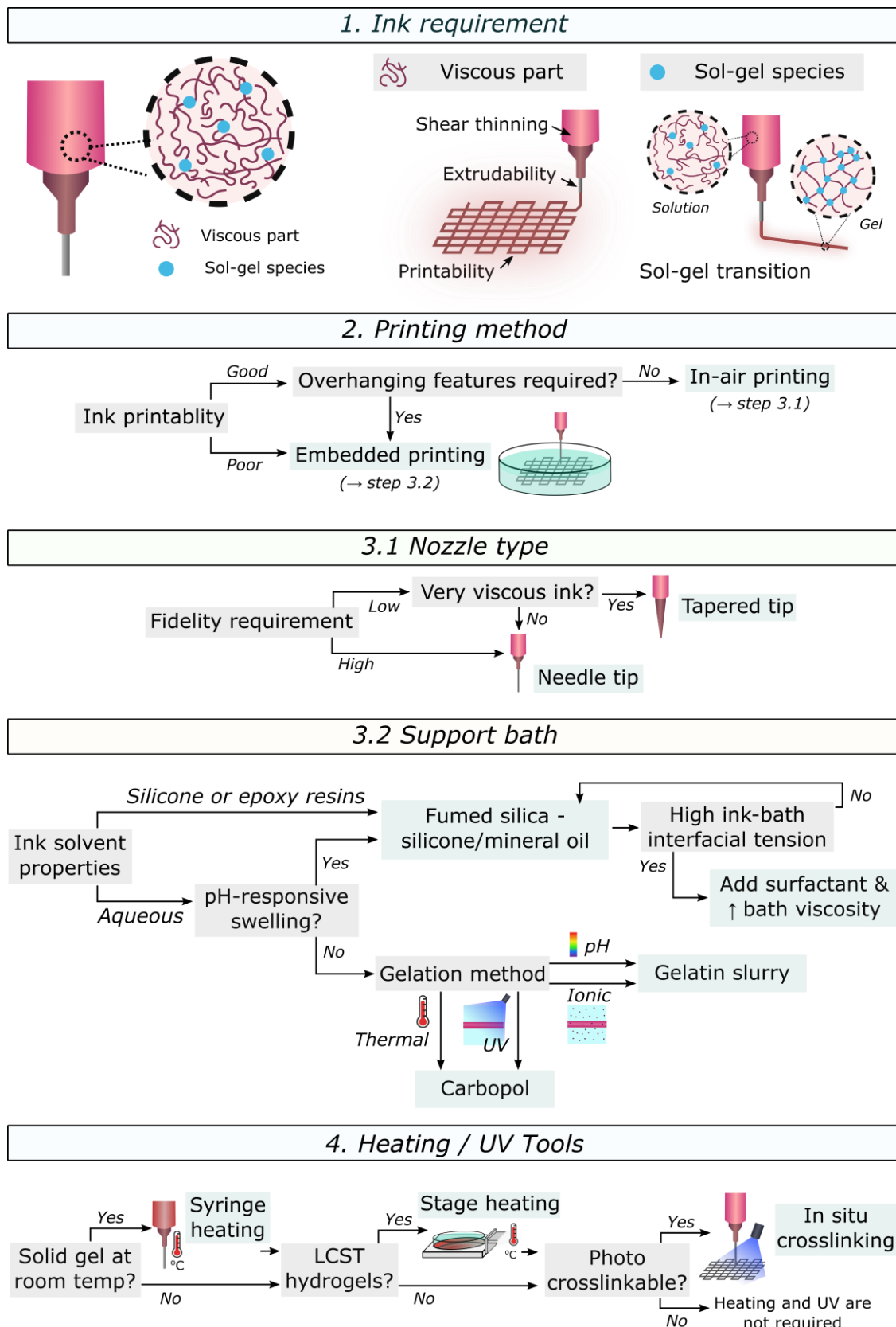


Figure 4.17| Decision flowchart guiding the selection of a suitable printing approach.

## 4.4 Conclusions

This chapter first demonstrates the versatile potential of the extrusion-based printing platform I developed in **Chapter 3**. The platform can freely accept unconventional geometry inputs, including coordinates, equations and pictures, beyond the standard CAD model input used in 3D printing. A broad range of unconventional operations was showed, such as creation of sacrificial templates, automated cell suspension dispensing, printing heterogeneous constructs, printing with variable speed and non-planar printing. In addition, by utilising a suitable support bath and the auxiliary tools offered by the platform, a wide range of hydrogels and silicone elastomers, including materials with poor printability, was successfully printed. This platform has been reproduced by my colleague, Yaqi Sheng. The satisfactory performance of the setup demonstrated here suggests the possibility of using custom-made printers as affordable alternatives to commercial 3D printers for soft material fabrication.

Through providing the rationale for the printing strategies I employed for fabricating a wide variety of materials, this chapter proposes a conceptual guideline on the selection of appropriate printing approaches for different soft materials. This information will be particularly useful for new users who are unfamiliar with the properties of different inks and supportive baths, helping them efficiently design a printing strategy for their needs and saving the trial-and-error effort. Taken together, the finding reported in this chapter might facilitate the wide adoption of the extrusion based printing technology, paving the way for innovative fabrication strategies for different biomedical applications, such as tissue engineering, flexible electronics and soft robotics.

## Chapter 5

# 3D Printed Biomimetic Cochleae and Machine Learning Co-modelling Provides Clinical Informatics for Cochlear Implant Patients

*This chapter utilises excerpts of a research paper written by the Author and published in Nature Communications [271].*

### 5.1 Introduction

The use of neuromodulation implants and bioelectronic devices has been increasing rapidly, and is anticipated to form a new era of medicine [272, 273]. By delivering local electrical stimuli to tissues, these electronic implants restore lost neural functions in tissues or nerves, or modulate signalling patterns for therapeutic outcomes [273, 274]. Electrical cochlear implants (CIs) are by far the most widely used neuromodulation electronic implants, with well over 500,000 CIs having been implanted worldwide [275], and their prevalence is only expected to grow more rapidly with the projected increase in the elderly population [272, 275]. Bypassing the malfunctioning peripheral auditory mechanisms by direct neural stimulation, the CI electrode array is designed to restore sound perception (see **Box 5.1** for further background about CIs). It also attempts, in broad terms, to reproduce the tonotopic architecture of the cochlea by delivering frequency specific programmed stimulation at localised regions of the cochlear lumen; this in turn stimulates separate auditory neural elements [276, 277] (**Figure 5.1**), with lower sound frequencies represented apically and higher frequencies basally.

A major limitation of today's neural prostheses is their imprecise control of the administered stimulus, arising from the intrinsic conductive nature of biological tissues [278, 279], and particularly of the biological fluids in the inner ear [276, 280]. This limitation is well exemplified by the 'current spread' problem of CIs, where the uncontrolled spread of electrical

stimulus leads to off-target excitation of the neighbouring auditory nerve fibres (thus causing a mismatch or ‘smeared’ representation in the perceived sound from that intended) [280] (**Figure 5.1**). Cochlear anatomy, tissue conductivity, and implant positioning are suggested to be the primary patient-specific factors controlling the intracochlear voltage distribution induced by CIs [280–283]. In particular, cochlear anatomy (in terms of size and shape) is variable [284], with different levels of volumetric conductance of cochlear fluids affecting the intracochlear voltage induced by stimulation. Moreover, pathophysiological conditions could affect electrical conductivity of the cochlear bony walls, and thus CI induced electric fields [285]. As the cochlea is embedded deep inside the temporal bone and has a complex anatomy, its electrical characteristics are difficult to quantify in a living subject. As a result, a model that deciphers how different characteristics of a patient’s cochlea affect the stimulus spread would be a valuable tool for predicting and optimizing the stimulus signals, and provide insights into factors controlling the large variation in patient-specific CI performance and sound perception.

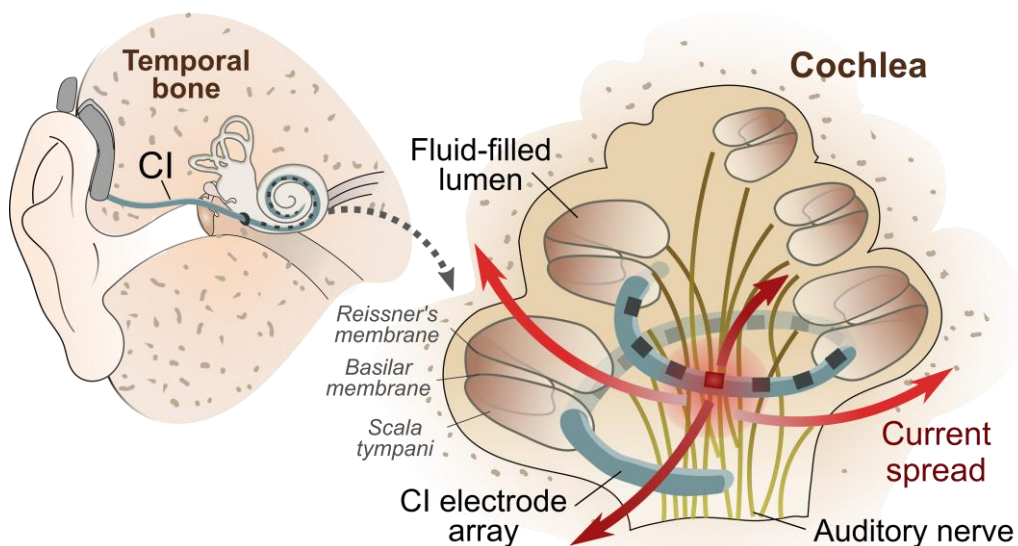


**Figure 5.1| Schematic of the auditory system and the cochlea with a CI implanted.** The ‘current spread’ problem induced by a stimulated electrode of the CI electrode array is indicated.

Although various physical and computational models have been developed for CI testing [280, 283, 286–288], they are insufficient to evaluate the stimulus spread in human cochleae. Animal models are well-established for *in vivo* CI testing, but due to the drastic differences between the cochlear anatomies of humans and animals [289], incomplete insights into human responses are obtained [272, 274]. Though human cadavers can provide anatomical

fidelity, they are limited in supply and have altered electrical properties due to preservation and post-mortem changes [290]. *In silico* approaches, such as finite element modelling (FEM), can overcome ethical, sample availability and cost issues [291]. However, existing FEM modelling is limited by several factors, including scant knowledge of the electrical properties of live human cochlear tissues to fit different *in vivo* cases [292], the inability to capture patient-dependent anatomically-guided CI positioning, and the underdetermined boundary conditions and physical/empirical law descriptions [286] (discussed in **Section 5.3.10**).

To establish a robust modelling framework for interpreting clinical CI testing data, here I created a library of 3D printed cochlear models ( $n = 82$ ). These biomimetic cochleae capture the diverse geometries that human cochlear lumens can take, along with a spectrum of bone tissue resistivities, using ranges reported in *in vivo* human studies. Using these models, a broad spectrum of clinically representative electric field imaging (EFI) profiles (normalised intracochlear voltage distribution along the CI electrode array) was acquired by varying the electro-anatomical characteristics of the models. Then, by inputting EFI profiles acquired from the biomimetic cochleae as the training dataset, a neural network machine learning model termed 3PNN (3D printing and neural network co-modelling, overview shown in **Figure 5.2**) was established, which provides powerful clinical informatics such as deciphering patient-specific attributes of CI current spread, and inferring patient-dependent cochlear tissue resistivity.

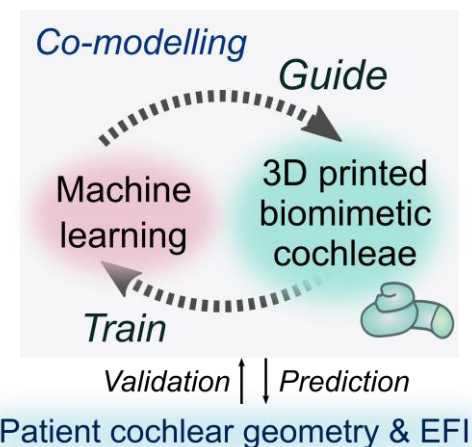


**Figure 5.2|** Overview of the 3PNN co-modelling framework for providing clinical informatics.

### Box 5.1 - Background of cochlear implants

In healthy auditory systems (**Figure 5.3a**), cochleae transduce the mechanical vibration of the cochlear fluid caused by sound into neural signals by means of the auditory hair cells located on the basilar membrane. When these hair cells are damaged or absent due to genetic diseases, severe to profound hearing loss can be resulted. Unlike hearing aids which amplify sound, cochlear implants are surgically implanted neuroprostheses that bypass the damaged hair cells and directly stimulate the auditory nerve using electrical impulse to partially restore hearing in patients who have severe to profound hearing loss.

The device consists of external and internal parts. The external part converts sounds into electrical stimulation codes; The internal part connects to the external part via a magnet and has a surgically implanted electrode array composed of 12 to 22 electrodes [276] (**Figure 5.3b**). The electrode array design is intended to restore the tonotopic organisation of human cochleae (**Figure 5.3c**), where high-frequency sounds are processed at the cochlear apex and low-frequency sounds are processed at the cochlear base [339]. According to the received sound frequency, a specific electrode is activated to electrically stimulate a portion of the auditory nerve, in attempts to restore the auditory perception [339] (**Figure 5.1**).

‘Electric field imaging’ (also known as transimpedance matrix or impedance field telemetry) are clinical measurements acquired by the implanted electrode array via CI telemetry for monitoring the functioning of the implanted electrodes [340]. The measurements sample the intracochlear voltage distribution along the implanted electrode array of the cochlear implant, hence providing insights on the flow of the current-induced voltage in individual patients [340, 341].

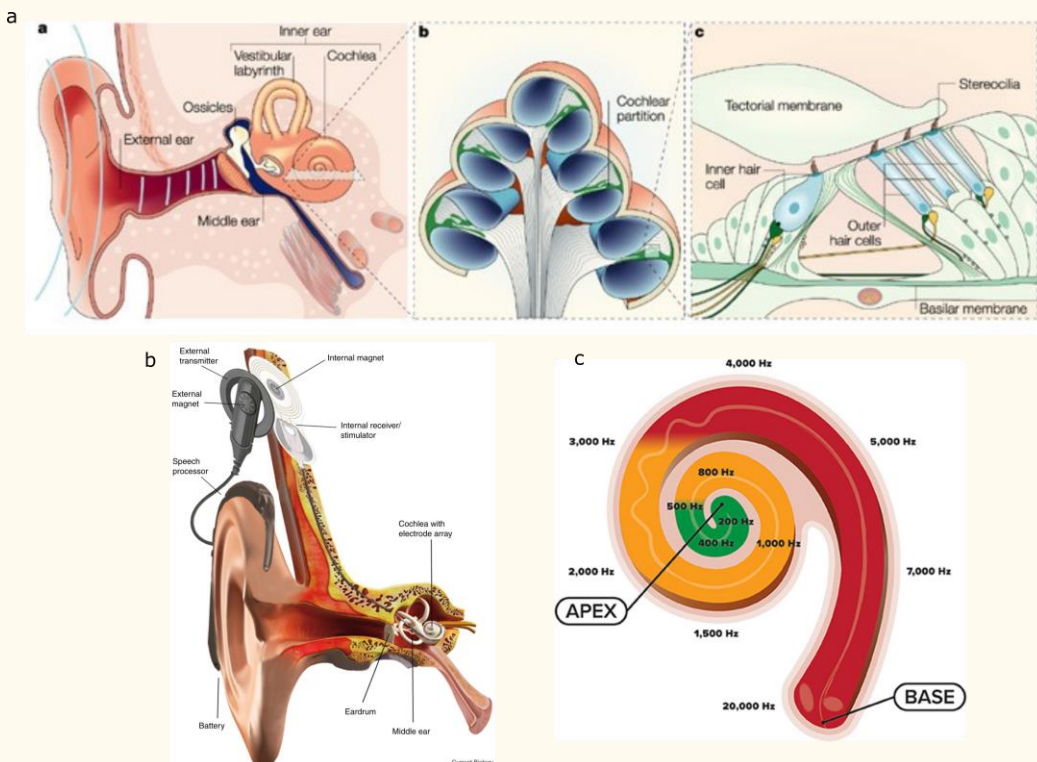


**Figure 5.3|** a) Sound transduction process in healthy auditory systems, where sound vibrations are transduced into nerve impulses by the hair cells in cochleae. b) Sketch of a cochlear implant showing the external and internal parts of the device. c) The tonotopic organisation of human cochleae. Reproduced from [276, 342, 343].

## 5.2 Materials and Methods

### 5.2.1 3D printing material preparation

The fugitive ink was prepared by dissolving 30 w/v% Pluronic F127 (P2443, Sigma-Aldrich) in a 1 w/v% NaCl (10616082, Fisher Scientific) solution. For creating 3D printed models made of PDMS or electro-mimetic bone matrices, PDMS elastomer (Sylgard<sup>TM</sup> 184 Dow, 10:1 base polymer to curing agent ratio) was used. The pre-crosslinked mixture was poured in a petri dish, and degassed in a vacuum desiccator for at least 3 hours prior to printing. For preparing 3D printed models made of hydrogels, hydrogels were prepared with 1 w/v% NaCl solution as the base solution according to their weight/volume concentration (w/v%) listed in **Figure 5.13**. The types of hydrogels investigated were gelatin from porcine skin (G1890, Sigma-Aldrich), xanthan gum (G1253, Sigma-Aldrich), agarose (A9539, Sigma-Aldrich), gellan gum (P8169, Sigma-Aldrich); the types of fillers were talc (243604, Sigma-Aldrich), hydroxyapatite (21223, Sigma-Aldrich) and PDMS microbeads.

### 5.2.2 Embedded 3D printing of biomimetic cochleae

All models were fabricated using the robotic printer developed in **Chapter 3**. Five model descriptors (basal lumen diameter, taper ratio, cochlear width, cochlear height, and matrix resistivity) were used to define the model features. Definition of the model descriptors can be found in **Table 5.4**. Prior to the fabrication process, the structure of the microchannels in the PDMS matrix was designed on Slic3R (version 1.3.0, <https://slic3r.org/>) by varying the fill density setting for tuning the void fraction,  $f_{void}$ , in the electro-mimetic bone matrix (**Figure 5.3a**), and therefore the resistivity of the electro-mimetic bon matrices.  $f_{void}$  was estimated using the following equation  $f_{void} = (A_{channel} \times d_{printing\ path}) / V_{matrix}$ , where  $A_{channel}$  = average cross-sectional area of the microchannel derived from the mean diameter of the microchannels (**Figure 5.3b**),  $d_{printing\ path}$  = total distance of the printing path and  $V_{matrix}$  = total volume of the matrix. The printing path of the microchannel structure was then converted to G-code using Slic3R.

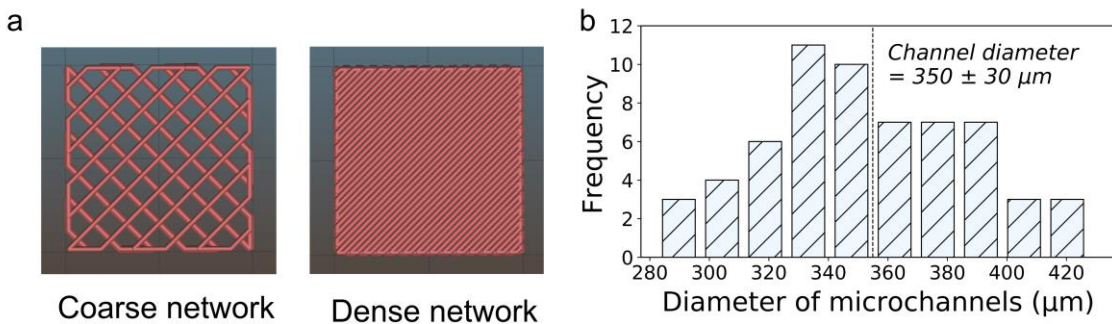


**Figure 5.4| Microchannel network of the electro-mimetic bone matrix.** **a)** Examples of a coarse network and a dense network designed on Slic3R by varying the fill density setting. **b)** A histogram of the diameter of the microchannels in the electro-mimetic bone matrices, measured from the microscopic images of the matrices ( $n = 61$  measured over 7 independent samples fabricated with different densities of microchannels).

In the fabrication process, first, the sacrificial interconnected grid network designed above was embedded printed inside uncured PDMS using a 30 w/v% Pluronic F127 ink. At ambient temperature, Pluronic F127 ink at 30 w/v% (dissolved in 1 w/v% NaCl) retains its 3D structural integrity inside the PDMS matrix, and the interconnected network provides sufficient mechanical support for the following embedded printing of a cochlea-shaped structure. Next, a cochlea-shaped spiral was printed inside the electro-mimetic bone matrix. The printing path of this cochlea-shaped structure was defined by the four geometric descriptors and a spiral trajectory derived from the mathematical model of human cochlear geometry developed by Pietsch et al. [293]. The correlation between the dimensions of the features and the process parameters of the printer can be found in **Figure 5.4**. The basal lumen diameter of the 3D printed cochlea was controlled by the extrusion parameter of the printer (that is the  $t_s$ , time between consecutive steps of the stepper motor), while the taper ratio was controlled by the speed ratio (the ratio of the speed of the stage when printing the apex of the cochlear lumen to the speed of the stage when printing the base). The width and the height of the printed cochlear lumen were governed by the width and the height scaling ratios of the mathematical model of human cochleae [293]. The distances between the edges of the model and the printed cochlear lumen were at least 4 mm to ensure that the boundary was far enough and will not cause any effect on the EPI measurement. The total printing time of a model ranges from 30 min to 3 hrs depending on the density of the embedded interconnected channels. After printing, the matrix was cured at 60 °C in an oven for 3 hrs and stored in a bath of 1 w/v% NaCl solution at 4 °C for dissolving the sacrificial Pluronic F127 embedded in the electro-mimetic bone matrix. The NaCl bath was changed several times to ensure that all Pluronic F127 inside the matrix was

removed. In total, 82 biomimetic cochlear models with different combinations of model descriptors were fabricated. The specifications of the 82 models can be found in **Table 5.1**. The linear biomimetic cochlear models were fabricated using the same method according to the electroanatomical features stated in **Figure 5.35b**.

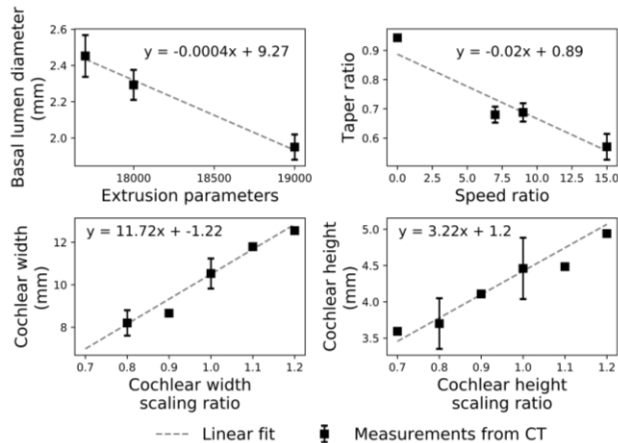


**Figure 5.5| Correlation of the actual dimensions of the model descriptors measured from  $\mu$ -CT and the process parameters of the custom-built 3D printer.**  $n = 1 - 25$  measurements examined over 31 samples. Data are presented as mean values  $\pm$  SD.

The hydrogel and hydrogel-filters models were similarly fabricated but without the procedure of creating the microchannel networks. The composition of the models tested in this study can be found in **Figure 5.13**. The hydrogel and hydrogel-filters solutions were heated at 40 °C during printing to maintain a liquid state. The models were then solidified at room temperature via thermal crosslinking [294]. The appearances of the models are showed in **Figure 5.5**.

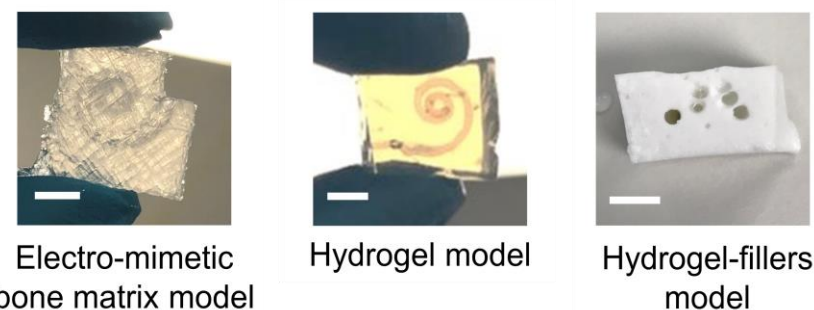


**Figure 5.6| Appearance of 3D printed cochlear models made of an electro-mimetic bone matrix, a hydrogel, and a hydrogel-filters matrix.** The translucent appearance of our electro-mimetic bone matrix model may help direct visualisation of the insertion depth of the CI electrode array inside its cochlear lumen, in contrast to the opaque appearance associated with a hydrogel-filters model. Scale bar = 5 mm.

**Table 5.1| Specifications of the 82 biomimetic cochleae used in 3PNN training.**

ID	BL <sub>d</sub> (mm)	Infill density	T <sub>ra</sub>	W <sub>c</sub> (mm)	h <sub>c</sub> (mm)	ID	BL <sub>d</sub> (mm)	Infill density	T <sub>ra</sub>	W <sub>c</sub> (mm)	h <sub>c</sub> (mm)		
1	101315	2.38	40	0.58	10.53	4.38	42	181313	2.38	80	0.79	10.53	4.38
2	103611	2.38	40	0.70	10.53	4.38	43	182435	2.5	100	0.58	10.53	4.38
3	111858	2.38	20	0.89	10.53	4.38	44	182512	2.38	60	0.70	10.53	3.81
4	113438	2.38	60	0.75	10.53	3.53	45	182642	2.38	80	0.70	10.53	4.38
5	114233	2.38	20	0.79	10.53	4.38	46	183027	2.5	80	0.89	10.53	4.38
6	115419	2.38	20	0.75	10.53	4.38	47	184306	2.38	100	0.70	10.53	4.38
7	132606	2.5	80	0.79	10.53	4.38	48	184732	2.38	60	0.79	10.53	4.66
8	134101	2.5	80	0.70	10.53	4.38	49	185300	2.38	80	0.58	10.53	4.38
9	141658	1.98	20	0.89	10.53	4.38	50	190432	2.38	60	0.79	12.66	4.38
10	144838	2.38	20	0.89	12.66	4.38	51	190741	2.5	80	0.58	12.66	4.38
11	151206	2.38	20	0.89	10.53	4.95	52	190950	2.5	20	0.75	10.53	4.38
12	154018	2.38	20	0.89	10.53	3.53	53	191703	1.98	100	0.89	10.53	4.38
13	154044	2.5	60	0.89	10.53	4.38	54	191812	2.5	80	0.58	10.53	4.95
14	155132	2.38	60	0.79	10.53	4.38	55	192713	1.98	80	0.75	10.53	4.38
15	155320	1.98	80	0.79	10.53	4.38	56	192815	1.98	20	0.75	10.53	4.38
16	155745	2.38	60	0.79	8.4	4.38	57	193039	2.5	100	0.79	10.53	4.38
17	160132	2.5	60	0.79	10.53	4.38	58	194304	2.5	20	0.79	10.53	4.38
18	160340	1.98	40	0.89	10.53	4.38	59	194958	2.38	100	0.58	10.53	4.38
19	160727	2.5	40	0.58	10.53	4.38	60	195345	2.5	100	0.89	10.53	4.38
20	161812	2.38	40	0.75	10.53	4.38	61	201816	2.38	80	0.79	8.4	4.38
21	162224	2.38	60	0.75	10.53	4.38	62	201817	2.5	60	0.70	10.53	4.38
22	162924	1.98	40	0.79	10.53	4.38	63	202412	1.98	60	0.89	10.53	4.38
23	163834	1.98	100	0.79	10.53	4.38	64	202511	2.38	80	0.79	9.46	4.38
24	164032	2.5	40	0.89	10.53	4.38	65	202935	2.38	60	0.79	10.53	4.95
25	164808	2.38	80	0.79	10.53	3.81	66	203048	2.5	20	0.58	10.53	4.38
26	165017	2.5	60	0.75	10.53	4.38	67	204543	2.38	20	0.58	10.53	4.38
27	165303	2.38	20	0.79	10.53	4.95	68	204710	2.38	40	0.79	11.59	4.38
28	170130	2.5	20	0.89	10.53	4.38	69	204849	2.5	100	0.70	10.53	4.38
29	170529	2.38	80	0.58	9.46	4.38	70	210029	2.38	60	0.70	11.59	4.38
30	170641	2.5	40	0.79	10.53	4.38	71	210113	1.98	40	0.75	10.53	4.38
31	171752	1.98	60	0.79	10.53	4.38	72	211311	2.38	100	0.75	10.53	4.38
32	171916	1.98	20	0.79	10.53	4.38	73	212720	2.38	80	0.70	12.66	4.38
33	172217	2.5	40	0.70	10.53	4.38	74	213253	2.38	80	0.79	10.53	4.95
34	172338	2.38	60	0.58	10.53	4.38	75	214126	2.38	60	0.79	10.53	3.81
35	173932	2.38	40	0.89	10.53	4.38	76	215112	2.5	60	0.58	10.53	4.95
36	174214	2.38	80	0.75	10.53	4.38	77	220834	1.98	60	0.70	10.53	4.38
37	174631	2.5	80	0.58	10.53	4.38	78	221747	2.38	60	0.70	10.53	4.38
38	174812	2.5	60	0.58	10.53	4.38	79	221826	1.98	100	0.75	10.53	4.38
39	175842	2.38	40	0.79	10.53	4.38	80	223926	2.38	100	0.79	10.53	4.38
40	175858	2.38	80	0.89	10.53	4.38	81	225051	1.98	40	0.70	10.53	4.38
41	175925	2.5	100	0.75	10.53	4.38	82	233930	1.98	60	0.75	10.53	4.38

### 5.2.3 EFI measurements in 3D printed biomimetic cochleae

Prior to measurement, the 3D printed biomimetic cochleae were flushed with a 1 w/v% NaCl solution to ensure no bubble trapped in the microchannels and the cochlear lumen of the models. 1 w/v% NaCl solution was used here as it has a similar resistivity to the cerebrospinal fluid, which has similar ionic composition to the conductive perilymph inside human cochleae [295] (**Figure 5.6**).

All EFI (or transimpedance matrix) measurements of the 3D printed models were obtained using either an Advanced Bionics (AB) HiRes 90K® implant with HiFocus™ 1J electrode array (CI<sup>1J</sup>), an Advanced Bionics HiRes™ Ultra implant with HiFocus™ SlimJ electrode array (CI<sup>SlimJ</sup>) or a Cochlear™ Nucleus® Profile with slim straight electrode (CI522). Both CI<sup>1J</sup> and CI<sup>SlimJ</sup> have 16 electrodes in total with electrode 1 being the apical-most electrode and electrode 16 being the basal-most electrode. CI522 has 22 electrodes in total with electrode 22 being the apical-most electrode and electrode 1 being the basal-most electrode. The electrode array was inserted in the cochlear lumen of the model until the distal marker of the electrode array was positioned at the lumen opening of the model, as illustrated in **Figure 5.6b**, and the model was placed on top of the extracochlear case ground of the CI (known as the ‘case ground’ of CI<sup>1J</sup> and CI<sup>SlimJ</sup>, or the ‘MP2 plate extracochlear electrode’ of CI522). The EFI profiles were acquired using the telemetry function of the CI with either the AB Volta version 1.1.1 software (research only) or Custom Sound® EP 5.1 (with research option) using the default stimulation and recording settings. The default stimulation and recording setting used in AB Volta software is a biphasic pulse with pulse width and amplitude of 36 µs (equivalent Fourier fundamental frequency ~14 kHz) and 32 µA, and a maximum sampling rate of 56 kHz, whereas Custom Sound® EP 5.1 employs a setting of a biphasic pulse with pulse width and amplitude of 25 µs (equivalent Fourier fundamental frequency ~20 kHz) and 125 µA respectively. During the acquisition of EFI, each electrode was activated individually at a time in monopolar mode, and subsequently other electrodes measured the resulting voltage at their positions. All electrodes on the electrode array were activated one-by-one to generate the entire EFI profile. Electrodes 12 and 16 of the CI<sup>1J</sup> electrode array were missing as received, but this does not affect the measurements of other electrodes and the general shape of the EFI profile. For all the data presentations, the on-stimulation EFI data (contact impedance) were not compared, due to the fact that on-stimulation EFI data is dominated by the electrode interface resistance [280, 296] and do not inherently reflect the electroanatomical characteristics of

human cochleae (or the 3D printed biomimetic cochleae); and on-stimulation EFI data varies over time [297] and among different CIs.

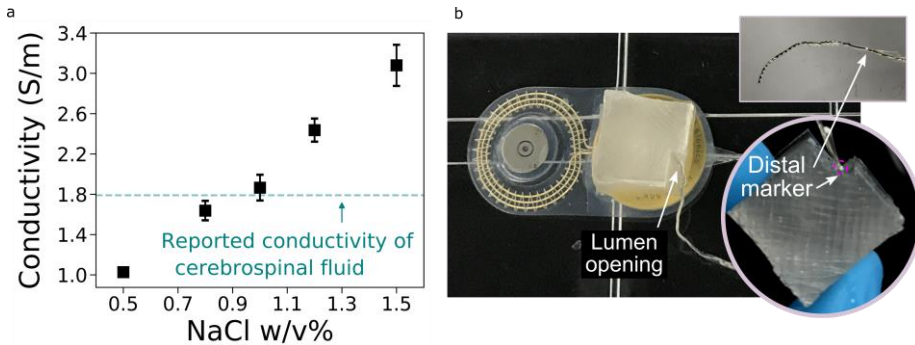


**Figure 5.7| a)** Electrical conductivity of NaCl solutions at various concentrations at ambient temperature ( $n = 4$  independent samples). Data are presented as mean values  $\pm$  SD. **b)** Photo demonstrating the insertion of a CI electrode array in a biomimetic cochlea during EFI measurements.

### 5.2.4 Resistivity measurements

#### *Resistivities of NaCl solutions, hydrogels and hydrogel-filters matrices*

Impedance properties of NaCl solutions at various concentrations (**Figure 5.6a**), hydrogel and hydrogel-filters matrices (**Figure 5.13**) were measured using a four-terminal configuration with Solartron 1260 impedance analyser and SMaRT 3.0.1 software. In this configuration, the current was passed through the sample using two  $1.25 \text{ cm}^2$  square electrode plates, and the voltage was measured using two separate inner electrodes. Resistivity was converted from the plateau impedance magnitude using the following relation,

$$\rho = |z| \frac{A}{d} \quad (5.1)$$

where  $\rho$  = the resistivity of the sample (plateau value),  $|z|$  = the plateau impedance magnitude,  $A$  = the area of the electrode plate in contact with the sample, and  $d$  = the spacing between the two inner electrodes, which was  $8.4 \text{ mm}$  here.

#### *Resistivities of electro-mimetic bone matrices*

The resistivity of the electro-mimetic bone matrix  $\rho_{matrix}$  associated with the plateau impedance magnitude ( $\sim 300 \text{ Hz} - 100 \text{ kHz}$ ) was determined using transmission line method ( $n \geq 3$ ). In this method, each sample was segmented into at least 4 segments. Impedance of each segment was obtained using a two-terminal configuration with Solartron analyser, and the width of each

segment was measured. The total impedance  $Z_{tot}$  can be expressed by  $Z_{tot} = Z_c + Z_{sample}$ , where  $Z_c$  is the contact impedance between the electrode plates and the samples, and  $Z_{sample}$  is the impedance of the sample. The plateau value of the total impedance magnitudes  $|Z_{tot}|$  of the segments were therefore plotted against the widths of the segments  $L$ , and a linear regression was then used to fit the experimental data.  $\rho_{matrix}$  was determined by multiplying the gradient of the linear regression  $\frac{\partial|Z_{tot}|}{\partial L}$  with the area of the electrode plate in contact with the sample  $A$ , denoted as follows:

$$\rho_{matrix} = A \frac{\partial|Z_{tot}|}{\partial L} \quad (5.2)$$

### 5.2.5 Electrochemical impedance spectroscopy (EIS) measurements

*The EIS measurements were collected by my collaborator, Chen Jiang, from the Department of Engineering.*

Electrochemical impedance spectroscopy measurements of a human cadaveric cochlea in a head, and 3D printed cochlear models made of hydrogel and electro-mimetic bone matrix were carried out using an impedance analyser (RS PRO LCR-6100) with a three-terminal configuration [298]. The measurements were taken at frequencies ranging from 10 Hz to 100 kHz, which covers the most common operating frequencies of CIs.

### 5.2.6 Micro-computed tomography scans of the 3D printed biomimetic cochleae

CT scans of samples were acquired using a micro-CT microscope (ZEISS Xradia 510 Versa) with the following scanning parameters: Source filter LE2, tube voltage 80 kV, tube current 88 mA, exposure time 2 s, Bin 2, image taken 1024 and pixel size 17.8  $\mu\text{m}$ . The volume rendering of the samples was carried out using 3D Slicer (Version 4.10.2, [www.slicer.org/](http://www.slicer.org/) [299]). The dimensions of the samples were measured using the measurement tool in 3D Slicer.

To evaluate the positions of electrodes in the samples and to avoid the image distortion caused by the metallic artifacts from electrodes, pre- and post-insertion CT scans of the samples were acquired. CT volume of the cochlear lumen of the sample was rendered from the pre-insertion CT scan where there is no metallic artifact, whereas CT volume of the electrode array in the sample was rendered from the post-insertion CT scan. The two CT volumes were then aligned, and the relative position of each electrode from the centre of the cross-sectional plane

of the cochlear lumen was measured using ImageJ. The 2D images of the electrode array inside the cochlear lumen of the samples were acquired using the following parameters: tube voltage 80 kV, tube current 88 mA, exposure time 5 s, Bin 2 and pixel size 25.6  $\mu\text{m}$ .

### 5.2.7 Patient EFI profiles and CT scans

*The patient EFI profiles and CT scans were provided from my collaborators in Prof. Manohar Bance's research group.*

The use of anonymous patient EFI profiles with or without paired CT scans in the study was approved by the University of Cambridge Human Biology Research Ethics Committee (HBREC.2019.42) and the Cambridge Biomedical Research Centre (Ref: A095451). Informed consent from the human participants is not required for this study as the clinical data used here are retrospective and anonymous. In total, 128 clinical intra-operative EFIs (also known as transimpedance matrix profiles) were used in this study. Of the 128 profiles, 91 profiles (without paired CT scan data) were kindly provided by Advanced Bionics<sup>®</sup> and the rest were obtained from 37 anonymous patients (31 with paired CT scan data and 6 without paired CT data) who have undergone cochlear implantation at the Emmeline Centre for Hearing Implants in Cambridge, UK. As the implant types of the EFIs provided by Advanced Bionics<sup>®</sup> are not known, their insertion depths were assumed to be equal to the suggested insertion depth of HiFocus<sup>TM</sup> 1J electrode array. The 37 anonymous EFI profiles acquired in our centre were randomly chosen to represent the variation in the patient data without CT scans ( $n = 97$ ). Out of the 37 EFI profile data sourced from our centre, 6 profiles were acquired from the Advanced Bionics HiRes 90K<sup>®</sup> implant with HiFocus<sup>TM</sup> 1J electrode array, 17 profiles from the Advanced Bionics HiRes<sup>TM</sup> Ultra implant with HiFocus<sup>TM</sup> SlimJ electrode array, 6 profiles from the Cochlear<sup>TM</sup> Nucleus<sup>®</sup> Profile Plus with slim straight electrode CI622, and 8 profiles from the Cochlear<sup>TM</sup> Nucleus<sup>®</sup> Profile with slim straight electrode CI522. These EFI profiles were collected using the telemetry function of the CI with either the AB's Volta 1.1.1 software (research only) and the Custom Sound<sup>®</sup> EP 5.1 software (with TIM research option) using the default stimulation and recording settings.

Thirty-one CT scans of the patients (which had paired EFI) implanted via the round window approach with either a HiFocus<sup>TM</sup> SlimJ electrode array ( $n = 17$ ), a Cochlear<sup>TM</sup> Nucleus<sup>®</sup> CI622 electrode ( $n = 6$ ), or a Cochlear<sup>TM</sup> Nucleus<sup>®</sup> CI522 electrode ( $n = 8$ ) were used in the validation of 3PNN. They were obtained as part of the routine pre-operative assessment

at the Emmeline Centre for Hearing Implants, and were acquired in helical scan mode using Siemens scanners (Siemens Flash and Siemens Definition AS) with tube voltage of 120 kV and automatic tube current ranging from 139 to 214 mA. The images were reconstructed at a resolution of 0.4 x 0.4 x 0.4 mm using Siemens 80u bone reconstruction algorithm in axial plane.

### 5.2.8 Development of 3PNN

*The neural network model was developed by my collaborator, Chon Lok Lei. I performed the hyperparameter tuning and simulations. The codes of the model are available on Github (<https://doi.org/10.5281/zenodo.5353394> [271])*

#### **Forward-3PNN**

3PNN was developed by employing a multilayer perceptron (MLP), a class of feedforward artificial neural network (NN), to learn the mapping from the inputs (the 5 model descriptors of the biomimetic cochleae, the stimulus position and the recording position) to the outputs (EFI, also known as transimpedance matrix profiles). A MLP model is a fully connected network that consists of an input layer, hidden layers and an output layer of perceptrons (or nodes), and by varying the weight of how each of the nodes are connected, it approximates the complex relationship between the inputs and the output [300]. The activation function of the nodes was chosen to be the rectified linear unit (ReLU) function. Tensorflow [301] (version 2.1.0), an open-source Python library, was used to construct the MLP models. 3PNN was trained using backpropagation with the Adam stochastic optimization method [302]. Since 3PNN was developed based on the EFI profiles acquired by AB HiFocus<sup>TM</sup> 1J electrode array with electrodes at 2 – 18.5 mm along the cochlear lumen [303], the predictable positions of EFIs are 2 – ~18.5 mm along the cochlear lumen.

#### ***Hyperparameter tuning of the neural network model***

The performance of NN models depends on a good setting for hyperparameters, a grid search varying the number of hidden layers from 1 to 10 (1, 2, 3, 5, 10) and nodes from 16 to 64 (16, 24, 32, 64) was used to determine the best performing hyperparameters. For each combination of hyperparameters, a 10-fold cross-validation, a standard procedure for estimating the

performance of neural network models [304], was performed. In the 10-fold cross validation (**Figure 5.7a**), the dataset of 82 EFI profiles, associated with a variety of electroanatomical cochlear features, was randomly split into 10 subsets. One subset was used as an unseen subset (test subset) for prediction while the remaining subsets were used for training.

The best performing hyperparameters were defined as the hyperparameters that yield the highest average  $R^2$  score and the smallest average median absolute percentage error (MAPE) in 10-fold cross-validation [304]. The model trained with 1 hidden layer and 32 nodes was found to have the highest average  $R^2$  score (0.87) and a smallest MAPE (11.9%) (**Figure 5.7c**). Hence, this set of hyperparameters was selected for training the final NN model. After tuning the hyperparameters, 3PNN was retrained on the full dataset with the best performing hyperparameters to produce the final model.

### ***Inverse 3PNN***

Inverse prediction was carried out by the Approximate Bayesian Computation-Sequential Monte Carlo (ABC-SMC) algorithm [305]. ABC is a computational framework under Bayesian statistics that uses a sequence of intermediate threshold  $[\varepsilon_0 > \varepsilon_1 > \varepsilon_2 > \varepsilon_3 > \dots > \varepsilon_f]$  to converge towards the optimal approximate posterior distribution through a number of intermediate posterior distributions. Here, the algorithm infers the distribution of the model descriptors that leads to an EFI profile with a MAPE less than a predefined threshold ( $\varepsilon_f$ ) to the given EFI profile.  $\varepsilon_f$  was determined as the smallest MAPE the programme could reach from the previous threshold level within two hours when running the programme with a threshold sequence from 20% to 2% in increments of 0.5% (predictions with unknown geometric descriptors) or 0.1% (predictions with known geometric descriptors), which is subject to the noise level of the data. To approximate the final posterior distribution (which does not have a closed-form expression), for each inverse prediction, 1,000 samples of the posterior distribution of the model descriptors were plotted. PINTS [306], an open-source Python package, was used to perform the inference and sampling.

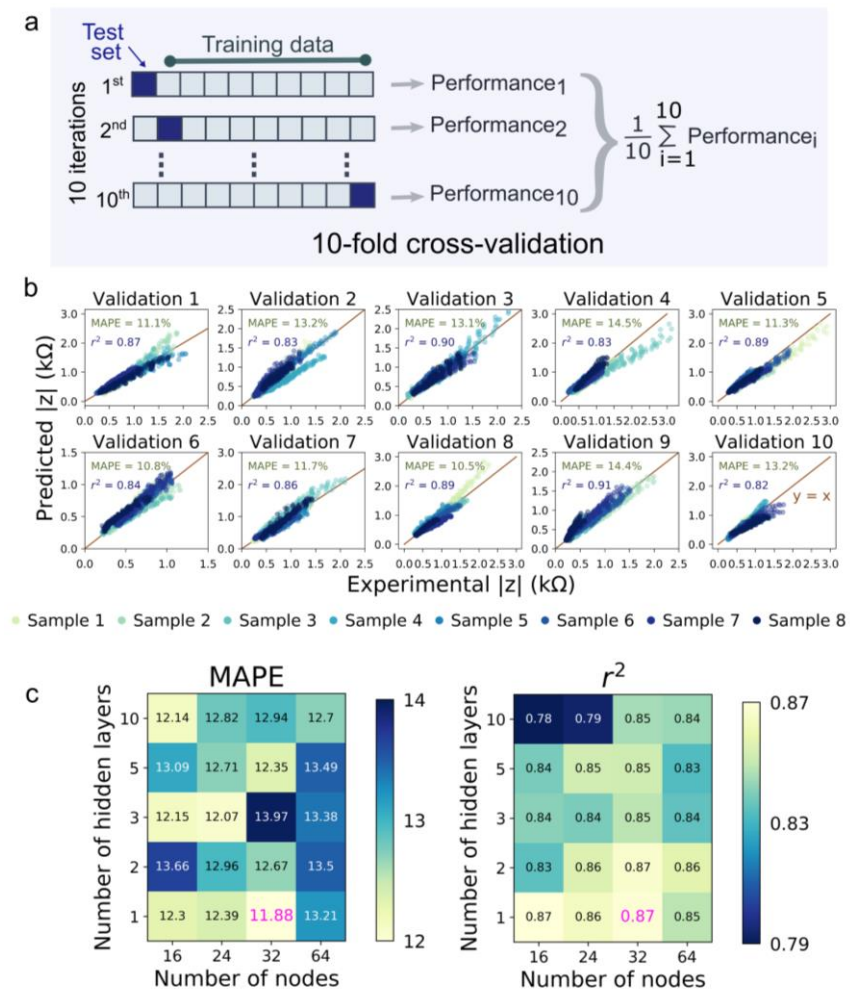


**Figure 5.8| Hyperparameter tuning of the neural network model.** **a)** Schematic showing the concept of 10-fold cross-validation. **b)** An example showing the comparison between the predictions and the actual experimental off-stimulation EFI data of  $\text{CI}^{1J}$  in a 10-fold cross validation. Each colour represents an unseen sample in an iteration. The deviation of the points from the identity line (shown as red lines) indicates how much the predicted values deviate from the experimental data. The average median absolute percentage error (MAPE) and the average  $R^2$  score were used to quantify the predictive performance of the NN model. **c)** Figure summarises the average MAPE and the average  $R^2$  scores obtained in the 10-fold cross-validations when training the model at different combinations of hyperparameters.

### 5.2.9 Clinical predictions of 3PNN

As this study aims to predict the most likely EFI outcomes, in all predictions, the stimulating and the recording electrode positions were assumed to follow the CI specification (see **Table 5.2**). In the validation of forward-3PNN, patients' model descriptors measured from their CT scans and the mean reported resistivity of live human skulls (9.3 kΩcm) were used as the inputs in the forward predictions of patient EFIs. EFI arising from off-stimulation positions up to 18.6 mm along the cochlear lumen were predicted and compared with the corresponding EFI measurements acquired in patients. Each forward prediction takes ~ 0.4 s. For all inverse predictions performed in this study, patients' model descriptors were predicted using their off stimulation EFI profiles up to 18.6 mm along the cochlear lumen.

**Table 5.2| Input values of the stimulating and the recording electrode positions of different electrode types used in 3PNN.**

CI electrode array	Electrode spacing (mm)	Electrode positions along the CI (mm)
Advanced Bionics® HiFocus™ SlimJ electrode (CI <sup>SlimJ</sup> )	1.3	[3, 4.3, 5.6, ..., 17.3, 18.6]
Advanced Bionics® HiFocus™ 1J electrode (CI <sup>1J</sup> )	1.1	[2, 3.1, 4.2, ..., 17.4, 18.5]
Cochlear™ Nucleus® slim straight electrode (CI622)	0.9	[3.85, 4.75, 5.65, ..., 17.35, 18.25]
Cochlear™ Nucleus® slim straight electrode (CI522)	0.9	[3.85, 4.75, 5.65, ..., 17.35, 18.25]

### 5.2.10 Production of 3D printed models that give patient-specific EFI profiles

Two extreme on-demand 3D printed models that give patient-specific EFI profiles were fabricated using the medians of the predicted model descriptors acquired from inverse-3PNN, (matrix resistivity 6.5 versus 0.7 kΩcm, taper ratio 0.95 versus 0.71, basal lumen diameter 2.4 versus 2.3 mm, cochlear width 9.6 versus 11.8 mm, and cochlear height 4.3 versus 3.9 mm). The EFIs of the models were measured using a HiFocus™ 1J electrode array, which is the same type of electrode implanted in the patients.

**Table 5.3|** The final MAPE thresholds used in the inverse predictions.

Predictions with unknown geometric features		Predictions with known geometric features		
Subjects	Final MAPE threshold ( $\epsilon_f$ )	Subjects	Final MAPE threshold ( $\epsilon_f$ )	
CI <sup>SlimJ</sup>	Subject 1 <sup>SlimJ</sup>	8% <sup>†</sup>	Subject 1 <sup>SlimJ</sup>	5% <sup>§</sup>
	Subject 2 <sup>SlimJ</sup>	10% <sup>†</sup>	Subject 2 <sup>SlimJ</sup>	10.1% <sup>§</sup>
	Subject 3 <sup>SlimJ</sup>	8% <sup>†</sup>	Subject 3 <sup>SlimJ</sup>	8% <sup>§</sup>
	Subject 4 <sup>SlimJ</sup>	8% <sup>†</sup>	Subject 4 <sup>SlimJ</sup>	8% <sup>§</sup>
	Subject 5 <sup>SlimJ</sup>	7% <sup>†</sup>	Subject 5 <sup>SlimJ</sup>	4% <sup>§</sup>
	Subject 6 <sup>SlimJ</sup>	8.5% <sup>†</sup>	Subject 6 <sup>SlimJ</sup>	5.7% <sup>§</sup>
	Subject 7 <sup>SlimJ</sup>	5% <sup>†</sup>	Subject 7 <sup>SlimJ</sup>	12.8% <sup>§</sup>
	Subject 8 <sup>SlimJ</sup>	6% <sup>†</sup>	Subject 8 <sup>SlimJ</sup>	10.8% <sup>§</sup>
	Subject 9 <sup>SlimJ</sup>	11% <sup>†</sup>	Subject 9 <sup>SlimJ</sup>	16.7% <sup>§</sup>
	Subject 10 <sup>SlimJ</sup>	5% <sup>†</sup>	Subject 10 <sup>SlimJ</sup>	7.2% <sup>§</sup>
	Subject 11 <sup>SlimJ</sup>	6% <sup>†</sup>	Subject 11 <sup>SlimJ</sup>	9.9% <sup>§</sup>
	Subject 12 <sup>SlimJ</sup>	5.5% <sup>†</sup>	Subject 12 <sup>SlimJ</sup>	10.8% <sup>§</sup>
	Subject 13 <sup>SlimJ</sup>	7% <sup>†</sup>	Subject 13 <sup>SlimJ</sup>	11.7% <sup>§</sup>
	Subject 14 <sup>SlimJ</sup>	3.5% <sup>†</sup>	Subject 14 <sup>SlimJ</sup>	5.5% <sup>§</sup>
	Subject 15 <sup>SlimJ</sup>	6% <sup>†</sup>	Subject 15 <sup>SlimJ</sup>	8.8% <sup>§</sup>
	Subject 16 <sup>SlimJ</sup>	6% <sup>†</sup>	Subject 16 <sup>SlimJ</sup>	10% <sup>§</sup>
	Subject 17 <sup>SlimJ</sup>	4% <sup>†</sup>	Subject 17 <sup>SlimJ</sup>	7.6% <sup>§</sup>
CI <sup>I622</sup>	Subject 1 <sup>CI622</sup>	9% <sup>†</sup>	Subject 1 <sup>CI622</sup>	13.2% <sup>§</sup>
	Subject 2 <sup>CI622</sup>	7% <sup>†</sup>	Subject 2 <sup>CI622</sup>	13% <sup>§</sup>
	Subject 3 <sup>CI622</sup>	3% <sup>†</sup>	Subject 3 <sup>CI622</sup>	36.5% <sup>§</sup>
	Subject 4 <sup>CI622</sup>	11% <sup>†</sup>	Subject 4 <sup>CI622</sup>	15% <sup>§</sup>
	Subject 5 <sup>CI622</sup>	11% <sup>†</sup>	Subject 5 <sup>CI622</sup>	14% <sup>§</sup>
	Subject 6 <sup>CI622</sup>	9.5%	Subject 6 <sup>CI622</sup>	7.7% <sup>§</sup>
CI <sup>I522</sup>	Subject 1 <sup>CI522</sup>	7% <sup>†</sup>	Subject 1 <sup>CI522</sup>	10.9% <sup>§</sup>
	Subject 2 <sup>CI522</sup>	11% <sup>†</sup>	Subject 2 <sup>CI522</sup>	13.2% <sup>§</sup>
	Subject 3 <sup>CI522</sup>	8% <sup>†</sup>	Subject 3 <sup>CI522</sup>	6.9% <sup>§</sup>
	Subject 4 <sup>CI522</sup>	3% <sup>†</sup>	Subject 4 <sup>CI522</sup>	8.3% <sup>§</sup>
	Subject 5 <sup>CI522</sup>	6% <sup>†</sup>	Subject 5 <sup>CI522</sup>	10.8% <sup>§</sup>
	Subject 6 <sup>CI522</sup>	6% <sup>†</sup>	Subject 6 <sup>CI522</sup>	11.8% <sup>§</sup>
	Subject 7 <sup>CI522</sup>	7.5% <sup>†</sup>	Subject 7 <sup>CI522</sup>	12.5% <sup>§</sup>
	Subject 8 <sup>CI522</sup>	6.5% <sup>†</sup>	Subject 8 <sup>CI522</sup>	13.7% <sup>§</sup>
CI <sup>IJ</sup>	Subject 1 <sup>IJ</sup>	6% <sup>‡,*</sup>	<sup>†</sup> Validation of inverse-3PNN (Figure 5.25b.ii, Figure 5.26)	
	Subject 2 <sup>IJ</sup>	5% <sup>‡,*</sup>	<sup>‡</sup> On demand patient-specific model (Figure 5.31b)	
	Subject 3 <sup>IJ</sup>	4%*	<sup>*§</sup> Estimation of patient-specific resistivity with unknown geometric descriptors (*) and known geometric descriptors (§) (Figure 5.33)	
	Subject 4 <sup>IJ</sup>	10%*		
	Subject 5 <sup>IJ</sup>	10%*		
	Subject 6 <sup>IJ</sup>	6%*		

### 5.2.11 Finite element modelling of the intracochlear voltage distribution in cochlea

Finite element analyses were solved using the electric currents (ec) interface of the AC/DC module in COMSOL Multiphysics 5.5. Four types of COMSOL models were built in this study – 1) a simplified spiral model without the membrane structures, 2) a spiral model with the basilar membrane and the Reissner's membrane, 3) models using the 3D volumes of patients' cochleae and 4) a linear uncoiled model without the membrane structures (**Figure 5.15**, **Figure 5.34d.ii** and **Figure 5.35**).

#### *Spiral model Creation*

The spiral cochlea geometry in **Figure 5.15** and **Figure 5.35a** was constructed according to the geometry descriptors stated in their figure captions. In detail, the cochlea geometry was formed using the sweep operation to sweep a planar circle along a parametric curve that describes the spiral trajectory of human cochleae [293]. The diameter of the planar circle was set to decrease along the parametric curve from the base to the apex linearly using the scale factor operation. Using a similar sweep operation, the geometry of the CI electrode array was built according to the geometry of the Advanced Bionics (AB) HiFocus™ 1J electrode array [303]. In the model with the membrane structures (**Figure 5.15a.i**), the membrane geometries were constructed in the same way using the sweep operation. The reported thicknesses of the Basilar membrane and the Reissner's membrane are 4  $\mu\text{m}$  and 2.5  $\mu\text{m}$  in literature [281, 307]. To minimise computational errors of meshing small element, the thickness of the Basilar membrane was enlarged by a factor of 8 here. Resistivity values from literature were adopted to define the resistivities of the domains (see **Figure 5.8a**) [281, 286, 308–310]. The permittivity effect of materials was assumed to be negligible in this study. A user-controlled mesh was applied, and a mesh convergence test was conducted to find a reasonable mesh size of the domains (**Figure 5.8b**). It was found that the computational cost can be minimized when the bone domain (sphere) and the remaining domains (cochlear lumen, implant, Basilar membrane and Reissner's membrane) were meshed with two different element sizes (top and the bottom panels). Result was considered as converged when the result exhibited less than 5% difference to the result generated from the finest mesh, and the corresponding mesh size was selected in our study (highlighted in black in **Figure 5.8b**). The chosen mesh sizes of the domains are also summarised in **Figure 5.8a**.

#### *Linear model Creation*

A linear cylinder with tapered end and the geometry of the CI electrode array were constructed according to the dimensions stated in **Figure 5.35b** and the geometry specification of HiFocus™ 1J electrode array [303]. The mesh sizes and the resistivity of the domain were the same as those chosen in the spiral model.

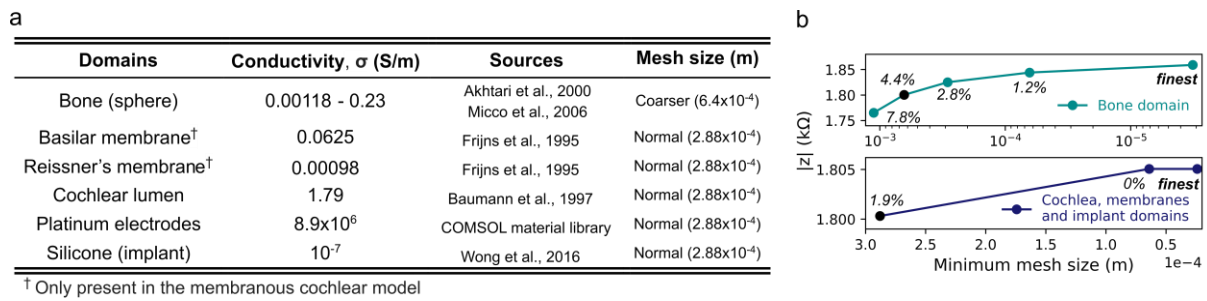


**Figure 5.9| Domain properties of the COMSOL cochlear models.** a) Conductivities  $\sigma$  and the mesh sizes of the domains of the finite element models adopted in our study. Ref: [281, 286, 308–310]. b) Results of the mesh convergence test performed on the membranous cochlear model (Figure 5.15a.i) with conductivity of the bone domain = 0.0102 S/m. The graph shows the transimpedance magnitude  $|z|$  obtained in simulating the scenario of the stimulating position at electrode 1 and the recording position at electrode 2. Simulations were carried out with different mesh sizes. The annotations on the graph show the percentage difference relative to the result generated by the finest mesh. The selected mesh sizes were highlighted in black.

### *Creation of models with patients' cochlear CT volumes*

The CAD files of the patients' 3D volumes of cochleae were imported to COMSOL using the CAD import module. The geometry of the CI electrode array was built using the same method as described above.

### *Simulation setting*

In the simulations, each electrode of the implant was activated at a stimulation impulse of 800  $\mu$ A one at a time. The simulated EFI profile was obtained by evaluating the surface average of voltage of each electrode plane in each electrode stimulation. The transimpedance magnitude  $|z|$  was determined by dividing the surface averaged voltage by the stimulation impulse. Each COMSOL simulation takes  $\sim 2$  min.

$$|z| = \frac{\text{Voltage,V}}{\text{Stimulation impulse,I}_{\text{stim}}} \quad (5.3)$$

### 5.2.12 Statistical method

Median absolute percentage error (MAPE) was chosen as the error measure in this study because it presents the percentage change due to the error and avoids being too sensitive to outliers. The MAPE between the predicted EFIs ( $EFI_{pred}$ ) and the experimental EFIs ( $EFI_{exp}$ ), and the MAPE between the predicted geometric descriptors and the actual CT-measurements were evaluated using Equations (5.4 – 5.6) and Equation (5.7) respectively, where  $a_{ij,exp}$  and  $a_{ij,pred}$  are the entries in  $EFI_{exp}$  and  $EFI_{pred}$ , and  $G_{CT}$  and  $\{G_1, G_2, \dots, G_{1000}\}$  are the CT-measured geometric features and the 1,000 predicted geometric features. Similarity is defined by Equation (5.8).

$$EFI_{exp} = \begin{bmatrix} a_{11,exp} & \cdots & a_{1j,exp} \\ \vdots & \ddots & \vdots \\ a_{i1,exp} & \cdots & a_{ij,exp} \end{bmatrix} \quad (5.4)$$

$$EFI_{pred} = \begin{bmatrix} a_{11,pred} & \cdots & a_{1j,pred} \\ \vdots & \ddots & \vdots \\ a_{i1,pred} & \cdots & a_{ij,pred} \end{bmatrix} \quad (5.5)$$

$$MAPE_{EFI} = \text{median of } \left\{ \frac{|a_{11,pred} - a_{11,exp}|}{a_{11,pred}}, \frac{|a_{12,pred} - a_{12,exp}|}{a_{12,pred}}, \dots, \frac{|a_{ij,pred} - a_{ij,exp}|}{a_{ij,pred}} \right\} \times 100\% \quad (5.6)$$

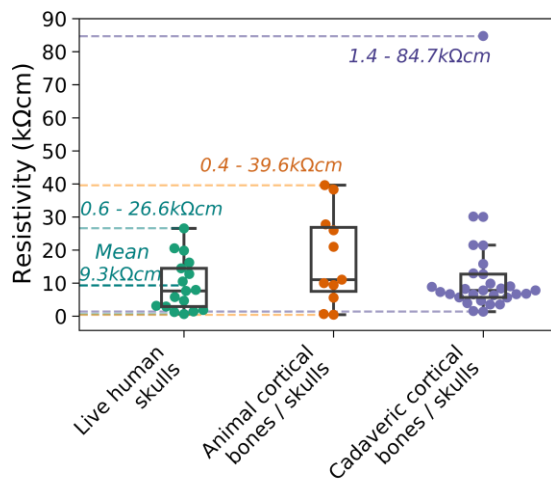
$$MAPE_{\text{geometric features}} = \text{median of } \left\{ \frac{G_1 - G_{CT}}{G_{CT}}, \frac{G_2 - G_{CT}}{G_{CT}}, \dots, \frac{G_{1000} - G_{CT}}{G_{CT}} \right\} \times 100\% \quad (5.7)$$

$$\text{Similarity (\%)} = 100 (\%) - MAPE (\%) \quad (5.8)$$

## 5.3 Results and Discussion

### 5.3.1 Designable electro-mimetic bone matrices

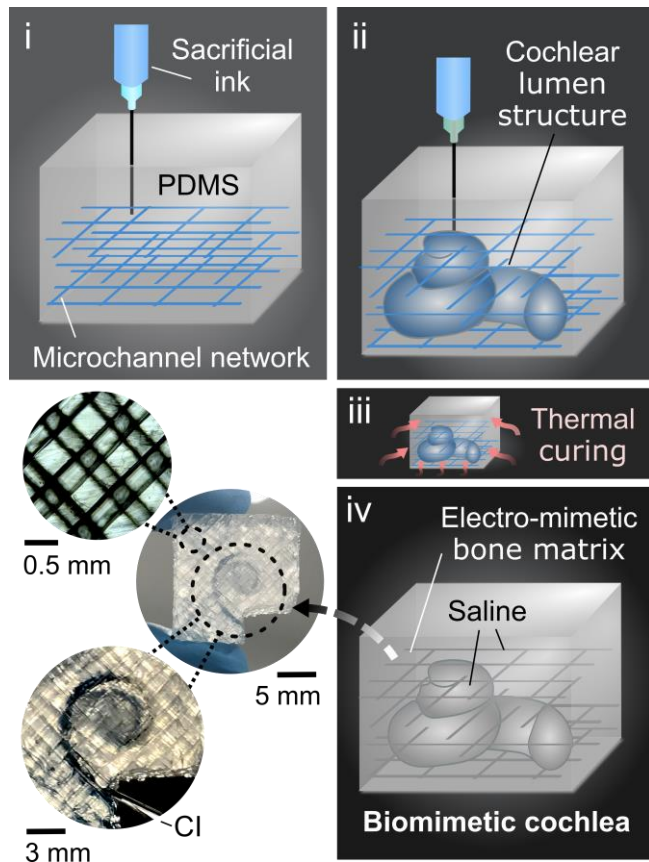
The human cochlea is a spiral-shaped hollow organ embedded in the temporal bone (**Figure 5.1**). Since there was no established report of *in vivo* cochlear tissue conductivities, the first goal was to establish a printable material system that could emulate the range of reported bone tissue conductivities (hereafter, termed electro-mimetic bone matrix). *In vivo* human studies estimated that the electrical resistivities of human skulls vary widely between 0.6 to 26.6 kΩcm, depending on the site, composition, age and porosity [311–315] (**Figure 5.9**).



**Figure 5.10| Resistivities of live human, animal and human cadaveric cortical bones or skulls reported in literature [281, 309–319].**

To reproduce the mesoscale electrical properties of bone, we take inspiration from the micro-architecture of bones, which consists of conductive fluid-filled interconnected pores surrounded by a poorly conductive mineralised phase [316]. Thus, we structured an electro-mimetic bone matrix that exhibits interconnected saline-filled channels inside a crosslinked PDMS (polydimethylsiloxane) elastomer. The interconnected channels were created by embedded printing a Pluronic F127 sacrificial ink in pre-crosslinked PDMS (**Figure 5.10**), permitting flexible and precise tuning of the void density and therefore, the resistivity of the electro-mimetic bone matrices. Comparing this printing method with stereolithography, Pluronic F127 can be easily removed after printing [132] and further enhances the wettability of PDMS due to its amphiphilic nature. The channels were then filled with a physiological

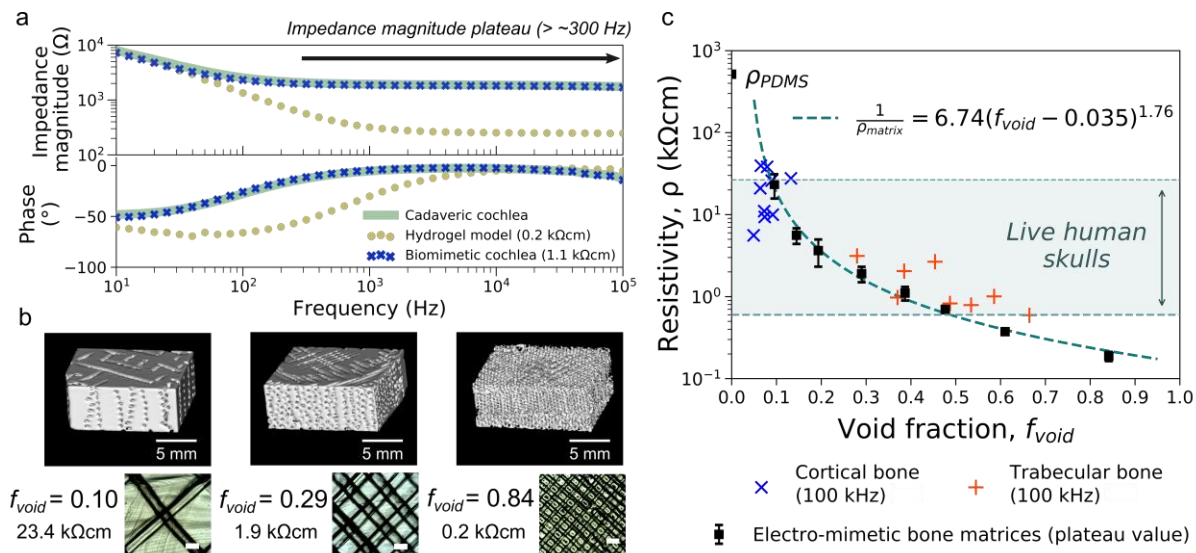
saline, which is hypothesised to be important for emulating the electrical impedance properties of bone tissues, as pores in bone are normally wet with extracellular fluids.



**Figure 5.11| Schematic of the embedded 3D extrusion printing strategy to produce the electro-mimetic bone matrices and the biomimetic cochleae.**

The electrochemical impedance spectroscopy (EIS) measurements in **Figure 5.11a** show that an electro-mimetic bone matrix can be designed to exhibit impedance properties matching those of a cadaveric cochlear bone in a human head for the entire frequency range ( $f = 10 \text{ Hz} - 100 \text{ kHz}$ ) studied in EIS. In particular, the Fourier fundamental frequency associated with the EFI stimulation pulse (estimated to be  $f \sim 14 \text{ kHz}$  to  $\sim 20 \text{ kHz}$  depending on CI type) lies in the frequency-independent impedance magnitude plateau region. By varying the void fraction in the electro-mimetic bone matrix from 20% to 84%, the resistivity of the matrix that is derived from the impedance magnitude plateau, can be tuned from 0.2 to  $23.4 \text{ k}\Omega\text{cm}$  (**Figure 5.11b**), covering almost the entire reported resistivity range of live human skull tissues [311–315] (0.6 –  $26.6 \text{ k}\Omega\text{cm}$ , **Figure 5.11c**). To describe the correlation between the resistivity of the electro-mimetic bone matrix  $\rho_{matrix}$  and  $f_{void}$ , the electro-mimetic bone matrix was

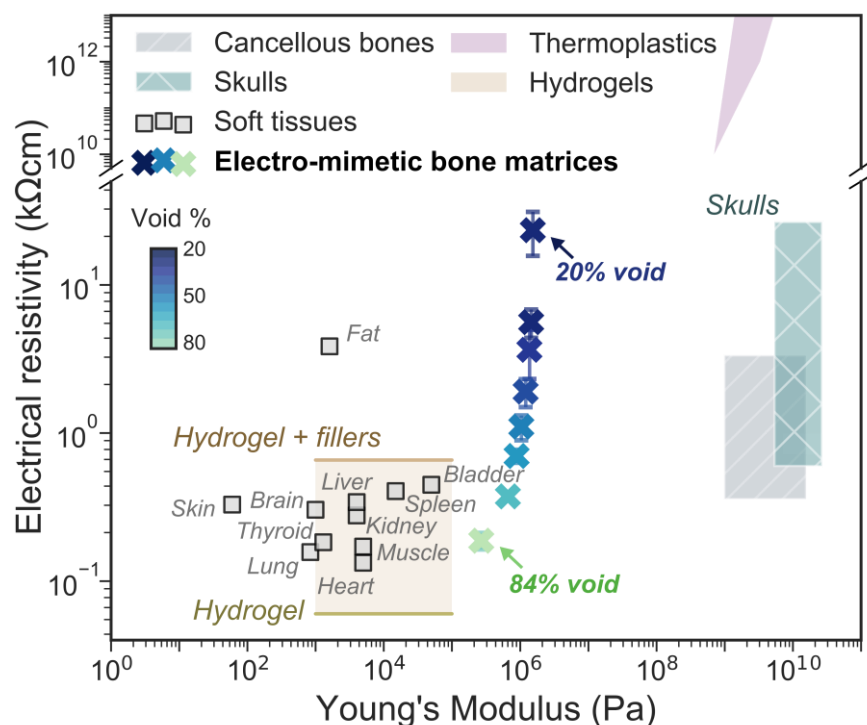
assumed to behave as a conductor-insulator composite. The resistivity of such composite can be described by a percolation equation with the form  $1/\rho_{matrix} = \alpha(f_{void} - f^*)^\beta$ , where  $\alpha$  and  $\beta$  are fitting coefficients, and  $f^*$  is known as the percolation threshold (the minimum volumetric fraction of the saline-filled void for electrical current to percolate from one side to the other [320]). With the assumption that an electrical percolation network will first be established when there are two diagonal channels in the matrix,  $f^*$  is found to be 0.035 and a fitting equation with the form  $1/\rho_{matrix} = 6.74(f_{void} - 0.035)^{1.76}$  was obtained after experimental data fitting.



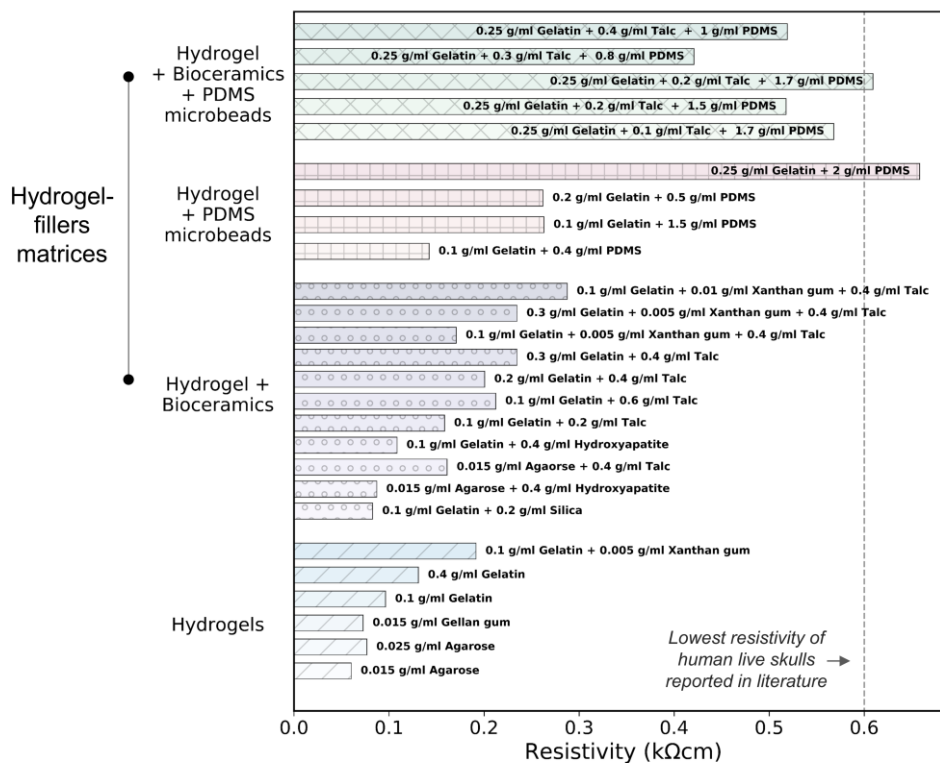
**Figure 5.12| Electrical properties of electro-mimetic bone matrices.** **a)** Bode plot showing the impedance properties of a cadaveric cochlea in a human head, and 3D printed cochlear models made of an electro-mimetic bone matrix and a hydrogel. The frequency range associated with the impedance magnitude plateau is indicated. **b)**  $\mu$ -CT reconstructed images (top) and optical microscopic images (bottom) of the electro-mimetic bone matrices at different volumetric void fractions ( $f_{void}$ ). Scale bar of the optical microscopic images = 500  $\mu$ m. The resistivities of the matrices were determined from their plateau impedance magnitude and the size of samples.  $n = 3$  independent samples. **c)** Resistivity of the electro-mimetic bone matrices (plateau value,  $n = 3$  independent samples) as a function of  $f_{void}$ , compared to the reported resistivities of bovine cortical and trabecular bones [316]. Data are presented as mean values  $\pm$  SD.

**Figure 5.12** shows a material property chart summarising the electrical resistivity and the Young's modulus for a range of biological tissues and polymeric materials. The 3D printed electro-mimetic bone matrices cover a wide resistivity range, which cannot be imitated by a single printable material (i.e. thermoplastics or hydrogels) alone or a hydrogel-filters matrix (i.e. bioceramics and PDMS microbeads dispersed in hydrogels) (**Figure 5.13**). In addition, these hydrogel-based matrices are soft and fragile, which will lead to inconsistent electrical

properties over time. Apart from electrical resistivity, Young's modulus of the model is also an important consideration for electronic implant testing. Adopting PDMS as the solid phase of the electro-mimetic bone matrix not only facilitates the ease of embedded printing, but also imparts favourable mechanical properties as a CI testing platform. With a Young's modulus in the  $10^6$  Pa range, the force associated with CI electrode insertion (0.004 N) was assumed not to induce a significant deformation to the matrix [321]. At the same time, the compliance of the matrix mitigates mechanical damage to the fine electrodes of a CI, which is commonly experienced when inserting CI electrode arrays repeatedly in cadaveric samples (modulus of hard tissues  $> 10^9$  Pa). Hence, multiple insertions can take place for the same CI electrode array, which is of practical importance due to the time-consuming fabrication and costs associated with a fully functioning CI. Overall, the above results suggest the electro-mimetic bone matrices to be a suitable material system for creating electroanatomical models of human cochleae.



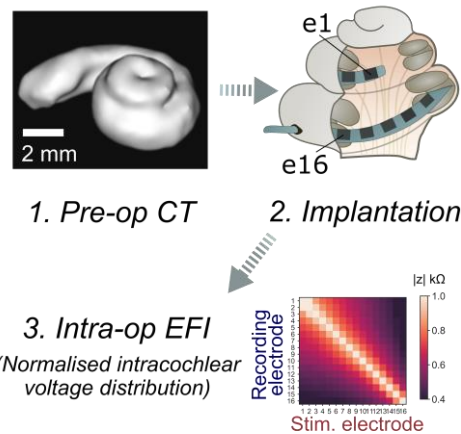
**Figure 5.13| A map of resistivity versus Young's modulus** of human tissues, thermoplastics, the hydrogel-filters matrices, and the electro-mimetic bone matrices (plateau values) tested in this study ( $n = 3$  independent samples). The compositions of the hydrogel and hydrogel-filters matrices tested here are listed in Figure 5.13. Young's moduli of the electro-mimetic bone matrices were estimated by scaling the Young's modulus of pure PDMS (1.7 MPa at a curing temperature of 60 °C [100]) linearly with the  $f_{void}$  of the matrix. Tissues and thermoplastics data, and the Young's modulus of hydrogels were compiled from literature [261, 311–316, 322–325].



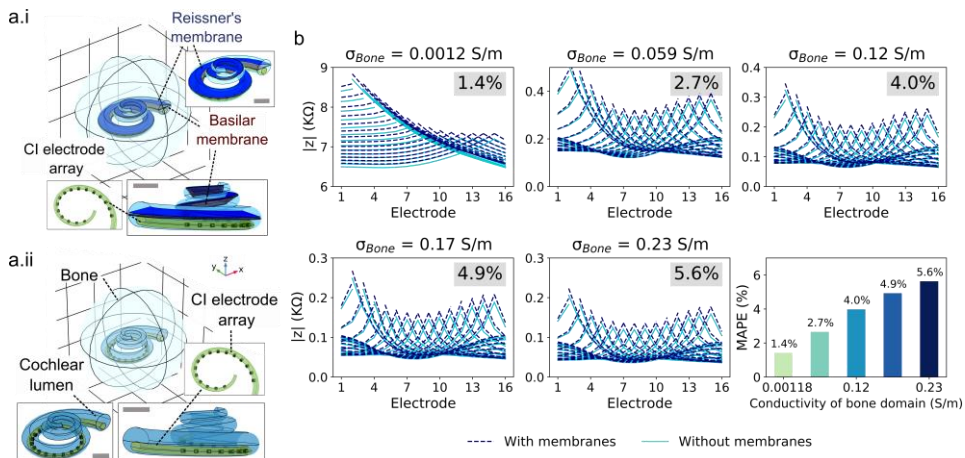
**Figure 5.14| Resistivity (plateau value) of the hydrogel matrices and hydrogel-filler matrices (hydrogel-bioceramics matrices, hydrogen-PDMS microbeads matrices and hydrogel-bioceramics-PDMS microbeads matrices) tested in this study.**

### 5.3.2 3D printed biomimetic cochleae

Clinically, a CI electrode array is inserted into the scala tympani, one of the three cochlear ducts [285] (**Figure 5.1**). As a coarse-grained approach to replicate the electroanatomical features of a CI implanted cochlea, we approximate the cochlea as one ensemble spiral cavity with continuously narrowing diameter, and omit the inner soft-tissue membranous structures inside the cochlea, such as the basilar membrane and Reissner's membrane. This is because, firstly, in a typical patient's pre-operative CT scan as routine clinical assessment (**Figure 5.14**), the scan resolution only permits the identification of the shape of the ensemble cochlear lumen and not the fine microanatomical soft tissue structures; and secondly, the preliminary finite element modelling shows that the effect of the basilar membrane and the Reissner's membrane inside a cochlea on the off-stimulation EFI profile is likely to be insignificant, as the boundary impedances are dominated by surrounding bone tissues (**Figure 5.15**). Therefore, the biomimetic cochleae were constructed by embedded 3D extrusion printing a tapered and spiral-shaped



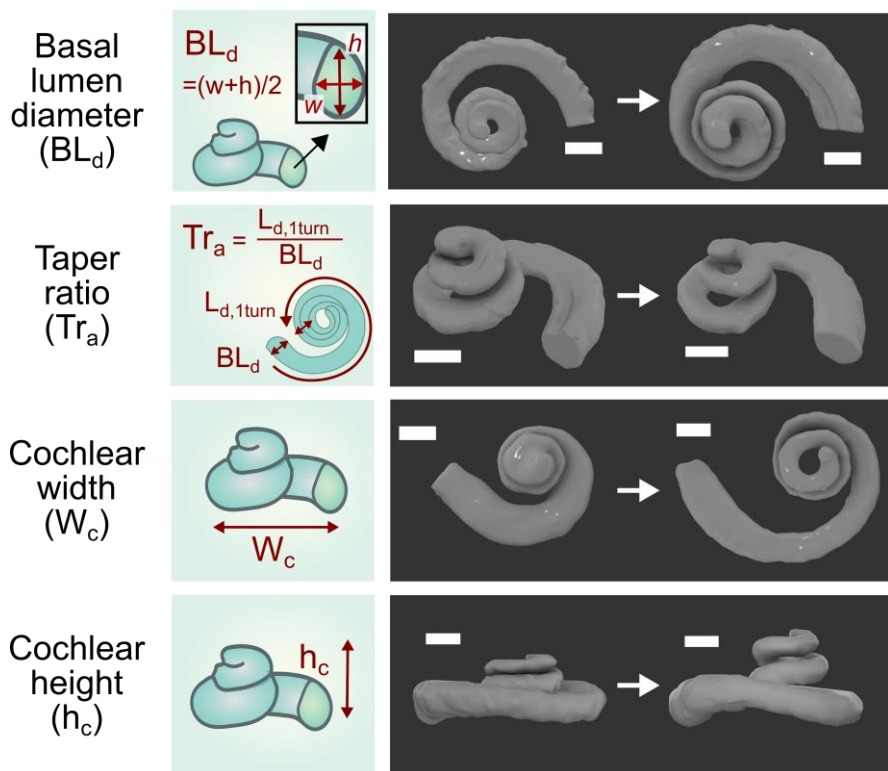
**Figure 5.15| Schematic of the routine CI assessment process.** 1. Pre-operative CT scan of a patient's cochlea, which typically only has sufficient resolution to reveal the ensemble spiral-shaped cavity of a cochlea; 2. Implantation of the electrode array of a CI in the scala tympani of the cochlea; 3. Acquisition of an intra-operative EFI (electric field imaging) profile from a patient, which is derived from recording the induced intracochlear voltage  $V$  measured at each electrode upon injecting consecutive current pulses at each electrode in the array. The voltage measurements are then converted to transimpedance magnitude  $|z|$  by normalising the voltage  $V$  with the stimulation current impulse  $I_{stim}$  ( $|z| = V / I_{stim}$ ). The off-stimulation (off-diagonal) measurements in the EFI present information about the tissue impedance [280].



**Figure 5.16| a)** Finite element model of cochlea i) with the Reissner's membrane and the Basilar membrane and ii) without the intracochlear membranous structures. Scale bar = 2 mm. **b)** Simulated off-stimulation EFIs generated from the membranous cochlear model and from the simplified cochlear model with different bone domain conductivities,  $\sigma_{bone}$ . The models have the following geometric descriptors –  $BL_d = 2.1$  mm,  $Tr_a = 0.62$ ,  $W_c = 10.5$  mm and  $h_c = 4.4$  mm. Definitions of the geometric descriptors can be found in Table 5.4. In the simulations here, the ground was set to be infinitely far away from the cochlea.  $\sigma_{bone}$  was varied from 0.0012 to 0.23 S/m to consider the wide variation in the reported conductivity of skulls and cortical bones in live human, animals and cadavers [281, 309, 318, 319, 310–317]. The values at the upper right of the graphs indicate the MAPE (median absolute percentage error) between the simulated EFIs of the membranous cochlear model and the simplified model. As shown in the graph, MAPE increases with  $\sigma_{bone}$ . Hence, the largest MAPE between the two models happened at  $\sigma_{bone} = 0.23$  S/m with a MAPE only  $\sim 6\%$ .

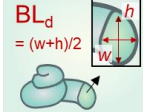
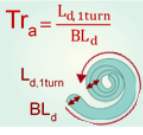
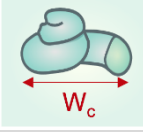
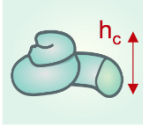
cochlear lumen cavity inside an electro-mimetic bone matrix (**Figure 5.10**). The spiral-shaped cavity was filled with a physiological saline to mimic the ionic conduction milieu in the cochlea (perilymph) (see **Figure 5.6**) and the conduction properties at the electrode-electrolyte interface.

Since the size and the shape of a cochlea is unique to each individual and can vary greatly from person-to-person [284, 326, 327], four geometrical descriptors were assigned to parametrically describe the reported anatomical variations in CI implanted human cochleae; they are basal lumen diameter, taper ratio, cochlear width and cochlear height (see **Figure 5.16** and definitions in **Table 5.4**). For electroanatomical modelling of cochleae, a fifth descriptor, the matrix resistivity, was incorporated. The matrix resistivity is controlled by the void fraction of the electro-mimetic bone matrix. In total, 82 biomimetic cochleae were printed at different combinations of model descriptors. With this physical model library, a broad spectrum of the electroanatomical features of human cochleae was artificially reconstructed.



**Figure 5.17|**  $\mu$ -CT reconstructed images of the spiral lumen of the biomimetic cochleae with different features of geometric descriptors.

**Table 5.4| Definitions and the ranges of the model descriptors investigated in this study in comparison with the reported variation in human cochleae [284, 327–329].**

Model descriptors	Definitions	Human variation	Range of the model descriptors investigated
Matrix resistivity, $\rho_{\text{matrix}}$ (kΩcm)		Resistivity of the electro-mimetic bone matrix	0.6 – 26.6 $0.2 \pm 0.1$ – $23 \pm 4$
Basal lumen diameter, $BL_d$ (mm)		The average of the width (w) and the height (h) of the cross-sectional area of the entrance of the cochlear lumen	1.6 – 2.6 $2.00 \pm 0.02$ – $2.50 \pm 0.02$
Taper ratio, $Tr_a$		The ratio of the lumen diameter at 1 turn ( $L_{d,1\text{turn}}$ ) to the basal lumen diameter ( $BL_d$ )	0.3 – 1.0 $0.60 \pm 0.01$ – $0.90 \pm 0.06$
Cochlear width, $W_c$ (mm)		The largest distance from the entrance to the contralateral wall	7.4 – 11.9 $7.30 \pm 0.04$ – $12.7 \pm 0.3$
Cochlear height, $h_c$ (mm)		The largest distance between the apical-most point and the basal-most point of the cochlea	4.3 – 6.2 $3.5 \pm 0.1$ – $5.0 \pm 0.1$

**Figure 5.17a** shows high-resolution  $\mu$ -CT scans of a cadaveric cochlea and an exemplar 3D printed biomimetic cochlea with a CI inserted. It is worth noting that the CI electrode-to-spiral centre distance displayed in the 3D printed cochleae matches closely with the electrode-to-modiolus distances measured clinically from patients' CT scans [330] (**Figure 5.17b**). Despite only 4 geometric descriptors being used to describe patient cochlear geometry, biomimetic cochleae with similar patients' geometric descriptors can approximately capture the overall contour of the cochlear lumen which encapsulates the length of the CI array (up to 1.5 turn,  $n = 3$ , see **Figure 5.17c**). Hence, similar plain X-ray imaged electrode positions and the angular insertion depths were observed in the biomimetic cochleae and in the patients implanted with the same type of CI (**Figure 5.17d**). Statistically, the dependence of the CI angular insertion depth on the cochlear width was also similar, comparing the biomimetic cochlea data and the patient data (**Figure 5.17e**). This gives further confirmation that the 3D

printed cochleae have adequate structural rigidity and anatomy to provide geometrically-guided implant insertion and positioning. It should be noted that since the 3D printed cochleae do not present the intracochlear membrane structures, the associated volume restriction effects on CI electrode positioning might not be fully captured in the 3D printed models (the effect is studied in **Section 5.3.9.2**).

Next, intracochlear EFI profiles (normalised intracochlear voltage distribution) of the biomimetic cochleae were acquired with a CI<sup>1J</sup> (Advanced Bionics HiRes 90K® implant with HiFocus™ 1J electrode) electrode array inserted. EFI samples the intracochlear voltage (V) along the electrode array in response to a current injection or a stimulation impulse ( $I_{stim}$ ) at each electrode (**Figure 5.14**). The off-stimulation measurements in EFI profiles contain information about the induced voltage spread characteristics of the cochlea. EFIs and similar measures (e.g. transimpedance matrix from Cochlear Corporation® or Impedance Field Telemetry from MED-EL®) are commonly used as part of the routine CI clinical assessment.

To further demonstrate the importance of having a realistic bone matrix resistivity in reproducing the patient EFI profile, models made of materials with contrasting conduction properties, hydrogels (representing the highly conductive case) and solid PDMS (representing the insulating case) were also fabricated. **Figure 5.18** shows the mean patient EFI profile derived from 97 patients compared with the EFI profiles of the 3D printed models with different matrix material properties. I found that the solid PDMS model led to a steeper and extremely asymmetrical EFI profile (as seen in the stimulation at the medial electrode), strongly mismatched with real patient profiles. In comparison, the conductive hydrogel model resulted in a low magnitude EFI profile, which sits outside the patient population EFI. By replicating realistic bone resistivities with electro-mimetic bone matrices, the biomimetic cochlea can be designed to match real patient stimulus spread characteristics. In addition, with the use of PDMS as the base material of the biomimetic cochleae, the models are long-lasting and can be used multiple times (**Figure 5.19**).

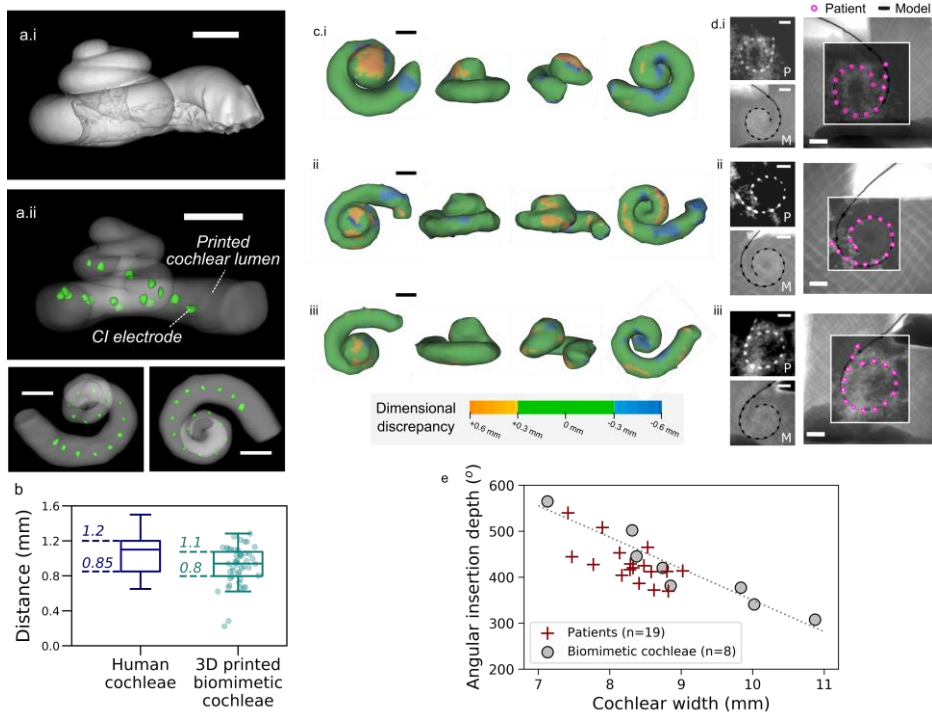


**Figure 5.18| 3D printed biomimetic cochleae enable geometrically-guided CI positioning.** **a)** µ-CT reconstructed images of **(i)** a cadaveric cochlea and **(ii)** the lumen of an exemplar 3D printed biomimetic cochlea with CI electrode array (marked green) implanted. Scale bar = 2 mm. **b)** The electrode-to-spiral centre distance ( $n = 48$ ) of the biomimetic cochleae, compared to the electrode-to-modiolus distance of human cochleae with the same CI electrode type implanted (HiFocus™ 1J electrode array), replotted from literature [330]. **c)** Comparison of the dimensional discrepancies between patients' cochlear CT and the lumen of the 3D printed biomimetic cochleae that have similar geometrical descriptors. The dimensional discrepancy is encoded with color with a defined tolerance of  $\pm 0.3$  mm, which is the mean pixel size of the patients' CT scans, using AutoDesk Recap Photo. Their geometrical descriptors are as follows: i)  $BL_d \sim 2.2$  mm,  $Tr_a \sim 0.81$ ,  $W_c \sim 8.9$  mm and  $h_c \sim 4.6$  mm, ii)  $BL_d \sim 2.0$  mm,  $Tr_a \sim 0.9$ ,  $W_c \sim 8.7$  mm and  $h_c \sim 4.7$  mm and iii)  $BL_d \sim 2.0$  mm,  $Tr_a \sim 0.87$ ,  $W_c \sim 8.4$  mm and  $h_c \sim 4.8$  mm. Scale bar = 2 mm. **d)** The overlap x-ray image showing the electrode positions in the patients' cochleae (P) showed in **(c)** and their corresponding 3D printed models (M). They were implanted the same type of electrode ( $CI^{SlimJ}$ ), and their corresponding angular insertion depths are i)  $\sim 420^\circ$ , ii)  $\sim 429^\circ$  and iii)  $380^\circ$ . Scale bar = 2 mm. **e)** The relationship between the angular insertion depth of the CI electrode array and the cochlear width in patients' cochleae ( $n = 19$ ) and in the 3D printed biomimetic cochleae ( $n = 8$ ) with different geometric descriptors.

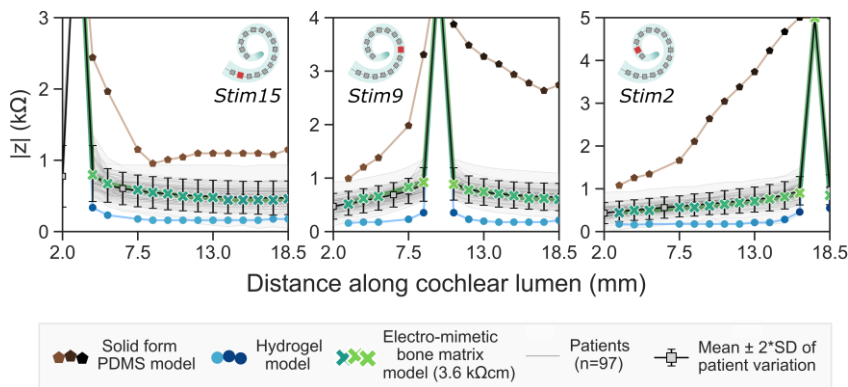


**Figure 5.19| Comparison of the mean patient EFI profile ( $n = 97$ ), and the EFI profiles obtained from 3D printed models made of hydrogel, solid PDMS and electro-mimetic bone matrix (3.6 kΩcm). The mean patient EFI was derived from 97 clinical EFIs, on the assumption that the insertion depths follow the suggested insertion depth of CI<sup>11</sup>. EFIs induced by the stimulations of the basal electrode (electrode 15), the medial electrode (electrode 9) and the apical electrode (electrode 2) were shown.**

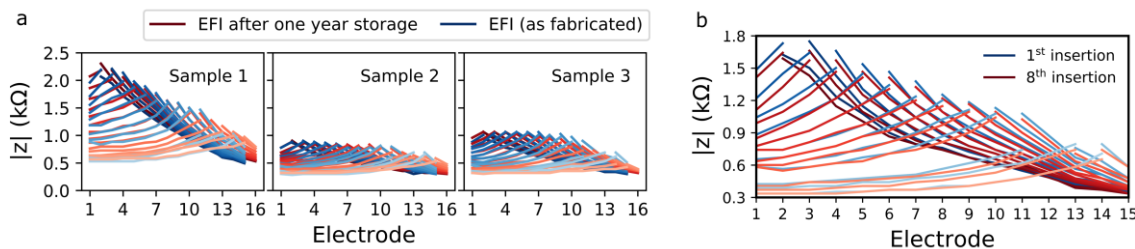


**Figure 5.20| Long-lasting properties of the biomimetic cochleae. a)** EFIs measured in the same electro-mimetic bone matrix cochlear model before and after a year storage. **b)** EFIs measured in the same electro-mimetic bone matrix cochlear model after multiple CI insertions. No significant change is observed, illustrating the reusable property of our PDMS-based electro-mimetic bone matrix model. This also confirms that the applied force during CI insertions will not impose any significant deformation to the shape of the cochlear lumen of the model.

### 5.3.3 Development of the neural network model

*The neural network model was developed by my collaborator, Chon Lok Lei. I performed the simulations.*

By training a neural network (NN) machine learning model with the dataset of EFI profiles acquired from the 3D printed biomimetic cochleae, a 3D printing and neural network co-modelling (3PNN) framework (**Figure 5.20**) was established to model the relationship between the electroanatomical features of the CI implanted biomimetic cochleae and EFIs as a function of CI electrode position. The NN model built with the optimised hyperparameters exhibits a

good prediction accuracy (a MAPE of 11.9% in the 10-fold cross-validation, see **Materials and Methods 5.2.8**). **Section 5.3.3.1** discusses the reasons for using neural network modelling instead of other existing computational models.

To support various application needs, forward-3PNN and inverse-3PNN were developed. Forward-3PNN is used when patients' cochlear geometry is known (i.e. through a pre-operative CT scan), and the algorithm can predict the most probable off-stimulation EFIs arising from different electroanatomical descriptors of a cochlea. The patient-specific EFI prediction covers the initial 2 – 18.5 mm section of a CI electrode array from different manufacturers that may have different electrode positions and spacings. Inverse-3PNN is used when a patient EFI is given, and the algorithm can infer the most probable distribution of the electroanatomical descriptors (i.e. the four geometric descriptors and the cochlear tissue resistivity) of the patient's cochlea.

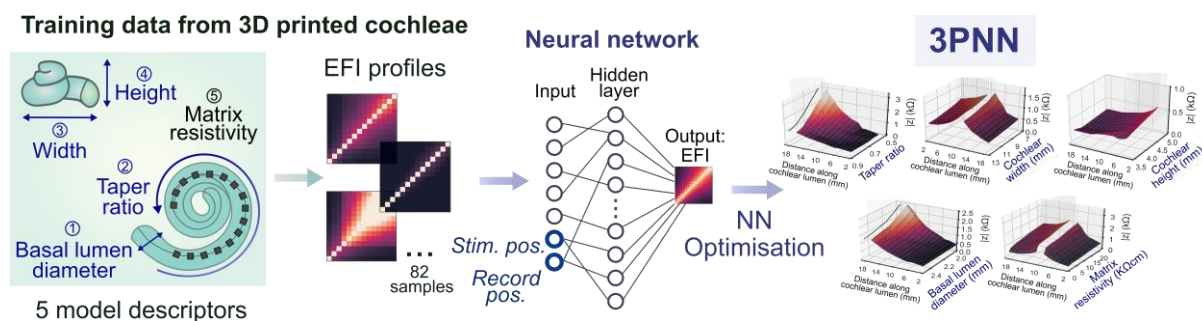


**Figure 5.21| Schematic of the workflow of 3PNN.** The hyperparameters of 3PNN were tuned using 10-fold cross-validation to achieve the best predictive performance (see **Section 5.2.8**). In summary, the input layers of the neural network consist of 7 parameters – basal lumen diameter, taper ratio, cochlear height, cochlear width, matrix resistivity, an array of the stimulating electrode positions and an array of the recording electrode positions. One hidden layer with 32 nodes is used; the output of the NN model is a transimpedance matrix (known as EFI for Advanced Bionics® implants, or transimpedance matrix for Cochlear Corporation® implants), of which the dimension equals to the product of the dimension of the recording position array and the dimension of the stimulating position array.

### 5.3.3.1 Rationale for using neural network as a modelling approach compared to existing modelling approaches

Computational models that correctly describe the behaviour of experimental data are beneficial when large amount of experimental data is needed for recognising trends in datasets. Experiments are typically time-consuming and sometimes expensive to perform, thus, computational models can be used as a surrogate model to predict the outcome without the need of additional experiments. Computational models also make determining some physically relevant parameters possible. Therefore, choosing the right modelling approach is of particular importance to reduce the discrepancy between predictions and experimental results.

This study proposed the use of a multilayer perceptron (MLP) neural network (NN) to model how the EFI depends on the cochlear resistivity, basal lumen diameter, taper ratio, cochlear width and cochlear height. Alternative methods such as the classical parametric regression models and the 'lumped parameter models' were comparatively evaluated for the application.

Parametric regression models often require knowledge of the explicit theoretical functional form that describes the data behaviour. This method is inappropriate for this study because there is no theoretical functional form that well describes the voltage distribution from a current source in a heterogeneous medium. On the contrary, artificial neural networks are purely data-driven models. They are known as universal approximators — they have the ability to learn complex and non-linear mappings between the inputs and outputs without the need of knowledge of the explicit model dynamics [331]. Therefore, neural networks usually outperform and achieve a better fit than classical regression models when 1) the explicit functional form of the data behaviour is not known/perfect, 2) non-linearities are involved, and 3) the number of variables is large. These properties are beneficial for modelling the problem of this study.

Several studies have developed 'lumped parameter models' to simulate the *in vivo* EFI profiles [280, 332, 333]. These models (**Figure 5.21a**) simplify the description of the spatially varied electrical resistance of cochleae with a discrete electrically equivalent circuit consisting of a number of parameters, which may have direct physical meanings. To explore the feasibility of using a lumped parameter model to build an analytical model for the application here, we examined whether solutions of parameters are identifiable in backward calculation from EFI profiles. The code for solving the lumped parameter model was generated by my collaborator,

Chon Lok Lei. We attempted to infer the parameters of the lumped parameter model from patients' EFI profiles. The lumped parameter model used in these studies was based on the 1<sup>st</sup> order leaky transmission line tissue model (**Figure 5.21a**) developed by Vanpoucke et al. [280]. **Figure 5.21b** shows the solutions of the parameters found from 4 patients' EFI profiles. For each patient EFI, the model was solved 3 times to check if the solutions were converged. We found that several parameters of the lumped parameter model were non-identifiable with our patients' EFI data. In particular, the parameters at the basal-most and apical-most ends (electrodes 1 and 16) could be inconsistent in different iterations. In addition, the results indicate that the transversal resistance  $r_T$  changes abruptly across the electrode array. Previous study from Vanpoucke *et al.* attributed this abrupt dip at e7 – e8 to the current drain through facial nerve [280]. However, in our results, the dip happened at several locations along the electrode array, not just at e7 – e8. This may suggest  $r_T$  extrapolated at specific electrode location may not be physically meaningful. Most importantly, the lumped parameter model is not able to reveal the anatomical dependence of EFI.

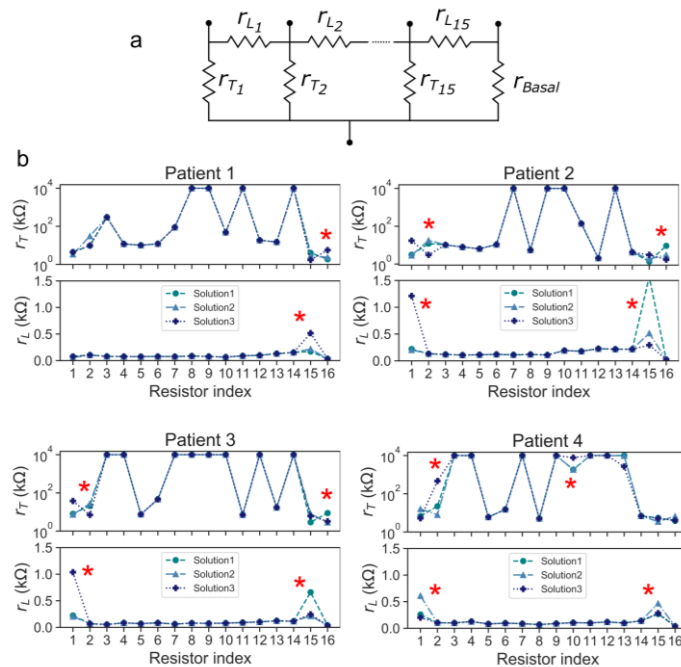


**Figure 5.22| a)** A 1<sup>st</sup> order **lumped parameter model** proposed by Vanpoucke et al. for modelling the electrical volume conduction within cochleae [280]. Each segment represents a section of an uncoiled cochlea between subsequent electrodes. The longitudinal resistors ( $r_L$ ) represent the current flow along the cochlear lumen, the transversal resistors ( $r_T$ ) represent the current flow through the lateral and modiolar bony structures, and the basal resistor ( $r_{Basal}$ ) represents the resistance between the base of cochlea and the reference electrode. **b)** The solutions of the parameters of the lumped parameter model solved by backward calculation of 4 patients' EFI profiles. \* denotes the parameter identifiability issue of the model where the solutions were different over 3 iterations.

### 5.3.4 Applicability of 3PNN on different electrode types

3PNN was trained by EFI profiles acquired from the 3D printed cochleae using HiFocus<sup>TM</sup> 1J electrode array (CI<sup>1J</sup>). To show the broad applicability of 3PNN on different electrode types first, I measured EFIs in the same 3D printed models using different types of CI electrode arrays (CI<sup>1J</sup>, HiFocus<sup>TM</sup> SlimJ electrode array (CI<sup>SlimJ</sup>) and Cochlear<sup>TM</sup> Nucleus<sup>®</sup> slim straight electrode CI522)) and examined the effects of different electrode types on EFIs. **Figure 5.22a** compares the off-stimulation EFI measurements of CI<sup>1J</sup> and CI<sup>SlimJ</sup> ( $n = 6$ ), and the off-stimulation EFI between CI<sup>1J</sup> and CI522 ( $n = 9$ ). It is important to note that CI<sup>1J</sup>, CI<sup>SlimJ</sup> and CI522 were manufactured by different CI companies, and have different electrode spacings (**Table 5.2**). The 3D printed models here were randomly selected and exhibited different model descriptors (**Figure 5.22c**). The results show that the off-stimulation EFIs measured in the same model by the different CI electrode types have very similar overall shape and trend.

Next, the applicability of 3PNN beyond the CI<sup>1J</sup> electrode array was confirmed in **Figure 5.22b**, where 3PNN was used to predict the off-stimulation EFIS (for up to 18.5 mm) of CI<sup>SlimJ</sup> and CI522 electrode arrays. The prediction accuracy of CI<sup>SlimJ</sup> and CI522 off-stimulation EFIs complies with the prediction accuracy of CI<sup>1J</sup> EFIs, with ~10% MAPE. This finding provides confidence that 3PNN can be broadly implemented for different CI electrode arrays and EFIs are predominantly governed by the cochlear electroanatomy.

### 5.3.5 Clinically validated 3PNN shows high statistical predictive performance

The clinical applicability of 3PNN was validated using routinely acquired clinical data of different implant types. In total, 31 paired sets of patient's CT scan and EFI profile were used for validation. They were acquired using either a CI<sup>SlimJ</sup> ( $n = 17$ ), a CI622 ( $n = 6$ ), or a CI522 ( $n = 8$ ). The clinical EFIs used here were randomly selected to capture two standard deviations of the mean patient profile derived from 97 patients (**Figure 5.23**). Here, the inputs of the stimulating and the recording electrode positions were assumed to follow the suggested insertion depths for predicting the most likely outcomes. Starting with the forward-3PNN, the patients' off-stimulation EFI profiles were predicted based on the four geometric descriptors measured from their CT scans, while taking the matrix resistivity input as 9.3 kΩcm (the mean reported resistivity of live human skulls [311–315]). Without any model adjustment for the different CI types, 28 out of the 31 EFI reconstructions achieve a MAPE (median

Experimental off-stimulation EFIs acquired by different CIs in biomimetic cochleae

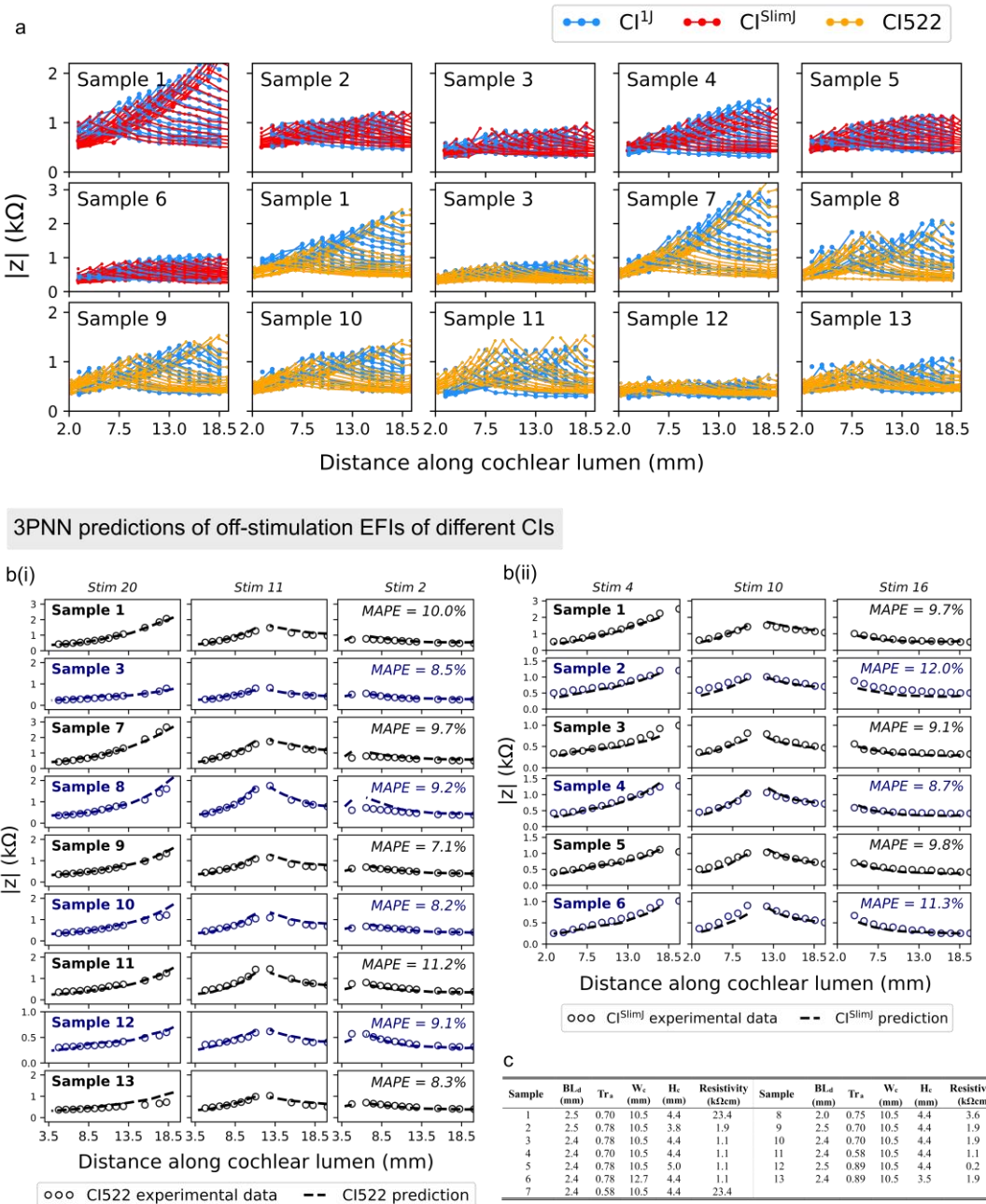


**Figure 5.23| Applicability of 3PNN on different electrode types.** a) Experimental off-stimulation EFIs or transimpedance matrices acquired by either CI<sup>1J</sup>, CI<sup>SlimJ</sup> or CI522 in same biomimetic cochlea samples. b) Accuracy of 3PNN in predicting (i) CI522 transimpedance matrices and (ii) CI<sup>SlimJ</sup> EFIs. MAPE is used as a measure of the discrepancy between the predicted and the experimental data measured in the biomimetic cochleae. c) Specifications of the samples tested here.

absolute percentage error)  $< 12\%$  (**Figure 5.24**), despite of the limited resolution of patients' cochlear CT scans, and the substitution of the unknown patient cochlear tissue resistivities with the reported mean human skull resistivity. For a selected patient (subject 4<sup>CI522</sup>) whose EFI profile matches the population mean EFI ( $n = 97$ ), forward-3PNN was shown to achieve a MAPE = 8.6% for the EFI reconstruction (**Figure 5.25a-b**). The capability of 3PNN to give patient-dependent EFI predictions is confirmed in **Table 5.5**, which cross-compares the MAPEs calculated between the patients' EFIs and the 3PNN predictions, and the MAPEs between the patients' EFIs and the population mean.

Next, we validated our 3PNN by inversely inferring the distribution of the four cochlear geometric descriptors that could match a patient's off-stimulation EFI profile with a similarity  $> 89\%$  (Similarity (%) = 1 – MAPE (%)). Comparing the predicted distributions of the geometric descriptors with the corresponding patient's features measured from their CT scans, the median MAPE is  $\leq 8\%$  (**Figure 5.26**). The above high statistical prediction accuracy demonstrates the capacity of 3PNN to autonomously predict clinical EFIs or patients' cochlear features for different electrode types without further need to adjust the machine learning model that is trained by the dataset acquired from the CI<sup>1J</sup>.

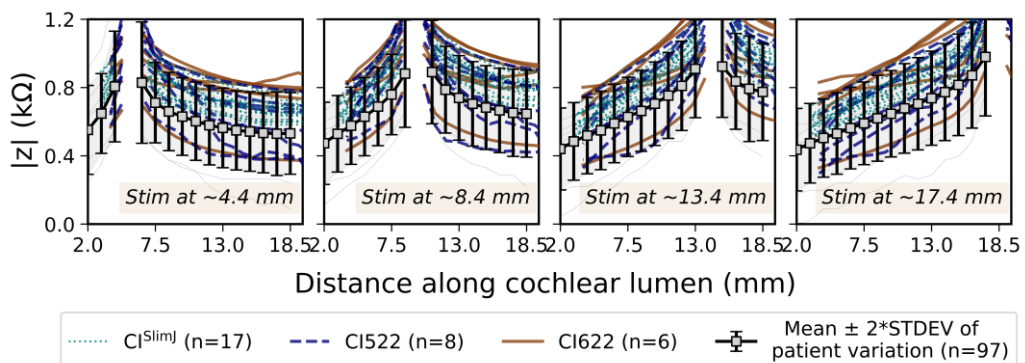


**Figure 5.24|** The clinical EFIs ( $n = 31$ ) used in the validation of 3PNN to represent the EFI variation in patient population ( $n = 97$ ). STDEV: Standard deviation.

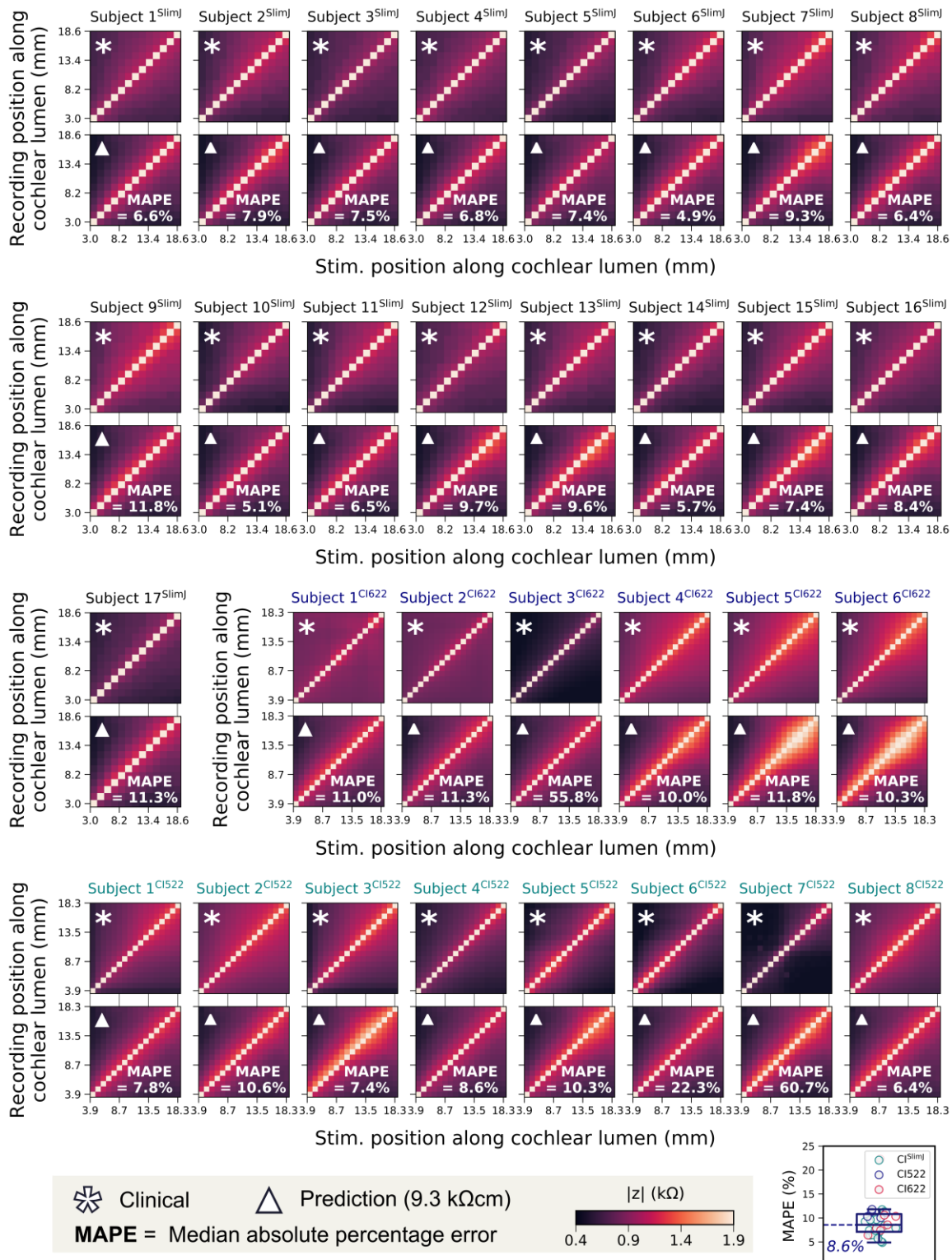
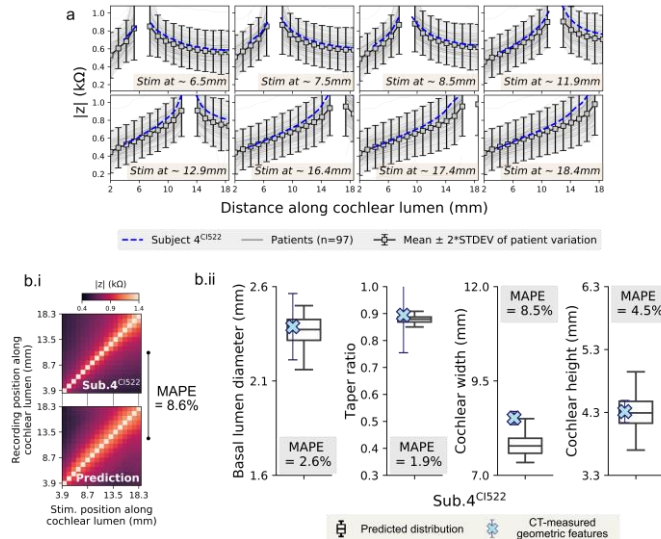


Figure 5.25| Validation of forward-3PNN.



**Figure 5.26| a)** Comparison of the mean patients' EFI profile (derived from 97 profiles) and the profile of subject 4<sup>CI522</sup>. **b)** Performance of (i) forward-3PNN and (ii) inverse-3PNN on subject 4<sup>CI522</sup>.

**Table 5.5| 3PNN performance compared with the MAPE obtained from the population mean EFI.**

	Subjects	MAPE between the 3PNN-predicted EFI and the actual subject's EFI (%)	MAPE between the mean patient EFI and the actual subject's EFI (%)
CI <sup>SlimJ</sup>	Subject 1 <sup>SlimJ</sup>	6.6	21.4
	Subject 2 <sup>SlimJ</sup>	7.9	18.9
	Subject 3 <sup>SlimJ</sup>	7.5	13.3
	Subject 4 <sup>SlimJ</sup>	6.8	19.0
	Subject 5 <sup>SlimJ</sup>	7.4	8.1
	Subject 6 <sup>SlimJ</sup>	4.9	17.0
	Subject 7 <sup>SlimJ</sup>	9.3	25.2
	Subject 8 <sup>SlimJ</sup>	6.4	23.5
	Subject 9 <sup>SlimJ</sup>	11.8	29.7
	Subject 10 <sup>SlimJ</sup>	5.1	10.8
	Subject 11 <sup>SlimJ</sup>	6.5	17.2
	Subject 12 <sup>SlimJ</sup>	9.7	20.3
	Subject 13 <sup>SlimJ</sup>	9.6	18.9
	Subject 14 <sup>SlimJ</sup>	5.7	11.0
	Subject 15 <sup>SlimJ</sup>	7.4	18.9
CI <sup>622</sup>	Subject 1 <sup>CI622</sup>	11.0	29.0
	Subject 2 <sup>CI622</sup>	11.3	23.0
	Subject 3 <sup>CI622</sup>	55.8	7.0
	Subject 4 <sup>CI622</sup>	10.0	38.2
	Subject 5 <sup>CI622</sup>	11.8	40.6
	Subject 6 <sup>CI622</sup>	10.3	41.4
CI <sup>522</sup>	Subject 1 <sup>CI522</sup>	7.8	36.2
	Subject 2 <sup>CI522</sup>	10.6	39.2
	Subject 3 <sup>CI522</sup>	7.4	37.5
	Subject 4 <sup>CI522</sup>	8.6	28.2
	Subject 5 <sup>CI522</sup>	10.3	24.5
	Subject 6 <sup>CI522</sup>	22.3	16.2
	Subject 7 <sup>CI522</sup>	60.7	5.0
	Subject 8 <sup>CI522</sup>	6.4	29.9
<b>Median</b>		<b>8.6</b>	<b>21.4</b>
<b>Interquartile range (IQR)</b>		<b>7.1 – 10.8</b>	<b>16.6 – 29.3</b>

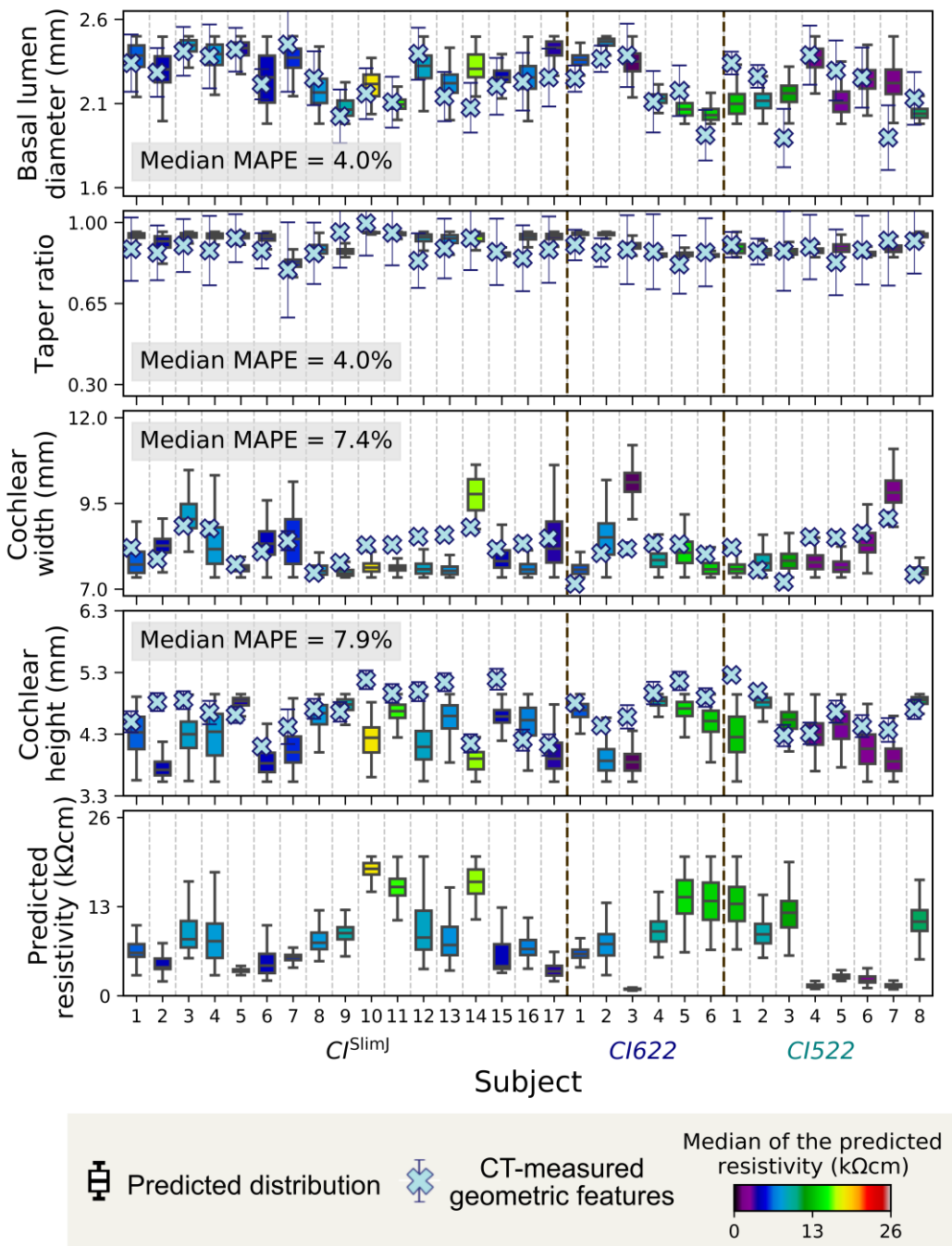


**Figure 5.27| Validation of inverse-3PNN.** The predicted posterior distributions were found using inverse-3PNN and were approximated by sampling 1,000 points in each prediction. Detailed values of the MAPE threshold used in each prediction can be found in Table 5.3. The colours of the boxplots indicate the median of the predicted resistivity. Error bars of the patients' CT-measured geometric features are approximated as half pixel size of the CT scans. The predictions of the patient-specific cochlear resistivity could not be validated due to no reported method of measuring cochlear resistivity of live human.

### 5.3.6 Effect of cochlear electroanatomy on CI voltage spread

With the validated 3PNN model, we proceeded to investigate how the CI voltage spread characteristics could be affected by the four geometric descriptors and the matrix resistivity. Using forward-3PNN, we simulated EFI profiles by sweeping through different combinations of the 5 model descriptors (Example shown in **Figure 5.27**). In total, 3125 (5x5x5x5x5) combinations were evenly sampled to represent the entire modelling space of the 5 model descriptors, and were used to predicted their off-stimulation EFIs.

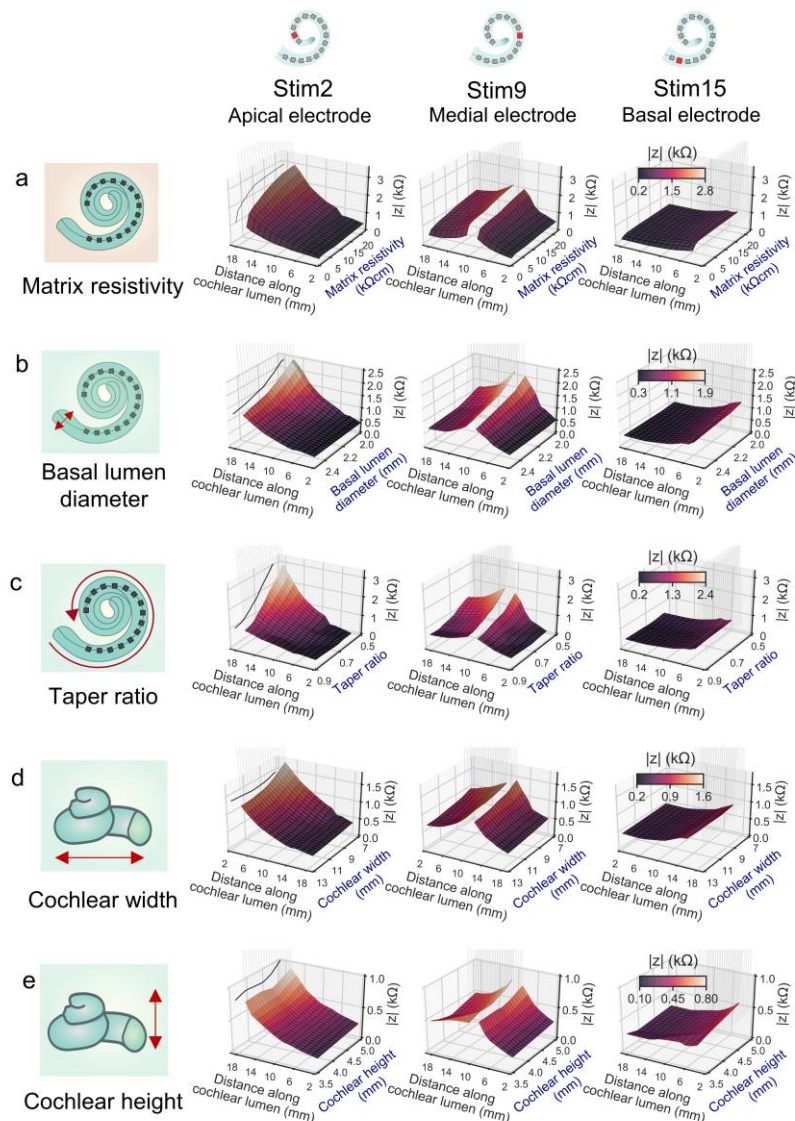


**Figure 5.28| Example showing the trend of the predicted EFI profiles along the 5 model descriptors.** In each graph, only one descriptor varies, while other descriptors are held constant. For visualization purpose, only the transimpedance magnitude  $|z|$  induced by the stimulations at the apical electrode (electrode 2), the medial electrode (electrode 9) and the basal electrode (electrode15) were shown here.

To parameterise the voltage spread characteristics for each predicted EFI profile, we fitted a power law following Equation (5.9), to each stimulus spread toward the apex and toward the base (detailed example shown in **Figure 5.28a – c**),

$$|z| = \frac{V}{I_{stim}} = A|x|^{-b} + C \quad (5.9)$$

where  $|z|$  is transimpedance magnitude,  $V$  is voltage between the recording electrode and the ground electrode,  $I_{stim}$  is stimulation impulse current,  $x$  is distance between the stimulating and the recording intracochlear electrodes along the CI,  $A$  and  $b$  are fitting coefficients, and  $C$  is baseline constant of the EFI, which is defined as the minimum value of the EFI.

Equation (5.9) was adopted here because, theoretically, volume conduction from a point source in a homogeneous medium should follow an inverse relationship with the form of  $|z| = \frac{1}{4\pi\sigma r}$  (where  $\sigma$  is conductivity of the homogeneous medium and  $r$  is distance between the stimulating and the recording intracochlear electrode) [334], and the constant  $C$  captures the baseline feature of EFIs as  $|z|$  approaches the baseline when  $x \rightarrow \infty$ . To evaluate the goodness-of-fit of Equation (5.9), two other potential functional forms (Equations (5.10) and (5.11)) that are able to represent the decay features and the baseline features of EFIs were also evaluated (**Figure 5.29**). The equations were fit to clinical EFIs of different electrode types ( $n = 75$ ), following the method described in Figure 5.28a – c. MAPE between the clinical data and the expected values from the fitting is used as a measure of the goodness-of-fit. The result supports the use of Equation (5.9) to describe EFI features as Equation (5.9) has the lowest MAPE.

$$|z| = \frac{A}{x} + C \quad (5.10)$$

$$|z| = Ae^{-x} + C \quad (5.11)$$

where  $A$  and  $b$  are fitting coefficients, and  $C$  is baseline constant of the EFI.

To quantify the slope of the stimulus spreads, we computed the derivative of Equation (5.9) fitted EFI with respect to  $x$  (Equation (5.12)) for toward the apex or toward the base directions **Figure 5.28d**, and used the mean slope at the  $x = 1$  mm position ( $\overline{\text{Slope}}_{x=1\text{mm}}$ ) as an indicator of the sharpness of voltage drop toward the apex and the base of the cochlea. As shown in **Figure 5.30**, the voltage drop is found to be shallower (smaller  $\overline{\text{Slope}}_{x=1\text{mm}}$  value) in cochleae with larger basal lumen diameter and less tapered cochlear lumen (i.e. taper ratio closer to 1). Therefore, it is predicted that cochleae with these geometric features could

experience broader ‘current spread’, which may activate neurons over a broader spatial region (thus broader spectral convolution). It should be noted, however, that the activation function for neurons should also be considered for a more sophisticated prediction of the induced firing of neurons [335].

$$\frac{d|z|}{dx} = -Abx^{-b-1} \quad (5.12)$$

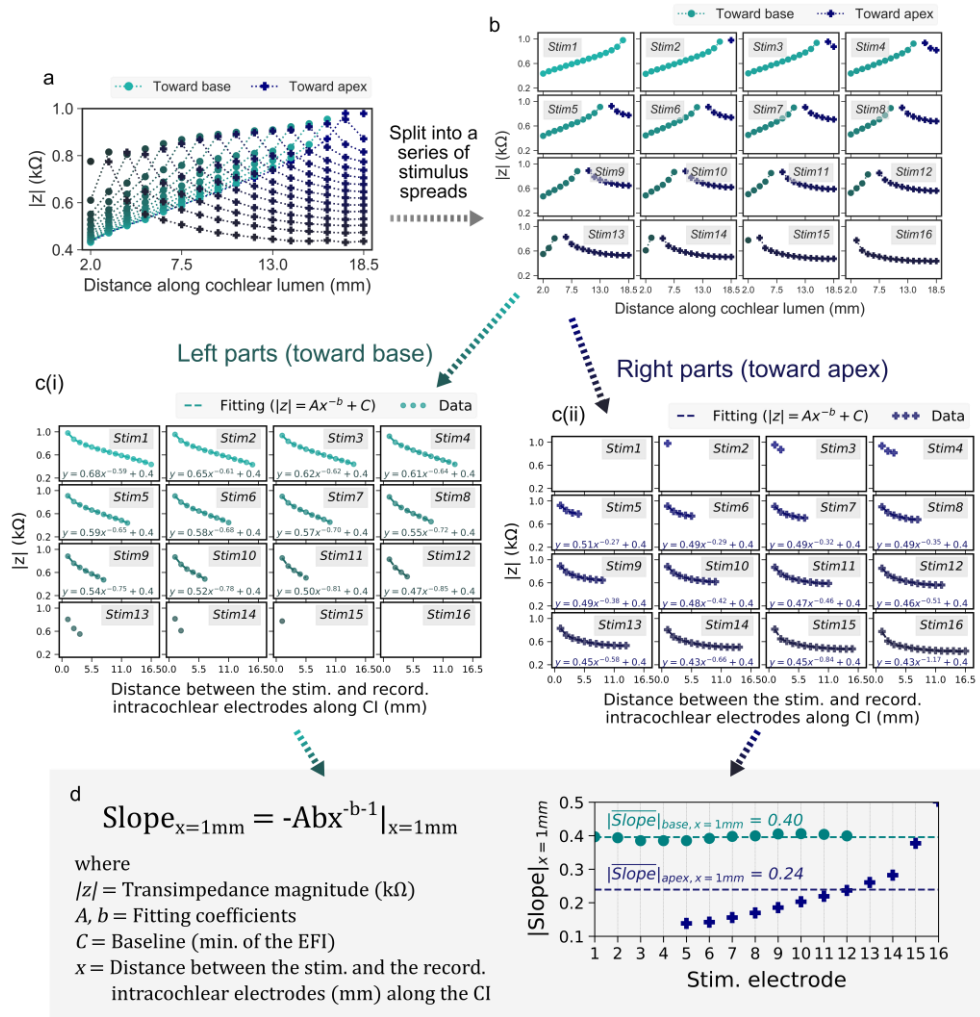


**Figure 5.29| Example of the power-law fitting analysis of EFIs.** **a)** An EFI profile with colours indicating the spreads toward the apex and the base. **b)** The profile was split into a series of stimulus spreads. Each stimulus spread is induced by a stimulation of a CI electrode. **c)** Each stimulus spread is split into two parts – **(i)** spread toward the base (left) and **(ii)** spread toward the apex of a cochlea (right). The x-axis was converted to the distance between the stimulating and the recording intracochlear electrodes along the CI. Fitting of a power law equation ( $|z| = Ax^{-b} + C$ ) was performed for each directional stimulus spread that has a minimum of 4 points. **d)** The slope of each stimulus spread was computed by calculating the derivative of the fitting equation with respect to x. The graph summarises the magnitudes of  $|\text{Slope}|_{x=1\text{mm}}$  of the stimulus spreads toward the apex and toward the base associated with different stimulating electrodes. The mean of the spreads toward the apex ( $|\text{Slope}|_{\text{apex}, x=1\text{mm}}$ ) and the mean of the spreads toward the base ( $|\text{Slope}|_{\text{base}, x=1\text{mm}}$ ) are used to quantify the sharpness of voltage drop toward the base and the sharpness toward the apex in an EFI.

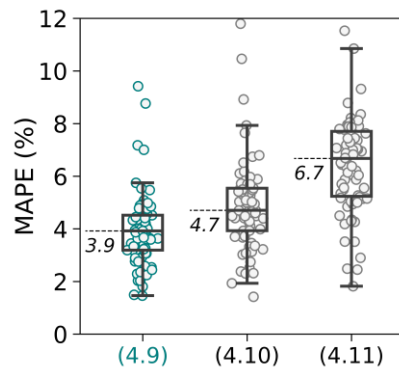


**Figure 5.30| Goodness-of-fit test to evaluate the choice of the fitting forms.**

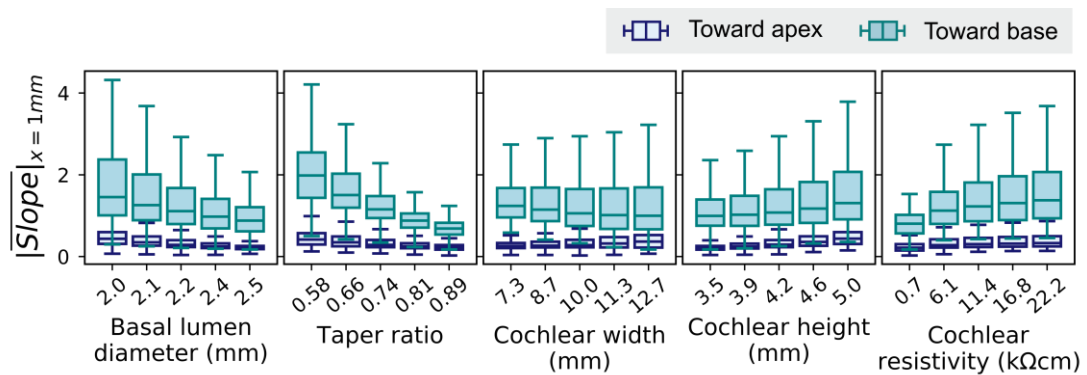


**Figure 5.31| The trend of  $Slope_{x=1mm}$  of the stimulus spreads toward the cochlear apex and the cochlear base across each model descriptor. The line in the box represents the median of the  $Slope_{x=1mm}$  of 625 (5x5x5x5) predicted samples.**

### 5.3.7 On-demand creation of biomimetic cochleae inheriting patient EFIs

The clinical validation of 3PNN demonstrates that the 3D printed biomimetic cochleae can reproduce the off-stimulation EFIs of CI users with high fidelity, despite the physical simplicity of the models. With this validated platform, its application was to construct on-demand cochlear models that can yield patient-specific off-stimulation EPI profiles. **Figure 5.31a** shows the process to generate the patient-specific biomimetic cochlear model, where inverse-3PNN was used to deduce the distribution of the model descriptors that could match each patient's off-stimulation EPI profile with an average similarity over 90% (**Figure 5.31b**), and the patient cochlear model was then fabricated by 3D printing with a predicted set of the model descriptors. As shown in **Figure 5.31c**, the EPI profiles measured from the 3D printed biomimetic cochleae show good resemblance to their corresponding patients' off-stimulation EPI profiles, with  $\text{MAPE} < 12\%$ , while the patients' EPI profiles show a dissimilarity of  $> 30\% \text{ MAPE}$ .

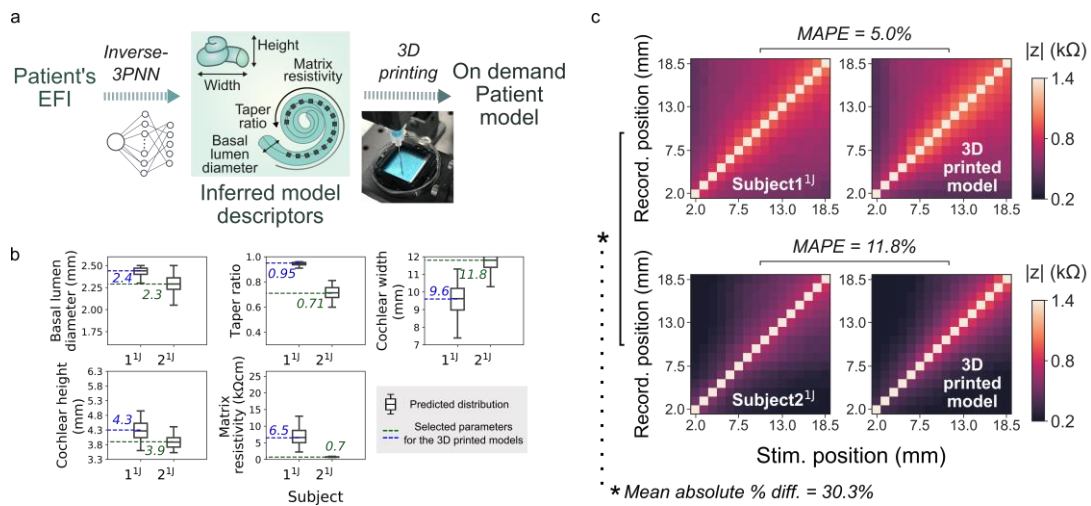


**Figure 5.32| On-demand creation of biomimetic cochleae for replicating patient EFIs.** **a)** Schematic showing the process to generate the patient-specific biomimetic cochlear model. **b)** The predicted distributions of the model descriptors of subjects 1<sup>J</sup> and 2<sup>J</sup>, and the selected parameters for fabricating on-demand patient-specific biomimetic cochleae, which were the median of the predicted descriptors. **c)** Comparison of the off-stimulation EFIs of two patients and the off-stimulation EFIs acquired in their corresponding biomimetic cochleae.

Beyond the application of reproducing patient-specific EFI profile with a physical 3D printed model, 3PNN further points to the potential occurrence of atypical EFI profiles, such as the ‘mid-dip’ characteristics observed in patients. The ‘mid-dip’ characteristic (**Figure 5.32**), which is distinguished by a dip in the EFI profile at the medial electrodes, has not been given a clear clinical explanation. It is uncertain whether unusual implantation orientations or patient-specific cochlear biologic properties could be the origin. By visualising the positions of electrodes in the 3D printed models with  $\mu$ -CT imaging, it was found that the electrode position, which was guided by the cochlear geometry, could be a potential explanation. In the model with the ‘mid-dip’ characteristics, the electrode positions appear to change abruptly (left panel in **Figure 5.32c**), where electrode 8 (e8) was adjacent to two ‘near-wall’ electrodes (e9 and e10) that were in close proximity to the spiral centre. This sudden decrease in the electrode-to-wall distance can potentially cause a slight increase in the EFI profile, hence a dip at e8 in the profile. On the contrary, in the model without the ‘mid-dip’ characteristics, the electrode positions changed gradually. This suggests that the relative position of the electrode to the neighbouring electrodes and the lumen wall can be one of the causes giving rise to the mid-dip abnormality in the EFI profile.

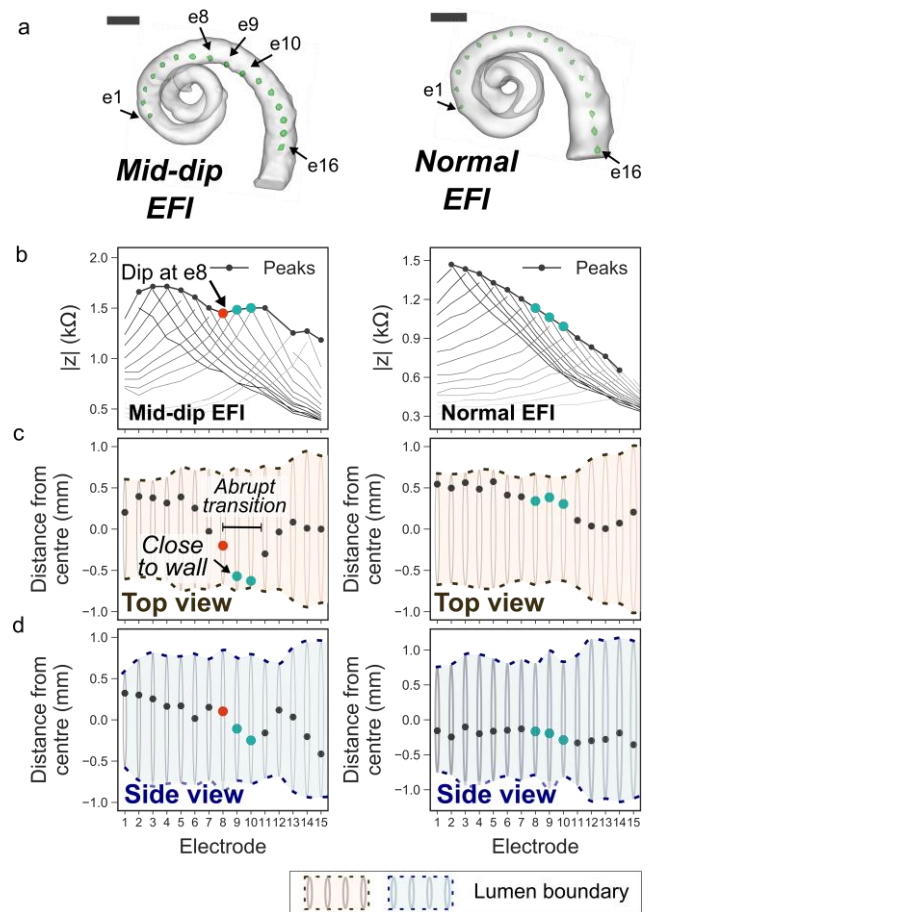


**Figure 5.33| The electrode positions in a model showing an atypical ‘mid-dip’ EFI profile (left) and a model with a typical EFI profile (right).** a) Reconstructed 3D  $\mu$ -CT volumes of the cochlear lumens of the biomimetic cochleae with a CI electrode array inserted (marked green). Scale bar = 2 mm. b) Off-stimulation EFI profiles of the models with the peaks indicating the maximum transimpedance,  $|z|$  of the spread distributions at off-stimulation positions. c) Top view and d) side view of the cochlear lumens of the models, showing the positions of the electrodes in the lumens of the models relative to the lumen wall. Distance in the negative direction refers to the distance towards the cochlear centre, vice versa. Electrode 8 (red) and electrodes 9 – 10 (blue) are highlighted to contrast the electrode contour which generates the mid-dip EFI.

### 5.3.8 Informing patient-specific cochlear tissue resistivity

As the absolute resistivity of patients' temporal bones near the cochlear vicinity cannot be measured non-invasively in living subjects, the inverse-3PNN offered in this study further presents a unique capability in inferring the resistivities of patients' cochlear tissues based on their individual EFI profiles. **Figure 5.33** shows the ranges of the patient-specific resistivities ( $n = 37$ ), which were deduced with unknown geometric descriptors for subjects<sup>1J</sup> 1 – 6 and with paired pre-operative CT (thus known patient geometric descriptors) for the remaining 31 subjects. All the predicted patient resistivity ranges (0.6 – 20.3 kΩcm) lie within the reported resistivity range of live human skulls (0.6 – 26.6 kΩcm) [311–315]. In particular, the mean predicted patient cochlear resistivity (6.6 kΩcm,  $n = 37$ ) is close to the mean reported resistivity of live human skulls (9.3 kΩcm) [311–315].

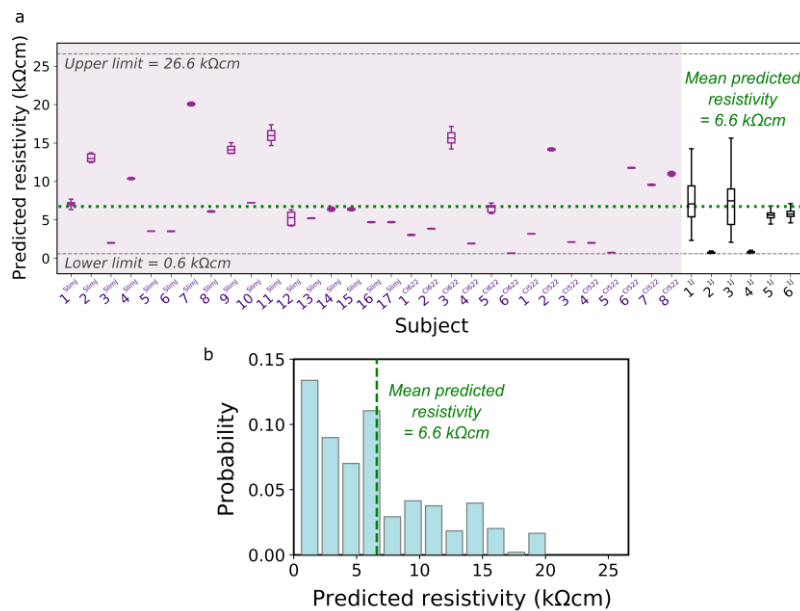


**Figure 5.34| 3PNN estimating patient-specific resistivity of the cochlear tissue.** **a)** Cochlear resistivity predictions of subjects 1 – 6<sup>1J</sup> ( $n = 6$ ) were carried out with unknown patients' geometric descriptors, whereas the rest ( $n = 31$ ) were undertaken with the information of the geometric descriptors measured from their cochlear CT scans. The grey dotted lines show the reported upper and lower limits of *in vivo* human skull resistivities [311–315]. **b)** A histogram showing the distribution of the predicted cochlear resistivity of all patients ( $n = 37$ ). The mean predicted resistivity was found to be 6.6 kΩcm.

### 5.3.9 Potential uncertainty in 3PNN

Several potential sources of uncertainty are noted in 3PNN. These include the discrepancy caused by the absence of the intracochlear membranes in the 3D printed models, the uncertainties in the measurements of the low-resolution clinical CT scans, the deviations in the vertical position of CI electrode array in cochlear lumen, the deviations in the CI electrode insertion depth due to different surgical practices, and the dimensional discrepancy between the patient's cochlea and the cochlear lumen described using the four geometrical descriptors. The absence of the intracochlear membranes in the 3D printed models have been studied in **Figure 5.15**. The potential effects of other uncertainties on EFIs are studied below and are summarized in **Table 5.6**. In addition, the 3D printed cochleae did not account for the frictional force generated during CI electrode insertions beneath the basilar membrane in human cochleae, which may occasionally cause electrode array buckling or even intracochlear trauma affecting CI performance [336, 337]. The friction could have attributed to the localised buckling configuration of the CI electrode array captured in the 3D model giving the 'mid-dip' EFI. Future studies can explore the possibility of incorporating the membranous structures into 3D printed cochlear models, and coupling computational mechanics in the modelling process.

#### *5.3.9.1 Effect of the uncertainty in the CT measurements of the geometric features on off-stimulation-EFI predictions*

The uncertainty in the CT measurements is assumed to be half pixel size of the patient's CT scan. **Figure 5.34a** shows that the MAPE between the predicted EFI using raw measurements and the predicted EFI when a geometric descriptor is subject to  $\pm$  uncertainty. The impact of the uncertainty in basal lumen diameter, cochlear width and cochlear height on the EFI predictions is low, while the uncertainty in taper ratio might cause an significant effect on the predictions with a median MAPE  $\sim 7\%$ .

#### *5.3.9.2 Effect of the vertical position of the electrode array in the cochlea on off-stimulation EFIs*

As the biomimetic cochleae did not mimic the intracochlear membrane structures, the volumetric restriction on the placement of the electrode caused by the membranes cannot be captured in the 3D printed cochlear model. Finite element modelling was used to investigate the effect on off-stimulation EFIs obtained when the vertical position (z-position) of the

electrode array was shifted by 0.5 mm or 1 mm for different matrix resistivities (**Figure 5.34b**). The effect was found to be negligible with a MAPE just < 0.5% when the matrix resistivity of the model was set to 9.3 kΩcm (the mean resistivity of live human skull). The MAPE is increased to ~ 5% when the vertical position was shifted by 1 mm in an extreme model that has a matrix resistivity of 0.6 kΩcm (the lowest bound of the resistivity of live human skull) [311–315].

### ***5.3.9.3 Effect of the deviations in the CI electrode insertion depth due to different surgical practices***

To investigate how much the surgical variation in the insertion depth affects EFIs, the change in EFIs were evaluated when there was a ± 2 mm difference in the typical insertion depth using the 3D printed models ( $n = 18$ ) (**Figure 5.34c**). Overall, an 8% median MAPE is observed.

### ***5.3.9.4 Effect of the dimensional discrepancy between the patient's cochlea and the cochlear lumen described using the four geometrical descriptors on off-stimulation EFIs***

Comparing the patient's cochleae and the cochlear lumens described by the four geometric descriptors (**Figure 5.17c**), most region of the 3D volumes up to 1.5 cochlear turn has a dimensional discrepancy less than ± 0.3 mm. Therefore, sensitivity analyses were performed to investigate the effect of EFIs when the cochlear lumen diameter was subject to ± 0.3 mm via 1) 3PNN (by changing the input values of basal lumen diameter and taper ratio) and by (2) FEM (by enlarging and shrinking the 3D volume of the patient's cochlea by ± 0.3 mm). **Figure 5.34d** shows that the resulting MAPEs obtained from both methods range from 2% to 20.8%, depending on the matrix resistivity. The median MAPE is 4.8% in 3PNN and 8.1% in FEM.

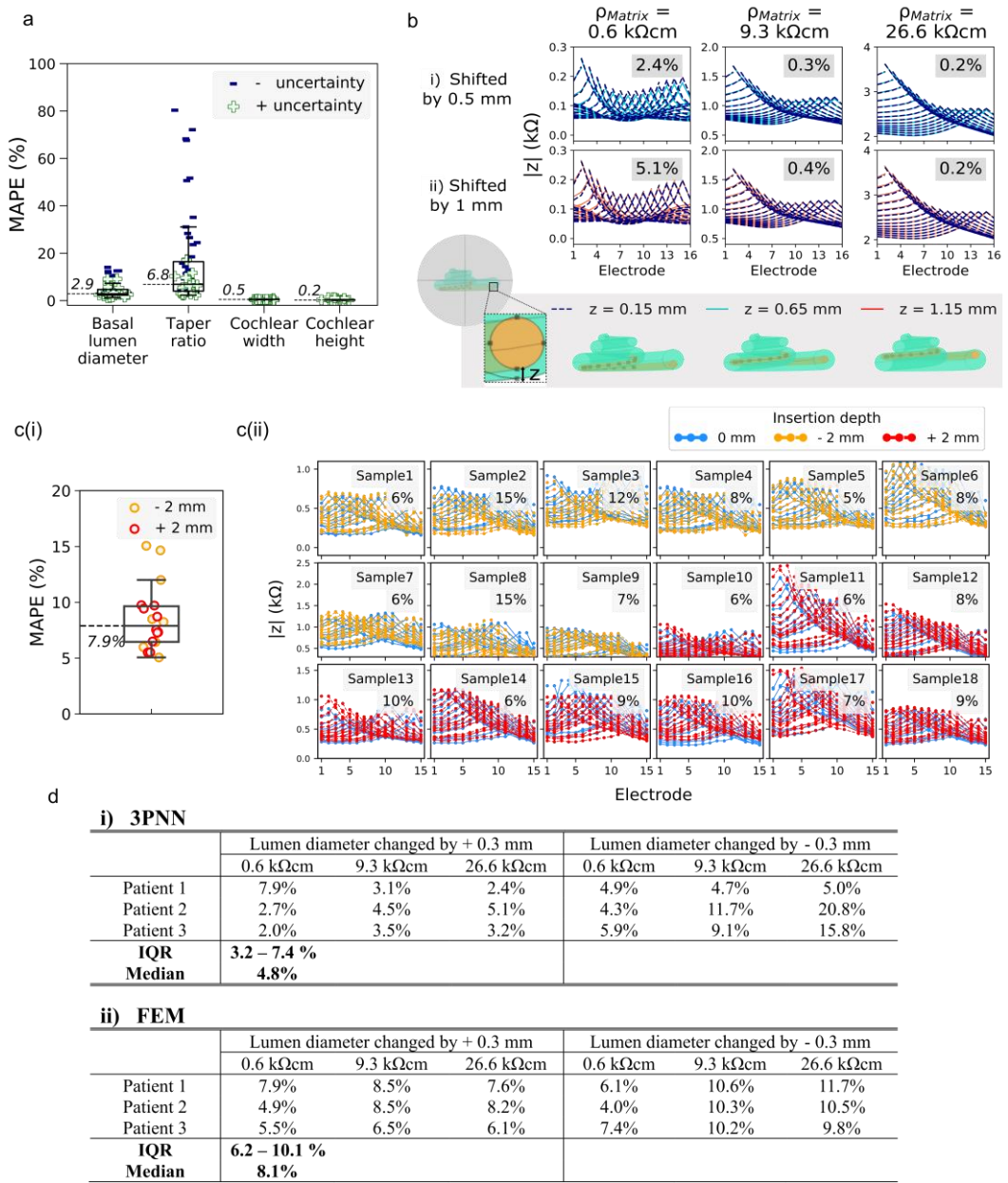


**Figure 5.35| Sensitivity analyses assessing the effect of the potential sources of uncertainty on EFIs.** **a)** The effect of the uncertainty in the CT measurements of the geometric features on EFI predictions.  $n = 62$  predictions based on the CT measurements of 31 patients. **b)** The effect on off-stimulated EFIs when the vertical position (z-position) of the electrode array is shifted by (i) 0.5 mm and (ii) 1 mm for different matrix resistivities. The value at the upper right indicates the MAPE between the z-shifted and the reference (no-shifted) cases. The geometrical features of the COMSOL model are the same as the conditions used in the model without the membrane structures in **Figure 5.15a.ii** and the ground was placed at the outer surface of the 8 mm radius sphere. **c (i)** Boxplot summarised the MAPEs of **(ii)** the experimental CI<sup>1J</sup> EFIs acquired when there was a  $\pm 2$  mm variation in the electrode insertion depth in the 3D printed models ( $n = 18$ ). **d)** The MAPE between the simulated EFIs when the lumen diameter is subject to  $\pm 0.3$  mm at different matrix resistivities computed by i) 3PNN and ii) FEM. IQR = interquartile range.

**Table 5.6| Table summarised the potential uncertainties in 3PNN, and their estimated effect on off-stimulation EFIs.** BL<sub>d</sub> = basal lumen diameter, ρ<sub>matrix</sub> = matrix resistivity, Tr<sub>a</sub> = taper ratio, W<sub>c</sub> = cochlear width and h<sub>c</sub> = cochlear height. IQR = interquartile range.

Potential uncertainty in 3PNN	Approximated error on EFI (MAPE)			
Absence of the membranous structures in the 3D printed models ( <i>Figure 5.15</i> )	IQR = 2.8 – 5.0% Median = 4% (n = 5)			
Uncertainty in patients' CT measurements ( <i>Figure 5.34a</i> )	BL <sub>d</sub>	IQR = 2.3 – 4.7%, Median = 2.9% (n = 62)	Tr <sub>a</sub>	IQR = 4.0 – 16.4%, Median = 6.8% (n = 62)
	W <sub>c</sub>	IQR = 0.4 – 0.5%, Median = 0.5% (n = 62)	h <sub>c</sub>	IQR = 0.2 – 0.3%, Median = 0.2% (n = 62)
Uncertainty in z-position of CI electrode array in cochlear lumen (shifted from 0.5 – 1 mm) ( <i>Figure 5.34b</i> )	IQR = 0.3% - 2.8% Median = 0.4% (n = 6)			
Variation in CI insertion depth due to different surgical practices (± 2 mm) ( <i>Figure 5.34c</i> )	IQR = 6.4 – 9.6% Median = 7.9% (n = 18)			
Geometrical discrepancy between patient cochlea and model's geometry (± 0.3 mm) ( <i>Figure 5.34d</i> )	IQR = 3.2 – 7.4% (3PNN) or 6.2 – 10.1% (FEM) Median = 4.8% (3PNN) or 8.1% (FEM) (n = 18)			

### 5.3.10 Limitation of finite element modelling

The 3PNN co-modelling approach proposed in this study provides a complementary, statistical and data-driven approach derived from 3D printed biomimetic cochleae. Comparing with FEM, 3PNN utilises physical models to bypass the sensitivity in the choice of boundary conditions and undetermined physical laws that were normally faced by FEM. The choice of the boundary condition was known to be undetermined in simulating cochlear stimulation via FEM [286]. In monopolar cochlear stimulation, the return electrode lies outside the physical domain of the model, hence, there is no boundary condition that can perfectly match the *in vivo* situation [286]. As shown in **Figure 5.35a**, the simulated FEM profile is greatly affected by the choice of the boundary condition. Although placing the ground at the lumen opening in FEM (condition I) yields the EFIs most matching to the experimental EFIs, the resemblance is still not ideal. In addition, even condition VII in FEM exactly mimics the five electroanatomical features of the 3D printed models and the grounding condition employed in experiments, FEM cannot reproduce the results of the physical models due to the undetermined modelling parameters. When performing the same comparative study for a linear geometry, as shown in **Figure 5.35b**, the MAPE can be > 180%. Hence, the physical phenomenon descriptions provided by FEM might be incomplete. However, it should be noted that any computational modelling has both advantages and disadvantages. The benefits of FEM are still manifold, which notably includes the possibility of studying individual boundary condition/parameter at

a time with a graphical user interface. Additionally, FEM has been adopted as an ancillary measure at several points in this study to validate several assumptions undertaken in 3PNN that are not easily examined by 3PNN alone (e.g. how the presence of the intracochlear membranes affects EFIs).

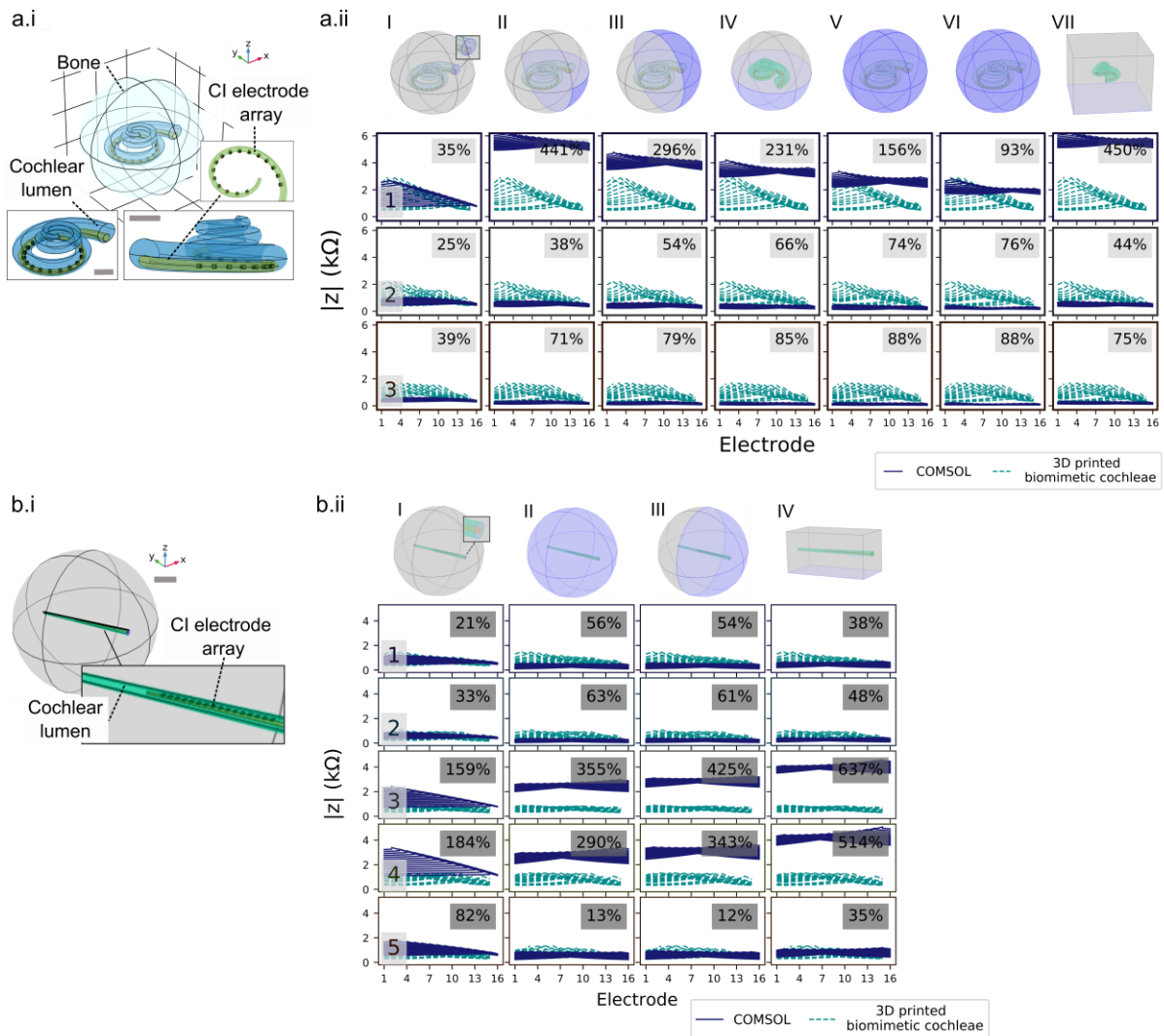


**Figure 5.36| The effect of boundary conditions on finite element modelling of cochlear stimulation.** **a.i)** FEM of a simplified spiral cochlea without the membrane structures. Scale bar = 2 mm. **a.ii)** Off-stimulation EFI profiles simulated with the common choices of boundary conditions used in literature, in comparison with the experimental results acquired from the corresponding 3D printed cochlear models that have the same electroanatomical model descriptors as the COMSOL models. The FEM boundary conditions studied here are ground at **(I)** the cochlear lumen opening, **(II)** a quarter of the outer surface, which is near the lumen opening, of the 8 mm radius sphere. **(III)** half of the outer surface of the 8 mm radius sphere, **(IV)** the bottom half of the outer surface of the 8 mm radius sphere, **(V)** the outer surface of the 8 mm radius sphere, **(VI)** the outer surface of an infinitely surrounding sphere, and **(VII)** the bottom surface of a 20x20x15 mm cuboid, as highlighted in blue. 3 models are examined here. They

have the same geometric features ( $BL_d = 2.38$  mm,  $Tr_a = 0.59$ ,  $W_c = 10.5$  mm,  $h_c = 4.4$  mm) but different matrix resistivities (model 1: 23.4 k $\Omega$ cm, model 2: 1.9 k $\Omega$ cm and model 3: 0.7 k $\Omega$ cm). **b.i)** FEM of a linear uncoiled cochlea without the membrane structures. Scale bar = 10 mm. **b.ii)** Off-stimulation EFIs simulated using four different choices of boundary condition, in comparison with the experimental results acquired from the corresponding 3D printed linear cochlear models that have the same electroanatomical model descriptors as the COMSOL models. The boundary condition examined here are ground at **(I)** the cochlear lumen opening, **(II)** the outer surface of the 30 mm radius sphere, **(III)** half of the outer surface of the 30 mm radius sphere, and **(IV)** the bottom surface of a 40.6x15x15 mm cuboid, as indicated in blue. 4 linear models were examined here. They have the following electroanatomical features – Model 1:  $BL_d = 2.38$  mm,  $Tr_a = 1$ ,  $L_c = 40.6$  mm, and  $R_m = 23.4$  k $\Omega$ cm; Model 2:  $BL_d = 2.38$  mm,  $Tr_a = 0.79$ ,  $L_c = 40.6$  mm, and  $R_m = 1.9$  k $\Omega$ cm; Model 3:  $BL_d = 2.38$  mm,  $Tr_a = 0.79$ ,  $L_c = 40.6$  mm, and  $R_m = 1.9$  k $\Omega$ cm; Model 4:  $BL_d = 2.5$  mm,  $Tr_a = 0.59$ ,  $L_c = 40.6$  mm, and  $R_m = 3.6$  k $\Omega$ cm; The values at the upper right of the graphs indicate the MAPEs between the simulated EFIs and the experimental EFIs.  $BL_d$  = basal lumen diameter,  $Tr_a$  = taper ratio,  $W_c$  = cochlear width and  $h_c$  = cochlear height.

## 5.4 Conclusion

This study created a physical library of 3D printed biomimetic cochlear models that statistically captures the reported broad spectrum of off-stimulation EFI profiles of CI patients, which are dependent on the patterns of electrical conduction through tissues. The 3D printed cochlear models can be used multiple times and were designed with impedance-tunable electromimetic bone matrices that display suitable mechanical stiffness for geometrically-guided CI electrode insertion, while limiting damage to CI electrodes during insertion. Complementary to FEM, the 3D printed biomimetic cochleae offer a robust physical means to replicate the dynamics of ionic conduction and the electron-ion interaction in cochleae with implanted CIs. This is useful as it bypasses the sensitivity in the choice of boundary conditions that are required in FEM (**Figure 5.35**), and it intrinsically captures physical phenomena that could be difficult to replicate fully in FEM.

The use of standard-of-care patient CT scans in 3PNN is practical for clinical translation because high-resolution micro-CT scans cannot be performed in living patients. As the associated resolution of clinical CT scans does not allow for detailed construction of cochlear surface contours, nor the inclusion of the membranous structures (~2 to 4  $\mu$ m thick as reported in literature [281, 307]), 3PNN does not aim to capture the thorough structural details of human cochleae. It should be noted that the accuracy of 3PNN could be subject to several uncertainties.

The effects of the uncertainties are summarised in **Table 5.6**.

Adopting machine learning along with parametric descriptions of the cochlear geometry, 3PNN requires only a fraction of the computation time per EFI prediction (estimated 300 times faster) compared to our FEM models (for Intel i5 CPU). The fast and automated nature of 3PNN facilitates the generation of sufficient amount of simulated data for deciphering trend and sensitivity in a high dimensional problem. This is imperative for solving the ‘volume conduction’ problem, the first step in computational neuroengineering for modelling electrical stimulation in a biological structure [291]. This work also suggests that the intracochlear excitation spread can be largely reproduced by physically replicating the volumetric conduction within the cochlear lumen and the cochlear tissue vicinity without biological components. Further studies that evaluate the correlation between the intracochlear voltage distribution and the excitation of neural cells will be of particular benefit to expand the use of 3PNN in modelling the signal perception at the neuronal level.

The framework proposed in this study could potentially provide the first approach to readily infer the *in vivo* bulk resistivity of individual patient’s cochlear bone matrix via CI telemetry. Validation of the accuracy of the cochlear tissue resistivity prediction is not performed in the current work; this is because, as of yet, there is no reported method to measure cochlear tissue resistivity in live patients. In the present work, a default resistivity value of 9.3 k $\Omega$ cm (mean resistivity of live human skull) was used to approximate the patient-specific resistivity of cochleae tissues in forward-3PNN. Thus, providing future validation to the inferred mean cochlear tissue resistivities (e.g. 6.6 k $\Omega$ cm,  $n = 37$ ) can potentially further improve the predictive power of forward-3PNN. Alternatively, future investigations which explore the correlation between the 3PNN inferred cochlear tissue resistivity and the cochlear physiological and pathological status, may provide a foundation for the use of CI telemetry as a diagnostic indicator. This might enable the detection of early abnormalities after CI implantation, without resorting to imaging methodologies that use ionizing radiation in patients (which particularly should be avoided in children).

Overall, 3PNN was demonstrated to be predictive for correlating the off-stimulation EFI and the geometric parameters collected from clinical patient CTs, without the need for model adjustment and re-calibration. This was validated with clinical EFI data of four different CI types (up to a position of 18.5 mm along the cochlear lumen), and 28 out of 31 predictions show good accuracy, MAPE < 12% (median MAPE = 8.6%). Therefore, the co-modelling framework has a potential capability of forecasting the stimulation performance of CIs from different manufacturers, hence assisting the development of CI electrode arrays tailored to

patient's cochlear anatomy. Comparing to conventional animal and cadaver models, the 'print-and-learn' modelling concept proposed here offers a physical-manipulatable, ethical and economic approach, which may help reduce the need for animal experiments. Complemented with FEM, 3PNN could form a building block for future cochlear digital twins for CI testing. With the rising usage of neuromodulating electronic implants, the 'print-and-learn' co-modelling concept proposed here is anticipated to facilitate the physical modelling and digital twin innovation of other bioelectronic implant prototypes, beyond its applications in CIs.

# Chapter 6

## Conclusions and Future Work

### 6.1 Conclusions

3D extrusion-based printing holds promises for facile fabrication of a wide variety of soft materials, offering the potential to manufacture innovative systems with better biomimicry in structures and compositions. As yet, the innovation and wide adoption of extrusion-based soft material printing technology grapples with problems of high cost and lacking guideline for the standardisation of the printing process. Although many previous published studies have demonstrated the applications of 3D printing in producing biology-inspired anatomical models with excellent shape resemblance, these models usually lack functionality and hence are not capable to provide insights into clinical problems that are anatomy-dependent. Therefore, this thesis focuses on 1) developing a replicable and versatile 3D extrusion printing platform for soft materials as an affordable alternative to commercial systems, 2) proposing a rational guideline on the decision of printing methods for soft materials, and 3) developing a modelling technique that combines 3D printing and machine learning to model the electroanatomical-dependent ‘current spread’ phenomena evoked by neuromodulation implants in human tissues. The principal findings of my research work are summarised below.

#### 6.1.1 Development of a printing platform for soft materials

A customisable and low-cost extrusion-based printing platform was developed from scratch using simple mechanical components, 3D printed parts, and a compact robotic arm. The cost of the platform starts from £900 for a single printhead system to £1900 for a fully equipped system with four printheads, syringe and stage heaters, and an UV module. Enabled by the hackable programmes I developed in this work, the platform offers fully flexible operations and accepts unconventional geometry inputs, (i.e. coordinates, equations, and pictures), beyond the standard 3D CAD model input offered by commercial printers.

Comparing to commercial printing platforms, this platform offers significant cost saving and a high degree of customisability that allows unprecedented operations, such as non-planar printing and printing with variable speed. The control programme is user-friendly and was designed for users who had no prior programming experience. With the use of a robotic arm, the platform can be compact in size and is easy to install. The detailed instruction of the assembly method and the programme design provided in this study can promote the replicability of the platform, hence new users can contribute towards the future development of the platform. Several limitations of the platform are noted. They are the payload limit (0.5 kg) and the inferior precision and repeatability of the robotic arm ( $\sim 200 \mu\text{m}$ ). However, the 0.5 kg capacity should suffice most lab-based operations, and the position repeatability problem encountered when fabricating multi-material objects can be overcome by the manual calibration system offered by the platform, which helps users to readjust the location for creating well-aligned objects.

### **6.1.2 An investigation on methods for soft material printing**

With the extrusion-based printing platform I developed, I explored methods for fabricating a wide range of soft materials, ranging from naturally derived hydrogels (e.g. collagen), synthetic hydrogels, pH-responsive hydrogels (e.g. polyacrylic acid) to silicone elastomers. I tested the printability of inks in different supportive baths reported in previous literature. The finding here reveals the importance of auxiliary tools (i.e. UV and heating systems) and the choice of supportive baths on the success of printing. Specifically, I proposed the use of oil-based baths for silicone resin-based inks and pH-responsive hydrogels; gelatin slurry for hydrogels that crosslink via ionic and pH methods, and Carbopol for thermal- and photo-crosslinkable hydrogels. The rational guide proposed in this study might help new users efficiently design appropriate fabrication methods for their applications. Further research could be undertaken to systematically investigate the effect of different factors, such as rheology, surface tension and ionic charge of the support bath and the ink, on the ink printability (discussed in **Section 6.2.3**). This information will enable a comprehensive perspective for the standardisation of the technology.

### 6.1.3 3D printed biomimetic cochleae and machine learning co-modelling provides clinical informatics for cochlear implant patients

The work here integrates 3D extrusion printing technology with neural network machine learning model (termed ‘3PNN’) for interpreting clinical electric field imaging (EFI) profiles of CI patients. The 3D printed cochleae were created with tuneable electro-anatomy to capture the human variability, and were able to replicate clinical scenarios of EFI profiles at the off-stimuli positions. Several applications of this co-modelling framework were demonstrated, including autonomous predictions of patient EFI or cochlear geometry, unfolding the electro-anatomical factors causing CI stimulus spread, on-demand printing of patient-specific models that gave similar patient EFI profile for CI testing, and inference of patients’ *in vivo* cochlear tissue resistivity by CI telemetry. Nonetheless, it should be noted that the predictions are subject to several uncertainties, such as the uncertainties in the clinical CT measurements and the variation in the CI electrode array insertion depth due to different surgical practices, etc.

3PNN does not aim to capture the exact geometrical details of human cochleae. Specifically, 3PNN uses four geometrical descriptors to describe the shape of cochlear lumens, and the matrices of the 3D biomimetic models do not imitate the porous and spatially heterogeneous bone structure. The reason is twofold. First, this makes 3PNN practical for clinical translation as clinical CT scans do not typically have sufficient resolution revealing the detailed structures of the patients’ cochleae. Second, this allows ease of interpretation and reduces modelling time and cost. The fact that the intracochlear excitation spread can be largely reproduced by physical *in vitro* models without any biological components also suggests that it is unnecessary to imitate the full setting of clinical scenarios, but rather important to choose appropriate representative features when modelling complex real-world problems. Taken together, I envisage that the co-modelling principle proposed in this study could facilitate other areas of clinical modelling and promote the digital twin innovations for electrical prostheses in healthcare.

## 6.2 Future work

### 6.2.1 Further development of the custom-made 3D extrusion printing platform

Several potential improvements of the platform can be made to further advance its user-friendliness and functionality. As discussed in [Chapter 3](#), the setup can be advanced by the incorporations of 1) an automatic calibration system for efficient operations, 2) cooling systems for printing protein-based hydrogels, 3) a retraction mechanism for preventing the ink from oozing during transition between print paths and 4) a multi-channel microfluidic printhead for rapid material switching in heterogeneous material printing. Further to these, novel printheads can be developed to advance the printing methods. For example, inclusions of coaxial printheads and copper electrode printheads will permit fabrication of core-shell structures and ionoprinting [338]. Micropipette printheads will enable small volume depositions, which is desirable for inks that are present in small quantities, such as cell pellets and organoids. Preliminary work has been done in developing a micropipette printhead (**Figure 6.1**). However, an alignment issue has been observed with the current design, causing inaccurate deposition. The design of the micropipette printhead should be improved in the future to ensure the central alignment of the micropipette. Lastly, a graphical user interface (GUI) for operation control might make the platform more accessible and easier to use, however it should be noted that the use of a GUI reduces the customisability of the platform.

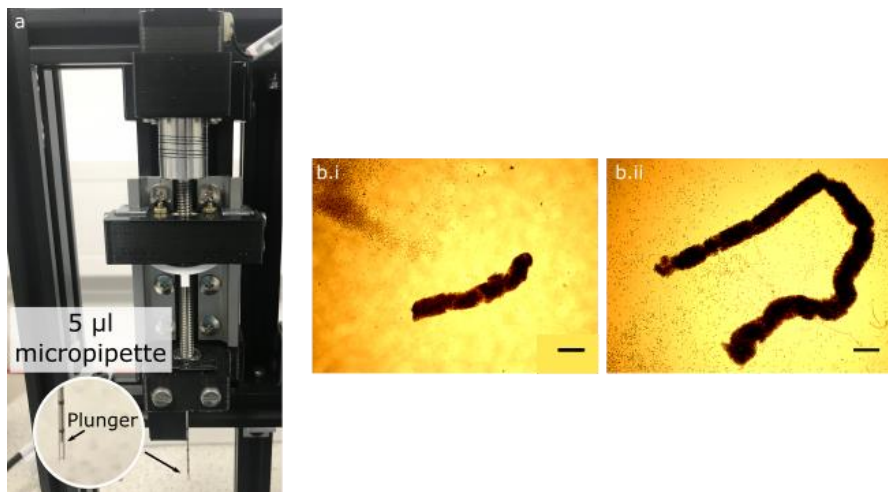


**Figure 6.1|** **a)** A preliminary prototype of a micropipette printhead that is designed to couple with a 5  $\mu\text{l}$  or 10  $\mu\text{l}$  PCR micropipette. **b)** Preliminary results showing i) a 5 mm and ii) a 15 mm line made of cell pellet and Matrigel printed using the micropipette printhead shown in (a). Scale bars = 1 mm.

### 6.2.2 Fabrication of complex pH-responsive soft actuators

In [Chapter 4](#), the morphing behaviours of 2D pH-responsive strips made of PAA filaments at different infill angles were investigated. Future work should further examine the effect of different strip sizes and heterogeneous infill patterns on the shape evolution for a complete understanding on the anisotropic swelling mechanism. Structures of heterogeneous print paths can be designed and fabricated using the picture geometry input offered by the printer. With the oil-based support bath proposed in Chapter 4, it will be intriguing to fabricate three-dimensional complex structures made of more than one pH-responsive hydrogels to form dual-responsive systems. Potential candidates are PAA that swells in alkali and chitosan that swells in acid. These dual-responsive systems might offer possibility for achieving complicated and multi-directional actuations for uses in biocompatible soft robots.

### 6.2.3 Rheological and interfacial measurements of inks and support baths

*Due to COVID restrictions, there was a restricted accessibility to the rheometer, hence the rheology of the inks and the support baths was not studied in Chapter 4.*

In [Chapter 4](#), a conceptual guideline for printing soft materials is proposed based on empirical observation, and the capability of the support baths previous reported in literature, including gelatin slurry developed in FRESH v1.0 method (gelatin type A) [52], Carbopol [122] and fumed silica-mineral oil baths [168], were assessed.

To further enable the standardisation of the printing process and provide a comprehensive guideline, a systematic study should be carried out to quantify the relationship between the print fidelity and the rheological of the inks and the bath, such as storage modulus ( $G'$ ) and viscosity. As ionic interaction between the bath and the ink can tremendously increase the viscosity and  $G'$  of the printed ink, examining the effect of the ionic charge of the bath on the embedded printability of the ink would be beneficial. In addition, beyond the support baths tested in this study, the performance of other commonly used support baths in literature, such as gelatin slurry (type B) developed in FRESH v2.0 [136] and agarose fluid gel [163], should be assessed to attain a broader investigation. Lastly, as the surface tension between the ink and the bath is highly crucial to the printability in phase difference systems, it would be advantageous to further examine the use of surfactants in arresting the shape evolution in these systems. The scope of work proposed here could greatly benefit the research community, saving the time-consuming trial-and-error process for finding an appropriate printing method.

#### **6.2.4 Further improvement on the 3PNN co-modelling framework**

A few uncertainties have been noted in the 3PNN framework. These uncertainties hamper the accuracy in modelling the electric-field imaging profiles of cochlear implant patients. The accuracy of a neural network model in general can be improved with the amount of input dataset. Therefore, more 3D printed cochlear models capturing a wider range of geometric descriptors should be fabricated to increase the prediction accuracy of 3PNN. Apart from this, further study can be undertaken to construct a spatially heterogeneous architecture in the electro-mimetic bone matrices of the 3D printed cochlear models for mimicking the spatially-dependent tissue properties of human cochleae.

## References

1. Capel AJ, Rimington RP, Lewis MP, Christie SDR (2018) 3D printing for chemical, pharmaceutical and biological applications. *Nat. Rev. Chem.* 2:422–436
2. Daly AC, Prendergast ME, Hughes AJ, Burdick JA (2021) Bioprinting for the Biologist. *Cell* 184:18–32
3. Zhang YS, Oklu R, Dokmeci MR, Khademhosseini A (2018) Three-dimensional bioprinting strategies for tissue engineering. *Cold Spring Harb Perspect Med* 8:
4. Truby RL, Lewis JA (2016) Printing soft matter in three dimensions. *Nature*
5. Bajaj P, Schweller RM, Khademhosseini A, West JL, Bashir R (2014) 3D biofabrication strategies for tissue engineering and regenerative medicine. *Annu. Rev. Biomed. Eng.*
6. Wallin TJ, Pikul J, Shepherd RF (2018) 3D printing of soft robotic systems. *Nat. Rev. Mater.*
7. Hull CW (1984) Apparatus for production of three-dimensional objects by stereolithography
8. Murphy S V., Atala A (2014) 3D bioprinting of tissues and organs. *Nat. Biotechnol.*
9. Wong KC (2016) 3D-printed patient-specific applications in orthopedics. *Orthop. Res. Rev.*
10. Sun W, Starly B, Daly AC, Burdick JA, Groll J, Skeldon G, Shu W, Sakai Y, Shinohara M, Nishikawa M, Jang J, Cho DW, Nie M, Takeuchi S, Ostrovidov S, Khademhosseini A, Kamm RD, Mironov V, Moroni L, Ozbolat IT (2020) The bioprinting roadmap. *Biofabrication*
11. Ngo TD, Kashani A, Imbalzano G, Nguyen KTQ, Hui D (2018) Additive manufacturing (3D printing): A review of materials, methods, applications and challenges. *Compos. Part B Eng.*
12. Dizon JRC, Espera AH, Chen Q, Advincula RC (2018) Mechanical characterization of 3D-printed polymers. *Addit. Manuf.*

13. Cambridge University Engineering Department (2019) Materials Data Book 2011 Edition
14. Zhou LY, Fu J, He Y (2020) A Review of 3D Printing Technologies for Soft Polymer Materials. *Adv. Funct. Mater.*
15. Vaicekauskaite J, Mazurek P, Vudayagiri S, Skov AL (2020) Mapping the mechanical and electrical properties of commercial silicone elastomer formulations for stretchable transducers. *J Mater Chem C*
16. Ahmed EM (2015) Hydrogel: Preparation, characterization, and applications: A review. *J. Adv. Res.*
17. Das S, Basu B (2019) An Overview of Hydrogel-Based Bioinks for 3D Bioprinting of Soft Tissues. *J. Indian Inst. Sci.*
18. Brandl F, Sommer F, Goepferich A (2007) Rational design of hydrogels for tissue engineering: Impact of physical factors on cell behavior. *Biomaterials*
19. Annabi N, Tamayol A, Uquillas JA, Akbari M, Bertassoni LE, Cha C, Camci-Unal G, Dokmeci MR, Peppas NA, Khademhosseini A (2014) 25th anniversary article: Rational design and applications of hydrogels in regenerative medicine. *Adv Mater* 26:85–124
20. Drury JL, Mooney DJ (2003) Hydrogels for tissue engineering: Scaffold design variables and applications. *Biomaterials* 24:4337–4351
21. Lutolf MP, Raeber GP, Zisch AH, Tirelli N, Hubbell JA (2003) Cell-responsive synthetic hydrogels. *Adv Mater*
22. Malda J, Visser J, Melchels FP, Jüngst T, Hennink WE, Dhert WJA, Groll J, Hutmacher DW (2013) 25th anniversary article: Engineering hydrogels for biofabrication. *Adv. Mater.*
23. GhavamiNejad A, Ashammakhi N, Wu XY, Khademhosseini A (2020) Crosslinking Strategies for 3D Bioprinting of Polymeric Hydrogels. *Small*
24. Kim D, Kim S, Jung S (2021) Fabrication and characterization of polysaccharide metallohydrogel obtained from succinoglycan and trivalent chromium. *Polymers (Basel)*
25. M.A. Mateesc, P. Ispas-Szabo, E. Assaad (2015) Chitosan-based polyelectrolyte complexes as pharmaceutical excipients. In: *Controlled Drug Delivery*. Woodhead

- Publishing, pp 127–161
26. Alberts B, Johnson A, Lewis J (2002) The Extracellular Matrix of Animals. *Mol Biol Cell*
  27. Hospodiuk M, Dey M, Sosnoski D, Ozbolat IT (2017) The bioink: A comprehensive review on bioprintable materials. *Biotechnol. Adv.*
  28. Farokhi M, Aleemardani M, Solouk A, Mirzadeh H, Teuschl AH, Redl H (2021) Crosslinking strategies for silk fibroin hydrogels: Promising biomedical materials. *Biomed. Mater.*
  29. Baumgartner M, Hartmann F, Drack M, Preninger D, Wirthl D, Gerstmayr R, Lehner L, Mao G, Pruckner R, Demchyshyn S, Reiter L, Strobel M, Stockinger T, Schiller D, Kimeswenger S, Greibich F, Buchberger G, Bradt E, Hild S, Bauer S, Kaltenbrunner M (2020) Resilient yet entirely degradable gelatin-based biogels for soft robots and electronics. *Nat Mater*
  30. Zolfagharian A, Kaynak A, Khoo SY, Kouzani AZ (2018) Polyelectrolyte soft actuators: 3D printed chitosan and cast gelatin. *3D Print Addit Manuf*
  31. Highley CB, Rodell CB, Burdick JA (2015) Direct 3D Printing of Shear-Thinning Hydrogels into Self-Healing Hydrogels. *Adv Mater*
  32. Okamoto A, Miyoshi T (2002) A BIOCOMPATIBLE GEL OF HYALURONAN. In: *Hyaluronan*
  33. Gasperini L, Mano JF, Reis RL (2014) Natural polymers for the microencapsulation of cells. *J. R. Soc. Interface*
  34. Zia KM, Tabasum S, Khan MF, Akram N, Akhter N, Noreen A, Zuber M (2018) Recent trends on gellan gum blends with natural and synthetic polymers: A review. *Int. J. Biol. Macromol.*
  35. Patel J, Maji B, Moorthy NSHN, Maiti S (2020) Xanthan gum derivatives: Review of synthesis, properties and diverse applications. *RSC Adv.*
  36. Habib A, Sathish V, Mallik S, Khoda B (2018) 3D printability of alginate-carboxymethyl cellulose hydrogel. *Materials (Basel)*
  37. Jain S, Sandhu PS, Malvi R, Gupta B (2013) Cellulose derivatives as thermoresponsive

- polymer: An overview. *J. Appl. Pharm. Sci.*
38. Wang Y, Zhang L, Lu A (2020) Highly stretchable, transparent cellulose/PVA composite hydrogel for multiple sensing and triboelectric nanogenerators. *J Mater Chem A*
39. Demirtaş TT, Irmak G, Gümüşderelioğlu M (2017) A bioprintable form of chitosan hydrogel for bone tissue engineering. *Biofabrication*
40. Subramani R, Izquierdo-Alvarez A, Bhattacharya P, Meerts M, Moldenaers P, Ramon H, Van Oosterwyck H (2020) The Influence of Swelling on Elastic Properties of Polyacrylamide Hydrogels. *Front Mater*
41. Valentin TM, Dubois EM, Machnicki CE, Bhaskar D, Cui FR, Wong IY (2019) 3D printed self-adhesive PEGDA-PAA hydrogels as modular components for soft actuators and microfluidics. *Polym Chem*
42. Zeugolis DI, Paul RG, Attenburrow G (2008) Engineering extruded collagen fibers for biomedical applications. *J Appl Polym Sci*
43. Wu W, Deconinck A, Lewis JA (2011) Omnidirectional printing of 3D microvascular networks. *Adv Mater*
44. Tsai YL, Theato P, Huang CF, Hsu S hui (2020) A 3D-printable, glucose-sensitive and thermoresponsive hydrogel as sacrificial materials for constructs with vascular-like channels. *Appl Mater Today*
45. Gauvin-Rossignol G, Legros P, Ruel J, Fortin MA, Bégin-Drolet A (2018) Sugar glass fugitive ink loaded with calcium chloride for the rapid casting of alginate scaffold designs. *Heliyon*
46. Jin Y, Chai W, Huang Y (2018) Fabrication of Stand-Alone Cell-Laden Collagen Vascular Network Scaffolds Using Fugitive Pattern-Based Printing-Then-Casting Approach. *ACS Appl Mater Interfaces*
47. Lankalapalli S, Kolapalli VRM (2009) Polyelectrolyte complexes: A review of their applicability in drug delivery technology. *Indian J. Pharm. Sci.*
48. Nasti A, Zaki NM, De Leonardis P, Ungphaiboon S, Sansongsak P, Rimoli MG, Tirelli N (2009) Chitosan/TPP and chitosan/TPP-hyaluronic acid nanoparticles: Systematic

- optimisation of the preparative process and preliminary biological evaluation. *Pharm Res*
49. Interchim EDTA and EGTA chelating agents
  50. Anil A, Jose J (2021) Self-assembled Hydrogels: An Overview. In: Jiya Jose, Sabu Thomas, Vijay Kumar Thakurs (eds) *Nano Hydrogels*. Springer, Singapore, pp 247–261
  51. Silver FH (1981) Type I Collagen Fibrillogenesis in Vitro ADDITIONAL EVIDENCE FOR THE ASSEMBLY MECHANISM\*
  52. Hinton TJ, Jallerat Q, Palchesko RN, Park JH, Grodzicki MS, Shue H-J, Ramadan MH, Hudson AR, Feinberg AW (2015) Three-dimensional printing of complex biological structures by freeform reversible embedding of suspended hydrogels. *Sci Adv* 1:e1500758–e1500758
  53. Wolf MT, Daly KA, Brennan-Pierce EP, Johnson SA, Carruthers CA, D’Amore A, Nagarkar SP, Velankar SS, Badylak SF (2012) A hydrogel derived from decellularized dermal extracellular matrix. *Biomaterials*
  54. Zhang YS, Khademhosseini A (2017) Advances in engineering hydrogels. *Science* (80-. ).
  55. Taylor M, Tomlins P, Sahota T (2017) Thermoresponsive Gels. *Gels*
  56. Klouda L, Mikos AG (2008) Thermoresponsive hydrogels in biomedical applications. *Eur. J. Pharm. Biopharm.*
  57. Choi YJ, Jun YJ, Kim DY, Yi HG, Chae SH, Kang J, Lee J, Gao G, Kong JS, Jang J, Chung WK, Rhie JW, Cho DW (2019) A 3D cell printed muscle construct with tissue-derived bioink for the treatment of volumetric muscle loss. *Biomaterials*
  58. Desai M, Jain NJ, Sharma R, Bahadur P (2000) Temperature and salt-induced micellization of some block copolymers in aqueous solution. *J Surfactants Deterg*
  59. Mizrahy S, Peer D (2012) Polysaccharides as building blocks for nanotherapeutics. *Chem Soc Rev*
  60. Seliktar D (2012) Designing cell-compatible hydrogels for biomedical applications. *Science* (80-. ).
  61. Altomare L, Bonetti L, Campiglio CE, De Nardo L, Draghi L, Tana F, Farè S (2018)

- Biopolymer-based strategies in the design of smart medical devices and artificial organs. *Int. J. Artif. Organs*
62. Wan W, Dawn Bannerman A, Yang L, Mak H (2014) Poly(Vinyl Alcohol) Cryogels for Biomedical Applications. *Adv Polym Sci*
63. Strandman S, Zhu XX (2016) Self-Healing Supramolecular Hydrogels Based on Reversible Physical Interactions. *Gels*
64. Pereira AC, Oliveira AEF, Bettio GB (2019)  $\beta$ -Cyclodextrin electropolymerization: mechanism, electrochemical behavior, and optimization. *Chem Pap*
65. Zhang H, Zhang F, Wu J (2013) Physically crosslinked hydrogels from polysaccharides prepared by freeze-thaw technique. *React Funct Polym*
66. Hua M, Wu S, Ma Y, Zhao Y, Chen Z, Frenkel I, Strzalka J, Zhou H, Zhu X, He X (2021) Strong tough hydrogels via the synergy of freeze-casting and salting out. *Nature*
67. Hassan CM, Peppas NA (2000) Structure and applications of poly(vinyl alcohol) hydrogels produced by conventional crosslinking or by freezing/thawing methods. *Adv. Polym. Sci.*
68. Nakano T, Nakaoki T (2011) Coagulation size of freezable water in poly(vinyl alcohol) hydrogels formed by different freeze/thaw cycle periods. *Polym J*
69. Sinawang G, Osaki M, Takashima Y, Yamaguchi H, Harada A (2020) Biofunctional hydrogels based on host–guest interactions. *Polym. J.*
70. Yue K, Trujillo-de Santiago G, Alvarez MM, Tamayol A, Annabi N, Khademhosseini A (2015) Synthesis, properties, and biomedical applications of gelatin methacryloyl (GelMA) hydrogels. *Biomaterials*
71. Xu H, Casillas J, Krishnamoorthy S, Xu C (2020) Effects of Irgacure 2959 and lithium phenyl-2,4,6-trimethylbenzoylphosphinate on cell viability, physical properties, and microstructure in 3D bioprinting of vascular-like constructs. *Biomed Mater*
72. Sydney Gladman A, Matsumoto EA, Nuzzo RG, Mahadevan L, Lewis JA (2016) Biomimetic 4D printing. *Nat Mater*
73. Hoffman AS (2012) Hydrogels for biomedical applications. *Adv. Drug Deliv. Rev.*
74. Akhtar MF, Hanif M, Ranjha NM (2016) Methods of synthesis of hydrogels ... A review.

- Saudi Pharm. J.
75. Grevesse T, Versaevel M, Gabriele S (2014) Preparation of Hydroxy-PAAm hydrogels for decoupling the effects of mechanotransduction cues. *J Vis Exp*
76. Kolesky DB, Homan KA, Skylar-Scott MA, Lewis JA (2016) Three-dimensional bioprinting of thick vascularized tissues. *Proc Natl Acad Sci U S A*
77. Weisel JW, Litvinov RI (2017) Fibrin formation, structure and properties. *Subcell Biochem*
78. Gong JP (2010) Why are double network hydrogels so tough? *Soft Matter*
79. Sun JY, Zhao X, Illeperuma WRK, Chaudhuri O, Oh KH, Mooney DJ, Vlassak JJ, Suo Z (2012) Highly stretchable and tough hydrogels. *Nature*
80. Chimene D, Kaunas R, Gaharwar AK (2020) Hydrogel Bioink Reinforcement for Additive Manufacturing: A Focused Review of Emerging Strategies. *Adv. Mater.*
81. Dragan ES (2014) Design and applications of interpenetrating polymer network hydrogels. A review. *Chem. Eng. J.*
82. Chen Q, Chen H, Zhu L, Zheng J (2015) Fundamentals of double network hydrogels. *J. Mater. Chem. B*
83. Haque MA, Kurokawa T, Gong JP (2012) Super tough double network hydrogels and their application as biomaterials. *Polymer (Guildf)*.
84. Gong JP, Katsuyama Y, Kurokawa T, Osada Y (2003) Double-network hydrogels with extremely high mechanical strength. *Adv Mater*
85. Lim HL, Hwang Y, Kar M, Varghese S (2014) Smart hydrogels as functional biomimetic systems. *Biomater. Sci.*
86. Rizwan M, Yahya R, Hassan A, Yar M, Azzahari AD, Selvanathan V, Sonsudin F, Abouloula CN (2017) pH sensitive hydrogels in drug delivery: Brief history, properties, swelling, and release mechanism, material selection and applications. *Polymers (Basel)*.
87. Swift T, Swanson L, Geoghegan M, Rimmer S (2016) The pH-responsive behaviour of poly(acrylic acid) in aqueous solution is dependent on molar mass. *Soft Matter*
88. Yuan Y, Chesnutt BM, Haggard WO, Bumgardner JD (2011) Deacetylation of chitosan:

- Material characterization and in vitro evaluation via albumin adsorption and pre-osteoblastic cell cultures. *Materials (Basel)*
89. Khan S, Ranjha NM (2014) Effect of degree of cross-linking on swelling and on drug release of low viscous chitosan/poly(vinyl alcohol) hydrogels. *Polym Bull*
90. Sadeghi M, Hosseinzadeh H (2008) Synthesis of starch-poly(sodium acrylate-co-acrylamide) superabsorbent hydrogel with salt and pH-responsiveness properties as a drug delivery system. *J Bioact Compat Polym*
91. Duan J, Liang X, Zhu K, Guo J, Zhang L (2017) Bilayer hydrogel actuators with tight interfacial adhesion fully constructed from natural polysaccharides. *Soft Matter*
92. Jabbari E, Tavakoli J, Sarvestani AS (2007) Swelling characteristics of acrylic acid polyelectrolyte hydrogel in a dc electric field. *Smart Mater Struct*
93. Han D, Farino C, Yang C, Scott T, Browe D, Choi W, Freeman JW, Lee H (2018) Soft Robotic Manipulation and Locomotion with a 3D Printed Electroactive Hydrogel. *ACS Appl Mater Interfaces*
94. Morales D, Palleau E, Dickey MD, Velev OD (2014) Electro-actuated hydrogel walkers with dual responsive legs. *Soft Matter*
95. Therriault D, White SR, Lewis JA (2003) Chaotic mixing in three-dimensional microvascular networks fabricated by direct-write assembly. *Nat Mater*
96. Jin Y, Compaan A, Chai W, Huang Y (2017) Functional Nanoclay Suspension for Printing-Then-Solidification of Liquid Materials. *ACS Appl Mater Interfaces*
97. Hinton TJ, Hudson A, Pusch K, Lee A, Feinberg AW (2016) 3D Printing PDMS Elastomer in a Hydrophilic Support Bath via Freeform Reversible Embedding. *ACS Biomater Sci Eng*
98. Lin NYC, Homan KA, Robinson SS, Kolesky DB, Duarte N, Moisan A, Lewis JA (2019) Renal reabsorption in 3D vascularized proximal tubule models. *Proc Natl Acad Sci U S A*
99. Truby RL, Wehner M, Grosskopf AK, Vogt DM, Uzel SGM, Wood RJ, Lewis JA (2018) Soft Somatosensitive Actuators via Embedded 3D Printing. *Adv Mater*
100. Johnston ID, McCluskey DK, Tan CKL, Tracey MC (2014) Mechanical characterization

- of bulk Sylgard 184 for microfluidics and microengineering. *J Micromechanics Microengineering*
101. Bandyopadhyay A, Vahabzadeh S, Shivaram A, Bose S (2015) Three-dimensional printing of biomaterials and soft materials. *MRS Bull*
  102. Markstedt K, Mantas A, Tournier I, Martínez Ávila H, Hägg D, Gatenholm P (2015) 3D bioprinting human chondrocytes with nanocellulose-alginate bioink for cartilage tissue engineering applications. *Biomacromolecules*
  103. Zheng Z, Eglin D, Alini M, Richards GR, Qin L, Lai Y (2020) Visible Light-Induced 3D Bioprinting Technologies and Corresponding Bioink Materials for Tissue Engineering: A Review. *Engineering*
  104. Turksen K (2015) Bioprinting in regenerative medicine
  105. Duocastella M, Patrascioiu A, Fernández-Pradas JM, Morenza JL, Serra P (2012) On the correlation between droplet volume and irradiation conditions in the laser forward transfer of liquids. *Appl Phys A Mater Sci Process*
  106. Kelly BE, Bhattacharya I, Heidari H, Shusteff M, Spadaccini CM, Taylor HK (2019) Volumetric additive manufacturing via tomographic reconstruction. *Science* (80- )
  107. Bernal PN, Delrot P, Loterie D, Li Y, Malda J, Moser C, Levato R (2019) Volumetric Bioprinting of Complex Living-Tissue Constructs within Seconds. *Adv Mater*
  108. Ma X, Qu X, Zhu W, Li YS, Yuan S, Zhang H, Liu J, Wang P, Lai CSE, Zanella F, Feng GS, Sheikh F, Chien S, Chen S (2016) Deterministically patterned biomimetic human iPSC-derived hepatic model via rapid 3D bioprinting. *Proc Natl Acad Sci U S A*
  109. Huh JT, Yoo JJ, Atala A, Lee SJ (2020) Three-dimensional bioprinting for tissue engineering. In: *Principles of Tissue Engineering*. Elsevier, pp 1391–1415
  110. Bagheri A, Jin J (2019) Photopolymerization in 3D Printing. *ACS Appl Polym Mater*
  111. Miri AK, Nieto D, Iglesias L, Goodarzi Hosseinabadi H, Maharjan S, Ruiz-Esparza GU, Khoshakhlagh P, Manbachi A, Dokmeci MR, Chen S, Shin SR, Zhang YS, Khademhosseini A (2018) Microfluidics-Enabled Multimaterial Maskless Stereolithographic Bioprinting. *Adv Mater*
  112. Ge Q, Chen Z, Cheng J, Zhang B, Zhang YF, Li H, He X, Yuan C, Liu J, Magdassi S,

- Qu S (2021) 3D printing of highly stretchable hydrogel with diverse UV curable polymers. *Sci Adv*
113. Mironi-Harpaz I, Wang DY, Venkatraman S, Seliktar D (2012) Photopolymerization of cell-encapsulating hydrogels: Crosslinking efficiency versus cytotoxicity. *Acta Biomater*
114. Li X, Liu B, Pei B, Chen J, Zhou D, Peng J, Zhang X, Jia W, Xu T (2020) Inkjet Bioprinting of Biomaterials. *Chem. Rev.*
115. Lewis JA (2006) Direct ink writing of 3D functional materials. *Adv Funct Mater*
116. Murphy S V., Skardal A, Atala A (2013) Evaluation of hydrogels for bio-printing applications. *J Biomed Mater Res - Part A*
117. Davoodi E, Sarikhani E, Montazerian H, Ahadian S, Costantini M, Swieszkowski W, Willerth SM, Walus K, Mofidfar M, Toyserkani E, Khademhosseini A, Ashammakhi N (2020) Extrusion and Microfluidic-Based Bioprinting to Fabricate Biomimetic Tissues and Organs. *Adv. Mater. Technol.*
118. Shi L, Carstensen H, Höglz K, Lunzer M, Li H, Hilborn J, Ovsianikov A, Ossipov DA (2017) Dynamic Coordination Chemistry Enables Free Directional Printing of Biopolymer Hydrogel. *Chem Mater*
119. Senior JJ, Cooke ME, Grover LM, Smith AM (2019) Fabrication of Complex Hydrogel Structures Using Suspended Layer Additive Manufacturing (SLAM). *Adv Funct Mater*
120. O'Bryan CS, Bhattacharjee T, Niemi SR, Balachandar S, Baldwin N, Ellison ST, Taylor CR, Sawyer WG, Angelini TE (2017) Three-dimensional printing with sacrificial materials for soft matter manufacturing. *MRS Bull*
121. Shiwarski DJ, Hudson AR, Tashman JW, Feinberg AW (2021) Emergence of FRESH 3D printing as a platform for advanced tissue biofabrication. *APL Bioeng.*
122. Bhattacharjee T, Zehnder SM, Rowe KG, Jain S, Nixon RM, Sawyer WG, Angelini TE (2015) Writing in the granular gel medium. *Sci Adv*
123. O'Bryan CS, Bhattacharjee T, Hart S, Kabb CP, Schulze KD, Chilakala I, Sumerlin BS, Sawyer WG, Angelini TE (2017) Self-assembled micro-organogels for 3D printing silicone structures. *Sci Adv*

124. Compaan AM, Song K, Huang Y (2019) Gellan Fluid Gel as a Versatile Support Bath Material for Fluid Extrusion Bioprinting. *ACS Appl Mater Interfaces*
125. Dubbin K, Hori Y, Lewis KK, Heilshorn SC (2016) Dual-Stage Crosslinking of a Gel-Phase Bioink Improves Cell Viability and Homogeneity for 3D Bioprinting. *Adv Healthc Mater*
126. Grosskopf AK, Truby RL, Kim H, Perazzo A, Lewis JA, Stone HA (2018) Viscoplastic Matrix Materials for Embedded 3D Printing. *ACS Appl Mater Interfaces*
127. Rodriguez MJ, Dixon TA, Cohen E, Huang W, Omenetto FG, Kaplan DL (2018) 3D freeform printing of silk fibroin. *Acta Biomater*
128. Skylar-Scott MA, Uzel SGM, Nam LL, Ahrens JH, Truby RL, Damaraju S, Lewis JA (2019) Biomanufacturing of organ-specific tissues with high cellular density and embedded vascular channels. *Sci Adv*
129. Luo G, Yu Y, Yuan Y, Chen X, Liu Z, Kong T (2019) Freeform, Reconfigurable Embedded Printing of All-Aqueous 3D Architectures. *Adv Mater*
130. Leblanc KJ, Niemi SR, Bennett AI, Harris KL, Schulze KD, Sawyer WG, Taylor C, Angelini TE (2016) Stability of High Speed 3D Printing in Liquid-Like Solids. *ACS Biomater Sci Eng*
131. Muth JT, Vogt DM, Truby RL, Mengüç Y, Kolesky DB, Wood RJ, Lewis JA (2014) Embedded 3D printing of strain sensors within highly stretchable elastomers. *Adv Mater*
132. Kolesky DB, Truby RL, Gladman AS, Busbee TA, Homan KA, Lewis JA (2014) 3D bioprinting of vascularized, heterogeneous cell-laden tissue constructs. *Adv Mater*
133. Blaeser A, Duarte Campos DF, Weber M, Neuss S, Theek B, Fischer H, Jahnens-Dechent W (2013) Biofabrication Under Fluorocarbon: A Novel Freeform Fabrication Technique to Generate High Aspect Ratio Tissue-Engineered Constructs. *Biores Open Access*
134. Shin S, Kwak H, Shin D, Hyun J (2019) Solid matrix-assisted printing for three-dimensional structuring of a viscoelastic medium surface. *Nat Commun*
135. Duarte Campos DF, Blaeser A, Weber M, Jäkel J, Neuss S, Jahnens-Dechent W, Fischer H (2013) Three-dimensional printing of stem cell-laden hydrogels submerged in a hydrophobic high-density fluid. *Biofabrication*

136. Lee A, Hudson AR, Shiwartski DJ, Tashman JW, Hinton TJ, Yerneni S, Bliley JM, Campbell PG, Feinberg AW (2019) 3D bioprinting of collagen to rebuild components of the human heart. *Science* (80- )
137. Noor N, Shapira A, Edri R, Gal I, Wertheim L, Dvir T (2019) 3D Printing of Personalized Thick and Perfusionable Cardiac Patches and Hearts. *Adv Sci*
138. Ding H, Chang RC (2018) Printability study of bioprinted tubular structures using liquid hydrogel precursors in a support bath. *Appl Sci*
139. Spencer AR, Shirzaei Sani E, Soucy JR, Corbet CC, Primbetova A, Koppes RA, Annabi N (2019) Bioprinting of a Cell-Laden Conductive Hydrogel Composite. *ACS Appl Mater Interfaces*
140. Jeon O, Lee YB, Hinton TJ, Feinberg AW, Alsberg E (2019) Cryopreserved cell-laden alginate microgel bioink for 3D bioprinting of living tissues. *Mater Today Chem*
141. Isaacson A, Swioklo S, Conn CJ (2018) 3D bioprinting of a corneal stroma equivalent. *Exp Eye Res*
142. Bordoni M, Karabulut E, Kuzmenko V, Fantini V, Pansarasa O, Cereda C, Gatenholm P (2020) 3D Printed Conductive Nanocellulose Scaffolds for the Differentiation of Human Neuroblastoma Cells. *Cells*
143. Park SM, Kim HW, Park HJ (2020) Callus-based 3D printing for food exemplified with carrot tissues and its potential for innovative food production. *J Food Eng*
144. Chen S, Jang TS, Pan HM, Jung H Do, Sia MW, Xie S, Hang Y, Chong SKM, Wang D, Song J (2020) 3D freeform printing of nanocomposite hydrogels through in situ precipitation in reactive Viscous fluid. *Int J Bioprinting*
145. Bao G, Jiang T, Ravanbakhsh H, Reyes A, Ma Z, Strong M, Wang H, Kinsella JM, Li J, Mongeau L (2020) Triggered micropore-forming bioprinting of porous viscoelastic hydrogels. *Mater Horizons*
146. Mirdamadi E, Tashman JW, Shiwartski DJ, Palchesko RN, Feinberg AW (2020) FRESH 3D Bioprinting a Full-Size Model of the Human Heart. *ACS Biomater Sci Eng*
147. Štumberger G, Vihar B (2018) Freeform perfusable microfluidics embedded in hydrogel matrices. *Materials (Basel)*

148. Wang Z, Florczyk SJ (2020) Freeze-FRESH: A 3D printing technique to produce biomaterial scaffolds with hierarchical porosity. *Materials (Basel)*
149. Bhattacharjee T, Gil CJ, Marshall SL, Urueña JM, O'Bryan CS, Carstens M, Keselowsky B, Palmer GD, Ghivizzani S, Gibbs CP, Sawyer WG, Angelini TE (2016) Liquid-like Solids Support Cells in 3D. *ACS Biomater Sci Eng*
150. Lee S, Sani ES, Spencer AR, Guan Y, Weiss AS, Annabi N (2020) Embedded 3D Bioprinting of Gelatin Methacryloyl-Based Constructs with Highly Tunable Structural Fidelity. *Adv Mater*
151. Jin Y, Compaan A, Bhattacharjee T, Huang Y (2016) Granular gel support-enabled extrusion of three-dimensional alginate and cellular structures. *Biofabrication*
152. Nelson AZ, Kundukad B, Wong WK, Khan SA, Doyle PS (2020) Embedded droplet printing in yield-stress fluids. *Proc Natl Acad Sci U S A*
153. Zhao J, Hussain M, Wang M, Li Z, He N (2020) Embedded 3D printing of multi-internal surfaces of hydrogels. *Addit Manuf*
154. Krishnamoorthy S, Zhang Z, Xu C (2019) Biofabrication of three-dimensional cellular structures based on gelatin methacrylate–alginate interpenetrating network hydrogel. *J Biomater Appl*
155. Ning L, Mehta R, Cao C, Theus A, Tomov M, Zhu N, Weeks ER, Bauser-Heaton H, Serpooshan V (2020) Embedded 3D Bioprinting of Gelatin Methacryloyl-Based Constructs with Highly Tunable Structural Fidelity. *ACS Appl Mater Interfaces*
156. Afghah F, Altunbek M, Dikyol C, Koc B (2020) Preparation and characterization of nanoclay-hydrogel composite support-bath for bioprinting of complex structures. *Sci Rep*
157. Liu W, Zhang YS, Heinrich MA, De Ferrari F, Jang HL, Bakht SM, Alvarez MM, Yang J, Li YC, Trujillo-de Santiago G, Miri AK, Zhu K, Khoshakhlagh P, Prakash G, Cheng H, Guan X, Zhong Z, Ju J, Zhu GH, Jin X, Shin SR, Dokmeci MR, Khademhosseini A (2017) Rapid Continuous Multimaterial Extrusion Bioprinting. *Adv Mater*
158. Rocca M, Fragasso A, Liu W, Heinrich MA, Zhang YS (2018) Embedded Multimaterial Extrusion Bioprinting. *SLAS Technol*

159. Basu A, Saha A, Goodman C, Shafranek RT, Nelson A (2017) Catalytically Initiated Gel-in-Gel Printing of Composite Hydrogels. *ACS Appl Mater Interfaces*
160. Jeon O, Lee Y Bin, Jeong H, Lee SJ, Wells D, Alsberg E (2019) Individual cell-only bioink and photocurable supporting medium for 3D printing and generation of engineered tissues with complex geometries. *Mater Horizons*
161. Cidonio G, Cooke M, Glinka M, Dawson JI, Grover L, Oreffo ROC (2019) Printing bone in a gel: using nanocomposite bioink to print functionalised bone scaffolds. *Mater Today Bio*
162. Mendes BB, Gómez-Florit M, Hamilton AG, Detamore MS, Domingues RMA, Reis RL, Gomes ME (2020) Human platelet lysate-based nanocomposite bioink for bioprinting hierarchical fibrillar structures. *Biofabrication*
163. Moxon SR, Cooke ME, Cox SC, Snow M, Jeys L, Jones SW, Smith AM, Grover LM (2017) Suspended Manufacture of Biological Structures. *Adv Mater*
164. Mirdamadi E, Muselimyan N, Koti P, Asfour H, Sarvazyan N (2019) Agarose slurry as a support medium for bioprinting and culturing freestanding cell-laden hydrogel constructs. *3D Print Addit Manuf*
165. Highley CB, Song KH, Daly AC, Burdick JA (2019) Jammed Microgel Inks for 3D Printing Applications. *Adv Sci*
166. Song KH, Highley CB, Rouff A, Burdick JA (2018) Complex 3D-Printed Microchannels within Cell-Degradable Hydrogels. *Adv Funct Mater*
167. Jin Y, Chai W, Huang Y (2017) Printability study of hydrogel solution extrusion in nanoclay yield-stress bath during printing-then-gelation biofabrication. *Mater Sci Eng C*
168. Jin Y, Song K, Gellermann N, Huang Y (2019) Printing of hydrophobic materials in fumed silica nanoparticle suspension. *ACS Appl Mater Interfaces*
169. Greenwood TE, Hatch SE, Colton MB, Thomson SL (2021) 3D printing low-stiffness silicone within a curable support matrix. *Addit Manuf*
170. Savoji H, Davenport Huyer L, Mohammadi MH, Lun Lai BF, Rafatian N, Bannerman D, Shoaib M, Bobicki ER, Ramachandran A, Radisic M (2020) 3D Printing of Vascular

- Tubes Using Bioelastomer Prepolymers by Freeform Reversible Embedding. *ACS Biomater Sci Eng*
171. Abdollahi S, Davis A, Miller JH, Feinberg AW (2018) Expert-guided optimization for 3D printing of soft and liquid materials. *PLoS One*
  172. Menon A, Póczos B, Feinberg AW, Washburn NR (2019) Optimization of Silicone 3D Printing with Hierarchical Machine Learning. *3D Print Addit Manuf*
  173. Hajash K, Sparrman B, Guberan C, Laucks J, Tibbits S (2017) Large-scale rapid liquid printing. *3D Print Addit Manuf*
  174. Wehner M, Truby RL, Fitzgerald DJ, Mosadegh B, Whitesides GM, Lewis JA, Wood RJ (2016) An integrated design and fabrication strategy for entirely soft, autonomous robots. *Nature*
  175. Karyappa R, Ching T, Hashimoto M (2020) Embedded Ink Writing (EIW) of Polysiloxane Inks. *ACS Appl Mater Interfaces*
  176. Patrício SG, Sousa LR, Correia TR, Gaspar VM, Pires LS, Luís JL, Oliveira JM, Mano JF (2020) Freeform 3D printing using a continuous viscoelastic supporting matrix. *Biofabrication*
  177. Nair SK, Basu S, Sen B, Lin MH, Kumar AN, Yuan Y, Cullen PJ, Sarkar D (2019) Colloidal Gels with Tunable Mechanomorphology Regulate Endothelial Morphogenesis. *Sci Rep*
  178. Tomás H, Alves CS, Rodrigues J (2018) Laponite®: A key nanoplatform for biomedical applications? *Nanomedicine Nanotechnology, Biol. Med.*
  179. Zhao J, He N (2020) A mini-review of embedded 3D printing: Supporting media and strategies. *J. Mater. Chem. B*
  180. Therriault D, Shepherd RF, White SR, Lewis JA (2005) Fugitive inks for direct-write assembly of three-dimensional microvascular networks. *Adv Mater*
  181. Gerigk M, Bulstrode H, Shi HH, Tönisen F, Cerutti C, Morrison G, Rowitch D, Huang YY (2021) On-chip perivascular niche supporting stemness of patient-derived glioma cells in a serum-free, flowable culture. *Lab Chip* 21:2343–2358
  182. Moldovan NI, Hibino N, Nakayama K (2017) Principles of the kenzan method for

- robotic cell spheroid-based three-dimensional bioprinting. *Tissue Eng - Part B Rev*
183. Gao Q, He Y, Fu J zhong, Liu A, Ma L (2015) Coaxial nozzle-assisted 3D bioprinting with built-in microchannels for nutrients delivery. *Biomaterials*
184. Yu Y, Moncal KK, Li J, Peng W, Rivero I, Martin JA, Ozbolat IT (2016) Three-dimensional bioprinting using self-Assembling scalable scaffold-free “tissue strands” as a new bioink. *Sci Rep*
185. Holland I, Logan J, Shi J, McCormick C, Liu D, Shu W (2018) 3D biofabrication for tubular tissue engineering. *Bio-Design Manuf* 1:89–100
186. Akther F, Yakob SB, Nguyen NT, Ta HT (2020) Surface Modification Techniques for Endothelial Cell Seeding in PDMS Microfluidic Devices. *Biosensors*
187. Suntornnond R, Tan EYS, An J, Chua CK (2017) A highly printable and biocompatible hydrogel composite for direct printing of soft and perfusable vasculature-like structures. *Sci Rep*
188. Homan KA, Kolesky DB, Skylar-Scott MA, Herrmann J, Obuobi H, Moisan A, Lewis JA (2016) Bioprinting of 3D Convoluted Renal Proximal Tubules on Perfusionable Chips. *Sci Rep*
189. Miller JS, Stevens KR, Yang MT, Baker BM, Nguyen DHT, Cohen DM, Toro E, Chen AA, Galie PA, Yu X, Chaturvedi R, Bhatia SN, Chen CS (2012) Rapid casting of patterned vascular networks for perfusable engineered three-dimensional tissues. *Nat Mater*
190. Sooppan R, Paulsen SJ, Han J, Ta AH, Dinh P, Gaffey AC, Venkataraman C, Trubelja A, Hung G, Miller JS, Atluri P (2016) In Vivo Anastomosis and Perfusion of a Three-Dimensionally-Printed Construct Containing Microchannel Networks. *Tissue Eng - Part C Methods*
191. Pollet AMAO, Homburg EFGA, Cardinaels R, den Toonder JMJ (2020) 3D sugar printing of networks mimicking the vasculature. *Micromachines*
192. Bégin-Drolet A, Dussault MA, Fernandez SA, Larose-Dutil J, Leask RL, Hoesli CA, Ruel J (2017) Design of a 3D printer head for additive manufacturing of sugar glass for tissue engineering applications. *Addit Manuf*

193. Hamidi A, Tadesse Y (2020) 3D printing of very soft elastomer and sacrificial carbohydrate glass/elastomer structures for robotic applications. *Mater Des*
194. Koyata Y, Ikeuchi M, Ikuta K (2013) Sealless 3-D microfluidic channel fabrication by sacrificial caramel template direct-patterning. In: Proceedings of the IEEE International Conference on Micro Electro Mechanical Systems (MEMS)
195. Gelber MK, Bhargava R (2015) Monolithic multilayer microfluidics via sacrificial molding of 3D-printed isomalt. *Lab Chip*
196. Gelber MK, Kole MR, Kim N, Aluru NR, Bhargava R (2017) Quantitative Chemical Imaging of Nonplanar Microfluidics. *Anal Chem*
197. He Y, Qiu J, Fu J, Zhang J, Ren Y, Liu A (2015) Printing 3D microfluidic chips with a 3D sugar printer. *Microfluid Nanofluidics*
198. Zhang YS, Davoudi F, Walch P, Manbachi A, Luo X, Dell'Erba V, Miri AK, Albadawi H, Arneri A, Li X, Wang X, Dokmeci MR, Khademhosseini A, Oklu R (2016) Bioprinted thrombosis-on-a-chip. *Lab Chip*
199. Chang CC, Boland ED, Williams SK, Hoyng JB (2011) Direct-write bioprinting three-dimensional biohybrid systems for future regenerative therapies. *J. Biomed. Mater. Res. - Part B Appl. Biomater.*
200. Gao G, Park JY, Kim BS, Jang J, Cho DW (2018) Coaxial Cell Printing of Freestanding, Perfusionable, and Functional In Vitro Vascular Models for Recapitulation of Native Vascular Endothelium Pathophysiology. *Adv Healthc Mater*
201. Gong J, Schuurmans CCL, Genderen AM van, Cao X, Li W, Cheng F, He JJ, López A, Huerta V, Manríquez J, Li R, Li H, Delavaux C, Sebastian S, Capendale PE, Wang H, Xie J, Yu M, Masereeuw R, Vermonden T, Zhang YS (2020) Complexation-induced resolution enhancement of 3D-printed hydrogel constructs. *Nat Commun*
202. Hansen CJ, White SR, Sottos NR, Lewis JA (2011) Accelerated self-healing via ternary interpenetrating microvascular networks. *Adv Funct Mater*
203. Ji S, Almeida E, Guvendiren M (2019) 3D bioprinting of complex channels within cell-laden hydrogels. *Acta Biomater*
204. Xu Y, Hu Y, Liu C, Yao H, Liu B, Mi S (2018) A novel strategy for creating tissue-

- engineered biomimetic blood vessels using 3D bioprinting technology. *Materials (Basel)*
205. McMahon T, Zijl PCM Van, Gilad AA (2015) Creating Perfused Functional Vascular Channels Using 3D Bio-Printing Technology. *27:320–331*
206. Lee W, Lee V, Polio S, Keegan P, Lee JH, Fischer K, Park JK, Yoo SS (2010) On-demand three-dimensional freeform fabrication of multi-layered hydrogel scaffold with fluidic channels. *Biotechnol Bioeng*
207. Bertassoni LE, Cecconi M, Manoharan V, Nikkhah M, Hjortnaes J, Cristina AL, Barabaschi G, Demarchi D, Dokmeci MR, Yang Y, Khademhosseini A (2014) Hydrogel bioprinted microchannel networks for vascularization of tissue engineering constructs. *Lab Chip*
208. Norotte C, Marga FS, Niklason LE, Forgacs G (2009) Scaffold-free vascular tissue engineering using bioprinting. *Biomaterials*
209. Massa S, Sakr MA, Seo J, Bandaru P, Arneri A, Bersini S, Zare-Eelanjegh E, Jalilian E, Cha BH, Antona S, Enrico A, Gao Y, Hassan S, Acevedo JP, Dokmeci MR, Zhang YS, Khademhosseini A, Shin SR (2017) Bioprinted 3D vascularized tissue model for drug toxicity analysis. *Biomicrofluidics*
210. Toohey KS, Sottos NR, Lewis JA, Moore JS, White SR (2007) Self-healing materials with microvascular networks. *Nat Mater*
211. Wu W, Hansen CJ, Aragón AM, Geubelle PH, White SR, Lewis JA (2010) Direct-write assembly of biomimetic microvascular networks for efficient fluid transport. *Soft Matter*
212. Hansen CJ, Wu W, Toohey KS, Sottos NR, White SR, Lewis JA (2009) Self-healing materials with interpenetrating microvascular networks. *Adv Mater*
213. Li Z, Yang J, Li K, Zhu L, Tang W (2017) Fabrication of PDMS microfluidic devices with 3D wax jetting. *RSC Adv*
214. Cheng F, Cao X, Li H, Liu T, Xie X, Huang D, Maharjan S, Bei HP, Gómez A, Li J, Zhan H, Shen H, Liu S, He J, Zhang YS (2019) Generation of Cost-Effective Paper-Based Tissue Models through Matrix-Assisted Sacrificial 3D Printing. *Nano Lett*
215. Tseng TC, Hsieh FY, Theato P, Wei Y, Hsu S hui (2017) Glucose-sensitive self-healing hydrogel as sacrificial materials to fabricate vascularized constructs. *Biomaterials*

216. Ozbolat V, Dey M, Ayan B, Ozbolat IT (2019) Extrusion-based printing of sacrificial Carbopol ink for fabrication of microfluidic devices. *Biofabrication*
217. Dahlberg T, Stangner T, Zhang H, Wiklund K, Lundberg P, Edman L, Andersson M (2018) 3D printed water-soluble scaffolds for rapid production of PDMS micro-fluidic flow chambers. *Sci Rep*
218. Saggiomo V, Velders AH (2015) Simple 3D Printed Scaffold-Removal Method for the Fabrication of Intricate Microfluidic Devices. *Adv Sci*
219. Leung PYV (2017) Sugar 3D Printing: Additive Manufacturing with Molten Sugar for Investigating Molten Material Fed Printing. *3D Print Addit Manuf*
220. Gelber MK, Hurst G, Comi TJ, Bhargava R (2018) Model-guided design and characterization of a high-precision 3D printing process for carbohydrate glass. *Addit Manuf*
221. Khattak SF, Bhatia SR, Roberts SC (2005) Pluronic F127 as a cell encapsulation material: Utilization of membrane-stabilizing agents. *Tissue Eng*
222. Hözl K, Lin S, Tytgat L, Van Vlierberghe S, Gu L, Ovsianikov A (2016) Bioink properties before, during and after 3D bioprinting. *Biofabrication*
223. Gillispie G, Prim P, Copus J, Fisher J, Mikos AG, Yoo JJ, Atala A, Lee SJ (2020) Assessment methodologies for extrusion-based bioink printability. *Biofabrication*
224. Naghieh S, Sarker MD, Sharma NK, Barhoumi Z, Chen X (2020) Printability of 3D printed hydrogel scaffolds: Influence of hydrogel composition and printing parameters. *Appl Sci*
225. Bessler N, Ogiermann D, Buchholz MB, Santel A, Heidenreich J, Ahmmed R, Zaehres H, Brand-Saberi B (2019) Nydus One Syringe Extruder (NOSE): A Prusa i3 3D printer conversion for bioprinting applications utilizing the FRESH-method. *HardwareX*
226. Ioannidis K, Danalatos RI, Champeris Tsaniras S, Kaplani K, Lokka G, Kanellou A, Papachristou DJ, Bokias G, Lygerou Z, Taraviras S (2020) A Custom Ultra-Low-Cost 3D Bioprinter Supports Cell Growth and Differentiation. *Front Bioeng Biotechnol*
227. Pusch K, Hinton TJ, Feinberg AW (2018) Large volume syringe pump extruder for desktop 3D printers. *HardwareX*

228. Yenilmez B, Temirel M, Knowlton S, Lepowsky E, Tasoglu S (2019) Development and characterization of a low-cost 3D bioprinter. *Bioprinting*
229. Ozbolat IT, Chen H, Yu Y (2014) Development of “Multi-arm Bioprinter” for hybrid biofabrication of tissue engineering constructs. *Robot Comput Integr Manuf*
230. Shen EM, McCloskey KE (2021) Affordable, high-resolution bioprinting with embedded concentration gradients. *Bioprinting*
231. Fitzsimmons RE, Aquilino MS, Quigley J, Chebotarev O, Tarlan F, Simmons CA (2018) Generating vascular channels within hydrogel constructs using an economical open-source 3D bioprinter and thermoreversible gels. *Bioprinting*
232. UFACTORY uArm Swift & uArm Swift Pro Specifications
233. Embedding FR, Hydrogels S FRESH Blended Gelatin Slurry Preparation Protocol. 13–14
234. uArm-Developer/uArm-Python-SDK: New python library for Swift, Swift Pro. Accessed 7 Aug 2021
235. Allegro MicroSystems A4988 - DMOS Microstepping Driver with Translator and Overcurrent Protection. Accessed 7 Aug 2021
236. RS Components Ltd RS Pro Pro Hybrid, Permanent Magnet Stepper Motor 1.8°. Accessed 7 Aug 2021
237. drylin® lead screw, dryspin® high helix thread, right-hand thread, 1.4301 (304) stainless steel. Accessed 7 Aug 2021
238. International Rectifier IRLR8743PbF, IRLU8743PbF - HEXFET ® Power MOSFET
239. Allevi 3 - Allevi. Accessed 3 Dec 2021
240. Printheads - CELLINK. Accessed 3 Dec 2021
241. BIO X 3D Bioprinter - CELLINK. Accessed 3 Dec 2021
242. 3D-Bioplotter® Starter Series | EnvisionTEC. Accessed 3 Dec 2021
243. Bioprinter - The modular Solution for Tissue Engineering from GeSiM. Accessed 3 Dec 2021

244. Zhang YS, Haghiashtiani G, Hübscher T, Kelly DJ, Lee JM, Lutolf M, McAlpine MC, Yeong WY, Zenobi-Wong M, Malda J (2021) 3D extrusion bioprinting. *Nat Rev Methods Prim* 2021 11:1–20
245. Lee J, Kim KE, Bang S, Noh I, Lee C (2017) A desktop multi-material 3D bio-printing system with open-source hardware and software. *Int J Precis Eng Manuf*
246. Kahl M, Gertig M, Hoyer P, Friedrich O, Gilbert DF (2019) Ultra-low-cost 3D bioprinting: Modification and application of an off-the-shelf desktop 3D-printer for biofabrication. *Front Bioeng Biotechnol*
247. Spiesz EM, Yu K, Lehner BAE, Schmieden DT, Aubin-Tam ME, Meyer AS (2019) Three-dimensional patterning of engineered biofilms with a do-it-yourself bioprinter. *J Vis Exp*
248. Tashman JW, Shiawski DJ, Feinberg AW (2021) A high performance open-source syringe extruder optimized for extrusion and retraction during FRESH 3D bioprinting. *HardwareX*
249. Skylar-Scott MA, Mueller J, Visser CW, Lewis JA (2019) Voxelated soft matter via multimaterial multinozzle 3D printing. *Nature*
250. Deng J, Yuk H, Wu J, Varela CE, Chen X, Roche ET, Guo CF, Zhao X (2021) Electrical bioadhesive interface for bioelectronics. *Nat Mater*
251. Xu S, Zhang Y, Jia L, Mathewson KE, Jang KI, Kim J, Fu H, Huang X, Chava P, Wang R, Bhole S, Wang L, Na YJ, Guan Y, Flavin M, Han Z, Huang Y, Rogers JA (2014) Soft microfluidic assemblies of sensors, circuits, and radios for the skin. *Science* (80- )
252. Kim DH, Ahn JH, Won MC, Kim HS, Kim TH, Song J, Huang YY, Liu Z, Lu C, Rogers JA (2008) Stretchable and foldable silicon integrated circuits. *Science* (80- )
253. Rogers JA, Someya T, Huang Y (2010) Materials and mechanics for stretchable electronics. *Science* (80- ).
254. Lin S, Yuk H, Zhang T, Parada GA, Koo H, Yu C, Zhao X (2016) Stretchable Hydrogel Electronics and Devices. *Adv Mater*
255. Shepherd RF, Ilievski F, Choi W, Morin SA, Stokes AA, Mazzeo AD, Chen X, Wang M, Whitesides GM (2011) Multigait soft robot. *Proc Natl Acad Sci U S A*

256. Morin SA, Shepherd RF, Kwok SW, Stokes AA, Nemiroski A, Whitesides GM (2012) Camouflage and display for soft machines. *Science* (80- )
257. Nojoomi A, Arslan H, Lee K, Yum K (2018) Bioinspired 3D structures with programmable morphologies and motions. *Nat Commun*
258. Yuk H, Wu J, Sarrafian TL, Mao X, Varela CE, Roche ET, Griffiths LG, Nabzdyk CS, Zhao X (2021) Rapid and coagulation-independent haemostatic sealing by a paste inspired by barnacle glue. *Nat Biomed Eng*
259. Tavakoli S, Klar AS (2020) Advanced hydrogels as wound dressings. *Biomolecules*
260. Schroeder TBH, Guha A, Lamoureux A, Vanrenterghem G, Sept D, Shtein M, Yang J, Mayer M (2017) An electric-eel-inspired soft power source from stacked hydrogels. *Nature*
261. Yang C, Suo Z (2018) Hydrogel iontronics. *Nat. Rev. Mater.*
262. Mantha S, Pillai S, Khayambashi P, Upadhyay A, Zhang Y, Tao O, Pham HM, Tran SD (2019) Smart hydrogels in tissue engineering and regenerative medicine. *Materials* (Basel).
263. Rodell CB, Dusaj NN, Highley CB, Burdick JA (2016) Injectable and Cytocompatible Tough Double-Network Hydrogels through Tandem Supramolecular and Covalent Crosslinking. *Adv Mater*
264. Garciamendez-Mijares CE, Agrawal P, Martínez GG, Juarez EC, Zhang YS (2021) State-of-art affordable bioprinters: A guide for the DiY community. *Appl Phys Rev* 8:031312
265. GitHub - gcodetools. Accessed 27 Sep 2021
266. GitHub - Inkscape-centerline-trace. Accessed 27 Sep 2021
267. Gleadall A, Visscher D, Yang J, Thomas D, Segal J (2018) Review of additive manufactured tissue engineering scaffolds: relationship between geometry and performance. *Burn Trauma*
268. Zhu Z, Guo SZ, Hirdler T, Eide C, Fan X, Tolar J, McAlpine MC (2018) 3D Printed Functional and Biological Materials on Moving Freeform Surfaces. *Adv Mater*
269. Kanta J (2015) Collagen matrix as a tool in studying fibroblastic cell behavior. *Cell*

## Adhes Migr

270. Marcombe R, Cai S, Hong W, Zhao X, Lapusta Y, Suo Z (2010) A theory of constrained swelling of a pH-sensitive hydrogel. *Soft Matter*
271. Lei IM, Jiang C, Lei CL, de Rijk SR, Tam YC, Swords C, Sutcliffe MPF, Malliaras GG, Bance M, Huang YY (2021) 3D printed biomimetic cochleae and machine learning co-modelling provides clinical informatics for cochlear implant patients
272. Schiavone G, Lacour SP (2019) Conformable bioelectronic interfaces: Mapping the road ahead. *Sci Transl Med*
273. Birmingham K, Grdinaru V, Anikeeva P, Grill WM, Pikov V, McLaughlin B, Pasricha P, Weber D, Ludwig K, Famm K (2014) Bioelectronic medicines: A research roadmap. *Nat. Rev. Drug Discov.* 13:399–400
274. Famm K, Litt B, Tracey KJ, Boyden ES, Slaoui M (2013) A jump-start for electroceuticals. *Nature*
275. McRackan TR, Bauschard M, Hatch JL, Franko-Tobin E, Droghini HR, Nguyen SA, Dubno JR (2018) Meta-analysis of quality-of-life improvement after cochlear implantation and associations with speech recognition abilities. *Laryngoscope*
276. Macherey O, Carlyon RP (2014) Cochlear implants. *Curr. Biol.*
277. Drennan WR, Svirsky MA, Fitzgerald MB, Rubinstein JT (2014) Mimicking Normal Auditory Functions with Cochlear Implant Sound Processing : Past, Present, and Future. In: Waltzman SB, Roland JT (eds) *Cochlear Implants*, 3rd ed. Thieme Medical Publishers, Incorporated, pp 47–60
278. Ben-Menachem E (2002) Vagus-nerve stimulation for the treatment of epilepsy. *Lancet Neurol.*
279. Vöröslakos M, Takeuchi Y, Brinyiczki K, Zombori T, Oliva A, Fernández-Ruiz A, Kozák G, Kincses ZT, Iványi B, Buzsáki G, Berényi A (2018) Direct effects of transcranial electric stimulation on brain circuits in rats and humans. *Nat Commun*
280. Vanpoucke FJ, Zarowski AJ, Peeters SA (2004) Identification of the impedance model of an implanted cochlear prosthesis from intracochlear potential measurements. *IEEE Trans Biomed Eng*

281. Frijns JHM, de Snoo SL, Schoonhoven R (1995) Potential distributions and neural excitation patterns in a rotationally symmetric model of the electrically stimulated cochlea. *Hear Res*
282. Shepherd RK, Hatsushika S, Clark GM (1993) Electrical stimulation of the auditory nerve: The effect of electrode position on neural excitation. *Hear Res*
283. Nogueira W, Schurzig D, Büchner D, Penninger RT, Würfel W (2016) Validation of a cochlear implant patient-specific model of the voltage distribution in a clinical setting. *Front Bioeng Biotechnol*
284. Erixon E, Högstorp H, Wadin K, Rask-Andersen H (2009) Variational anatomy of the human cochlea: Implications for cochlear implantation. *Otol Neurotol*
285. Maura K. Cosetti (2014) Intraoperative Monitoring During Cochlear Implantation. In: Susan B. Waltzman, J. Thomas Roland (eds) *Cochlear Implants*, 3rd ed. Thieme Medical Publishers, Incorporated, pp 100–107
286. Wong P, George S, Tran P, Sue A, Carter P, Li Q (2016) Development and validation of a high-fidelity finite-element model of monopolar stimulation in the implanted Guinea pig cochlea. *IEEE Trans Biomed Eng*
287. Adunka O, Kiefer J, Unkelbach MH, Lehnert T, Gstoettner W (2004) Development and evaluation of an improved cochlear implant electrode design for electric acoustic stimulation. *Laryngoscope*
288. Huang CQ, Shepherd RK, Carter PM, Seligman PM, Tabor B (1999) Electrical stimulation of the auditory nerve: Direct current measurement in vivo. *IEEE Trans Biomed Eng*
289. Ekdale EG (2016) Form and function of the mammalian inner ear. *J Anat*
290. Opitz A, Falchier A, Linn GS, Milham MP, Schroeder CE (2017) Limitations of ex vivo measurements for in vivo neuroscience. *Proc Natl Acad Sci U S A*
291. Romeni S, Valle G, Mazzoni A, Micera S (2020) Tutorial: a computational framework for the design and optimization of peripheral neural interfaces. *Nat Protoc* 15:3129–3153
292. Malherbe TK, Hanekom T, Hanekom JJ (2015) The effect of the resistive properties of bone on neural excitation and electric fields in cochlear implant models. *Hear Res*

293. Pietsch M, Aguirre Dávila L, Erfurt P, Avci E, Lenarz T, Kral A (2017) Spiral Form of the Human Cochlea Results from Spatial Constraints. *Sci Rep*
294. Gill EL, Li X, Birch MA, Huang YYS (2018) Multi-length scale bioprinting towards simulating microenvironmental cues. *Bio-Design Manuf.* 1:77–88
295. Nin F, Yoshida T, Sawamura S, Ogata G, Ota T, Higuchi T, Murakami S, Doi K, Kurachi Y, Hibino H (2016) The unique electrical properties in an extracellular fluid of the mammalian cochlea; their functional roles, homeostatic processes, and pathological significance. *Pflugers Arch. Eur. J. Physiol.*
296. Jiang C, Singhal S, Landry T, Roberts I, De Rijk S, Brochier T, Goehring T, Tan YC, Carlyon RP, Bance M, Malliaras GG (2021) An Instrumented Cochlea Model for the Evaluation of Cochlear Implant Electrical Stimulus Spread. *IEEE Trans Biomed Eng* PP:
297. Parreño M, Di Lella FA, Fernandez F, Boccio CM, Ausili SA (2020) Toward Self-Measures in Cochlear Implants: Daily and “Homemade” Impedance Assessment. *Front Digit Heal* 2:582562
298. Jiang C, de Rijk SR, Malliaras GG, Bance ML (2020) Electrochemical impedance spectroscopy of human cochleas for modeling cochlear implant electrical stimulus spread. *APL Mater* 8:1–8
299. Fedorov A, Beichel R, Kalpathy-Cramer J, Finet J, Fillion-Robin JC, Pujol S, Bauer C, Jennings D, Fennessy F, Sonka M, Buatti J, Aylward S, Miller J V., Pieper S, Kikinis R (2012) 3D Slicer as an image computing platform for the Quantitative Imaging Network. *Magn Reson Imaging*
300. Hornik K, Stinchcombe M, White H (1989) Multilayer feedforward networks are universal approximators. *Neural Networks*
301. Abadi M, Barham P, Chen J, Chen Z, Davis A, Dean J, Devin M, Ghemawat S, Irving G, Isard M, Kudlur M, Levenberg J, Monga R, Moore S, Murray DG, Steiner B, Tucker P, Vasudevan V, Warden P, Wicke M, Yu Y, Zheng X (2016) TensorFlow: A system for large-scale machine learning. In: Proceedings of the 12th USENIX Symposium on Operating Systems Design and Implementation, OSDI 2016
302. Kingma DP, Ba JL (2015) Adam: A method for stochastic optimization. In: 3rd

International Conference on Learning Representations, ICLR 2015 - Conference Track  
Proceedings

303. Bionics A (2005) HiRes 90K® Surgeon's Manual for the HiFocus® Helix and HiFocus® 1j Electrodes
304. Kohavi R (1995) A Study of Cross-Validation and Bootstrap for Accuracy Estimation and Model Selection. *Int Jt Conf Artif Intell*
305. Toni T, Welch D, Strelkowa N, Ipsen A, Stumpf MPH (2009) Approximate Bayesian computation scheme for parameter inference and model selection in dynamical systems. *J R Soc Interface*
306. Clerx M, Robinson M, Lambert B, Lei CL, Ghosh S, Mirams GR, Gavaghan DJ (2019) Probabilistic Inference on Noisy Time Series (PINTS). *J Open Res Softw* 7:23
307. Harada Y, Harada Y (1983) Reissner's membrane. In: *Atlas of the Ear*. Springer Netherlands, pp 165–169
308. Baumann SB, Wozny DR, Kelly SK, Meno FM (1997) The electrical conductivity of human cerebrospinal fluid at body temperature. *IEEE Trans Biomed Eng*
309. Akhtari M, Bryant HC, Mamelak AN, Heller L, Shih JJ, Mandelkern M, Matlachov A, Ranken DM, Best ED, Sutherling WW (2000) Conductivities of three-layer human skull. *Brain Topogr*
310. Micco AG, Richter CP (2006) Electrical resistivity measurements in the mammalian cochlea after neural degeneration. *Laryngoscope*
311. Tang C, You F, Cheng G, Gao D, Fu F, Yang G, Dong X (2008) Correlation between structure and resistivity variations of the live human skull. *IEEE Trans Biomed Eng*
312. Akhtari M, Bryant HC, Mamelak AN, Flynn ER, Heller L, Shih JJ, Mandelkern M, Matlachov A, Ranken DM, Best ED, Dimauro MA, Lee RR, Sutherling WW (2002) Conductivities of three-layer live human skull. *Brain Topogr*
313. Hoekema R, Wieneke GH, Leijten FSS, Van Veelen CWM, Van Rijen PC, Huiskamp GJM, Ansems J, Van Huffelen AC (2003) Measurement of the conductivity of skull, temporarily removed during epilepsy surgery. *Brain Topogr*
314. Oostendorp TF, Delbeke J, Stegeman DF (2000) The conductivity of the human skull:

- Results of in vivo and in vitro measurements. *IEEE Trans Biomed Eng*
315. Fernandez-Corazza M, Turovets S, Luu P, Price N, Muravchik CH, Tucker D (2018) Skull modeling effects in conductivity estimates using parametric electrical impedance tomography. *IEEE Trans Biomed Eng*
316. Balmer TW, Vesztergom S, Broekmann P, Stahel A, Büchler P (2018) Characterization of the electrical conductivity of bone and its correlation to osseous structure. *Sci Rep*
317. Briaire JJ, Frijns JHM (2000) Field patterns in a 3D tapered spiral model of the electrically stimulated cochlea. *Hear Res*
318. Law SK (1993) Thickness and resistivity variations over the upper surface of the human skull. *Brain Topogr*
319. Saha S, Williams PA (1992) Electric and Dielectric Properties of Wet Human Cortical Bone as a Function of Frequency. *IEEE Trans Biomed Eng*
320. Armin Bunde, Jan W. Kantelhardt (2005) Diffusion and Conduction in Percolation Systems – Theory and Applications. In: Heijmans P, Jörg Kärger (eds) *Diffusion in Condensed Matter*. Springer, Berlin, pp 895–914
321. Majdani O, Schurzig D, Hussong A, Rau T, Wittkopf J, Lenarz T, Labadie RF (2010) Force measurement of insertion of cochlear implant electrode arrays in vitro: Comparison of surgeon to automated insertion tool. *Acta Otolaryngol*
322. A J Pearmain, A G Clegg (2013) Insulators. In: G R Jones (ed) *Electrical Engineer's Reference Book*, 15th ed. Elsevier Ltd, p 15
323. Faes TJC, Van Der Meij HA, De Munck JC, Heethaar RM (1999) The electric resistivity of human tissues (100 HZ-10 MHZ): A meta- analysis of review studies. *Physiol. Meas.*
324. Guimarães CF, Gasperini L, Marques AP, Reis RL (2020) The stiffness of living tissues and its implications for tissue engineering. *Nat. Rev. Mater.*
325. Rho JY, Tsui TY, Pharr GM (1997) Elastic properties of human cortical and trabecular lamellar bone measured by nanoindentation. *Biomaterials*
326. Pelliccia P, Venail F, Bonafé A, Makeieff M, Iannetti G, Bartolomeo M, Mondain M (2014) Cochlea size variability and implications in clinical practice. *Acta Otorhinolaryngol Ital*

327. Mori MC, Chang KW (2012) CT analysis demonstrates that cochlear height does not change with age. *Am J Neuroradiol*
328. Avci E, Nauwelaers T, Lenarz T, Hamacher V, Kral A (2014) Variations in microanatomy of the human cochlea. *J Comp Neurol*
329. Meng J, Li S, Zhang F, Li Q, Qin Z (2016) Cochlear size and shape variability and implications in cochlear implantation surgery. *Otol Neurotol*
330. Davis TJ, Zhang D, Gifford RH, Dawant BM, Labadie RF, Noble JH (2016) Relationship between electrode-to-modiolus distance and current levels for adults with cochlear implants. *Otol Neurotol*
331. Smith A, Mason AK (1997) Cost estimation predictive modeling: Regression versus neural network. *Eng Econ*
332. Suesserman MF, Spelman FA (1993) Lumped-Parameter Model for In Vivo Cochlear Stimulation. *IEEE Trans Biomed Eng*
333. Strelioff D (1973) A computer simulation of the generation and distribution of cochlear potentials. *J Acoust Soc Am*
334. Horch KW, Burgess PR (2004) Peripheral Nervous System. In: Kenneth W. Horch, Gurpreet S. Dhillon (eds) *Neuroprosthetics: Theory and Practice*, 2nd ed. World Scientific Publishing Co.Pte. Ltd., Singapore, pp 30–45
335. Rattay F (1999) The basic mechanism for the electrical stimulation of the nervous system. *Neuroscience*
336. Todd CA, Naghdy F, Svehla MJ (2007) Force application during cochlear implant insertion: An analysis for improvement of surgeon technique. *IEEE Trans Biomed Eng*
337. Zeng FG, Rebscher S, Harrison W, Sun X, Feng H (2008) Cochlear Implants: System Design, Integration, and Evaluation. *IEEE Rev Biomed Eng*
338. Palleau E, Morales D, Dickey MD, Velev OD (2013) Reversible patterning and actuation of hydrogels by electrically assisted ionoprinting. *Nat Commun*
339. Zeng FG (2004) Trends in Cochlear Implants. *Trends Amplif*
340. Mens LHM (2007) Advances in Cochlear Implant Telemetry: Evoked Neural Responses, Electrical Field Imaging, and Technical Integrity. *Trends Amplif*

341. de Rijk SR, Tam YC, Carlyon RP, Bance ML (2020) Detection of Extracochlear Electrodes in Cochlear Implants with Electric Field Imaging/Transimpedance Measurements: A Human Cadaver Study. *Ear Hear*
342. Frolenkov GI, Belyantseva IA, Friedman TB, Griffith AJ (2004) Genetic insights into the morphogenesis of inner ear hair cells. *Nat. Rev. Genet.*
343. Lahav A, Skoe E (2014) An acoustic gap between the NICU and womb: A potential risk for compromised neuroplasticity of the auditory system in preterm infants. *Front Neurosci*